Multi-Gigabit Millimeter Wave Communication Links

**Von der Fakultät für Informatik, Elektrotechnik und Informationstechnik
der Universität Stuttgart zur Erlangung der Würde eines Doktor-Ingenieurs (Dr.-Ing.) genehmigte Abhandlung**

Vorgelegt von

Dipl.-Ing. Jochen Antes

aus Birkenfeld/Nahe

Hauptberichter:	**Prof. Dr.-Ing. Ingmar Kallfass**
Mitberichter:	**Prof. Dr.-Ing. Thomas Kürner**

Tag der mündlichen Prüfung: **22.06.2015**

**Institut für Robuste Leistungshalbleitersysteme
der Universität Stuttgart
2015**

Acknowledgements

This dissertation originates from my work as a teaching and research associate under the supervision of Prof. Dr. Ingmar Kallfass, first at the Institut für Hochfrequenztechnik and Elektronik (IHE) at the Karlsruhe Institute of Technology (KIT) in Karlsruhe, Germany, later at the Institut of Robust Power Semiconductor Systems at the University of Stuttgart in Stuttgart, Germany. The results shown in this thesis were achieved in a close cooperation with the High Frequency Electronics group at the Fraunhofer Institute for Applied Solid State Physics (IAF) in Freiburg, Germany, where large parts of the MMIC-designs were realized. To the success of both this thesis and the research projects related with it, many people contributed in many different ways:

First and foremost, I would like to thank my academic supervisors, Prof. Dr. Ingmar Kallfass, Head of the ILH, and Prof. Dr. Thomas Kürner from the Institut für Nachrichtentechnik at the Technische Universität Braunschweig, Braunschweig, Germany for their support and many fruitful and enlightening discussions. Especially Prof. Kallfass provided the opportunities and environment to realize the work and experiments presented in this thesis and thereby made the thesis possible in the first place. Further I would like to express my warmest gratitude to Prof. Thomas Zwick, Head of the IHE, for welcoming me at his institute and providing the possibilities for various interesting research projects which contributed to the overall results of this work. All three have supported me both on a professional and on a personal level throughout the time of my research, and I am well aware of the fact that such encouragement is never to be taken for granted.

I am very grateful to Prof. Dr. Roth-Stielow for being the head of the thesis defense jury and Prof. Dr. Frühauf for completing the examination

board. Further, I would like to thank Prof. Dr. Oliver Ambacher, Head of the Fraunhofer-IAF, for the possibility to conduct parts of my research at his institute and for the access to the institute's excellent measurement equipment.

Furthermore, I would like to thank the colleagues at the IAF, the IHE and the ILH for their help and support as well as for a very pleasant working environment.
At the IAF, special thanks goes to Sandrine Wagner and Hermann Massler for their help and support during extensive measurement campaigns, also to Michael Kuri for bearing with and realizing my ideas. Axel Tessmann and Arnulf Leuther provided a deep insight into the MMIC technology as well as support during many circuit design phases. Thank you for that. With Daniel Bruch and Daniel Lopez-Diaz I had great times during layout and measurement campaigns and the Daniels are the best partners for business trips one could think of.
Amongst the many colleagues at the IHE, I would like to especially express my gratitude to Philipp Pahl, Tobias Mahler, Daniel Müller, Sebastian Diebold, Serdal Ayhan and Mario Pauli for making my time in Karlsruhe a very pleasant one, not only during working hours but also at countless evening events. My special thanks go to Ulrich Lewark with whom I not only shared an office but also the joys and sorrows of a Ph.D. student's life.
Further, I would like to thank the technical staff at the IAF and IHE, amongst others, Ronald Vester, Andreas Gallego, Mirko Nonnenmacher, Hans-Peter Stulz and Markus Riessle, for their professional help with various topics and ideas.
During my time at the ILH Florian Boes, Tobias Messinger and Dominik Meier worked together with me on many research projects and supported the outdoor measurement campaigns presented in this thesis. Also, together with Joachim Längst, Cristino Salcines and Christiane Kloz, they helped to create a pleasant atmosphere at the institute during and after work.
I am also very grateful to all the people whom I met in the course of the

research projects GISALI, ACcESS, MilliLink and Terapan. It was a pleasure to work with you on those promising topics.

Finally, I would like to thank my closest friends and family for their support through discussion and encouragement during the work on this thesis. Most of all I thank Friederike for the continuous supply with chocolate, ice-cream or distraction whenever it was needed, for her critical prove-reading of the thesis and particularly for motivating me to get things finished.

Abstract

This dissertation is concerned with the search for new approaches to realize multi-gigabit wireless communication links. To satisfy the consumers' growing demand for high-speed mobile connections, the achievable data rate in future wireless front- and backhaul applications, building the mobile network's backbone, but also in short range wireless connections, needs to be significantly increased. Following latest discussions and statements, data rates well beyond 10 Gbit/s will be necessary for these use cases.

To the present day, such wireless links are realized in the microwave regime, where the maximum data rates are limited by the restricted bandwidths achievable technologically at these carrier frequencies, as well as restraining frequency allocations. First approaches utilizing frequencies in the higher millimeter wave regime, i.e. above of 100 GHz, so far only operate with bandwidth-inefficient amplitude shift keying signals or use opto-electronics to generate a millimeter wave signal. The latter systems are also capable of using complex modulation formats but, up to now, are limited by comparably low transmit powers. To provide wireless links enabling multi-gigabit capacities combined with adequate reliability, new approaches in the realization of such systems will be necessary.

The use of electrical millimeter wave integrated circuits, capable of operating in this high frequency regime, will result in compact, light- weight and easy-to-deploy frontend components and also allow to transmit over much higher distances. Combining the advantages of extremely high bandwidths achievable with these circuits with the possibility of using bandwidth efficient complex modulation formats will take wireless communication to a new level. The challenge hereby is to relate effects introduced on component level to repercussions which appear on system level,

and, in a further step, reveal their impact and optimization potential.
In this thesis, the necessary aspects for the realization of all-electrical multi-gigabit wireless communication system in the millimeter wave regime are considered. A study of appropriate approaches of circuit topologies suitable to realize extremely broadband transmit and receive components allowing for multi-gigabit capability, as well as the design and realization of such circuits build the basis for a profound analysis of such transmission systems. An investigation of the wireless system's transmission quality under the influence of the frontend component's non-idealities reveal the system's limits but also the optimization potential. Finally, free space data transmission experiments are conducted to prove the feasibility of multi-gigabit communication links operating at such elevated frequencies.
In this dissertation, for the first time, system imperfections of millimeter wave communication links are related to the causative frontend non-ideality in a theoretical approach. The findings are verified by measurements. Furthermore, for the first time, outdoor transmission experiments across realistic distances unveiling the real potential of the proposed system solutions are shown.

Kurzzusammenfassung

Die vorliegende Dissertation beschäftigt sich mit der Suche nach neuen Ansätzen zur Realisierung von Multi-Gigabit-Funkkommunikationssystemen. Um die steigende Nachfrage der Verbraucher nach mobilen Datenverbindungen zu befriedigen, muss nicht nur die erzielbare Datenrate in zukünftigen drahtlosen Front- und Backhaul-Anwendungen, dem Rückgrat des Mobilfunknetzes, deutlich erhöht werden, sondern auch die der unterstüzenden drahtlosen Nahbereichsverbindungen. Aus aktuellen Diskussionen kann geschlossen werden, dass die benötigten Datenraten für diese Anwendungsszenarien deutlich über 10 Gbit/s liegen werden.
Bis heute werden solche drahtlose Verbindungen im Mikrowellenbereich realisiert, wo die maximale Datenrate durch die bei diesen Trägerfrequenzen erzielbaren Bandbreiten sowie durch strikte Frequenzzuweisungen eingeschränkt werden. Erste Ansätze, die die Nutzung von Frequenzen im hohen Millimeterwellenbereich, also bei Frequenzen über 100 GHz, verfolgen, verwenden bisher Signale mit einer bandbreiteninneffizienten Amplitudenumtastung oder verwenden optoelektronische Komponenten, um das Millimeterwellensignal zu erzeugen. Die letztgenannten Systeme sind zwar auch in der Lage mit komplexen Modulationsformaten zu arbeiten, sind aber bisher durch vergleichsweise geringe Sendeleistungen beschränkt. Um drahtlose Funkkommunikation mit Kapazitäten im Bereich von mehreren Gigabit pro Sekunde mit ausreichender Zuverlässigkeit zu entwickeln, werden neue Ansätze bei der Realisierung derartiger Systeme notwendig.
Die Verwendung von elektrischen monolithischen Millimeterwellenschaltungen zur Realisierung von Multi-Gigabit-Funksystemen führt zu kompakten, leichten und einfach einzusetzenden Frontend-Komponenten, die eine Signalübertragung über größere Entfernungen ermöglichen. Die

Kombination aus extrem hohen Bandbreiten durch diesen Schaltungsansatz und bandbreiteneffizienten komplexen Modulationsverfahren eröffnet neue Möglichkeiten für die erzielbaren Datenraten in der drahtlosen Kommunikation. Die Herausforderung hierbei liegt darin, die Auswirkungen der auf Komponentenebene entstehenden Nichtidealitäten mit den auf Systemebene auftretenden Effekten in Zusammenhang zu bringen und in einem weiteren Schritt deren Einfluss sowie das mögliche Optimierungspotenzial aufzuzeigen.
In dieser Arbeit werden die notwendigen Aspekte für die Realisierung von Multi-Gigabit-Funkkommunikationssystemen im Millimeterwellenbereich bestehend aus rein elektrischen Komponenten betrachtet. Eine Studie geeigneter Schaltungstopologien für die Realisierung extrem breitbandiger Sende- und Empfangskomponenten, sowie deren Design und Realisierung bilden die Basis für eine tiefgreifende Analyse solcher Übertragungssysteme. Eine Untersuchung der Übertragungsqualität des drahtlosen Systems unter dem Einfluss der nichtidealen Frontend-Komponenten zeigt nicht nur die Grenzen des Systems auf, sondern auch dessen Optimierungspotenzial. Abschließende Freiraum-Datenübertragungsexperimente zeigen die Machbarkeit solcher höchstdatenratiger Kommunikationsverbindungen in diesem extrem hohen Frequenzenbereich.
In dieser Dissertation wurden für Millimeterwellenfunksysteme erstmalig die Nichtidealitäten der Frontend-Komponenten mit den dadurch hervorgerufenen Systemeffekten in einen theoretischen Zusammenhang gebracht. Diese theoretischen Ergebnisse zeigen gute Übereinstimmungen zu vergleichenden Messungen am System. Darüber hinaus werden zum ersten Mal Freiraumübertragungsexperimente über realistische Distanzen mit Systemen in diesem Frequenzbereich präsentiert, die das tatsächliche Potenzial der vorgeschlagenen Systemlösung aufzeigen.

Contents

List of Abbreviations and Symbols

Abbreviations, upper case

3G	third generation [Represents the third generation of mobile telecommunication technology]
5G	5th generation mobile networks [Represents the next phase of mobile telecommunications standards beyond 4G/IMT-Advanced standards. 5G is planned to be available in 2020.]
AC	alternate current
A/D	analog-to-digital conversion
ADC	analog-to-digital converter
ADS	Advanced Design System
Amp	amplifier
ASK	amplitude shift keying
Att	attenuator
AWG	arbitrary waveform generator
AWGN	additive white Gaussian noise
BB	baseband
BBU	baseband unit
BER	bit error rate
BERT	bit error rate tester
BiCMOS	bipolar CMOS [an evolved semiconductor technology that integrates bipolar junction transistors and CMOS transistors in a single integrated circuit]
BPF	band pass filter
BPSK	binary phase shift keying
BSC	base station controller

BTS	base transceiver station
CMOS	complementary metal-oxide-semiconductor
CNR	carrier-to-noise ratio
CPW	coplanar waveguide
D/A	digital-to-analog conversion
DAC	digital-to-analog converter
DC	direct current
DDS	direct digital synthesis
DSB	double-sideband transmission
DSP	digital signal processing
EHF	extremely high frequency
EIRP	equivalent isotropically radiated power
ETSI	European Telecommunications Standards Institute
EVM	error vector magnitude
FEC	forward error correction
FFT	fast Fourier transform
FSO	free-space optical communication
FSPL	free-space path loss
GaAs	Gallium-Arsenide
GaN	Gallium-Nitride
GSM	Global System for Mobile Communication [originally: Groupe Spécial Mobile]
GW	gate width
HBT	heterojunction bipolar transistor
HEMT	high electron mobility transistor
HPF	high pass filter
Fraunhofer IAF	Fraunhofer Institute for Applied Solid State Physics
IEEE	Institute of Electrical and Electronics Engineers
IF	intermediate frequency
IMN	input matching network
InP	Indium-Phosphide
I/Q	inphase-quadrature
IR	image reject
Iso	isolator

ITRS	International Technology Roadmap for Semiconductors
ITU	International Telecommunication Union
KIT	Karlsruhe Institute of Technology
LNA	low noise amplifier
LO	local oscillator
LOS	line of sight
LPF	low pass filter
LSB	lower sideband
LTE	long term evolution [The standard is developed by the 3GPP (3rd Generation Partnership Project) and therefore also often called 3GPP LTE]
mHEMT	metamorphic high electron mobility transistor
MIMO	multiple-input multiple-output
MMIC	millimeter wave integrated circuit
MPA	medium power amplifier
OMN	output matching network
OOK	on-off keying
PA	power amplifier
PD	photo diode
PLL	phase-locked loop
PN	phase noise
PRBS	pseudo-random bit sequence
PSK	phase shift keying
QAM	quadrature amplitude modulation
QoS	Quality of Service
QPSK	quadrature phase shift keying
RF	radio frequency
RCL	rain cell length
RRH	remote radio head
RTD	resonant-tunneling diode
Rx	receiver
SBD	Schottky barrier diode
SD	Schottky diode

SG	signal generator
SG100G	Study Group 100 Gbit/s Wireless
SiGe	Silicon-Germanium
SNR	signal-to-noise ratio
SSB	single-sideband transmission
SWR	Südwestrundfunk (Southwest Broadcasting) [german regional public broadcasting corporation]
Tx	transmitter
USB	upper sideband
UTC-PD	uni-travelling-carrier photodiode
VCO	voltage controlled oscillator
VGA	variable gain amplifier
VSA	vector signal analysis
WLAN	wireless local area network
WPAN	wireless personal area network
WRC	World Radiocommunication Conference

Abbreviations, lower case

avg	average
bal	balanced topology [in the context of mixer topologies]
mmw	millimeter wave
rms	root-mean-square

Constants

c_0	speed of light [in vacuum: $c_0 = 299\,792\,458\,\mathrm{m/s}$]
e	Euler number [$e = 2.718\,281\,828\,4$]
k	Boltzmann constant [$k = 1.380\,648\,813 \times 10^{-23}\,\mathrm{J/K}$]

Greek symbols

α_{d}	constant phase difference between Tx and Rx LO
α_{r}	Gaussian distributed LO phase noise
β	specific absorption coefficient for rain attenuation
$\Delta\omega$	frequency offset
γ_{c}	specific attenuation due to fog
γ_{r}	specific attenuation due to rain
λ	wavelength
ω	carrier angular frequency
Φ_{rms}	root mean square phase noise power density
ϕ_{Rx}	receiver I/Q-phase imbalance
ϕ_{Tx}	transmitter I/Q-phase imbalance
ψ	constant offset
σ_1	constellation phase error caused by LO phase noise
σ_2	constellation phase error caused by total phase noise

Latin symbols

A	effective antenna area
B	bandwidth
C	channel capacity
CG	conversion gain
d	transmission distance
d_{Rx}	receiver DC-offset in I- or Q-path
d_{Tx}	transmitter DC-offset in I- or Q-path
E_{b}	energy per bit
E_{S}	energy per symbol

F	noise factor
f_c	carrier frequency
f_{LO}	LO frequency
f_{Max}	maximum frequency of oscillation
f_s	sampling frequency
f_T	transit frequency
G	gain
G_{ant}	antenna gain
G_{Rx}	receiver antenna gain
G_{Tx}	transmitter antenna gain
k_l	specific absorption coefficient for fog and clouds
k_r	specific absorption coefficient for rain attenuation
k_{Rx}	receiver I/Q-amplitude imbalance
k_{Tx}	transmitter I/Q-amplitude imbalance
L_{atm}	atmospheric attenuation
L_{fog}	additional attenuation due to fog
L_{rain}	additional attenuation due to rain
M	liquid water density in fog and clouds
n	multiplication factor of a frequency multiplier
N_0	noise power spectral density
NF	noise figure
N_{floor}	output noise floor of an oscillator
NF_{Rx}	total receiver noise figure
P_{1dB}	1-dB compression point
PAR	peak-to-average-power ratio
P_{avg}	average power
P_b	bit error probability
P_{out}	output power
P_{peak}	peak power
$P_{r,BB}$	received baseband signal power
P_t	transmit power
Q	quality factor
R	rain rate
$r_{1,max}$	maximum radius of the first Fresnel zone

R_b	bit rate
P_r	receive power
T	temperature
T_0	starting time of a measurement
t	time

List of Figures

List of Tables

1 Multi-Gigabit Millimeter Wave Wireless Communication

Wireless communication, denoting the transmission of information by the use of electromagnetic waves propagating between a transmitting and a receiving device, is an omnipresent form of information exchange. From the synchronization of a radio-controlled clock, where only one bit per second needs to be transmitted, to the mobile phone standard Global System for Mobile Communication (GSM), transmitting several thousand bits per second, through to current wireless local area network (WLAN) systems with peak data rates of up to 300 million bits per second, wireless communication technology is an indispensable part of everyday life which has experienced an enormous growth during the last decades expected to go on in the future. A prediction of the progress concerning wireless communication systems provides important information for future developments and markets, and also triggers necessary impulses for exploring new fields of research. Therefore, researchers as well as the communication industry observe the advances of data rate in wireless communication systems and try to find rules describing its development. In 2004, J. H. Yoakum presented a chart describing the data rate growth for the three main types of telecommunication systems, i.e. wireline, nomadic[1] and wireless networks in a time line starting from 1976 [Che04]. When considering this progress, it can be found that the data rates in both nomadic and wireless systems grow at nearly the same rate, following an exponential curve with a doubling of data rate roughly ever 18 months. Yoakum extrapolated this curve to predict the wireless capacity for future

[1] Nomadic network describes a network technology which provides wireless connectivity in a limited, well-defined area, for example Bluetooth or WLAN connectivity.

wireless systems and named this law in data rate growth *Edholm's law*, after his colleague Phil Edholm [Web07, Esm06]. In the same context Edholm stated that the observed continuous growth is strongly dependent on the consumer's need for ever-higher data rates and believed that one day this need will be satisfied, which would bring an immediate end to Edholm's law. In the same year, H. Eslambolchi observed a similar behavior of wireless data rate increase and stated that this growth followed exactly Moore's Law[2] [Che04]. Seven years later, in 2011, Fettweis et al. showed that the increase in data rate for wireless networks, not only cellular and WLAN but also for what he calls *short range point-to-point networks*, still follows the Moore's Law driven International Technology Roadmap for Semiconductors (ITRS) [FGK11]. Identifying an increase in data rate by a factor of ten in every five years (verified between 1995 and 2010), Fettweis et al. predicted that a data rate of 100 Gbit/s should be achieved for short range wireless links, whereat they address point-to-point links working at distances of up to 1 m with zero mobility[3] in the year 2015.
The results of the above observations prove that over the past 35 years, there has undoubtably been a continuous growth in data rate across most important wireless communication scenarios. But are today's wireless communication systems and transmission speeds already satisfying the consumers' needs, bringing Edholm's law to an end, or are there new applications and technologies which further drive the development towards ever higher data rates?
A further indicator for the development in wireless communications, are the mobile data traffic reports, conducted by several network and communication technology providers. Amongst others, those reports provide evaluations for the total number of mobile subscriptions as well as mobile

[2] In 1965 Gordon Moore proclaimed, that the number of transistors in an integrated circuit doubles approximately every two years [Moo98]. This law, although slightly altered over the years (now not only the number of transistors but also their performance is described by Moore's law and the time span for a doubling in performance is reduced to 18 month), still holds true and is one of the main driving factors for the integrated circuit technologies, building the basis for the International Technology Roadmap for Semiconductors (ITRS).

[3] Zero mobility describes scenario where the transmitting and receiving device are stationary at a fixed position with no relative movement to each other.

data traffic and thereby provide an insight into the tendency of consumer's needs. In one study from 2011, a 2.6-fold growth in overall global mobile traffic combined with a doubling in mobile network speed was observed for the year 2010 [Cis11]. Also an increase of the average connection speed for handheld mobile devices from 101 kbit/s in 2009 to 215 kbit/s in 2010 was identified, which even surpasses the prediction by Edholm's law. Relying on this data, a 10-fold increase in mobile connection speed, exceeding 2.2 Mbit/s in 2015 was predicted. In a follow up study from 2014, the average mobile network connection speed again doubled from 526 kbit/s in 2012 to 1387 kbit/s in 2013. For the subsequent years, the authors see a more timid progress and the average connection speed is expected to double only until 2018 [Cis14]. Both studies show that video streaming services are already one of the largest contributors to the total mobile traffic and will become even more relevant in the future. Following these two studies, although the growth in network speed follows Edholm's Law, a slow down in mobile network traffic can already be observed and is expected to get more distinct in the near future. The authors of the study presume to be one of the reasons for the slow down what is stated in the study's conclusion: "Backhaul[4] capacity must increase so mobile broadband, data access, and video services can effectively support consumer usage trends and keep mobile infrastructure costs in check" [Cis14]. Similar results have been obtained by a report from 2013, based on completely different data surveys than the previous study. The authors forecast a ten-fold growth in total mobile traffic, video streaming applications being one of the main contributors, between 2013 and 2019, and also see the development of high capacity backhaul networks as one of the key elements for the mobile communication of the future [Eri13, Eri14].
In conjunction with the shown data rate growth for mobile connections, also the capacities of the underlying mobile backhaul networks as well

[4]In a hierarchical mobile communications network, backhaul describes the links connecting the network core or backbone to the smaller subnetworks at deeper hierarchical levels, for example connecting the widely distributed base transceiver stations (BTSs) of the mobile network to the superordinated base station controller (BSC). Backhaul networks can be built by either using wired or wireless solutions, depending on the capacity requirements.

as the supportive nomadic networks (providing alternative connections at places where the demanded capacity cannot be handled via the mobile system alone) have to be increased. Historically, backhaul networks were built by using copper lines, but with the introduction and prevalence of smartphones and other smart-devices, both demanding huge amounts of mobile data traffic, these capacities are no longer sufficient for backhauling the fast third generation (3G) and long term evolution (LTE) signals, still less for the next generation of mobile connection called 5th generation mobile networks (5G). Therefore, the network operators upgrade to optical fiber connections as well as wireless point-to-point links in the microwave range for their backhaul networks. While optical fiber technologies provide data rates up to 100 Gbit/s, high performance transmission over distances of several kilometers and guaranteed availabilities, their deployment, especially in urban areas, is often expensive and time consuming. In 2009, trenching costs in an urban area could easily reach 250 000 $ per mile [Wel09]. In contrary, microwave links, while usually fast and easy to deploy, suffer from limited capacities and reduced availability under severe weather conditions. The commercially available data rates for such links range from several Mbit/s up to 3 Gbit/s, the latter being sufficient for backhauling the existing 3G and LTE signals between different cell towers [Mak12]. On the higher layers of the backhaul's hierarchy, closer to the network core, where traffic from multiple cell towers is aggregated, capacities of 40 and even 100 Gbit/s will be necessary. Nevertheless, following [Wel09], over 1 million point-to-point microwave links for mobile backhauling were sold worldwide in 2008 and it is stated in [AH13] that a high capacity wireless solution will get more and more important. The distances which needs to be bridged in such backhaul applications are between 1 and 5 km in urban or suburban areas. Considerung rural areas, much higher ranges are needed [AH13]. Besides backhaul networks, typical application scenarios for multi-gigabit wireless communication links are wireless data kiosk applications[5] and

[5]The data kiosk describes a scenario where the user wants to download a huge amount of data to a hand-held device in a short amount of time and within a restricted reception

wireless personal area networks (WPANs). The data rates aimed at in such networks range up to 100 Gbit/s, but with transmission distances in the range of several meters. In a WPAN, two or more nomadic devices can be connected at data rates up to several tens of Gbit/s to overcome a temporary cable solution, for example the connection between a high capacity storage device and a portable computer to run a complete backup in an extremely short time [Kür13]. Such kinds of applications are also addressed in a standardization approach by the IEEE 802.15 working group. In the recently formed task group IEEE 802.15 TG3d (100G), a technology independent standard for wireless systems operating in the high millimeter wave or sub-millimeter wave regime[6] and offering data rates up to 100 Gbit/s, shall be elaborated as an amendment on the IEEE 802.15.3[7] specification. Besides the mentioned WPAN, the applications of interest include wireless data centers, wireless intra-device communication as well as wireless front[8]- and backhauling [IEE13].

In conclusion, the consumer's growing demand for faster mobile networks and thereby on the underlying backhaul network, both confirmed by mobile traffic surveys, the research and development in high speed

area [FGK11].

[6] The operating frequency range can also be specified by giving the wavelength regime interchangeably to the frequency, vaguely corresponding to the resulting wavelength in a free-space transmission. Since the terms *microwave, millimeter wave* and *sub-millimeter wave range* are not strictly defined and used for different frequency ranges in various publications, the naming in this thesis will follow [Wil84], where the term *millimeter wave range* describes frequencies between 30 and 300 GHz, sometimes also called extremely high frequency (EHF), and the term *sub-millimeter wave* is a synonym for frequencies in the range from 300 to 3 THz. Consequently, the term *microwave* will be used for frequencies is the range of 3 to 30 GHz.

[7] "IEEE 802.15.3 is a standard for low-complexity, low-cost, low-power-consumption and high-data-rate wireless connectivity among multimedia devices supporting high levels of Quality of Service (QoS))." [IEE13]

[8] To further improve the capacities of future mobile networks, fronthaul architectures gain the interest of network operators. In such architectures, a single baseband unit (BBU), i.e. the system's baseband processing part, is connected to several remote radio heads (RRHs), i.e. the system's radio frequency (RF) frontend, via a wireless link or optical fiber. Thus, a higher density of antennas, implying a better network coverage, can be achieved with less effort in connecting the baseband processing units to the BSC.

wireless systems for nomadic scenarios and even more important, the IEEE standardization approaches, indicate that the end of Edholm's Law is not reached yet. They simultaneously show the industry's growing interest in high performance wireless communication links. To provide such wireless links enabling multi-gigabit capacities combined with adequate reliability, new approaches in the realization of such systems will be necessary.

1.1 The advantages of millimeter wave communication

According to Shannon's capacity limit for communication systems limited by additive white Gaussian noise [Sha84] as shown in equation (1.1), the channel capacity C, i.e. the amount of data that can be transmitted via this specific channel, depends on the channel's bandwidth B and the signal-to-noise ratio (SNR), i.e. the received signal power versus the noise power in the considered bandwidth:

$$C = B \cdot \log_2(1 + \mathrm{SNR}) \,. \tag{1.1}$$

Thus, in order to achieve wireless links for multi-gigabit capability, either the bandwidth or the SNR has to be increased. To determine in which way the resulting channel capacity is affected by such an increase, two cases shall be considered.
In a first attempt, the SNR is increased with the bandwidth B fixed, i.e. the received power increases while the noise power remain unchanged. Thus, the channel capacity from (1.1) can be approximated by $f(\mathrm{SNR}) \sim \log_2(1 + SNR)$.With the simplifications

$$\log_2(1 + x) \approx x \log_2(e) \,, \qquad x \approx 0 \tag{1.2}$$

$$\log_2(1 + x) \approx \log_2(x) \,, \qquad x \gg 1 \tag{1.3}$$

it can be seen, that for a low SNR regime, the capacity increases linearly, while for a high SNR regime it only increases logarithmically with the received power. This fact indicates that an increase of the channel capacity by a raise of the SNR will get power-inefficient for systems which already show a high SNR. For such systems, an increase of bandwidth would be the more efficient solution.
When considering an increase in channel capacity by a raise of bandwidth, equation (1.1) seems to indicate a linear dependency, which is indeed the case for increasing the bandwidth while maintaining a constant SNR. But since the received noise power also increases with the bandwidth, this would also imply an increase of the received power to keep the SNR constant. Considering a bandwidth increase combined with a constant receive power, i.e. the same power spread over a higher amount of bandwidth, resulting in an effectively reduced SNR, the channel capacity follows a function $f(\mathrm{B}) = B\log_2(1 + \frac{P_\mathrm{r}}{N_0 B})$, where P_r is the received power and N_0 is the noise power spectral density. For small bandwidths, corresponding to a high SNR, the channel capacity approximately equals the logarithm of the received power and scales linearly with the bandwidth. For high bandwidths, equation (1.2) can be applied again, simplifying (1.1) to

$$C = B\log_2(1 + \frac{P_\mathrm{r}}{N_0 B}) \approx B\left(\frac{P_\mathrm{r}}{N_0 B}\right)\log_2(e)\,, B \gg 1\,\mathrm{Hz}\,. \tag{1.4}$$

This relation indicates that in a high bandwidth regime, the channel capacity is proportional to the received power and nearly independent of the bandwidth, i.e. for a constant receive power and large bandwidths, the channel capacity is limited by $\frac{P_\mathrm{r}}{N_0}\log_2(e) \approx 1.44\frac{P_\mathrm{r}}{N_0}$. The above considerations are shown in more detail in [TV05].
In the context of wireless communication links for multi-gigabit applications discussed above, the two considerations show that in order to achieve a high channel capacity, both SNR and bandwidth, have to be taken into account and weighted against each other. Since many of today's wireless communication systems already work in the high SNR

regime and apply higher order modulation formats up to 64-quadrature amplitude modulation (QAM) to achieve data rates of several 100 Mbit/s [AH13], an increase in channel capacity involves a huge effort in system design. As shown in [KM13], the necessary SNR increase per bit increase in an M-QAM modulation scheme for additive white Gaussian noise (AWGN) channels is approximately 3 dB, which implies that the effort to switch from a 2-QAM to a 4-QAM modulation is approximately 3 dB, while resulting in a doubling of the data rate. In contrary, to switch from 256-QAM to 512-QAM modulation, while mandating another 3 dB SNR increase, only results in a 12.5 % raise in data rate but with requirements on the system's linearity and phase noise that are very hard to meet.

A much more efficient way to achieve the demanded channel capacities is the use of higher carrier frequencies which come along with higher usable bandwidths[9]. Wireless links operating in the millimeter wave, terahertz or optical domain, where large amounts of bandwidth are available and the principal feasibility of such links is already shown in [KHK+08, PTF+10, CAC+09], could be an excellent attempt to provide the needed data rates. So called free-space optical communication (FSO) links, operating in the infrared and near-infrared range, struggle with the influence of adverse weather effects, causing losses up to 100 dB/km and more [FM10, SMBF12]. In contrary, systems in the millimeter wave and low sub-millimeter wave region, roughly between 30 and 400 GHz can take advantage of a moderate influence of the atmosphere in defined frequency ranges [M. 13], as will be discussed later. Furthermore, systems using this frequency range can profit from reduced components sizes, scaling in relation to the wavelength of the carrier, as well as from the use of millimeter wave integrated circuits (MMICs) to realize the front-end components, allowing for a high level of integration and resulting in sys-

[9] As discussed in [Sen85], the bandwidth of a communication system is generally limited to a fixed fraction of the carrier frequency. Thus, the higher the carrier frequency, the larger the available transmission bandwidth. However, the exact fraction between the system's carrier frequency and available bandwidth depends on several parameter, mainly the system architecture and the technology used to build the frontend components.

tems which are light-weight and cost efficient as well as flexible and easy to deploy [HE11]. While the transmit component in such systems can either be implemented as electrical mixer circuits, modulating the data signal onto the carrier frequency, or as an optical device in the form of an uni-travelling-carrier photodiode (UTC-PD)[10], generating the transmit signal by photo-mixing two lasers, one unmodulated and one carrying the data signal, the system's receiver is always conducted as an electrical device, mostly in form of Schottky barrier diodes (SBDs) which detect the signal [DSB+14]. The drawbacks of a detection using SBDs are a limitation to amplitude detection, and a limited sensitivity. Schottky barrier diodes can also be used as downconverting mixer elements, thereby also allowing the detection of complex modulated data streams, but only with a limited bandwidth performance [JPS+10].
To decide which of the two possible transmitter architectures is the preferable, the comparison in [HKT+12] shall be invoked. There, one system with a UTC-PD and one with an MMIC-based mixer as a transmitter, both operating in the same frequency range between 116.5 and 133.5 GHz and both with similar system performance, are compared. In both systems, the same receiver in form of an MMIC-based amplitude shift keying (ASK) demodulator is used. The comparison shows that the MMIC-based system provides an output power of 16 dBm with an overall power consumption of 100 W, while the optical system provides an output power of 10 dBm, generated by an MMIC-based amplifier connected to the UTC-PD, with a total power consumption of 400 W. When considering the system size and complexity, in this case, the MMIC system is much more efficient. For the optical system considered here, in addition to the UTC-PD and amplifier, an optical modulator together with a voltage controlled oscillator (VCO) and a arrayed waveguide grating is used to modulate a single-mode laser and extract a two coherent laser lines with a spacing of 125 GHz. An

[10] As explained in [IKM+04], a UTC-PD only utilizes electrons as active carrier components, which allow for a high bandwidth and output current, combined with a wide-frequency tunability. Those characteristics make the UTC-PD an excellent candidate to convert a high-data rate communication signal delivered by an optical fiber into a electromagnetic wave which can be radiated via an antenna.

additional optical modulator is used to modulate one of these laser lines with the data signal. Photomixing of the modulated and unmodulated signals in the UTC-PD results in the wanted millimeter wave (mmw) transmission signal. Additionally several optical amplifiers are needed to generate appropriate optical power levels. In contrast, the electrical system only needs a local oscillator source followed by a frequency multiplier as well as the mmw modulator or mixer and two power amplifier stages. This makes the electrical solution much more power-, size- and weight-efficient. Nevertheless, as shown in [N. 13], each type of system is preferable for a specific application. The optical based system show advantages, where an identical data signal has to be delivered to many locations. Then the signal can be generated once at some kind of headquarter and delivered by an optical fiber to several remote sites, where then only an UTC-PD is needed to convert and convey the signal via an antenna. An electrical system is more advantageous in ad-hoc scenarios, where the system has to be set-up very quickly and has to be adaptable to different environments.

Conclusion: To realize compact, flexible and multi-functional high capacity wireless communication links, the most promising solution will be achieved by the use of electrical components operating in the millimeter wave frequency range in the form of millimeter wave integrated circuits.

1.1.1 Propagation loss factors in the millimeter wave regime

When considering wireless links for applications with transmission distances above several meters, in addition to the free-space path loss (FSPL)[11], which is the main loss factor in the link budget, the effects of atmospheric attenuation become more and more significant due to the interaction of

[11] In communication and radar systems, the FSPL describes the loss in signal strength of an electromagnetic wave propagating along a line-of-sight path through free space, with no obstacles blocking, reflecting or deflecting the signal. The free-space path loss is calculated via $FSPL = \frac{4\pi d}{\lambda}^2$, where d is the path length and λ the wavelength of the propagating signal.

the electromagnetic radiation with the atmosphere [MP05]. Under fair weather conditions, these effects result from water vapor absorption as well as from the oscillation of atmospheric gases causing absorption maxima due to molecular resonances at designated frequencies. The frequency ranges between those absorption maxima are called atmospheric attenuation windows. In adverse weather conditions, additional attenuation effects arise since the wavelength can be in the same dimension as rain drops or water droplets in fog or clouds. The accurate prediction of the atmospheric influences on the propagation behavior of electromagnetic waves is one of the most important issues for planning a long range wireless link, where knowledge of wave propagation, physical absorption mechanisms as well as meteorological effects and parameters have to be brought together. The International Telecommunication Union (ITU) has released recommendations on how to estimate the atmospheric effects for all frequencies up to 1 THz, separated by the influences due to a clear atmosphere [Rec09a], rain [Rec05, Rec07], clouds and fog [Rec09b], which are continuously refined, revised and compared to actual measurements [NIS+13, NAM13, KJYC13].
When plotting the curve describing the attenuation on a propagating electromagnetic wave caused by a clear atmosphere over frequency, as shown in figure 1.1, the absorption maxima and the atmospheric windows between them can be identified. For the millimeter and sub-millimeter wave regime up to 400 GHz, there are five atmospheric windows of different bandwidths, which are highlighted in figure 1.1. The first atmospheric window is located between 30 GHz, the beginning of the millimeter wave region, and 50 GHz, bordered by the oxygen absorption maximum located around 60 GHz. The following two windows, each providing a bandwidth around 43 GHz, are centered around 91 GHz and 147 GHz. The largest atmospheric attenuation window, with a bandwidth of 120 GHz, is located around 255 GHz. The last window is already located in the sub-millimeter wave regime, between 335 GHz and 365 GHz. Except for the last one, the atmospheric attenuation under fair weather conditions stays well below 10 dB/km, for frequencies below 100 GHz even below 1 dB/km. This additional attenuation and also the attenuation due to adverse weather effects

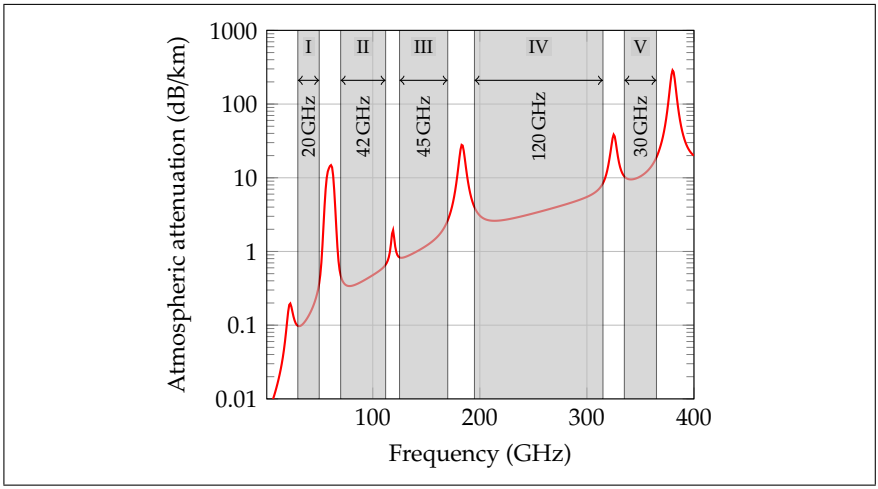

Figure 1.1: Specific attenuation of the atmosphere for frequencies between 1 and 400 GHz at a temperature of 20 °C, an air pressure of 1013 hPa and a water vapor density of 7.5 g/m^3. The atmospheric attenuation windows with their corresponding bandwidths are highlighted.

described above, have to be taken into account when determining the achievable transmission distance of a wireless link.

Conclusion: For transmitting data in the millimeter wave range over distances of several 100 m, the most suitable frequency bands are those located in the atmospheric attenuation windows around 40, 91, 147 and 255 GHz, where the additional attenuation stays well below 10 dB/km. In terms of highest available bandwidth, the atmospheric windows above the 60 GHz absorption line are more promising. Therefore, in the following, only these frequency ranges will be considered.

1.1.2 State of the art in millimeter wave wireless links

Now with the frequency bands of interest defined and discussed, a review of already existing wireless communication links[12] operating in this regimes for both commercially available and research related systems will give an insight into the achievable system performance.
The highest transmission distance in the millimeter wave range is achieved by the 120 GHz system already discussed above [HKT+12], which is capable of transmitting data rates of up to 10 Gbit/s over a distance of 5800 m with antenna gains at the transmitter and receiver of approx. 52 dBi. As already discussed in 1.1, this results are achieved both with a MMIC-based system and a system based on optical signal generation.
The highest data rate without the use of complex modulated data is shown in [DSB+14]. Here, a 40 Gbit/s ASK modulated data signal is generated by photo-mixing at an UTC-PD and radiated at 400 GHz. In the receiver, a 400 GHz subharmonic mixer is used to downconvert the signal to the baseband, where it is fed into a 45 GHz real-time oscilloscope for digital post-processing.
The highest absolute data rates of 54 and 50 Gbit/s are achieved by using complex modulation formats, the first one quadrature phase shift keying (QPSK), the latter 16-QAM and optically generated carriers at 100 and 87.5 GHz, respectively [PCD+11, LYZ+13]. In both experiments, subharmonic mixers are used to downconvert the received signal to the baseband where it is captured and digitally post-processed. Both authors show that the data rate can be further increased by using both the vertical and horizontal polarization plane, i.e. setting up one wireless link with horizontal polarization and a second one with vertical polarization. With this technique, in [PCD+11] a data rate of 100 Gbit/s is achieved. In [LYZ+13] two

[12] By wireless links, systems which transmit data via a free space channel are meant. In many publications, only back-to-back measurements, i.e. directly connecting the transmitter to the receiver, in some cases with an attenuator in between, are shown with the achievable transmission distance estimated out of these measurements. Since such measurements are only capable of showing the performance of the transmitter and receiver, but not the overall link performance including amplifiers and antennas and also neglect the influences of the channel, such results are not considered here.

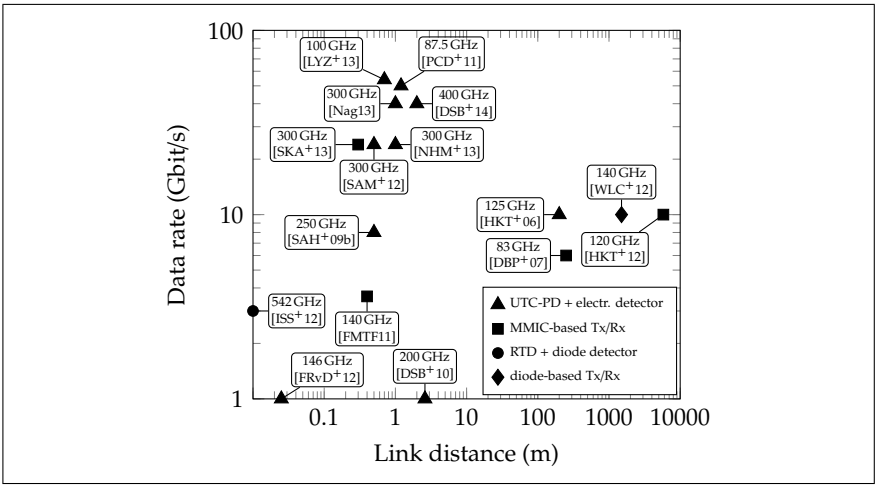

Figure 1.2: State of the art in mmw wireless communication systems, separated by the used technology. The achieved data rate for single channel and single polarization transmission is shown. The corresponding carrier frequencies are annotated at each entry.

wireless links at 100 GHz, each with a data rate of 54 Gbit/s, and two additional links at 37.5 GHz, each with a data rate of 56 Gbit/s, all with the polarization method, are set up. By combining the data rate of all four wireless links, an overall transmitted data rate above 400 Gbit/s could be achieved.

Although no commercial products utilizing carrier frequencies above 100 GHz exists, there are some commercially available point-to-point wireless links for high-speed front- and backhauling and low-latency applications operating in the frequency band between 71 and 86 GHz. Amongst a growing variety of providers, the two most impressive results are achieved with the two links presented in [E-b12] and [NEC14]. The first one provides data rates up to 3 Gbit/s over distances up to 8 km combined with adaptive modulation formats up to 64-QAM. The second link also provides data rates up to 3 Gbit/s with 256-QAM modulation and over dis-

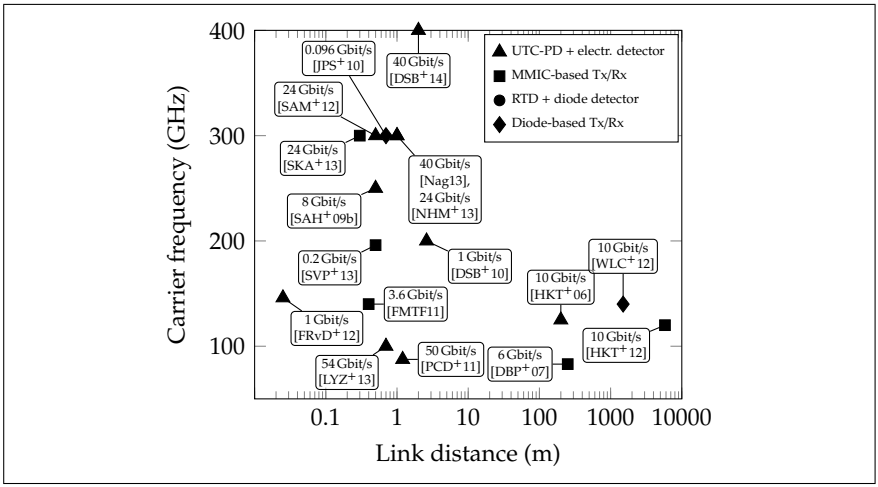

Figure 1.3: State of the art in mmw wireless communication systems, showing the carrier frequency versus the transmission distance. The corresponding data rates are annotated at each entry.

tances up to 4 km. As shown in [LP09], such links can for example be used to build a gigabit ethernet backbone network for the entire metropolitan area of Las Vegas. According to the authors, this wireless backbone network was much more cost-efficient than a comparable fiber network ($5 million compared to $75 million) and the latency is unmatched by any other network of the same size.

To compare the different systems, in figures 1.2 and 1.3 the most remarkable achievements in wireless link performances, published in the years between 2006 and 2014, in terms of data rate and carrier frequency are plotted over the corresponding transmitted distances and the respective other parameters attached at each point. The first figure shows that up to now, the highest data rates have been achieved by using opto-electrical systems, utilizing UTC-PDs and SBDs, but their achieved transmission distances are limited to several meters. Higher transmission distances are achieved by using fully electrical transmitters or at least MMIC-based

power amplifiers (PAs). It is notable that the achieved data rates seem to be independent of the used carrier frequency. This effect is due to the use of higher order complex modulation formats which seem to be implemented more easily at lower frequency ranges. In figure 1.3, the used carrier frequency is plotted versus the link distance, showing that up to now, transmission distances higher than 20 m are only reached by using moderate carrier frequencies of up to 140 GHz. Systems using carrier frequencies at 200 GHz and above are limited to distances up to 2 m, which might be enough for specific short-range indoor communication but are insufficient for the intended long-range applications. Since the free-space path loss and atmospheric attenuation effects increase with the carrier frequency, the limited transmission distance for the higher frequency bands is based on the limited output power of the UTC-PDs in the opto-electrical systems [HKT+12]. Also, in the all-electrical systems, although higher than for the UTC-PDs, only limited output power can be generated over the high bandwidths needed to transmit data rates above 10 Gbit/s.

Conclusion: The review of the state of the art corroborates the conclusions drawn above. Since the highest data rates are achieved either by the use of higher order complex modulation formats or by systems with extremely high bandwidths, to achieve the highest possible data rates, a combination of extremely broadband transmitters and receivers operating at mmw frequencies together with the use of complex modulation formats seems to be the most promising solution. To simultaneously achieve transmission distances above the reported ones of several meters, the state of the art shows, that the highest distances are achieved with the use of fully electrical transmit and receive circuits due to their higher available output powers.

1.2 System considerations

In the preceding discussions, the high millimeter wave region and the fully electrical MMIC-based approach are identified as the most promising way to realize multi-gigabit wireless communication systems for high-capacity data transmission. Consequently, the objective of this thesis is the realization of MMIC-based wireless frontends operating in the atmospheric attenuation windows discussed above, as well as to take wireless communication to a new level by combining the advantages of extremely high bandwidths with the possibility of complex modulation schemes.
To be able to define this goal more precisely and to derive appropriate system specifications, in the following, a review of the worldwide frequency regulations needs to be done to define allocated frequency bands for the intended applications. Furthermore, out of the variety of existing transmitting and receiving schemes, an appropriate system architecture, providing sufficient bandwidth for the targeted data rate, as well as a suitable transistor technology to realize the MMICs for this system have to be found. Finally, a review of appropriate baseband components and measurement equipment, necessary to prove the achieved results, is given.

1.2.1 Frequency allocation and regulations

The possibility of realizing and setting up a wireless communication link is not only determined by the availability of an atmospheric attenuation window. Also the worldwide mandatory frequency allocation plans, provided by the ITU [ITU12, Article 5, Section IV] as well as additional guidelines dispensed by national regulatory entities have to be taken into account. In the following, the allocations and regulations for the atmospheric windows discussed above, will be reviewed. Since this work will focus on realizing wireless links with the highest possible data rates by the use of extremely high bandwidth as shown in section 1.1, the frequency range between 30 and 60 GHz will not be further considered. Furthermore, this frequency range is already extensively described in the literature and the interested reader is referred to [HW11, YXVG11, Ema13].

1.2.1.1 Communication using the E-band

When considering the atmospheric window between 70 and 112 GHz, labeled with *II* in figure 1.1, there are two frequency bands dedicated to *fixed services*, i.e. radio communication between specified fixed points, which essentially include all applications of long-range, back- and fronthaul communication, by the ITU frequency allocation plan [ITU12, Article 1], one band between 71 to 76 GHz and the other between 81 to 86 GHz. The same frequency bands can also be used for *fixed satellite services*[13], the lower one in space-to-earth, the upper one for earth-to-space scenarios. As a synonym for these two frequency bands, the expression *E-band*[14], is widely used and will also serve as a synonym for these frequency bands in the following chapters.
The intermediate frequency band, between 76 and 81 GHz, is reserved for *radio astronomy* and *amateur satellite services*. Also, automotive radar applications are allowed to operate in this frequency range. The higher frequency bands from 86 up to 112 GHz are primarily reserved for radio astronomy and earth exploration applications, which may be shared with fixed services in limited bandwidth and transmit power. But in all cases, the operation of radio astronomy services have to be protected [ITU12, Article 5, Section IV, footnote 5.149], a fact which make those bands usable for communication links only within certain limits.
The European Telecommunications Standards Institute (ETSI) and German Federal Network Agency (Bundesnetzagentur für Elektrizität, Gas, Telekommunikation, Post und Eisenbahnen, BNetzA), which are the regulatory entities for Europe and Germany, respectively, released regulations regarding terrestrial point-to-point communication links located in

[13] A radiocommunication service between earth stations at given positions, when one or more satellites are used; the given position may be a specified fixed point or any fixed point within specified areas; in some cases this service includes satellite-to-satellite links, which may also be operated in the inter-satellite service; the fixed-satellite service may also include feeder links for other space radiocommunication services [ITU12, Article 1].

[14] The naming E-band can be misleading in this case, since the term E-band is also used for naming a frequency band, covering the range front 60 to 90 GHz, corresponding to the WR-12 waveguide band.

the E-band. In 2006, the ETSI [ETS06] limited the maximum equivalent isotropically radiated power (EIRP)[15] of the transmitter to a maximum of 75 dBm, while the maximum output power fed into the system's antenna is limited to 30 dBm. The minimum antenna gain is recommended to be 43 dBi. In a further approach from 2009, the E-band is treated in an annex [ETS09, annex UE]. The recommendations given there are identical to the ones provided by the BNetzA, where the available 10 GHz bandwidth is subdivided into several sub-channels, each with a bandwidth of 250 MHz [BNe11]. Also, different values for the minimum antenna gain and the EIRP values are given: The antenna gain should be at least 38 dBi, while the maximum EIRP is given as a function of antenna gain. For antenna gain above 55 dBi, the EIRP is limited to 85 dBm. For antenna gains between 55 and 45 dBi the maximum EIRP is calculated by

$$\mathrm{EIRP}_{\mathrm{max}} = 85 - (55 - \mathrm{G}_{\mathrm{ant}})\,\mathrm{dBm}\ , \tag{1.5}$$

where $\mathrm{G}_{\mathrm{ant}}$ is the used antenna gain. Equivalently, for antenna gains between 45 and 38 dBi, the allowed EIRP is defined by

$$\mathrm{EIRP}_{\mathrm{max}} = 75 - 2 \cdot (45 - \mathrm{G}_{\mathrm{ant}})\,\mathrm{dBm}\ . \tag{1.6}$$

1.2.1.2 Regulations in the D-band

In the D-band[16], or more specific in the frequency range between 125 and 170 GHz, depicted as region III in figure 1.1, point-to-point wireless links are partially allowed but again, have to share the bands with existing radio astronomy and earth exploration applications. Only the bands between 158.8 and 164 GHz as well as 167 and 174.8 GHz are primarily reserved for fixed services. Therefore, this frequency band will not be considered

[15] Equivalent isotropically radiated power describes to amount of power that a theoretical isotropic antenna would have to emit to equal the peak power density observed in the direction of maximum antenna gain of a radio communication transmitter.

[16] In terms of waveguide standards, the D-band waveguide covers the frequency range from 110–170 GHz, also referred to as WR-6.

further.

1.2.1.3 Activities in the 200 GHz range

The atmospheric attenuation window denoted as IV, the most broadband one in the frequency range up to 1 THz, is an interesting candidate for long-range wireless communication due to the still moderate attenuation values between 2.7 and 4.2 dB/km under clear sky conditions. However, when looking at the ITU frequency allocation, it can be seen, that most of this huge bandwidth is reserved for radio astronomy and earth exploration applications. In some frequency bands, namely 191.8–200 GHz, 209–226 GHz, 231.5–235 GHz, 238–241 GHz and 252–275 GHz, fixed services are also allowed, but again with the limitation that the operation of radio astronomy services has to be protected. Nevertheless, when adding all approved bands, a total bandwidth of 54.7 GHz is available for point-to-point wireless communication. To the author's best knowledge up to the present date, no national regulatory board provided has yet any further recommendations or regulations for this frequency range. Therefore, the approval of a communication link in this range has to be decided on a case-by-case basis by the responsible regulatory entity. However, since there is no existing regulation and furthermore both point-to-point links and the locations for radio astronomy applications are in well known and definite areas, also the coexistence for a specific link could be conceivable.

1.2.1.4 Frequency allocation above 275 GHz

For the frequency bands above 275 GHz and up to 3 THz, no frequency allocation and regulation exists at the moment. As discussed at the World Radiocommunication Conference (WRC) in 2012, the ITU states the frequency range from 275 to 3000 GHz as not allocated, but in a footnote defines certain frequency bands up to 1 THz as identified by administrations for passive service applications, i.e. radio astronomy and earth exploration services. In the same footnote it is stated that: "The use of the range 275–1000 GHz by the passive services does not preclude use of

this range by active services. Administrations wishing to make frequencies in the 275–1000 GHz range available for active service applications are urged to take all practicable steps to protect these passive services from harmful interference until the date when the Table of Frequency Allocations is established in the above-mentioned 275–1000 GHz frequency range. All frequencies in the range 1000–3000 GHz may be used by both active and passive services" [ITU12, Article 5, Section IV, footnote 5.565]. In [Kür12] it is stated that the use of large continuous frequency bands for THz communications requires the development of sharing concepts between THz communication and the passive services. Such concepts are already discussed with the result that due to the high propagation loss and attenuation in this frequency range, combined with the currently feasible small transmit powers and the high directivity, a coexistence of active and passive applications should be feasible without harmful interference for the passive ones [Cle10].

Conclusion: When considering the frequency allocations and regulations to determine suitable frequency bands for broadband high-capacity wireless links, the E-band with an overall bandwidth of 10 GHz and up to now very restrained regulatory provisions, is explicitly suitable for mmw wireless communication links. For systems with higher carrier frequencies, the attenuation window around 250 GHz, the most broadband one in the range up to 1 THz, is also very attractive. The frequency allocation for fixed services is not continuous over the entire atmospheric window, therefore a possible system should exclude the unauthorized bands. A solution for broadband applications could be the application for a exceptional permission for coexistence only valid for a specific system and operating location. Furthermore, systems operating at frequencies above 275 GHz are also very interesting, since there is no existing frequency allocation and the bandwidth limitation will not be set by prudential regulations but by the performance of the used technology. However, due to an increased atmospheric attenuation in this frequency range, such systems may be only suitable for short range and indoor applications.

1.2.2 Single-sideband or double-sideband

When considering the way of transmitting a signal in terms of the amount of spectrum covered by the RF signal, two kinds of transmission schemes can be distinguished. In a double-sideband transmission (DSB), the modulated sidebands are symmetrically arranged around the used carrier frequency, creating an upper sideband (USB) and a lower sideband (LSB) and resulting in a bandwidth of twice the intermediate frequency (IF) bandwidth. To generate a DSB signal, a classical single stage mixer cell can be used. In contrary to the DSB transmission, a signal only covering the same bandwidth as the applied IF signal can be generated. The resulting transmission signal in such a scheme is either located above or below the used carrier frequency in the RF spectrum. Therefore, this kind of transmission scheme is called single-sideband transmission and was for a long time favored by RF system engineers due a better performance in fading and multi-path environments, a better receiver performance, but also due to the savings in RF spectrum. A single-sideband transmission (SSB) signal can either be generated by applying appropriate filtering at the mixer's RF port to suppress the unwanted sideband, or by using a Hartley or a Weaver modulator, which inherently suppress the unwanted sideband during the modulation process by a proper phase shifting and superimposition [Wea56, HC13].
As is shown by J. P. Costas in his discussion about synchronous receivers [Cos57], a SSB system as no advantage over a DSB system, as long as synchronous detection is applied to the system's receiver (Rx), i.e. the receiver's local oscillator signal is manipulated in a way that its frequency and phase are equal to the transmitting carrier signal. In this case, the circuit complexity of the transmitter (Tx) is substantially reduced compared to the complicated SSB transmitters. The additional noise at the receiver, caused by the reception of two sidebands instead of only one for the SSB case, is compensated by the coherent addition of these two sidebands. Therefore, the signal-to-noise ratio is identical for both transmission schemes. The receiver complexity is considered to be identical

for both the DSB and the SSB transmission[17].

1.2.3 Why to use direct-conversion

The aspect to be considered is the method which is applied to convert the baseband frequency to the radio frequency (RF) range at the transmitter side, and back from the RF to the baseband for detection at the receiver side. There are two main methods established for data transmission systems, the superheterodyne concept [Arm21], and the direct conversion scheme, in the literature sometimes also called zero-IF conversion. For both schemes, a characteristic upconverter and downconverter exist, which could also be used interchangeably if an appropriate frequency plan is applied.
In a superheterodyne system, in the transmitter, shown in figure 1.4, an inphase-quadrature (I/Q)-modulator is used to modulate an intermediate frequency LO_2 with the information-carrying signal. This IF signal undergoes several stages of correction, equalization and amplification and is then fed into a mixing stage, upconverting the signal to the conveying RF range by mixing it with a carrier signal LO_1. In the downconverter, shown in figure 1.5, the received signal is translated back to an intermediate frequency again by applying a second local oscillator (LO) signal, which may, but does not have to, be identical in frequency with the upconverter's LO_1, where the filtering, amplification and other signal processing are more easily to perform than directly in the RF range. Before and after the first down-conversion process, a series of highly selective filters are necessary to suppress unwanted image signals in the RF spectrum and also the unwanted sideband generated by the downconversion. The processed IF signal is than routed to a demodulator stage, which recovers the contained information signal.

[17] Costas even found advantages of his DSB system over the common SSB systems of his time, but since he aimed for amplitude modulated transmission schemes in mostly military applications, these advantages are not applicable for the transmission systems covered by this thesis and therefore will not be further discussed. In the framework considered here, it is sufficient to perceive that no disadvantages arouse from the use of a DSB system.

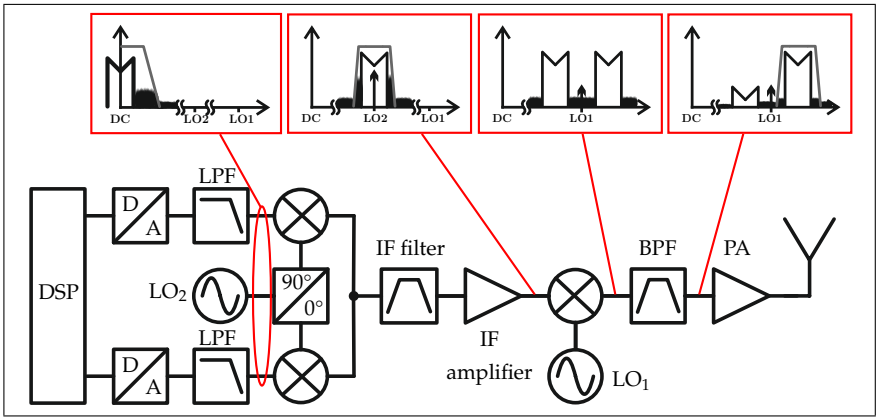

Figure 1.4: Schematic representation of a superheterodyne transmitter for single-sideband transmission. The data signal is modulated onto a low IF LO_2, after various intermediate stages like filtering and amplification, this signal is upconverted to the RF range with the carrier signal LO_1. After the upconverter stage, the wanted sideband is selected by appropriate filtering and fed into a PA for transmission. The inlays show a simplified spectrum at the different conversion stages. The simplified filter characteristics are shown in grey.

When using a direct-conversion scheme, the upconverting mixer is essentially used as a modulator, i.e. the mixer's LO, which in the cases considered by this thesis is located in the high millimeter wave range, is directly modulated by the data signal, resulting in an RF signal symmetrically arranged around the carrier frequency. At the receiver side, the received signal is directly downconverted to the baseband, literally to an intermediate frequency of 0 Hz, where the information included in the signal can be recovered. This leads to an elimination of the entire IF stages necessary for the superheterodyne setup, accompanied by a reduced complexity and component count. During the downconversion process, the signal must be reconstituted by some kind of phase correction method. Without a correct phase relation, the part of the RF spectrum which is

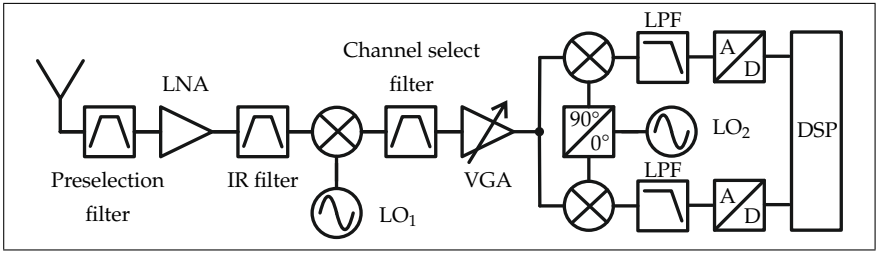

Figure 1.5: Schematic representation of a superheterodyne receiver with an image-reject filter for single-sideband reception and I/Q demodulation in the IF stage.

converted to the negative frequency axis can fold and superpose the part downconverted to the positive frequency axis, leading to signal corruption or even cancellation. To prevent this, quadrature downconversion, introduced in the following paragraph, can be used to separate the different parts of the downconverted RF spectrum into two phases. A vector detection scheme can then be used to reconstruct the signal. When in addition to the direct downconversion scheme, the receiver's LO signal is synchronized in phase with the incoming carrier frequency, a special case of synchronous reception called homodyne reception is formed.
I/Q-frequency conversion is a technique widely used in digital data transmission systems, where complex baseband data signals[18], separated in their in-phase (I) and quadrature (Q) component representing the corresponding real and imaginary part of the complex signal, have to be handled. It also builds the core component of the Weaver modulators mentioned above, which allow for SSB transmission and/or reception. When used in combination with complex modulation schemes, the quadrature mixer is most often called I/Q-mixer or -modulator. It basically consists of two independent mixer cells combined at their LO and RF port, but with the LO signals shifted by 90° for one of the cells. Thereby, in the mixer cell representing the I-path of the I/Q-mixer, the data is mixed with a cosine

[18] An thorough introduction to complex baseband signals, their composition and their representation in frequency domain is given in [Lyo08]

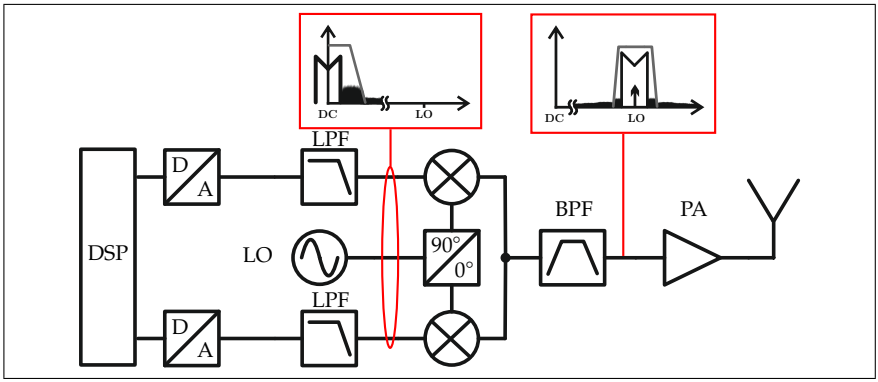

Figure 1.6: Schematic representation of a I/Q direct-upconverter. After digital to analog conversion and low-pass filtering of the digitally generated data stream, the signal is directly fed into the I/Q-upconverter stage, resulting in a frequency band centered around the mixer's LO frequency. After band-pass filtering, the signal is radiated via an antenna. The inlays show the simplified spectra of the complex baseband and the RF signal. The simplified filter characteristics are shown in grey.

wave, while in the cell representing the Q-path, the data is mixed with a sine wave. A schematic of a quadrature direct-conversion transmitter and receiver together with the resulting RF spectrum are shown in figure 1.6 and 1.7. It is also possible to realize the 90° phase shift in the RF path of the mixer, but since in most applications the local oscillator is mono-frequent while the RF path has to cover the entire transmission band, it is more convenient to shift the phase in the LO path.
The advantages of a superheterodyne setup on the transmitter side are the possibilities of correcting and equalizing the signal on the IF level after the modulation process. On the receiver side, the superheterodyne principle provide a high sensitivity and selectivity. The main disadvantage of this concept for the applications aspired for in this thesis, is the limitation of the usable bandwidth for data transmission to what is feasible at the intermediate frequency, while in a direct-conversion scheme,

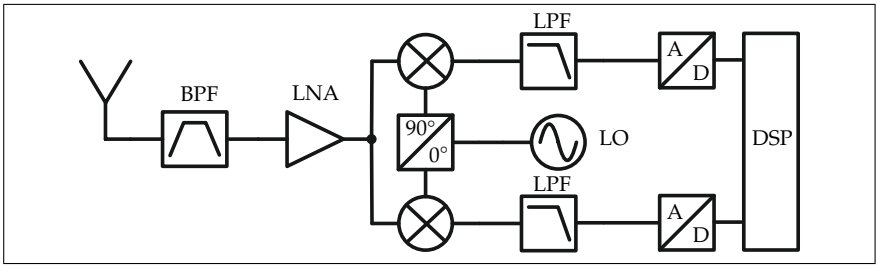

Figure 1.7: In the direct-conversion receiver, the conveyed signal is bandpass filtered, amplified and then directly downconverted to the baseband, separated into an I- and Q-channel. Both signals are then fed into analog-to-digital converters followed by digital signal processing.

the entire bandwidth provided by the RF mixer stage can be used for the information transmission. Another drawback is the much more complex circuit structure, where especially the highly selective filters are difficult to implement in monolithic integrated circuits. Inappropriate filtering and signal processing at the IF stages of a superheterodyne concept will cause severe losses in signal quality [Raz97]. Considering the direct-conversion scheme, the advantages besides the obvious and already mentioned bandwidth and complexity benefits, are that the phase noise of only one instead of two local oscillators contributes to the noise of the transmitted signal and the possibility to process the received signals in the baseband, which can be implemented more easily and in a less power consuming way than processing the data at an IF level [Abi95]. However, as will be seen later in this chapter, the latter contention is not applicable for the bandwidths and data rates aimed for in this thesis. The drawbacks arousing from the use of a direct-conversions scheme are an intrinsic sensitivity to direct current (DC)-offsets, an irreversible I/Q-imbalance, the increased susceptibility to signal corruption caused by spurs in the transmission band, as well as the necessity of an applicable reception structure to reconstruct the data signal. Nevertheless, following [Raz97] viable solutions to overcome or at least minimize the influence of these non-idealities can be found. Each

contribution and the possible solutions will be discussed in the following section.

Conclusion: The prospect of the highest possible bandwidth to transmit data signals, combined with an easier monolithic circuit integration and the possibilities to reduce the impact of its disadvantages make the direct-conversion the architecture of choice for the transmission systems developed in this thesis.

1.2.4 Overcoming the drawbacks of direct-conversion

As mentioned above and thoroughly discussed in [Raz97, Abi95, HW11], the direct-conversion architecture suffers from a set of problems, which have to be taken into account when realizing a communication system with this scheme. They can however be suppressed when already considered during the design of the frontend components.
At the transmitter, the most severe signal corruption is caused by an insufficient LO-to-RF isolation in the mixer stages, resulting in a portion of unmodulated LO signal in the conveyed RF signal, as indicated by the small arrow in the inlay of figure 1.6. As this LO frequency is centered right in the middle of the transmit band, energy at this frequency may cause bit errors and, with increasing energy, also lead to an early saturation of subsequent amplifying stages [Abi95]. One solution to reduce the amount of unmodulated LO signal in the output spectrum is the use of a balanced mixer design, suppressing the LO by destructive superposition [Poz05].
The problem of I/Q-mismatch, caused by amplitude and/or phase differences in the I- and Q-channel exists in both the up- and downconverter. An unequal signal handling in terms of amplitude and phase leads to an inaccurate modulation and demodulation process, corrupting the signal constellation, as shown for the case of a QPSK signal in figure 1.8, and thereby raising the bit error rate. To gain a more detailed insight into the effects introduced by amplitude and phase imbalances, a signal $x_{in}(t) = a\cos(\omega_C t) + b\sin(\omega_C t)$ shall be received, where ω_C represents the signal's carrier frequency and the included information is represented by

a and b, which are either -1 or 1. Lets further assume that these signals are downconverted by the receiver's LO signal tuned to ω_C, but with an amplitude error k_{Rx} and a phase error ϕ_{Rx} in the LO path of the downconverter's Q-branch, resulting in

$$\begin{aligned} x_{\mathrm{LO},I} &= 2\cos(\omega_C t) \\ x_{\mathrm{LO},Q} &= 2\,(1 + k_{\mathrm{Rx}})\cos(\omega_C t + \phi_{\mathrm{Rx}})\ , \end{aligned}$$

where the factor of 2 is included to simplify the results. After the downconversion process, the resulting baseband signals are

$$\begin{aligned} x_{\mathrm{BB},I} &= a \\ x_{\mathrm{BB},Q} &= (1 + k_{\mathrm{Rx}})\,b\cos(\phi_{\mathrm{Rx}}) - (1 + k_{\mathrm{Rx}})\,a\sin(\phi_{\mathrm{Rx}})\ . \end{aligned}$$

As can be seen, an amplitude error appears as a non-unity scaling factor in the amplitude, causing the constellation to be rectangular shaped, while a phase imbalance corrupts one channel with a fraction of the data pulses from the other channel. The influence of both effects are graphically depicted in figure 1.8 in the constellation plots, where the hollow symbols represent the ideal constellation points, while the filled symbols represent the distorted ones, and the corresponding time domain signals. It is notable, that while the amplitude error only corrupts one channel with a reduced receive level, which can be taken into account in the subsequent circuits, a phase error causes a more severe problem. Due to the cross-relation between both channels, the resulting signal-to-noise ratio is decreased, which is more obvious in the time domain waveforms [Raz97].

The mixer's amplitude imbalance can be improved by thorough chip design combined with independent gain control for the I- and Q-paths, phase imbalance can be minimized by using appropriate hybrid couplers like Lange- or tandem couplers, both capable of providing an accurate phase shift over a wide bandwidth [Lan69, CLC03]. Also, calibration

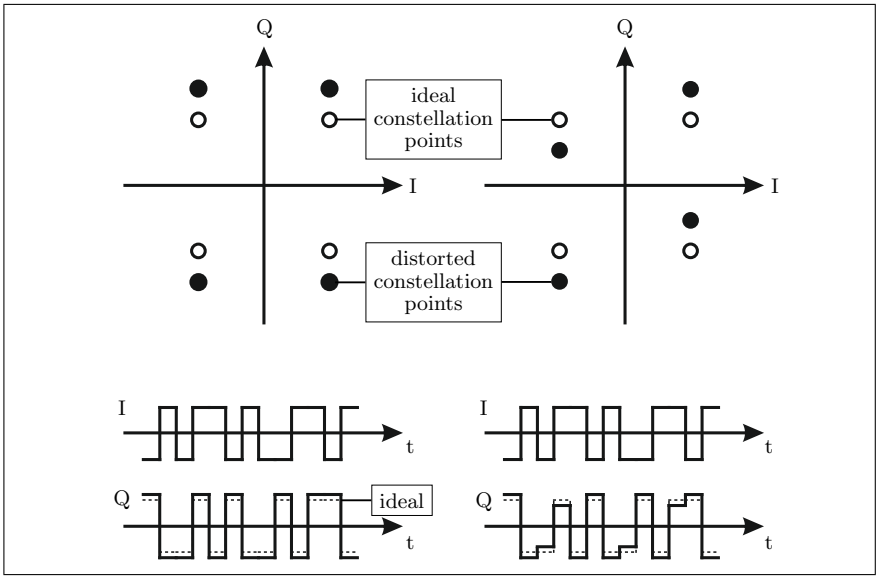

Figure 1.8: Effects of I/Q-imbalance on a QPSK modulated signal separated by amplitude (left) and phase (right) imbalance. In the top row, the influence of the imbalances as it is seen in the constellation diagram, in the bottom row the effects in the time domain signal are shown [Raz97].

techniques can be implemented into the circuit to reduce the imperfections as for example shown in [VFG07], but this demands the combination of analog and digital components in one chip, restricting the transistor technology to silicon-based structures where complementary metal-oxide-semiconductor (CMOS) logic is available, and would be hard to realize for the high bandwidths aimed for in this thesis.
Another problem in direct-conversion receivers are DC-offsets and, for non-synchronous setups, very low frequency components in the range of several Hz, which are generated by self-mixing processes inside the receiver as well as by a mixing of the receiver's LO signal with an unmodulated carrier present in the received signal. The latter one arises due to

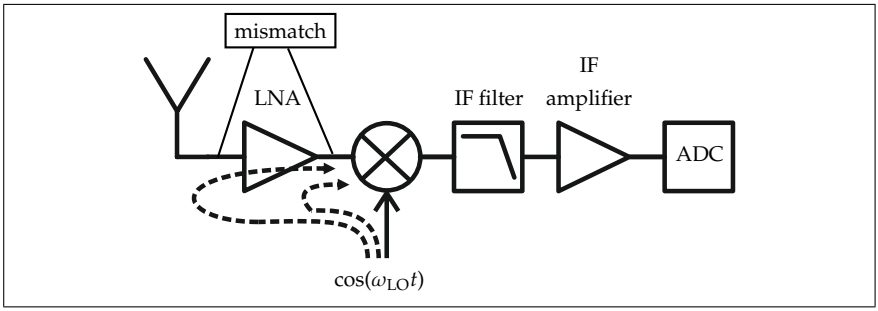

Figure 1.9: The LO self-mixing phenomenon due to insufficient LO suppression is caused by reflected portions of the LO at mismatches between mixer and LNA-stage or LNA and antenna and causes severe problems in direct-conversion mixers. The reflected signal enters the mixer stage again and mixes with the actual LO to a DC or low frequency signal in the mixer's output path, corrupting the wanted data signals [Raz97].

a slight but continuos drift of the independent LO sources for the transmitter and receiver against each other, resulting in low frequency spectral peaks or even DC-components in the middle of the complex baseband signal, dependent on the instantaneous difference between both. The DC-offsets introduced by self-mixing processes are generated internally in the receiver components. Parts of the LO signal leaking through the downconverter will be reflected at mismatches between the mixer and the low noise amplifier (LNA)-stage or between the LNA and the antenna as shown in figure 1.9. Depending on the position of the reflection, the reflected signal, possibly even amplified by the LNA's gain, is fed back to the mixer stage, where a mixing between the reflected signal and the receiver's LO signal itself occurs, resulting in a strong DC-component. Both effects reduce the signal-to-noise ratio or even saturate the detector stages subsequent to the downconverter.
To overcome these problems of strong DC and very low frequency components, either active or passive correction circuits, as for example shown in [LRPR04], or algorithms applied in the digital signal processing, as

shown in [Lee03] can be used. The analog solution is limited to a certain kind of modulation format and thereby reduces the flexibility of changing between different formats, while the digital solution is limited by the processing speed of the digital stages when capturing and processing data rates in the range of several Gbit/s. A much simpler solution is the usage of a high pass filter (HPF) and thereby alternate current (AC)-coupling the downconverter's output signal to the subsequent stages, which will essentially minimize the influence of the bothering spectral components. As shown by simulations in [Raz97], the corner frequency of the HPF has to be less than 0.1 % of the data rate for the signal degradation to be negligible. For a data rate of 1 Gbit/s, this results in a corner frequency of 1 MHz. High performance DC-blocks, which in principle form a HPFs, are available with corner frequencies as low as 30 kHz[19], available broadband baseband amplifiers for communication applications provide lower corner frequencies between 15 and 250 kHz[20]. Another possibility to reduce the influence of DC-offset on the transmission performance, again accompanied by a reduction of degree of freedom, is the use of DC-free modulation formats as for example discussed in [MM00].
While RF receivers in a superheterodyne scheme typically only suffer from third-order intermodulation, in direct-conversion also even-order distortion becomes problematic. These intermodulations are either caused by the second harmonic of the desired RF signal which is downconverted by the second harmonic of the LO signal, or by two strong interferers in close proximity to the desired RF channel entering the receiver and

[19] Examples for broadband high-performance DC-blocks are the products provided by Anritsu, covering a frequency range between 30 kHz and 65 GHz, which are used for the measurements in this thesis. More information on the Anritsu product can be found on their product page: http://www.anritsu.com/en-gb/products-solutions/products/v265.aspx, last accessed 04-07-2014.

[20] Examples for broadband baseband amplifiers are the product of SHF, providing broadband amplification covering a range from 15 kHz up to 58 GHz with a gain of 8 dB. More information can be found on SHF's product page: http://www.shf.de/communication/products/rf_broadband_amplifier/ultra_fast_rf_amplifier/, last accessed 04-07-2014. In the measurement setups for this thesis, most of the baseband amplification is performed with such broadband amplifiers.

experiencing a nonlinearity either in the LNA or mixer part. Thereby, a low frequency beat signal is generated, which can feed through to the IF port by a finite RF to IF isolation in the mixer stage.
Both cases are of minor interest for the applications considered in this thesis. Due to the frequency bands in the high millimeter wave range used in this work, the second harmonics of the RF and LO signals are at such high frequencies, that their influence can be neglected. The problem of external interferers is more severe, but since the intended systems will be highly directional and the attenuation for propagation signals due to the atmosphere is much higher than for signals in the microwave regime, as shown in figure 1.1, the probability of interferers, strong enough to cause severe signal distortion, is very low.
As already mentioned in section 1.2.3 and discussed in [Abi95], an appropriate digital baseband processing unit must be coupled to the analog frontend to make direct-conversion transmission a practical reality. Using a digital signal processor, carrier recovery as well as the clock and data recovery can be shifted to the digital domain, mandating extremely broadband analog to digital converters followed by an enormous computational power to process the bandwidths and data rate targeted in this thesis. A much more convenient method, which would at least reduce the constraints on the carrier recovering part in the digital domain, is the setup of a synchronous detection, often also called coherent detection, where the downconverting LO is identical in frequency and phase to the carrier signal. This implies the realization of some kind of carrier recovery in the analog domain, which has already been established in the microwave range, but since for the bandwidths and data rates commonly used for communication links operating in this regime it is easier and more cost-effective to implement the carrier recovery in the well developed and powerful digital part, only few realizations of analog carrier recovery circuits exist. In the millimeter wave range only two implementations for synchronous detection have been published [MTA08, HYW+11]. The drawback for such carrier recoveries is, that they are only suitable for one specific kind of modulation format.

Conclusion: For the systems in this thesis, the I/Q-imperfections will be minimized by proper design of the mixer stages where the gain of the I- and Q-mixer will be adjustable independent from each other. The influence of LO leakage and self-mixing will be reduced by the use of balanced mixer designs and the use of DC-blocks in the baseband path. To provide the highest possible flexibility in the choice of modulation scheme, the carrier recovery and demodulation process will be done in the digital domain with the help of proper measurement equipment.

1.2.5 Transistor technology

To realize compact frontend modules for wireless links in the frequency bands proposed above, with the capability of transmitting digitally modulated data signals and the possibility of monolithically integrating the entire analog frontend, i.e. amplifiers, mixers and multipliers, on a single MMIC, a transistor technology capable of handling frequencies up to several 100 GHz has to be found, which simultaneously provides an MMIC process with appropriate passive components such as resistors, capacitors and inductors[21]. The highest operating frequencies today are reached by high electron mobility transistors (HEMTs), achieving high carrier mobility due to a heterojunction between two compound semiconductor materials. The conduction band of the semiconductor is be formed to build a quantum well, a so called two-dimensional electron gas, in which the electrons can move without colliding with impurities [CK94, Mim02]. Commonly, III-V compound semiconductors[22] like Gallium-Nitride (GaN), Gallium-Arsenide (GaAs) or Indium-Phosphide

[21] The attempt for a level of integration as high as possible, resulting in systems which are compact and easy to deploy, mandates the commitment to one single transistor technology, which leads to a reasonable overall system performance. It cannot be excluded, that for the system's different building blocks better realizations in different transistor or even diode technologies might exist.

[22] Compound semiconductors are a composition of elements of at least two different groups from the periodic table of the elements. Consequently, III-V semiconductors are a composition of elements from the Boron group with three electrons in their outer energy level, and elements of the nitrogen group with five electrons in their outer energy level.

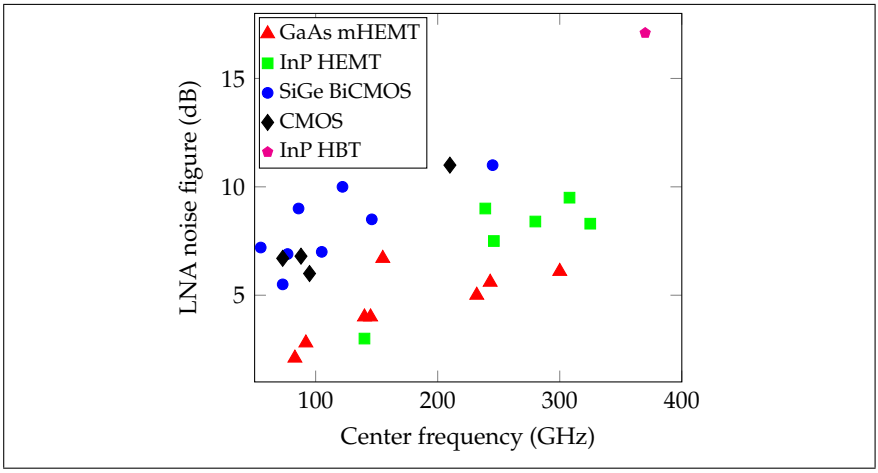

Figure 1.10: State of the art in LNA noise figures for different transistor technologies. A detailed comparison with the corresponding citations can be found in appendix B.

(InP) are used to achieve this effect, leading to the highest transit frequencies (f_T) as well as maximum frequencies of oscillation (f_{Max})[23], allowing the realization of broadband building blocks up to several 100 GHz combined with low noise figures.
Since the noise figure of the receiver's LNA will ultimately influence the overall system performance, this parameter will be used to determine which transistor technology fits best to realize the intended millimeter wave frontends. In figure 1.10, the state of the art on recently published LNA noise figures[24] at center frequencies between 50 and 350 GHz is

[23] f_T and f_{Max} describe the cutoff frequencies of a transistor, with f_T defined as the frequency where the short-circuit current gain becomes unity, and f_{Max} defined as the frequency where either the unilateral power gain or the maximum available gain becomes unity [SWL10].

[24] While the output power of a transmitter can be increased by simply adding an additional amplifier module, at the receiver, it is advantageous to have the lowest possible noise figure at the first stage and preferably monolithically integrated with the entire downcon-

given. Circuits realized in silicon based technologies, i.e. CMOS and Silicon-Germanium (SiGe) BiCMOS, as well as circuits realized in III-V semiconductor technologies, i.e. InP-heterojunction bipolar transistor (HBT), InP-HEMT and the GaAs-metamorphic high electron mobility transistor (mHEMT) technologies are compared. It can be seen, that the III-V technologies provide better noise performance over the entire frequency range of interest. Especially in the E-band, the mHEMT process achieves a noise figure 4 dB below the best silicon-based devices. Also, in the frequency range around 240 GHz, the mHEMT technology today provides the best available noise performance.

Conclusion: To achieve the best possible performance for the intended communications links, a noise figure as low as possible for the system's receiver is preferable. To achieve this, for the MMIC designs in the three frequency ranges defined above, an mHEMT technology is one of the most suitable technologies for the intended application. Such a technology is established by the Fraunhofer Institute for Applied Solid State Physics (Fraunhofer IAF) in Freiburg, Germany. This technology provides gate lengths of 20, 35, 50 and 100 nm and features all necessary passive components to realize MMICs [STK+11]. Since this technology was accessible via several research projects and the competitive InP-HEMT technologies are not commercially available, the chip designs in this thesis have been done using the Fraunhofer IAF technology.

1.2.6 Baseband equipment for multi-gigabit applications

When developing wireless communication links for multi-gigabit data transmission by using extremely high baseband bandwidths in the range of several tens of GHz, a crucial element to evaluate the performance of the wireless links is the availability of appropriate baseband equipment, i.e. data sources, providing a high-speed data stream for the transmitter as

verter structure for low losses. The importance of the loss in the first stage is described by Frii's equation $F_{\text{total}} = F_1 + \frac{F_2-1}{G_1} + \ldots + \frac{F_n-1}{G_1 G_2 \ldots G_{n-1}}$, showing the dominating noise influence of this stage [Fri44].

well as appropriate data sinks, which are capable of capturing the received IF signal and evaluating the errors introduced due to the transmission.

1.2.6.1 Bit error rate testers

The errors introduced by the transmission over a wireless link can be evaluated by using a pseudo-random bit sequence (PRBS)[25] as a transmit signal and comparing the received bit stream with this known bit sequence fed into the transmitter. The number of erroneous bits can be counted and allow for an estimation of the error probability of an actual transmitted data stream. This evaluation can be done using a bit error rate tester (BERT) which is able to generate, transmit and receive digital signals like PRBS patterns, and compare the received signal with the transmitted ones to identify errors. Current state of the art BERTs can provide data rates above 100 Gbit/s [MW10, pp. 274].
Although the BERT system provides the ultimate measure of system performance, it can only be used to a limited extent for characterizing such wireless links intended in this thesis. Since a BERT cannot perform any kind of carrier recovery, it can only be used in combination with synchronous systems. When no analog carrier recovery is available, the measurement with a BERT system is only possible for a coherent setup, where the transmitter and receiver share the same LO signal. Also, a BERT system is only capable of generating on-off-keying signals but no complex modulated data schemes. Additionally, a bit error rate (BER) measurement provides only limited insight into the origin of signal distortions causing the errors. To investigate on this, a vector signal analyses with an evaluation in terms of error vector magnitude (EVM) would be necessary, which will be thoroughly discussed later.

[25] Pseudo-random bit sequences are frequently used for the characterization of high-speed communication systems. A PRBS of a given length $2^N - 1$ contains all N-bit long sequences of possible permutations between ones and zeros except $N \cdot 0$ and its cycle length is $2^N - 1$ [MW10, Appendix C]

1.2.6.2 Arbitrary waveform generators and real-time oscilloscopes

A more flexible device which is also capable of generating complex modulated data signals is the arbitrary waveform generator (AWG), which allows to digitally process any wanted waveforms and convert them into an analog representation by the use of digital-to-analog converters (DACs). As a data sink for such signals, broadband real-time oscilloscopes build the counterpart to the AWGs. To use such devices for the measurements intended here, the bandwidths of the high-speed analog-to-digital converters (ADCs) and DACs inside these measurement instruments have to be in the same range as the wireless system's IF bandwidth. Furthermore, their sampling rate and resolution have to be high enough to accurately represent the original signal in the analog time domain and reconstruct the received signal back to the digital domain, i.e. following the Nyquist-Shannon-Theorem[26], for the sampling frequency $f_s \geq 2 \cdot f_{max}$, with f_{max} being the highest considered frequency, has to hold.
Today's state of the art AWGs feature sample rates up to 50 GS/s combined with a resolution of 10 bit and an analog bandwidth up to 15 GHz [Tek14]. The fastest real-time oscilloscopes provide sampling rates up to 160 GS/s combined with analog bandwidths of 63 GHz[27]. Another important parameter for such oscilloscopes is the memory depth, determining the time span which can be captured.
If not stated otherwise, for the measurements in this work, an Agilent M8190 AWG with a sampling rate of 12 GS/s, a 12 bit resolution and an analog bandwidth of 5 GHz is used. To capture the received signal, an Agilent DSO-X93204A real-time oscilloscope with an analog bandwidth

[26] In [Sha84], Shannon formulated a theorem regarding the relationship between frequency representation in time and frequency: If a function contains no frequencies higher than W in cycles per seconds (cps), it is completely determined by giving its ordinates at a series of points spaced $\frac{1}{2W}$ seconds apart, i.e. any function can be described by a series of samples, clocked at two times the maximum frequency W. He further explains: The intuitive justification is that if $f(t)$ contains no frequencies higher than W, it cannot change to a substantially new value in a time less than one-half cycle of the highest frequency, that is $\frac{1}{2W}$.

[27] A press release for this oscilloscope can be found via http://www.agilent.com/about/newsroom/presrel/2012/11apr-em12021.html, last accessed 04-07-2014

of 33 GHz and a sampling rate of 80 GS/s is used. The digital carrier recovery as well as the digital demodulation is performed by using the Agilent 89601A vector signal analysis (VSA) software to post-process the data streams captured by the oscilloscope [28].
The different processing steps performed by the oscilloscope and the VSA software are shown in figure 1.11 as a simplified schematic: The I- and Q-signals, fed into two channels of the oscilloscope, pass through a signal conditioning stage to ensure proper usage of the input dynamic of the following ADC-stages. After a signal processing stage and a time correction stage, performing digital filtering, digital downconversion and resampling if required, the two data streams are handled as one single I/Q time domain data stream, representing the complex data signal. All demodulation steps following the signal processing stage are realized by digital signal processing (DSP) algorithms. In a digital band pass filter (BPF), controlled via a user-defined frequency span, the signal bandwidth for the demodulation process is set. After the filtering, the user-defined center frequency is used in a carrier and symbol lock stage to perform a carrier recovery and calculate the frequency error, i.e. the deviation between the user set value and the recovered one. With the information about the symbol rate and modulation format, the symbol timing can be recovered and the received data stream can be locked to this timing sequence. The signal is now passed to a compensation stage, where an eventual DC-offset is calculated and removed. After additional baseband filtering, applying measurement filters as used in different kinds of communication systems, the signal stream, now called "I/Q-meas time" is passed to the error calculation stage. In parallel, the symbol timing information is used in a reference generator, to build a reference waveform, representing the waveform that would result after demodulating an ideal

[28] Information on the VSA software and detailed information on its capability can be found online via http://www.home.agilent.com/en/pd-1910360-pn-89601B/89600-vsa-software-transportable-license, last accessed 03-21-2014, and http://cp.literature.agilent.com/litweb/pdf/5989-1121EN.pdf, last accessed 03-21-2014. More information on the use of AWGs can be found in *The ABC's of Arbitrary Waveform Generation*, accessible via http://cp.literature.agilent.com/litweb/pdf/5989-4138EN.pdf, last accessed 05-10-2014.

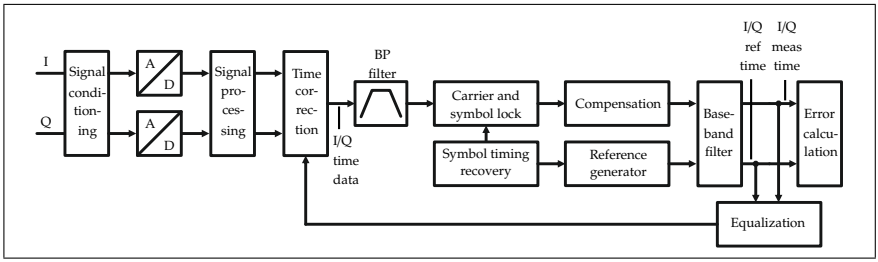

Figure 1.11: Simplified schematic of the baseband signal processing performed by the oscilloscope and the VSA software.

input signal. This waveform is called "I/Q-ref time". In the error calculation stage, this ideal waveform is compared to the "I/Q-meas time" signal to calculate the deviation between both. From this comparison the error vector magnitude but also other error information can be derived. More information about the VSA's demodulation process can be found in [Tec12b] and [Tec].
Besides carrier recovery and demodulation, the VSA software also provides the possibility of using an equalization filter on the received signal. An adaptive feed-forward equalizer[29] can be applied to the measurement signal to remove linear errors, i.e. group delay distortion, frequency response error as distortions due to reflections and multi-path behavior from the I/Q-modulated signal. The errors are calculated by comparing the "I/Q-meas time" and "I/Q-ref time" signals. The resulting filter characteristic is applied to the signal in the time correction stage, i.e. before the demodulation process starts. More information on the equalization process can be found in [Tec11].

[29] In an adaptive feed-forward equalizer, the filter performance is modified after each demodulation process, based on the achieved results. Therefore, demodulation circles are required until the optimum filter characteristic is found. The equalizer used in the VSA software does not use a training sequence, i.e. it works without knowledge of the transmitted signal.

1.2.6.3 High-speed DACs and ADCs

Although the evaluation method with a combination of AWG and real-time oscilloscope is suitable to characterize the wireless link performance, this solution is not able to provide real-time operation of the wireless link, mainly since the carrier recovery and the equalization is performed in a digital post-processing stage. To achieve real-time capability, high-speed DACs and ADCs have to be combined with real-time digital signal processing, in which the needed operations like adaptive modulation, carrier recovery, or equalization can be performed.
Up to now, the fastest commercially available DACs suitable for the applications intended here operate up to sample rates of 64 GS/s combined with an analog bandwidth of 15 GHz at resolution of 8 bit [Ded11]. Since the sample rate is significantly higher than the analog bandwidth of the devices, the generated signal can either be oversampled or the additional samples can be used to realize digital filters or pre-equalization. For the receiver side, the corresponding ADCs also provide samples rates up to 65 GS/s with bandwidths above 18 GHz [Ded10]. Combined with digital signal processing for carrier recovery, equalization and error correction as shown in [Ded11], such baseband equipment is perfectly suitable to realize real-time capable synchronous multi-gigabits wireless links including adaptive modulation formats, equalization and error correction. This kind of signal processing was originally designed for the use in high-speed optical fiber networks for data centers and on-board data transmission in backplanes up to data rates of 400 Gbit/s [Fuj12], but can now be reused for mmw wireless links.

1.2.6.4 Broadband baseband amplification

As mentioned above, broadband baseband amplifiers are needed to generate the optimum input signal for both the transmitter and the data sinks. There are several companies providing amplifiers with various gain values, all optimized for the use in communication systems, with lower cutoff frequencies in the kHz range and upper cutoff frequencies around 65 GHz.

For the measurements performed in this work, broadband amplifiers from SHF and Centellax are used. The SHF804TL[30] provides a gain of approximately 22 dB in a frequency range from 200 kHz up to 55 GHz and is used in this work to achieve the optimum level for the bit error rate measurements. The Centellax OA5MMDM[31] is a two-channel 18 dB amplifier with a bandwidth from 100 kHz up to 50 GHz optimized for the use with I/Q-signals. This amplifier is used in this work to post-amplify the received I- and Q-data in the transmission experiments with complex modulated data signals.

1.3 Thesis outline

With the findings of the system considerations, the above determined thesis objectives can now be defined more precisely. The following approach is found to be the most promising solution to realize multi-gigabit wireless links for future high-speed wireless applications:

- The highest data rates will be achieved by the use of extremely broadband data signals combined with complex modulation schemes in terms of quadrature amplitude and phase modulation.
- To provide the necessary absolute bandwidth for the transmission, the wireless systems will operate with carrier frequencies in the high millimeter wave regime.
- The frequency bands in this regime which are suitable for wireless data communication due to frequency allocation and regulatory issues are between 71 and 86 GHz, between 200 and 280 GHz and around 300 GHz.

[30] The data sheet for the SHF084TL is accessible online via http://www.shf.de/fileadmin/download/Amp/datasheet_shf804tl_v003.pdf, last accessed 04-08-2014.

[31] A description of the Centellax OA5MMDM is accessible online via http://www.centellax.com/products/telecom/modules/OA5MMDM, last accessed 04-08-2014.

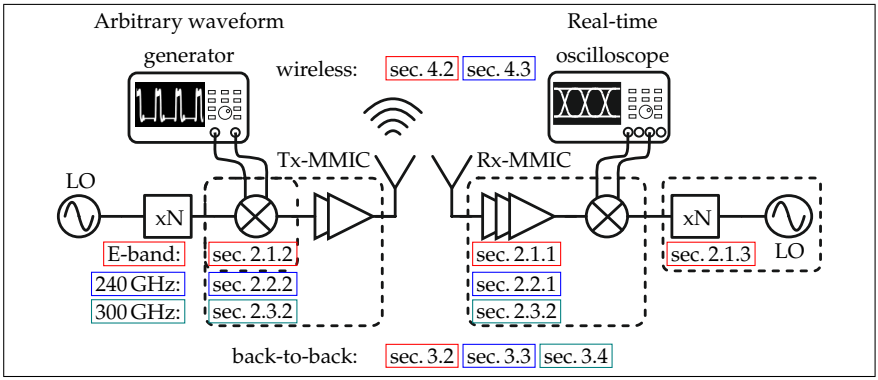

Figure 1.12: Basic setup of the wireless systems as realized in this thesis, together with links to the corresponding chapters for the E-band, the 240 GHz and the 300 GHz system, considering MMIC-design and characterization, back-to-back measurements, and wireless transmission experiments.

- By the use of millimeter wave frequencies together with monolithic integrated circuits, compact, light-weight and easy-to-deploy frontend components will be feasible.
- To achieve the high operating frequencies combined with the lowest possible noise figure, the metamorphic high electron mobility transistor technology by the Fraunhofer IAF will be used to realize the different building blocks.
- A direct conversion scheme will be used in both, the transmitter and receiver, to provide the highest possible IF bandwidth for the data signals.

An overview over the different parts and processes of this thesis for three wireless links operating in the frequency bands defined above, together with the corresponding relation to the chapters is given in figure 1.12. In more detail, the thesis is structured as follows:

Chapter 2 deals with the development and analysis of MMIC-based analog millimeter wave frontends for the realization of wireless communication links in the E-band and at 300 GHz. All realized components are characterized in terms of conversion gain, linearity, output power and noise figure by using single tone measurements. Starting from the choice of transistor topology, the complete design process is described. Furthermore, the characterization of already existing 240 GHz frontend components is shown.
In chapter 3, the system setup and analysis of the millimeter wave communication links in the E-band and at 240 GHz are described. The high-speed arbitrary waveform generator and broadband real-time oscilloscope mentioned above, are used as data source and sink to characterize the wireless links' performance in back-to-back environments. Thereby, the receiver sensitivity, the feasibility of different modulation formats and the links' transmission quality in terms of error vector magnitude can be determined independent from influences due to channel characteristics, atmospheric effects and other external disturbances. Additionally, the influence of the frontend components' non-idealities on the transmitted signal is studied.
Chapter 4 focuses on wireless data transmission experiments accomplished using both, the E-band and the 240 GHz communication system. In these investigations, the influence of the transmission channel as well as atmospheric effects and the antenna system can be examined.
In chapter 5 the findings of this thesis are discussed. Additionally, an outlook on future research foci is given.

2 MMIC-based Analog Frontends for Millimeter Wave Communication

With the objective to realize broadband millimeter wave wireless communication links for multi-gigabit applications by using purely electrical components, the first step is to design, develop and characterize the necessary analog frontends forming the key components of each of the planned wireless links. These frontend components provide the high carrier frequencies as well as the broadband IF interfaces, the basis for a high data rate capability.

The following chapter is subdivided into three main parts. The first part deals with the design approach and realization of an MMIC-based analog E-band frontend covering both dedicated frequency bands for terrestrial and extra-terrestrial communication. Starting with the choice of a suitable circuit topology for the mixer stage, the development process of all necessary components for the up- and downconverter circuits and the characterization of these components are described. The second part of the chapter illustrates the characterization of a 240 GHz frontend for wireless backhauling, comprising I/Q-transmitters and receivers, both featuring subharmonic frequency conversion together with RF amplification circuits. The third and final part shows the realization of an ultra-broadband 300 GHz MMIC-based chipset, which is developed for high-speed indoor communication systems. The achieved results are compared to the state of the art at the end of each of these parts.

2.1 Design and characterization of a multi-gigabit E-band frontend

For realizing a high-speed wireless link, transmitting data in the frequency bands 71 to 76 GHz and 81 to 86 GHz, both dedicated for telecom backhaul point-to point links and satellite up- and downlink applications as discussed in chapter 1.2.1, an analog frontend comprising I/Q-mixers for up- and downconversion, low noise amplifiers and a frequency generation stage are developed. Following the considerations in the preceding chapter, the frontend's RF bandwidth shall at least cover the frequency ranges determined by the ITU allocation plan in [ITU12] and the transmitter will be realized as a balanced mixer to prevent signal distortion due to a leaking LO signal. Furthermore, the frontend components are fabricated in the Fraunhofer IAF's 100 and 50 nm mHEMT technologies as thoroughly described in [Tes05, LTD+07]. To achieve a proper linearity and output power performance, upconverter, PA and multiplier are realized in the 100 nm technology [STK+11]. For the low noise amplifier as well as the downconverting mixer stage, the 50 nm technology is used due to a better noise performance [STK+11]. The mixer and LNA stages will be monolithically integrated on a single MMIC.
In this section, the design approach for the mixer circuits, followed by a static characterization on chip- and module-level are shown. The designs of the necessary LO generation as well as the amplification stages which will be used for the transmission experiments in the upcoming chapters, are realized by colleagues at the Fraunhofer IAF and Karlsruhe Institute of Technology (KIT) in the frame of a research project. The results in this chapter have partially been published in [23, 34].

2.1.1 I/Q-receiver design

To meet the system specifications for the planned E-Band communication link, an I/Q-receiver circuit, covering the RF frequency range from 71 to 86 GHz with an IF bandwidth of at least 5 GHz, is designed. To achieve the best possible noise figure, the circuits are designed in the Fraunhofer

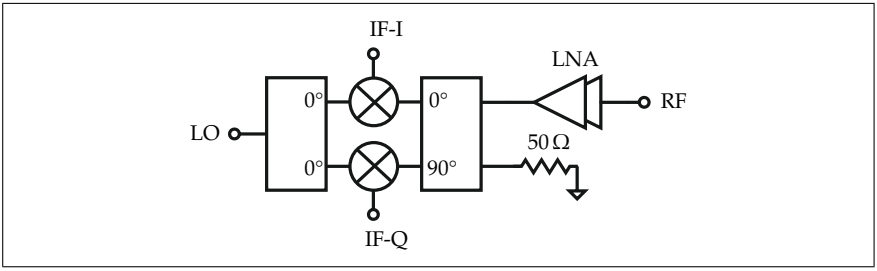

Figure 2.1: Schematic of the E-Band receiver topology, comprising the I/Q-mixer cell with a Wilkinson divider in the LO path as well as a Lange coupler and a two-stage LNA in the RF path.

IAF's 50 nm technology. In figure 2.1, a schematic of the receiver topology comprising the I/Q-mixer stage as well as a two-stage low noise amplifier is shown. The I/Q-mixer is realized by using two resistive mixer cells, a Lange coupler [Lan69, WL72] to form the necessary 90° phase difference for the I- and Q-channel, and a Wilkinson divider [Wil60] to provide the LO signal to both mixer cells. The design of the individual components will be shown in detail in the following. The LNA stage is realized by the Fraunhofer IAF and its layout file is provided to complete the receiver design.

2.1.1.1 Design of an E-band Wilkinson divider

To split the receiver's LO signal for the two single mixer cells which form the I- and Q-branch of the mixer, a Wilkinson divider in a coplanar 50 µm ground-to-ground spacing environment is designed. The Wilkinson divider follows a classical approach, with a line impedance of approximately 70 Ω in the $\lambda/4$-branches. For the 100 Ω resistance, the process' nickel-chromium layer is used to form an on-chip resistor. Figure 2.2 shows a chip photograph of the Wilkinson divider on the left side, which covers a chip space of approximately $350 \times 450\,\mu m^2$.
The simulation of the scattering parameters, as can be seen as dashed lines in figure 2.3 on the left, show a input port matching $|S_{11}|$ below

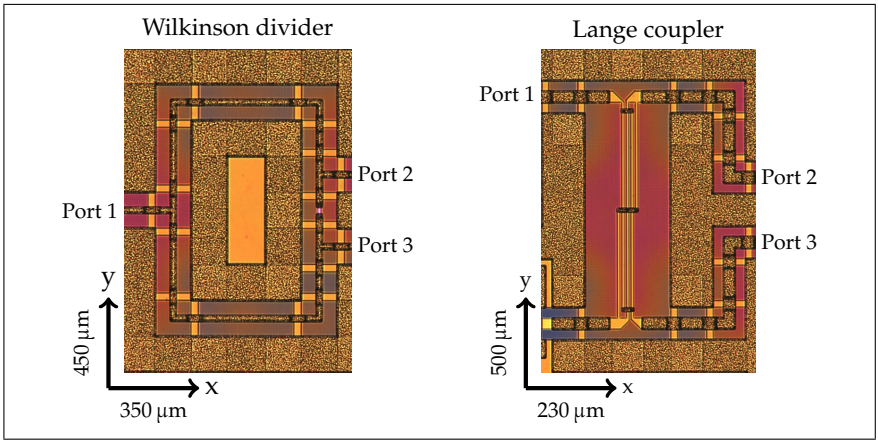

Figure 2.2: Chip photographs of the Wilkinson divider and Lange coupler as used for the realization of the E-band receiver circuit, with the port numbering as used for the measurement. The fourth port of the Lange coupler is terminated using a 50 Ω on-chip resistor.

−15 dB over the frequency range from 71 to 86 GHz, while the two output ports show a $|S_{22}|$ and $|S_{33}|$ below −28 dB in the same frequency range. Accordingly, the simulation results predict a well matched port impedance for all three ports, which is important for an integration with further circuit components. The insertion loss $|S_{21}|$ and isolation $|S_{32}|$ between the two divider branches are shown as dashed lines in figure 2.3 on the right. An insertion loss of approximately 0.5 dB over a frequency range from 60 to 100 GHz, combined with an isolation better than 15 dB is achieved. While the insertion loss of the divider is important for the power budgeting of the complete mixer circuit, a high isolation is important to prevent cross-talk between the mixer's I- and Q-branch.

The measurement results of the divider are shown as solid lines in figure 2.3. The comparison of simulation and measurement shows a good conformity for the port matching but a shift to lower frequencies for the output ports of approximately 12 GHz. Nevertheless, the impedance

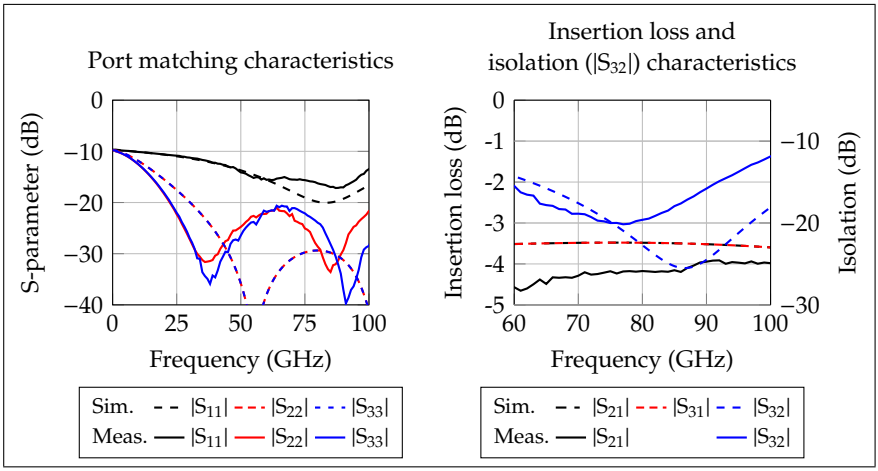

Figure 2.3: Comparison of the simulated and measured characteristics of the 77 GHz Wilkinson divider.

matching is still below −15 dB for the input and below −20 dB for the output ports in the frequency range of interest. When comparing the transmission and isolation characteristics, it can be seen that the measured insertion loss is 0.5 to 1 dB higher than in the simulation. The simulation of the isolation fits to the measurement for frequencies up to 75 GHz, for higher frequencies, the measured isolation is about 5 dB higher than the simulation predicted. Since the Wilkinson divider will be used in the LO path of the I/Q-mixer, the increased insertion loss can be compensated by applying a higher LO power, the reduced isolation will possibly cause a cross-talk between the LO channels of the mixer's I- and Q-branch, which can cause problems in combination with a poorly matched LO port of the attached mixer cells.

2.1.1.2 Lange coupler at 77 GHz

To generate the necessary phase difference of 90° for the mixer's I/Q-functionality, a Lange coupler is designed. To achieve a good coupling

performance, a four-finger design with a coupling length of 310 µm, a line width of 4 µm and a slot width of 3 µm is used. The unused coupler port is terminated with a 50 Ω on-chip resistor. A chip photograph is shown in figure 2.2 on the right.
The simulated scattering parameter in figure 2.4 on the left, show all port matching values $|S_{xx}|$ below 20 dB. The isolation $|S_{41}|$ is higher than 21 dB in the desired frequency range. When considering the coupling and phase performance in figure 2.4 on the right, the coupler shows an insertion loss between 0.5 dB and 1 dB as well as a maximum phase imbalance of 1°.
The corresponding measurement results are shown as solid lines in both plots of figure 2.4. The impedance matching and isolation of the Lange coupler differ only slightly from the simulated values. The coupling and phase characteristics are slightly worse than estimated by the simulation. The insertion loss is approximately 0.5 dB higher and the bandwidth is reduced but still covers the desired frequency range from 70 to 86 GHz. Also the phase imbalance in this frequency range increased to a value of ±1° around 92°.
Despite the slightly worse measured performance of the coupler compared to the simulation, the realized Lange coupler is suitable for the use in the planned I/Q-receiver circuit.

2.1.1.3 Mixer topology

As mentioned in the introductory part of this chapter, a resistive mixer topology is applied to realize the up- and downconverters for the intended millimeter wave wireless link. The resistive mixer is a widely used approach in broadband micro- and millimeter wave designs due to its simple topology and high linearity [Maa87, ALL+05, Zir06]. The fact that this topology operates without any DC-bias makes it less susceptible to circuit instabilities while simultaneously being an excellent candidate for low-power applications. A further advantage of the resistive mixer is its bi-directionality, allowing the use of the same device in an up- and downconversion scheme. Since the mixer operates without a drain voltage, only thermal noise is generated which is an additional advantage over

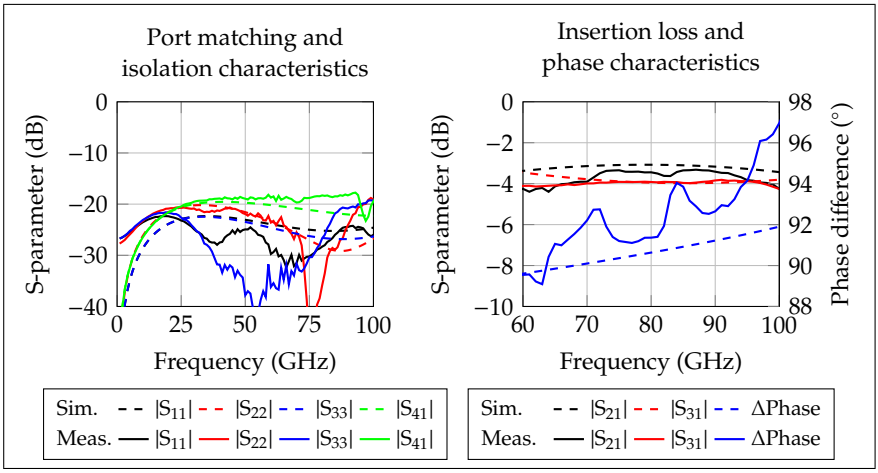

Figure 2.4: Comparison of the simulated and measured characteristics of the 77 GHz Lange coupler.

active mixer topologies [Maa93]. The disadvantages of this mixer topology are the high necessary LO drive, a higher conversion loss compared to active mixers, and the poor LO-to-RF isolation.

In the resistive mixer, the channel conductance of a common-source transistor configuration is modulated from pinch-off to fully conducting by an LO signal applied to the transistor's gate. Thereby, the channel conductance performs as a voltage-steered switch controlled by the large-signal LO. The RF is fed to the transistor's drain terminal, which is biased at zero volt, in a way that the low frequency output signal, representing the IF signal, results from the beating of the LO and RF signal [LK95, Maa93]. The IF signal is extracted at the drain, separated from the RF signal through a proper low-pass filtering structure. A deeper insight into the theory and modeling of resistive mixers is thoroughly discussed in several publications. Since this discussion is out of the focus of this thesis, the interested reader will find more information in [Kel77, Yhl07, Sal71, Maa93].

Despite its disadvantages, the resistive mixer topology is the most promis-

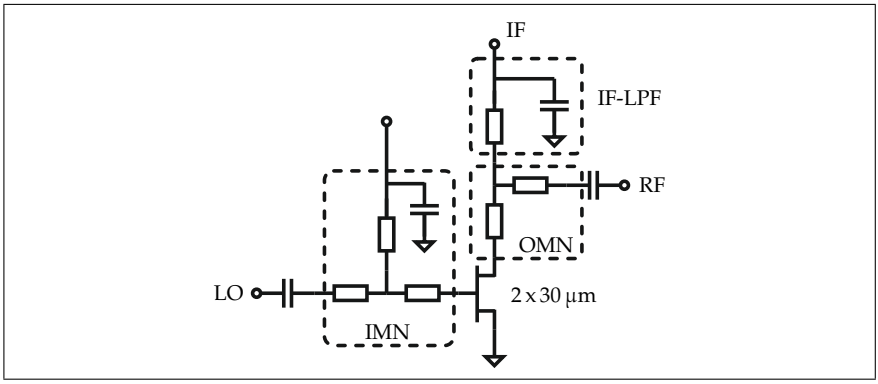

Figure 2.5: Simplified schematic of a single-ended resistive mixer cell as used in the I/Q-receiver shown in figure 2.1. The IMN, OMN as well as the LPF to extract the IF signal are highlighted.

ing candidate for realizing a broadband mixer stage with good linearity and reasonable conversion behavior. Its low complexity as well as the bi-directionality allow an uncomplicated system integration and a reuse of the identical mixer cell in the up- and downconverter circuits.

2.1.1.4 Design of an I/Q-mixer cell

The I/Q-mixer is set up by using two resistive mixer cells as shown in figure 2.5. The single cell is wideband-matched at the LO and RF port. The gate voltage for the mixer is applied via a $\lambda/4$-stub which together with two transmission lines form the input matching network (IMN) for the LO port. At the transistor drain, the IF signal is extracted via a $\lambda/4$-stub at 77 GHz in combination with a capacitance to ground forming an low pass filter (LPF). The $\lambda/4$-stub is also part of the mixer's output matching network (OMN). The two mixer cells are combined to an I/Q-mixer with the Wilkinson divider and the Lange coupler introduced above as shown in figure 2.1.
To determine the optimal transistor gate width (GW) for the mixer circuit,

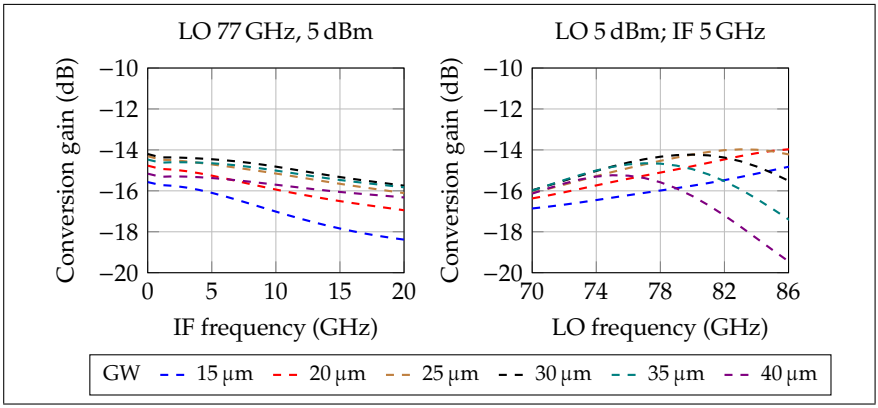

Figure 2.6: Simulated conversion gain versus IF (left) and RF (right) frequency for the transistor's gate width swept from 10 to 40 µm.

a simulation of the conversion gain versus both the IF frequency and the RF frequency is performed. For the first simulation, an LO input signal of 77 GHz and 5 dBm is used. The RF input signal is varied from 77.01 to 97.01 GHz, and the conversion gain for the resulting IF signal is calculated, while the gate width is swept from 10 to 40 µm. Thus, the minimum observed IF frequency is 10 MHz, the highest is 20 GHz. For the simulation of the conversion gain versus the RF frequency, the resulting IF signal is kept constant at a frequency of 5 GHz, and the LO and RF signal are swept for different gate widths. The results are shown in figure 2.6. Both simulations predict the best conversion performance for a gate width of 30 µm, with an IF bandwidth above 20 GHz and an RF bandwidth covering the desired bandwidth from 71 to 86 GHz centered at 79 GHz. Therefore, for the further design, a gate width of 30 µm is used.
After defining the necessary gate width, the matching for the LO port is modified for a sufficient large signal matching. Therefore, the LO power is varied between 0 and 10 dBm, while the matching circuit at the LO port of the mixer cells is manipulated. In figure 2.7 on the left, the resulting large signal matching at the mixer's LO port for the optimal matching circuit is

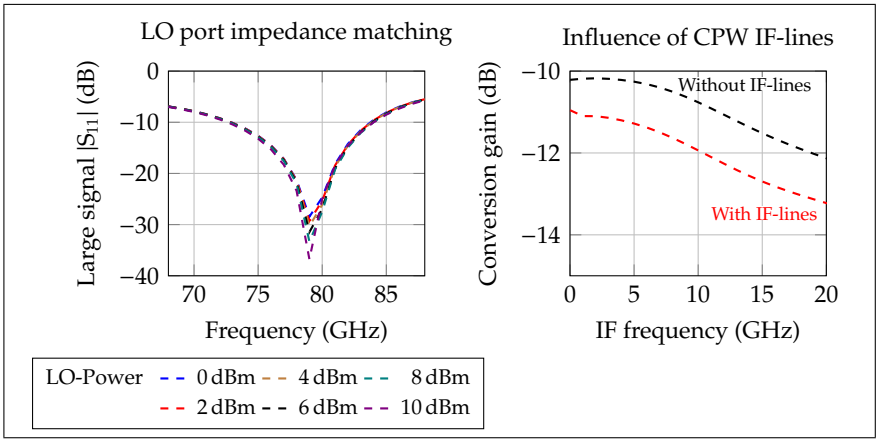

Figure 2.7: Large-signal s-parameter simulation of the I/Q-mixer cell's LO port with the LO input power varied (left). Simulated influence of the additional 14 µm CPW transmission lines in the IF path which are used to route the signal to one side of the MMIC (right).

shown as $|S_{11}|$. With this, there is only a small deviation with increasing power with a reasonably matched port over the desired frequency range. With respect to a later module integration, both IF ports have to be routed to one side of the chip, as can be seen in the mixer part of chip photograph in figure 2.8. Since both the I- and Q-signal path need the same electrical length to maintain the 90° phase relation for proper I/Q-operation, the transmission line of the I-path is extended and folded until it exhibits the same length as the Q-path. The physical line length of IF lines is approximately 800 µm. To save chip space and to allow for narrow bending when folding the I-channel line, a 14 µm ground-to-ground spacing coplanar waveguide (CPW) line is used. In figure 2.7 on the right, the conversion gains of the I/Q-mixer with and without these transmission lines in the IF paths are shown. As can be seen, these IF lines cause an additional loss of approximately 1 dB combined with a slight decrease of IF bandwidth.

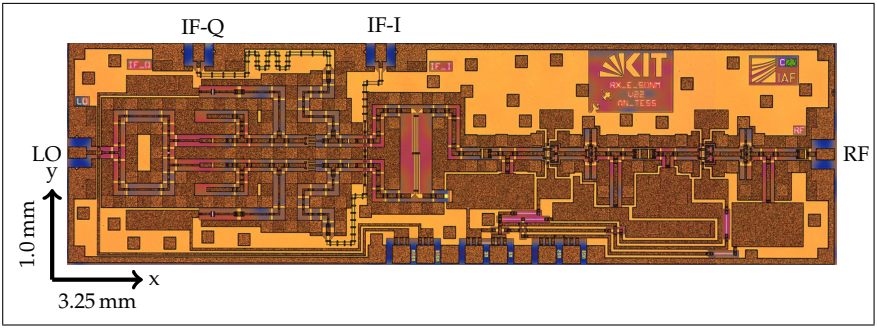

Figure 2.8: Chip photo of the 77 GHz receiver circuit, comprising the I/Q-mixer and a two-stage low noise amplifier.

In a further step, the I/Q-mixer is combined with the low noise amplifier to form the complete receiver circuit. The stand-alone LNA is designed by the Fraunhofer IAF and provides a measured small-signal gain of more than 22 dB combined with a noise figure below 2 dB over the entire bandwidth from 77 to 86 GHz [Tes14]. Due to the combination of both, the conversion gain of the receiver chip is expected to be approximately 11 dB. Since in an ideal case the resistive mixer only generates thermal noise as discussed during the topology decision, its noise figure can be estimated to be equal to the absolute value of its conversion loss. By following Friis's formula for the total noise of cascaded stages in equation (2.1), the noise figure of the complete receiver MMIC can be estimated to 2.2 dB.

$$F_{\text{total}} = F_1 + \frac{F_2 - 1}{G_1} + \ldots + \frac{F_n - 1}{G_1 G_2 \ldots G_{n-1}} , \tag{2.1}$$

where F_n and G_n are the noise figure and gain of the n-th stage, respectively.
A chip photograph of the manufactured receiver circuit is shown in figure 2.8. Since the LNA is designed at the Fraunhofer IAF, only a set of S-parameters extracted from the measurement of the stand-alone device

is available to perform the simulation. By this, a simulation of the gain improvement and the matching between the mixer and amplifier stage is possible. However, it is not possible to perform power budgeting or simulate the noise figure and the linearity of the entire circuit.

The simulation and measurement results for the I/Q-mixer combined with the LNA are shown in figures 2.9 and 2.10. In each plot, the simulation results, shown as dashed lines, are compared to the chip and module measurements as far as available.
The simulation of the conversion gain versus the LO input power in figure 2.9 on the left show a saturation of the conversion gain for input powers above 10 dBm. For this simulation, the LO frequency is set to a value of 77 GHz, the IF frequency is 5 GHz. The corresponding module measurements are performed with the same parameters but show an onset of saturation for an LO power of 6 dBm. Nevertheless, the shape of the measurement curve is similar. This indicates that the simulation predicts the conversion behavior adequately but is not capable of predicting the exact power value.
In figure 2.9 on the right, the simulation and measurements of the receiver's IF bandwidth are shown. The simulation is done at an LO frequency of 77 GHz with an LO power of 6 dBm and predicts a 3-dB IF bandwidth above 20 GHz. Compared to that, the chip measurement shows a 3 dB higher conversion gain than expected, which is most probably caused by the following effects: the complete receiver chip and the stand-alone LNA are processed on different wafer runs, which might result in different circuit gain due to process variations. Also, the LNA will see a slightly different termination than in the measurement of the stand-alone device, since the mixer's RF port might not be perfectly matched to 50 Ω. A process variation, resulting in slightly different behavior for each transistor results in an I/Q-amplitude imbalance at a maximum of 2 dB for an IF frequency of 20 GHz. In the desired bandwidth of 5 GHz, the conversion gain varies about 1 dB and the I/Q-imbalance is negligible. After the integration of the chip in a waveguide module, the resulting conversion gain and bandwidth are significantly reduced. This can be caused by losses in

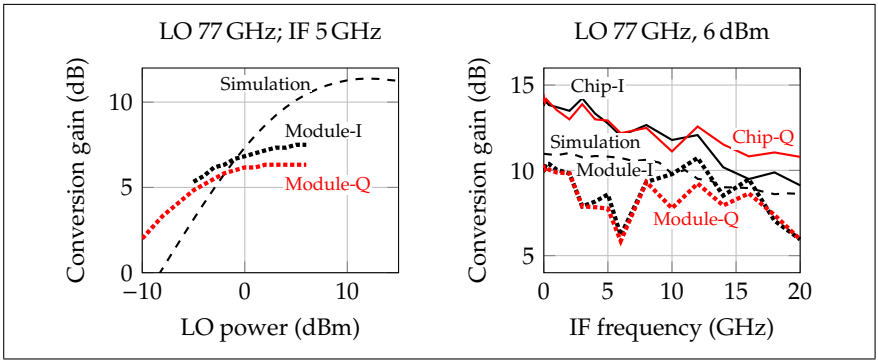

Figure 2.9: Comparison of the E-band I/Q-receiver module's conversion gain versus LO input power behavior to the simulation (left). IF bandwidth of the I/Q-receiver in simulation, MMIC and module measurement, each for the I- and Q-channel (right).

the bond wires and chip-to-waveguide transitions. Also, a mismatch in the routing of the I- and Q-channel's connection lines can cause a severe impact on the module performance. However, the module still provides a conversion gain of 10 dB combined with an 3-dB IF bandwidth above 5 GHz and an I/Q-imbalance below 1 dB in the desired bandwidth.
To evaluate the RF bandwidth of the receiver, a simulation with the LO and RF frequency swept at a constant offset of 5 GHz, for LO frequencies from 70 to 86 GHz is performed. The results in figure 2.10 show that the receiver covers the desired frequency range within a 1-dB bandwidth for an IF frequency of 5 GHz and therefore excellently meets the given specification. The measurement results for the waveguide module show a reduced conversion gain around 7 dB, also the bandwidth performance is worse compared to the simulation. This can also be caused by non-idealities in the module integration as explained above. Nevertheless, the desired RF bandwidth is covered within a 3-dB bandwidth.
A measurement of the receiver module's noise figure results in values around 2.85 dB ± 0.32 dB for a frequency range from 77 to 88 GHz. The decrease compared to the estimated noise value is caused by additional

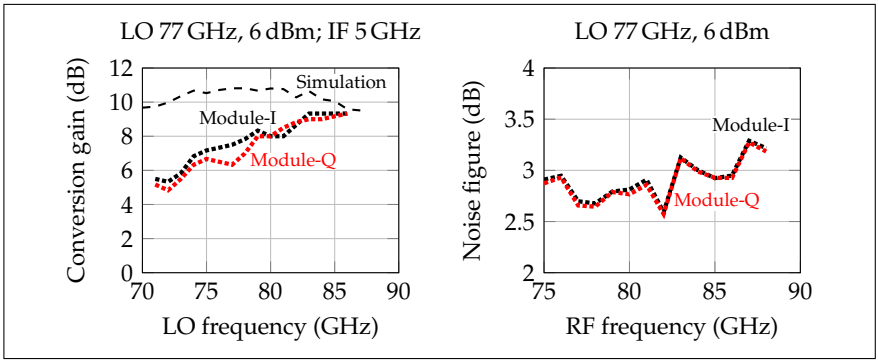

Figure 2.10: Simulation and measurement of the I/Q-receiver module's RF bandwidth with a fixed IF frequency (left). Measurement of the E-band receiver module's noise figure versus the RF frequency (right).

losses during the module integration as already observed for the conversion gain measurements.

2.1.2 Design of a balanced upconverter

The transmitter of the planned 77 GHz communication system has to meet the same bandwidth specifications as the I/Q-receiver. Additionally, since a leaked LO in the transmit signal may cause degradation in the quality of the data transmission, as discussed in chapter 1.2, a circuit with a high LO suppression has to be realized. To achieve a high linearity in the transmitter, the Fraunhofer IAF's 100 nm mHEMT technology is used. As indicated in figure 1.12, the E-band upconverter MMIC realized here will have no integrated RF amplifier stage to allow for a more flexible system setup[1]. For the transmission of complex modulated signals which demand a highly linear transmission system, the output signal of the

[1] Commonly, the transmitter of a wireless system comprises a mixing stage and an amplifying stage. Since in our specific case, the mixing stage is realized and packaged separately from the amplifiers, this device will from now on be called upconverter to distinguish it from actual transmitters.

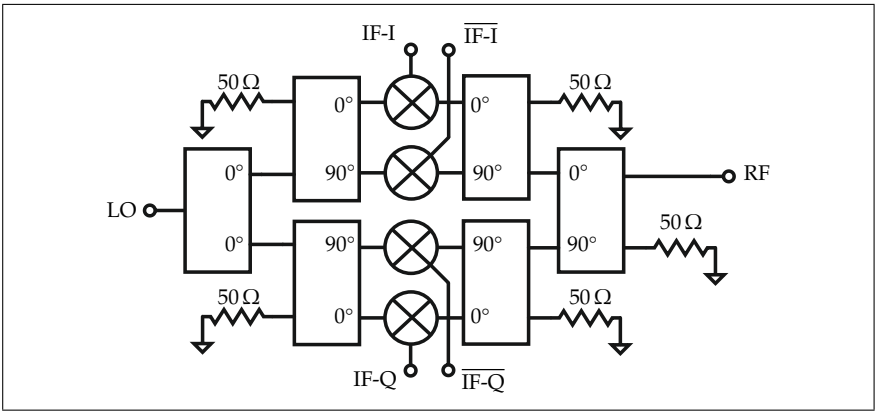

Figure 2.11: Simplified schematic of the balanced upconverter MMIC with a Lange coupler in the LO and RF path of both mixer branches to achieve a good LO suppression, and an additional Lange coupler and Wilkinson divider to realize the I/Q functionality.

upconverter can be fed directly into the power amplifier, which in this case operates in a very linear operation point. When transmitting simple modulation schemes like binary phase shift keying (BPSK), a medium power amplifier can be placed in between the upconverter and the power amplifier allowing an operation with maximum output power.
Due to its bidirectionally, the broadband resistive mixer stage designed for the E-band I/Q-receiver can be reused to realize the upconverter circuit by transferring it to the 100 nm technology. The balancing is realized by using a pair of the Lange couplers shown in section 2.1.1.2 and two mixer cells in both the I- and Q-channels LO and RF paths. The combination of two 90° phase shifts in the LO and RF paths with respect to the unshifted paths engender an LO suppression due to the overall phase difference of 180°. A simplified schematic of the balanced upconverter with the two Lange coupler in both the I- and Q-channel, as well as an additional Lange coupler and Wilkinson divider to realize the I/Q-functionality, can be seen in figure 2.11. To ensure a symmetric operation of the mixer cells in one

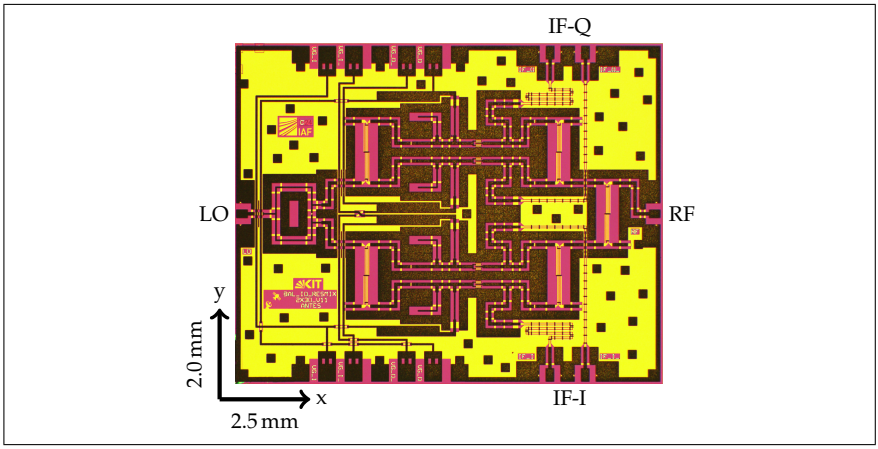

Figure 2.12: Chip photograph of the 77 GHz upconverter, comprising two Lange couplers for balancing each mixer cell of the converter's I- and Q-paths as well as a Wilkinson divider plus an additional Lange coupler for realizing the I/Q-functionality.

branch and to maximize the achievable conversion gain, a balanced IF signal has to be applied to the mixer. A chip photograph of the realized MMIC is shown in figure 2.12

To determine the upconverter's IF bandwidth, the LO signal is held constant at 77 GHz with a 15 dBm input power, the IF signal is swept up to 15 GHz with an input power of −5 dBm and the MMIC's output power is plotted versus the IF frequency. The simulation results as well as the results obtained in the MMIC measurement for the upper and the lower sideband are plotted in figure 2.13 on the left. As can be seen for the measurement, a 3-dB bandwidth of 12 GHz is achieved with a difference between upper and lower sideband of less than 1.7 dB. After module integration, the bandwidth performance is degraded. As can be seen in the module measurement results in figure 2.13 on the right for both the I- and Q-channel, a 3-dB bandwidth of approximately 4.5 dB is achieved.

The results are obtained by a power meter measurement, i.e. the shown power values represent a combination of the power in the upper and lower sideband as well as the power of the leaked LO signal. The power of the leaked LO signal is measured to be approximately −21 dBm, when no IF signal is applied to the mixer. The I/Q-imbalance is approximately 1 dB over an IF bandwidth of 12 GHz and increases to a value of 1.7 dB for IF frequencies up to 20 GHz.
A simulation of the upconverter's RF bandwidth, obtained by sweeping the LO frequency from 70 to 86 GHz at 14 dBm input power, while the IF is held constant at 2 GHz reveal a conversion gain of −11 dB in a 1-dB bandwidth of approximately 15 GHz without any significant differences between upper and lower sideband.
The upconverter's linearity and LO suppression characteristics are evaluated separately by sweeping the power of the IF signal from −6 to 15 dBm at an LO of 77 GHz and an IF of 2 GHz. The LO power is set to 8 dBm. Figure 2.14 shows the output power versus the applied IF power as simulated and for the measurement, separated for the lower (left) and the upper sideband (right) as well as for the I- and Q-channels. The corresponding LO suppression is also plotted. As can be seen, the measurement results are very well predicted by the simulation, even for the power conversion. The simulated 1-dB compression[2] occurs at an IF input power of 5 dBm, while the and measured 1-dB compression point occurs at approximately 2 dBm. The maximum achieved output power is −5.5 dBm for a 6 dBm IF signal. Also, the simulated power of the leaked LO signal fits to the measurement. For an operation of the upconverter at the 1-dB compression point, the leaked LO signal power is approximately 20 dB below the desired sidebands. Comparing the LO to RF suppression of approximately 38 dB obtained in this measurement with the suppression of 35 dB obtained in the IF bandwidth measurement without an IF signal applied, reveals that the suppression is dependent on the conversion behavior. The suppression increases when an IF signal is applied to the mixer. Also in

[2]The 1-dB compression point of an active device is defined as the operating point, where the actual gain is one dB below the its linear gain.

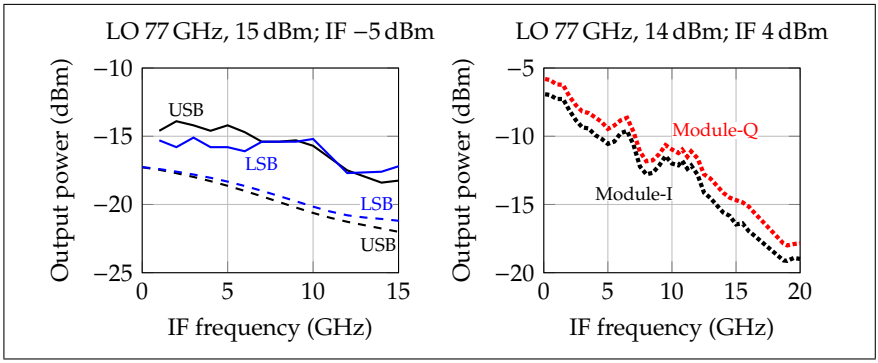

Figure 2.13: Comparison of the upconverter MMIC's simulated and measured IF bandwidth in the USB and LSB (left). Measurement of the upconverter's output power after module integration for the I- and Q-channel (right).

the measurement shown here, the I/Q-imbalance is approximately 1 dB. Furthermore, the difference between LSB and USB is negligible.

2.1.3 LO source realization

To provide a highly stable signal source for the planned communication system, a tunable phase-locked loop (PLL)-stabilized VCO circuit based on commercially available components at a center frequency of 9.6 GHz is realized by the Fraunhofer IAF. This VCO is followed by an MMIC-based frequency multiplier-by-eight, realized by the KIT [LTM+12]. Packaged into a waveguide module, the multiplier achieves a 3-dB bandwidth from 72 to 85 GHz with an output power of 8 dBm and a suppression of unwanted harmonics of more than 37 dBc. A combination of these devices can be used to provide the local oscillator signals for both the transmitter and receiver. To investigate the influence of the LO source on the transmission quality, instead of a VCO, an Agilent PSG E8257D analog signal generator operated at 9.6 GHz can be used to drive the frequency multiplier.

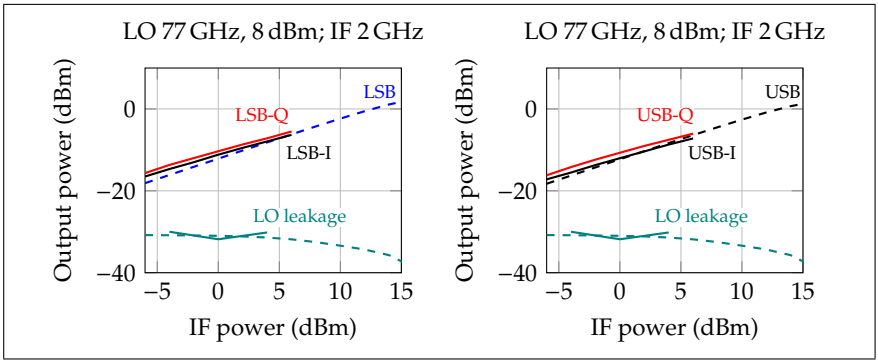

Figure 2.14: Simulation (dashed) and measurement of the balanced upconverter MMIC's output power for different IF input powers. The results for the I- and Q-channels are shown, separately for the lower (left) and upper (right) sideband. In both cases, also the simulation and measurement of the leaked LO behavior is shown.

In figure 2.15 on the left, the output spectra of the two VCO-based signal sources and of the Agilent signal source at 9.6 GHz are shown. The measurement is done with a spectrum analyzer with the span set to 120 MHz, a resolution bandwidth of 30 kHz and a video bandwidth of 300 Hz. As can can be seen, each signal source provides a stable output signal, but in the output spectra of the VCOs, spurs at 50 MHz offset from the carrier are existent, with a power relative to the desired output signal of approximately −43 and −27 dBc for VCO 1 and VCO 2, respectively. These spurs are caused by the internal PLL reference signal, which is not sufficiently suppressed by the loop filter [Kur14].
A characterization of the phase noise of these different signal sources performed with a signal source analyzer[3] reveals a phase noise of −115 dBc/Hz at an offset of 100 kHz for the Agilent signal source and a phase noise of −103 and −106 dBc/Hz for VCO 1 and VCO 2, respectively. When comparing both VCOs against each other, VCO 1 shows a better phase noise

[3]Signal source analyzer Agilent E5052B

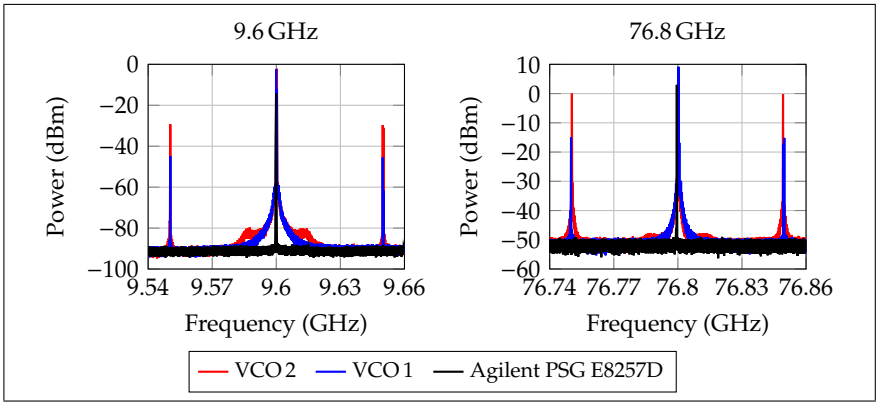

Figure 2.15: Output spectra of the different LO sources at a frequency of 9.6 GHz and after the frequency multiplier at 76.8 GHz. The measurements are done using a spectrum analyzer with a resolution bandwidth of 30 kHz and a video bandwidth of 300 Hz and, in case of the 76.8 GHz, with an attached downconverter.

performance but also a significantly higher spur at 50 MHz in its spectrum. A measurement of the frequency multiplier's output signal at 76.8 GHz driven by the different LO sources shown in figure 2.15 on the right reveal the same behavior as for the 9.6 GHz measurement, but it is remarkable that the suppression of unwanted spurs at the 50 MHz offset from the carrier is reduced by approximately 19 dB for both VCOs.
To determine the total phase noise which will degrade the signal quality in the later data transmission, one can calculate the phase noise after the multiplication stage by using equation (2.2), where n determines the multiplication factor [Cam98]. As shown for frequency multipliers built in a similar fashion using the same mHEMT technology and operating around 94 GHz in [LTM+11] and in [37] for a similar measurement setup using the multipliers considered here, the measured output phase noise of the frequency multipliers corresponds very well to the theoretically calculated phase noise. Therefore, the total phase noise (PN) can be reliably

Table 2.1: Comparison of the E-band receiver MMIC with state of the art.

Reference	CG (dB)	B_{IF} (GHz)	B_{RF} (GHz)	P_{1dB} (dBm)	NF (dB)	Type	Tech.
[CBYK+11] [1]	-4.5	-	5	-3.5	15.5	bal.	SiGe HBT
[HHR05] [2,3]	0.7	1	6	-8	(23)	bal.	SiGe HBT
[NLA+13] [1]	24	5.5	16	-22	6.6	bal.	SiGe HBT
[JK10]	-4.5	5	7	0	-	bal.	InP HBT
[TKY+11]	-16	-	15	-	-	I/Q	pHEMT
[TKB+13a] [1]	12	-	15	-	5.5	I/Q	pHEMT
[GFG+09]	-9	10	20	1	-	I/Q	mHEMT
This work [1,4]	14	15	15	>2	(2.85)	I/Q	mHEMT

[1] integrated LNA, [2] integrated IF amplifier, [3] *NF* simulated, [4] *NF* on module level

estimated by equation (2.2) and an identical behavior will be assumed for all multipliers considered in this thesis.

$$PN_{\text{mult, dBc/Hz}} = PN_{\text{source, dBc/Hz}} + 20\log(n) \tag{2.2}$$

2.1.4 Comparison to the state of the art

To relate the realized chipset to the state of the art, the key parameters conversion gain CG, IF bandwidth, RF bandwidth, 1-dB compression point P_{1dB} and noise figure NF of the receiver MMIC are listed in table 2.1 and compared to other published E-band receivers. The achieved conversion gain and RF bandwidth of the MMIC meet the state of the art, while the achieved IF bandwidth exceeds the design in [GFG+09] by 5 GHz at a comparable conversion gain. The high linearity results from the use of the resistive mixer topology. The comparison to the active approaches used in [HHR05] and [NLA+13] reveals the significantly higher P_{1dB}. The provided noise figure is based on a module-level measurement. Due to non-idealities introduced by the module integration, i.e. additional losses in the RF and IF bond wires, the MMIC's noise figure is even lower. Nevertheless, when comparing the Rx module's noise figure to the chip-level

Table 2.2: Comparison of the E-band upconverter MMIC with state of the art.

Reference	CG (dB)	B_{IF} (GHz)	B_{RF} (GHz)	$P_{out,\,1dB}$ (dBm)	Type	Tech.
[LYT+13]	0	-	20	-31	bal. I/Q	CMOS
[KBYC+12] [1]	20	-	5	11	I/Q	SiGe HBT
[KKKB14]	-10.5	5	5	-9	fund.	pHEMT
[KKK+10] [1]	15	2.5	2.5	16	fund.	pHEMT
[DDN12]	-11	>6	14	-	I/Q	pHEMT
[TKB+13b] [1]	29	-	5	21	bal.	pHEMT
[GZFG10]	-11	5	25	0	bal. I/Q	mHEMT
This work [2]	-10	12	(15)	-5.5	bal. I/Q	mHEMT

[1] with integrated PA, [2] B_{RF} simulated

noise figures in the literature, the achieved result outperform all the other designs.

The performance of the upconverter MMIC is compared to the state of the art in table 2.2 in terms of conversion gain CG, IF and RF bandwidth as well as the output power $P_{out,\,1dB}$ achieved at the 1-dB compression point. The realized upconverter provides a significantly increased IF bandwidth compared to values found in the literature. In terms of RF bandwidth, the achieved results meet the state of the art. When considering the targeted application of broadband communication, the IF bandwidth, determining the useable modulation bandwidth of a fixed carrier signal, is the parameter of interest. The RF bandwidth, defined as the bandwidth achieved when sweeping the LO signal while applying a fixed IF signal is of minor interest for the use in communication links. The comparison of the conversion gains and the output related P_{1dB} reveals a large variation between the shown designs. Some of the listed devices provide high conversion gains in combination with significantly higher output powers. This is due to the fact that in these cases the upconverter stages are integrated with a power amplifier, increasing both the conversion gain and output power.

The performance of the designs without the PA-stage cannot be separated for the information given in the publications. Therefore, a fair comparison in terms of conversion gain and output power to the upconverter realized here is not possible.

2.2 240 GHz frontend modules for high data rate wireless links

For realizing the broadband 240 GHz link for direct up- and downconversion scenarios, a set of MMIC-based waveguide modules, comprising an I/Q-upconverter, an I/Q-downconverter and appropriate frequency multipliers to provide the local oscillator for the frontend modules, are used. The MMICs forming the functional block inside these modules are designed and fabricated in the Fraunhofer IAF's 35 nm mHEMT technology. Further information on the stand-alone MMICs are published in [LDKT+12]. The MMIC design and development as well as the module integration of these MMICs into waveguide modules is already thoroughly discussed in [LDAF15]. Thus, the following section only focuses on the characterization of these receiver and transmitter frontend modules, which are made available for the transmission experiments in this thesis. The content of this section has partly been published in [5] and [35].

2.2.1 Receiver

The MMIC in the Rx module comprises a balanced subharmonic I/Q-mixer with the LO provided at a frequency of 120 GHz and a three stage LNA. Mounted into waveguide modules, the LO signal is routed via a WR-8 waveguide[4], while for the RF signal a WR-3 waveguide[5] is used.

[4] In terms of waveguide standards, the WR-8 waveguide, or F-band, covers the frequency range from 90-140 GHz.

[5] In terms of waveguide standards, the WR-3 waveguide covers the frequency range from 220-325 GHz. In some publications this frequency band is also referred to as H-band.

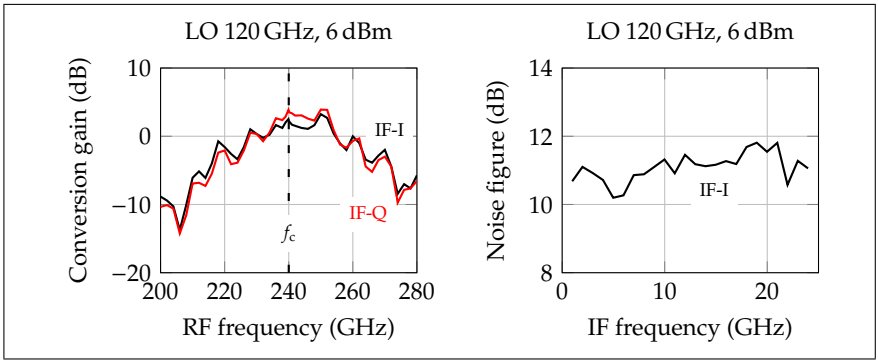

Figure 2.16: IF bandwidth measurement of the 240 GHz receiver module for the I- and Q- channel in both the USB and LSB (left). Double-sideband noise figure measurement of the receiver module's I-channel (right).

The conversion gain of the Rx module is measured using a constant LO signal at 120 GHz with a power level of 6 dBm. At the RF port a WR-3 waveguide attenuator is used to ensure small signal conditions and to prevent a saturation of the LNA. Since this LNA features approximately 30 dB of small signal gain and is saturated for an output power of approximately 0 dBm, the RF input power is set to power levels of −35 dBm. The down-converted signal is measured with a spectrum analyzer at both the IF-I and IF-Q port.
In figure 2.16 on the left, the conversion gain of the receiver module versus the RF frequency is plotted, while the LO signal is held constant at 120 GHz. A maximum conversion gain of 3.8 dB is measured at the IF-Q output, while the 3-dB bandwidth is approximately 20 GHz in both the I- and Q-channel. The I/Q-amplitude imbalance stays below 1.9 dB over the entire frequency range.
To characterize the receiver module in terms of noise figure, a hot-cold noise measurement setup, similar to the one explained in [4] is used. This allows for a measurement over the receiver's entire bandwidth. A measurement using a noise diode, as commonly done, would only allow

to measure within the diode's bandwidth, which is commonly around 4 GHz. To set up the hot-cold measurement, a horn antenna attached to the receiver module is pointing towards an absorber at room temperature to measure the hot point. After this, the absorber is chanced to an absorber cooled in liquid nitrogen at 77 K and the cold point is measured. The noise figure is then calculated using the Y-method. A detailed description of the hot-cold measurement setup can be found in [WLS+12]. The measurement is performed for a double-sideband setup, since no suitable bandpass filters in the frequency range around 240 GHz were available.
As can be seen in measurement results in figure 2.16 on the right, a noise figure of less than 12 dB over an IF frequency range of 24 GHz was measured in the I-channel for a double-sideband measurement. As shown in [4], the noise distribution is approximately the same for the I- and Q-channel.

2.2.2 Transmitter

Since the single-balanced resistive mixer used for the frequency conversion is inherently bidirectional as explained in section 2.1.1.3, the transmit MMIC can be composed by the same components as the receiver chip but with the LNA now used as a RF post-amplifier. Also the fabricated waveguide module is identical with the receiver module.
For the characterization of the transmitter module, the LO signal is kept constant at 120 GHz with a power level of 7 dBm, the IF signal is generated by using a frequency synthesizer which is swept from 1 to 40 GHz with a power level of 0 dBm. The output power is measured using a calorimetric power meter[6], which is only capable for measuring the sum of all spectral components in the frequency range determined by the attached waveguide. Since the lower cut-off for the WR-3 waveguide is around 170 GHz, the measured power is the sum of the two upconverted RF sidebands and the LO leakage at 2×120 GHz, the possibly leaked LO signal at 120 GHz cannot propagate through the WR-3 waveguide.

[6]Calorimetric power meter: Erickson PM1

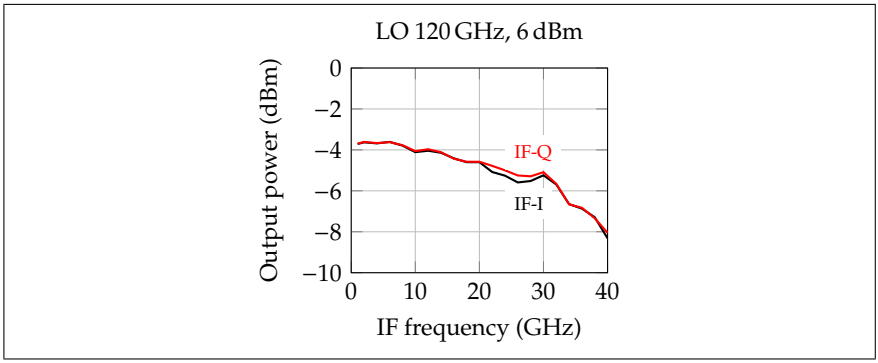

Figure 2.17: Double-sideband IF bandwidth measurement of the 240 GHz transmitter module's I- and Q-channel. The LO input power is set to 7 dBm, while the used IF power is 0 dBm.

The measured RF output power of the transmitter module versus the applied IF frequency at the I- as well as the Q-channel is shown in figure 2.17. As for the Rx, the unconnected IF port was left open during the measurements. In this setup, the transmitter achieves a maximum output power of −3.6 dBm at an IF frequency of 2 GHz. The 3-dB bandwidth of the transmitter module is 35 GHz.
To measure the carrier suppression of the upconverted signal with respect to the upper and the lower sideband, an harmonic mixer has been used. Since the employed mixer is uncalibrated, a very narrow IF of only 50 MHz is used for the measurements to ensure a constant conversion loss in both sidebands. Using this setup, a carrier suppression at 240 GHz of more than 12 dBc for both sidebands and IF channels is measured for an LO power of 7 dBm and −10 dBm IF power.

2.2.3 Comparison to the state of the art

In tables 2.3 and 2.4 the 240 GHz frontend modules are compared to the state of the art, separated by receive and transmit components. While there are several receiver circuits published in the frequency range be-

Table 2.3: Comparison of the 240 GHz receiver module with the state of the art.

Reference	CG (dB)	B_{IF} (GHz)	f_c (GHz)	f_{LO} (GHz)	NF_{DSB} (dB)	Tech
[GSL+13] [1]	-6	2	283	283	(38)	CMOS
[OHP11] [2]	16	10	220	110	(15)	HBT
[MSBS12] [3]	21	2.1	245	60	(16)	HBT
[EMG+13]	18	10	245	245	18	HBT
[MSB+13] [3]	10.6	3	245	60	(17)	HBT
[GWS+08]	2	4.5	220	110	8.4	mHEMT
this work [4]	3.8	20	240	120	12	mHEMT

[1] *NF* simulated, [2] *NF* estimated, [3] SSB-*NF*, [4] mmW waveguide module

tween 200 GHz and 300 GHz, most of them for radar and imaging applications, only one dedicated transmitter circuit can be found. Therefore, the 240 GHz transmitter module is also compared to existing opto-electrical communication links, which in this frequency range are typically set up by a combination of UTC-PDs. These components show an inherently large bandwidth. The system's bandwidth limitations are introduced by the limited baseband components. Thus, for the UTC-PDs, no IF bandwidth values are given in the publications.

For both receivers and transmitters the key characteristics, namely the RF center frequency f_c, the frequency of the used local oscillator f_{LO}, the used transistor or optical technology, the conversion gain CG as well as the 3-dB IF bandwidth are listed. Additionally, for receiver components the double-sideband noise figure NF, and for transmitters, the maximum output power P_{out} are shown.

Table 2.3 shows that the receiver module used in this thesis exhibits twice the 3-dB IF bandwidth than other circuits in this frequency range. Also, a reasonable noise figure is achieved, only surpassed by the MMIC shown in [GWS+08], which operates at a lower frequency and only provides a quarter of the bandwidth.

When comparing the transmitter module bandwidth performance to the state-of-the art, it surpasses the comparable transmitter MMIC in terms

Table 2.4: Comparison of the 240 GHz transmitter module with the state of the art.

Reference	CG (dB)	B_{IF} (GHz)	f_c (GHz)	f_{LO} (GHz)	P_{out} (dBm)	Tech
[ONFI05]	-23.5	-	240	n/a	-11	UTC-PD
[SAH+09a]	-	-	250	n/a	-7	UTC-PD
[29],[6]	-28	-	237.5	n/a	-13.5	UTC-PD
[AGW+11] [1]	-8	10	220	55	-6	mHEMT
this work [2]	-0.6	35	240	120	-3.6	mHEMT

[1] MMIC, [2] mmW waveguide module

of IF bandwidth by a factor of 3.5 at a similar carrier frequency. As explained above, for the UTC-PD devices no bandwidth data can be found. Considering the devices output power, which is undoubtedly one of the key characteristics for a communication system, it can be seen that the 240 GHz transmitter module used in this thesis provides the highest output power, which is its major advantage over the optical components.

2.3 MMICs for 300 GHz indoor communication

As described in chapter 1, the need for high-speed wireless data services such as wireless personal area networks, multimedia access or kiosk applications, drives the development of multi-gigabit indoor systems. Although there is ongoing research and already many existing applications in the 60 GHz band, these systems are still limited by the available bandwidth and hence in the achievable data rate. An increase in data rate can be achieved by elevated modulation formats such as 512-QAM or even 1024-QAM, which lead to extremely severe and hard-to-meet requirements concerning the components' performance in terms of linearity as well as system noise and phase noise. A data rate increase can also be achieved by the use of new transmission approaches like massive multiple-input multiple-output (MIMO), where hundreds of antennas combined in an-

tenna arrays are used to serve many terminals [LETM14]. The drawback of this approach is the enormous number of hardware components which are needed to setup the systems.
An alternative approach is the use of systems operating in the high millimeter and even submillimeter wave regime above 275 GHz where, at the time of writing, no frequency regulation exists. The huge available bandwidths as well as the small component sizes enable compact indoor systems which are capable of transmitting data rates of up to 100 Gbit/s over several meters, even by using simple modulation formats such as BPSK or QPSK. With slightly advanced modulation formats, the data rates can be increase even more. To pave the way towards ultra broadband THz communication systems for indoor applications, a fully integrated MMIC-based frontend is developed in this thesis. As for the 240 GHz components, the Fraunhofer IAF's 35 nm mHEMT technology with its high f_T of 515 GHz and f_{Max} above 1 THz will be used. This technology performance allows for a gain of more than 20 dB in combination with a noise figure below 7 dB in a LNA-stage in the 300 GHz range [LTD+13]. With an integration of mixer and amplifier stages on a single MMIC, these LNA parameters suggest that outstanding performance can be achieved for the intended 300 GHz transmit and receive circuits.
In the following section, the design approach, development and characterization of this 300 GHz MMIC chipset is described. The results have partially been published in [33].

2.3.1 Broadband single-balanced mixer MMICs for 300 GHz

As argued in section 2.1.1.3, the resistive mixer topology comes with a set of advantages for millimeter-wave applications. These advantages are even more present in the 300 GHz regime, where transistors with an extremely high f_T are necessary to realize multifunctional circuits. Additionally, transistor model verification is difficult and therefore seldom available in this frequency range, since accurate, reliable and reproducible measurements are still hard to perform. Here, the low circuit complexity

of the resistive mixer allow for a robust design with a high yield. Following this, the resistive mixer approach is the most promising for realizing the mixer cells for a set of 300 GHz up- and downconverters.
The designated IF bandwidth of the planned mixer is 25 GHz, resulting in an RF bandwidth of 50 GHz. Additionally, to prevent the saturation of the following stages as well as to suppress unwanted DC-offsets introduced by a self-mixing process of the LO signal as explained in chapter 1.2, a single-balanced mixer design will be realized for both the up- and downconverter to suppress the LO signal at the circuit's output. The balancing is done by using two 90°-hybrid couplers, one in the LO and one in the RF path, similar to the upconverter design in section 2.1.2. The phase shift of the LO signal introduced in both couplers sums up to a total phase difference of 180° at the mixer's RF port. For the addressed applications of high data-rate communication using different modulation schemes, both the up- and downconverter shall provide I/Q-functionality, demanding broadband IF ports with good performance in amplitude and phase balance in the I- and Q-branches.

2.3.1.1 Design of a broadband Wilkinson combiner

As explained for the E-band frontend, the I- and Q-branches of the two mixer cells have to be combined. In the approach for a 300 GHz frontend, a Wilkinson combiner in a coplanar 14 µm ground-ground-spacing environment is designed to combine the I- and Q-branches of the two single mixer cells. The combiner follows a classic approach with both $\lambda/4$-branches realized with a line impedance of approximately 70 Ω. For the 100 Ω resistance, the technology's nickel-chromium layer is used. A chip photograph of the realized Wilkinson combiner is shown in figure 2.18 on the left. The port matching is shown in figure 2.19 on the right. To meet the bandwidth requirements of 100 GHz, the input port could not be matched as well as the output ports, but the resulting $|S_{11}|$ is still better than 12 dB in the desired frequency range. As can be seen in figure 2.19 on the right, the combiner show an insertion loss of less than 1 dB in combination with an isolation $|S_{32}|$ better than 12 dB in a frequency range from 200 to 400 GHz.

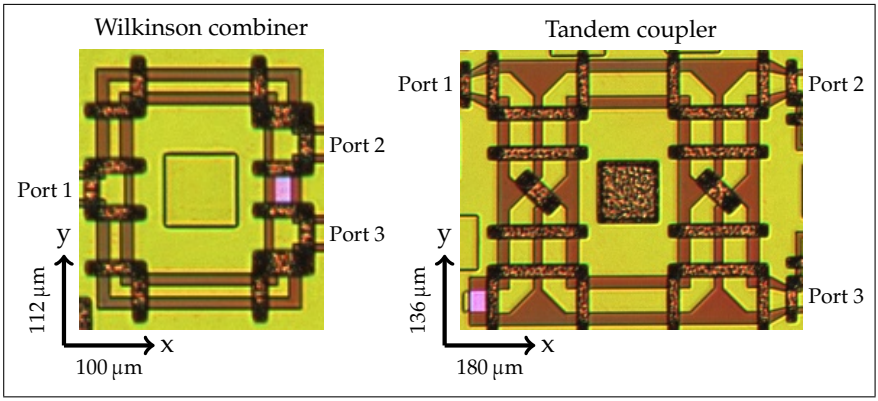

Figure 2.18: Chip photographs of the Wilkinson combiner and tandem coupler as used for the realization of the 300 GHz frontend, with the port numbering as used for the measurement. The fourth port of the tandem coupler is terminated using a 50 Ω on-chip resistor.

As explained for the E-band frontend, insufficient port matching or isolation can cause problems when integrating the component with other building blocks.

2.3.1.2 90°-hybrid coupler design

Since a completely integrated transmitter and receiver chip shall be realized, the necessary phase shift of 90° for the I/Q-functionality as well as for the balancing has to be generated by using a broadband on-chip coupler. For the I/Q-functionality, the phase balance, i.e. how accurate the wanted phase difference of 90° between the direct and the coupled path is met, is essential. As long as the coupler is used in the LO path and the LO is monofrequent, the coupler's bandwidth can be neglected. But when using two 90°-hybrids to form a single balanced mixer by placing one coupler in the mixer's LO and one in the RF path as explained above, the coupler bandwidth has to meet the bandwidth requirements set by the mixer's RF bandwidth.

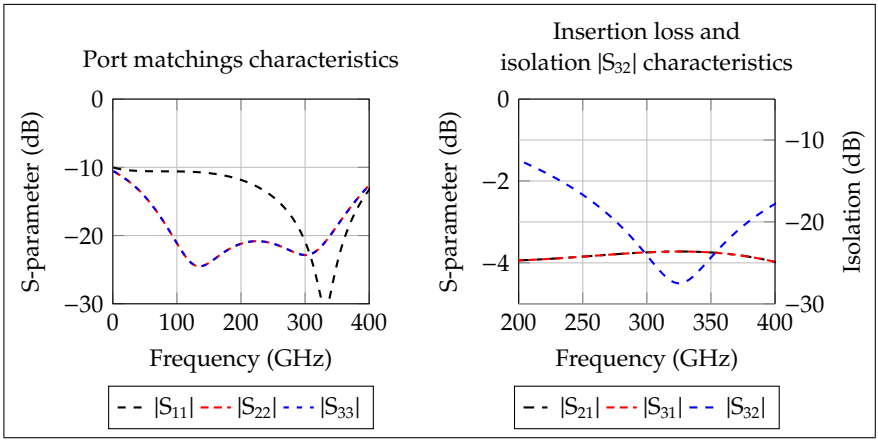

Figure 2.19: Simulated scattering parameter of the 300 GHz Wilkinson combiner. On the left, the matching for all three ports is shown. In the right plot, the insertion loss and isolation between the two combiner branches can be seen.

Amongst the multiplicity of 90°-hybrid approaches, the tandem coupler, although well-known and described [CLC03], up to now is only used in few MMIC designs since a technology with an air-bridge process is needed to connect the parallel-coupled lines which form the coupler [LLL+08, LHC+09, LAL+07]. Nevertheless, as described in [MHO+06], when utilizing an MMIC technology with air-bridge process, the tandem coupler provides a higher bandwidth and better phase balance combined with a smaller layout compared to the more conventional couplers.
Following these considerations, the tandem coupler shown in figure 2.18 on the right is realized to generate all necessary 90° phase shifts in the 300 GHz chipset. The coupler's chip size is $180 \times 136\,\mu m^2$, while the coupling length of the parallel-coupled lines is 89 µm. The $\lambda/4$ wavelength in the used process is calculated[7] to 97 µm. The length difference of the cou-

[7]The calculation of the line length is done by using the *line calc* tools of Agilent's Advanced Design System (ADS). This tool is capable to calculate the electrical length of different

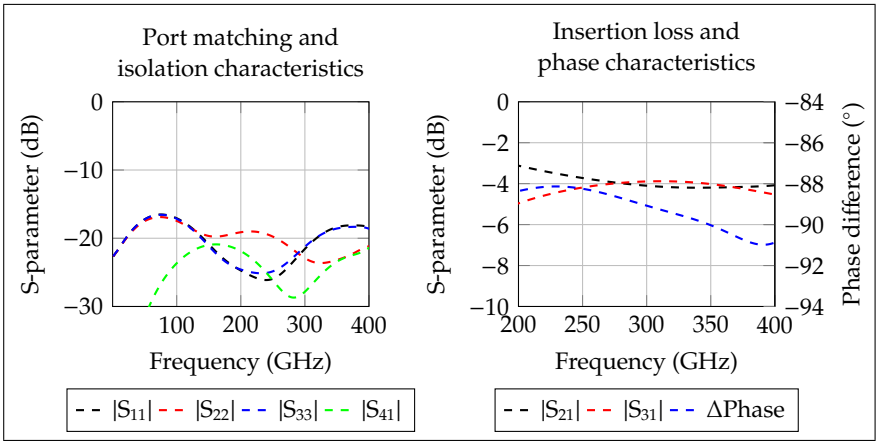

Figure 2.20: Simulated scattering parameter of the 300 GHz tandem coupler. The port matching as well as the isolation $|S_{41}|$ is shown in the left plot, the insertion loss as well as the phase difference between port two and three is shown in the right plot.

pling line can be explained by the broadside-coupling effect introduced by the air-bridge crossovers as explained in [MHO+06], which shortens the length for maximum coupling. The used line width in the coupler is 5 µm, while the coupling space is 3 µm. In figure 2.20 on the left, the simulated port matching as well as the isolation between port one and four $|S_{41}|$ is shown. The reflection loss of all ports $|S_{xx}|$ is better than 15 dB, while the isolation is better than 20 dB. When integrating this coupler with the other building blocks into a complete MMIC, the well matched ports will prevent reflections due to mismatched discontinuities, while the isolation will prevent crosstalk between the two mixer channels in the balanced mixer, or the I- and Q- branch when using the coupler in an I/Q-mixer setup.
The right plot of figure 2.20 shows the simulated insertion loss, coupling

transmission line types whilst taking into account all parameters defined by the substrate and layer process of the respective MMIC technology.

behavior and the phase difference between the two output ports in the frequency range from 200 to 400 GHz. The tandem coupler is slightly over-coupled in a frequency range from 280 to 367 GHz with an insertion loss around 1 dB, while the phase difference between the two output ports varies between 88.7 and 90.5° in this frequency range. Since the losses in transmission lines as well as waveguide to chip transitions increase with frequency, the insertion loss is an important contributor for the overall system power budget. A simulated value of 1 dB should be bearable for a future system integration. Also, the achieved phase stability of 89.5° ± 1° over a frequency range of nearly 90 GHz will ensure proper operation, both for the use in a balanced design as well as for an I/Q-mixer.

2.3.1.3 Single-balanced mixer design

The single-balanced mixer is realized by using a 2-finger common-ground transistor with a gate width of 7 μm in each finger in a passive fundamental resistive mixer configuration similar to the one already shown for the E-band mixer. Both the LO and RF ports of this cell are broadband matched around 300 GHz by using open stubs. The balancing of the mixer is done by using two of the tandem couplers shown above, one in the LO, one in the RF path, as shown in figure 2.21. The phase shifts of 90° generated at the coupler outputs sum up to a total phase difference of 180° at the mixer's output port and therefore, suppress the LO signal leaked through the mixer cells. The DC-bias for the two mixer cells is provided via $\lambda/4$-stubs and both the DC supply and the mixer's IF signal are fed to the mixer cells through the tandem couplers. This results in a reduced chip size, since the matching networks and the low-pass filter for the IF extraction can be designed independent from the mixer stages.
The stand-alone mixer is measured in a downconverter configuration, where the 300 GHz LO is provided via a frequency tripler module followed by an in-house 300 GHz amplifier. With this setup, a maximum LO power of −3 dBm, limited by the amplifier's maximum output power, can be fed into the mixer's LO port. The RF signal is generated using a commercial source module in the WR-3 waveguide band. The IF signal is measured

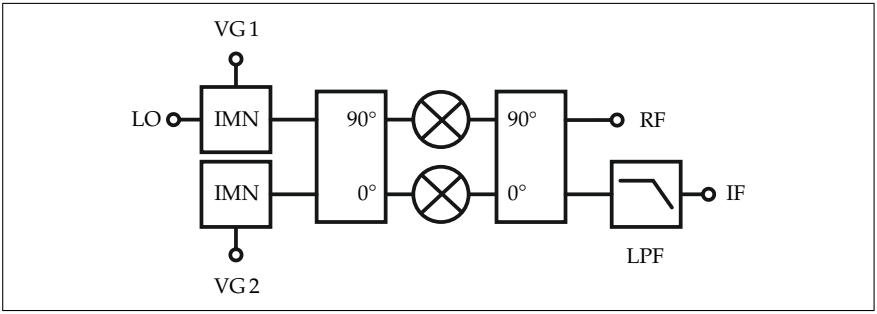

Figure 2.21: Simplified schematic of the single-balanced mixer, formed by combining two resistive mixers with one tandem coupler in the LO and one in the RF path. This configuration results in a suppression of the leaked LO at the RF port. Both the IF signal and the separate DC supply voltages are fed to the mixer core via the couplers.

using a spectrum analyzer.
In figure 2.22 on the left, the measured conversion gain versus the applied LO power compared to the simulation, as dashed line, is shown. For this measurement, an LO frequency of 300 GHz and an IF frequency of 200 MHz are used. As can be seen, with the available power of −3 dBm, the mixer cannot fully be driven into saturation. It shows a conversion gain of −18 dB for the available LO power. The slope of the measured curve indicates that a saturated operation can be achieved for lower LO powers than predicted by the simulation, which predicted saturation for input powers above 3 dBm. To verify this assumption, an LO source with higher output power would be necessary to drive the mixer into saturation, which is not available at the time writing.
The RF bandwidth of the mixer cell is measured by using a fixed frequency offset of 200 MHz between the LO and RF signal and sweeping the LO frequency between 280 and 318 GHz. This results in an IF signal of 200 MHz for each measurement point. The measurement results are shown in figure 2.22 on the right. The mixer cell shows a 3-dB RF bandwidth of 26 GHz from 284 to 310 GHz. Compared to the simulation,

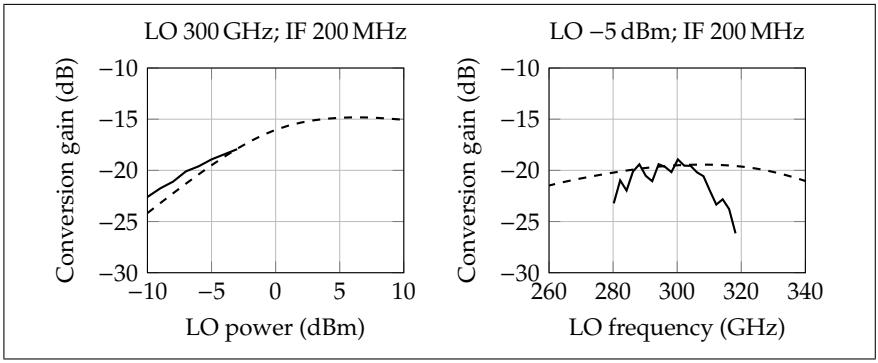

Figure 2.22: Simulation (dashed) and measurement of the single-balanced mixer's conversion gain versus the LO power (left). Comparison between simulation (dashed) and measurement of the mixer's RF bandwidth (right).

which is shown as dashed line, the measured bandwidth does not match the simulation. This can be explained by a reduced bandwidth of the used tandem couplers. To evaluate this effect, the tandem coupler has to be processed as a stand-alone device and measured thoroughly with a four-port measurement setup covering the coupler's entire bandwidth. At the time writing this thesis neither a stand-alone coupler nor a four-port measurement system covering the desired frequency range are available.

For the use of the mixer in a communication system, a parameter more interesting than the RF bandwidth is the IF bandwidth at a fixed LO frequency. Therefore, in an additional measurement, the LO is kept at 300 GHz and the RF input signal is swept to lower frequencies, representing the lower sideband of a received signal. The resulting IF bandwidth is shown in figure 2.23. The mixer cell shows a 3-dB bandwidth of approximately 40 GHz with a ripple of ±1 dB around −19 dB. The simulation, which is again shown as a dashed line, predicts a conversion gain of −16 dB with an IF bandwidth of 50 GHz. The remarkable match between simulation and measurement proves that both the transistor models as

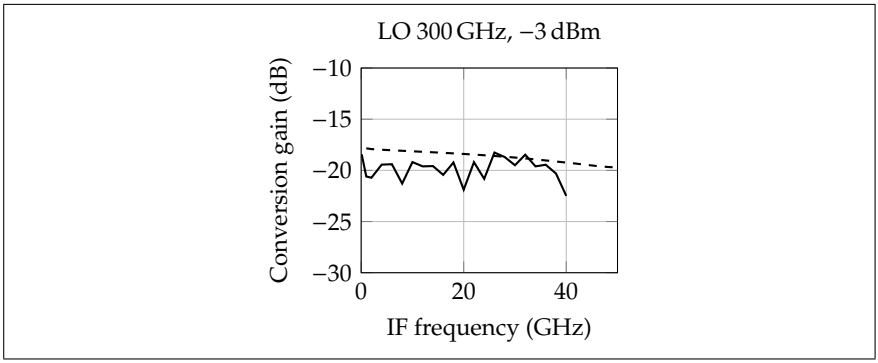

Figure 2.23: Simulation (dashed) and measurement of the mixer's conversion gain versus the IF frequency at a fixed LO frequency.

well as the models for the passive components are suitable even for the use in non-linear circuits in this elevated frequency range. The ripple on both the RF and IF bandwidth measurement is not necessarily caused by the device under test. When measuring at these high frequencies, also the performance of the measurement equipment has to be taken into account. Although using a thoroughly calibrated measurement setup, a variation in the RF source module's output power over time can be observed. This variation can be the reason for the ripple in the measured curve. To exclude this effect, either a more stable source module would be necessary, or a second one has to be used to perform a differential measurement. Due to limited measurement equipment covering this frequency range, such measurements cannot be performed at the time writing this thesis.

2.3.2 Fully-integrated I/Q-transmitter and receiver MMICs

In a further development step, the proposed stages will be integrated with a frequency tripler followed by a buffer amplifier in the mixer's LO path as well as a LNA or PA stage in the RF path to form complete transmit

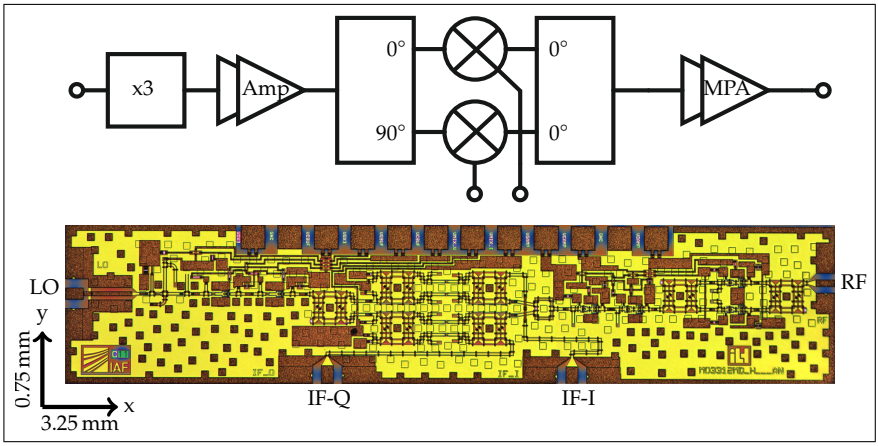

Figure 2.24: Chip photograph of the 300 GHz transmitter MMIC, comprising a frequency tripler with subsequent buffer amplifier, the I/Q mixer stage, realized by two single-balanced mixers as shown in figure 2.21, a Wilkinson and a tandem coupler, and a two-stage medium power amplifier in the RF path.

or receive circuits. These MMICs will build the basis for a terahertz communication system. To realize the I/Q-converters, two of the single-balanced mixer cells as shown above are combined via an additional tandem coupler in the LO path to generate the necessary 90° phase shift for the I- and Q-branch, and the Wilkinson combiner in the RF path.
Due to the use of the frequency tripler in the mixer's LO path, the LO signal for the MMIC can now be provided at a frequency of 100 GHz, where signals can be generated with a higher stability. The effects due to signal routing as well as waveguide to chip transitions are easier to handle at these lower frequencies [LTW+12]. To provide enough LO power for the mixer stage, the frequency tripler is followed by a two-stage buffer amplifier. Both the frequency tripler and the amplifier have already been published as stand-alone devices. The frequency tripler with the subsequent amplifier has been published in [LTW+12]. It provides an

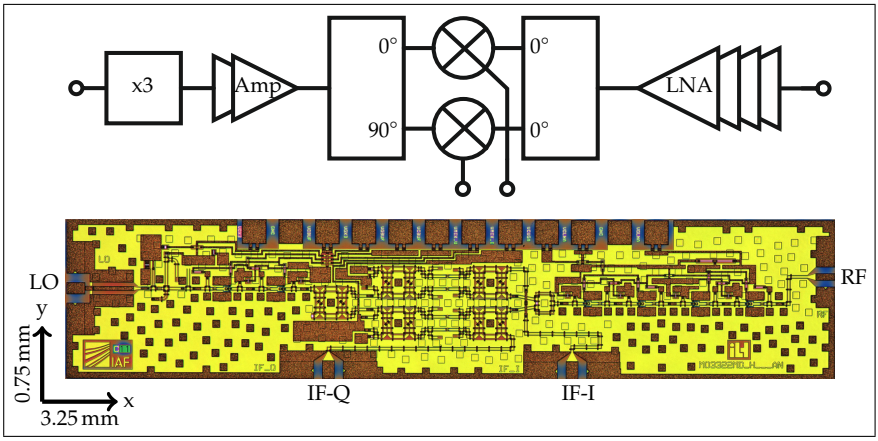

Figure 2.25: Chip photograph of the 300 GHz receiver MMIC, comprising a frequency tripler with subsequent buffer amplifier, the I/Q mixer stage, realized by two single-balanced mixers as shown in figure 2.21, a Wilkinson and a tandem coupler, and a four-stage low noise amplifier in the RF path.

output power around 0 dBm in a frequency range from 265 to 315 GHz. A first realization of the 2-stage cascode amplifier is shown in [TLM+08]. The S-parameter measurement of this device shows a small signal gain of 13.5 dB in a frequency range from 250 to 310 GHz.
The shown Wilkinson combiner, the two mixer cells and the tandem coupler form the core element of the planned transmitter and receiver MMICs. In the chip photographs in figure 2.24 and 2.25, the two single-balanced I/Q-mixer stages, realized as shown in figure 2.21, can be seen in the middle of the chip, easily identifiable by the four tandem couplers. Both the Wilkinson combine MMICs are optimized for a later module integration in a split-block waveguide module with all DC-voltages routed to one side of the chip and a separation of 1 mm between the IF ports to prevent coupling of the 40 GHz signals on the IF-board on which the IF signals are routed from the MMIC to the module's coaxial connectors. For a better

control over the mixer's I/Q-amplitude imbalance, the I- and Q- mixer's gate voltage can be controlled separately. Thereby, a divergent behavior between both mixer cells can be compensated.
Compared to the single-balanced mixer stages shown above, the expected performance of the I/Q-mixer in the complete circuit will show a higher conversion loss. The available LO power for the mixer stages is now reduced by 4 dB due to the additional tandem coupler in the LO path. Furthermore, in the RF path, the signal passes the Wilkinson combiner and suffers from the additional insertion loss of 1 dB. To overcome this shortcomings, and to achieve an improved system performance by increased linearity and high transmit power, in the transmitter chip a two-stage medium power amplifier is used. The measurement of the stand-alone device of this power amplifier shows a saturated output power of 7 dBm combined with a gain of 20 dB [Tes14]. For the receiver, a four-stage LNA is used to achieve a better noise performance and a high conversion gain. The stand-alone LNA provides a measured small signal gain of more than 20 dB over a frequency range from 220 to 320 GHz [TLM+10]. The device is expected to work even at higher frequencies, but could not be measured due to a limitation in the measurement equipment. The LNA's measured noise figure is approximately 6.5 dB at 300 GHz. The two amplifier circuits are provided in form of chip layouts by the Fraunhofer IAF in the frame work of joint research projects.
The characterization of the I/Q-receiver in terms of conversion gain is shown in figure 2.26. The measurement of the conversion dependency of the LO input power at 100 GHz is shown in the left plot. A saturation effect can be observed for input powers above 4 dBm, resulting in a conversion gain of approximately 11 dB. When considering the receiver's IF bandwidth, a significant decrease compared to the single-stage mixer behavior can be observed. The fully integrated MMIC only achieves a bandwidth of 12 GHz in the LSB and USB. The reason for this behavior is most possibly introduced by an impedance mismatch between the two stages, but a thorough investigation will be necessary to verify this. Since at the time writing this thesis, the LNA stage was only available in form of a layout, no proper simulation of the interstage matching between the

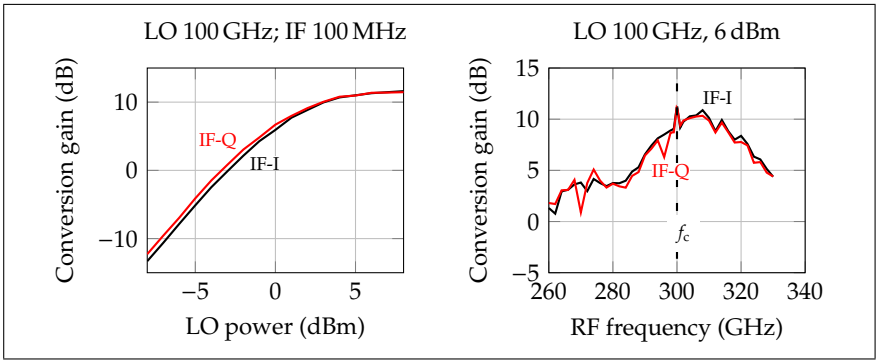

Figure 2.26: Measurement of the 300 GHz I/Q-receiver's conversion gain versus LO power (left). Measurement of the receiver's IF bandwidth in the upper and lower sideband for the I- and Q-channel (right).

two circuits can be performed. The I/Q-amplitude imbalance of the receiver MMIC is below 0.7 dB and can be further improved after a module integration by adjusting the mixer's gate voltages as explained above. A characterization of the Rx's noise figure in an on-wafer setup is not possible at the time writing this thesis. To measure this figure of merit, the MMIC needs to be integrated into a waveguide module, which was not possible in the framework of this thesis, but will be realized in a later state of an ongoing research project.
For the characterization of the transmitter's output spectrum the use of a spectrum analyzer is not recommended. Since only few measurement mixers are available in the 300 GHz region and all of these suffer from an extremely high conversion loss combined with a high ripple over the entire frequency range, measurements using this components will not be reliable for such broadband devices as considered here. To overcome this problem, the transmitter's output signal is measured by using a calorimetric power meter[8], providing very accurate power values but giving no insight into power distribution over the spectral components. The

[8]Calorimetric power meter Erickson PM1

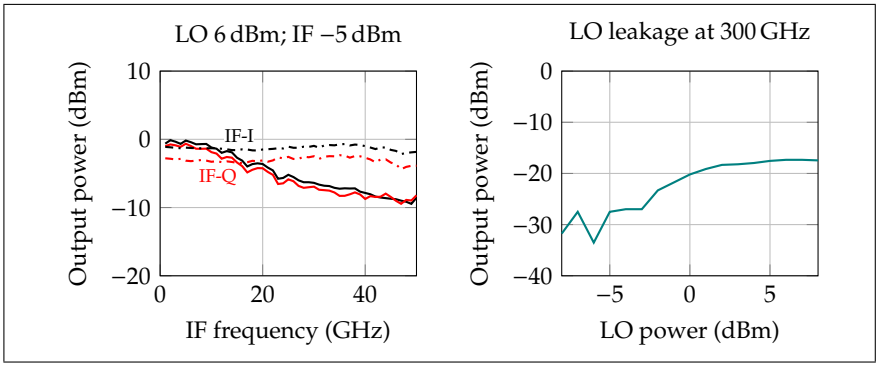

Figure 2.27: Measurement of the 300 GHz I/Q-transmitter's output power (left) for LO signals of 100 GHz (solid) and 90 GHz (dashed). Measurement of the LO leakage at 300 GHz for an input signal of 100 GHz.

drawback for such a measurement is that both sidebands are measured at once and it is not sure whether both sidebands have equal power, or whether one shows significantly more power than the other one. Also the power contribution of the leaked LO signal at 300 GHz is included in the power meter measurement. Nevertheless, this measurement does provide an insight into the chip's conversion behavior.

A measurement of the I/Q-transmitter's output characteristic at an LO input frequency of 100 GHz into the MMIC results in a 3-dB IF bandwidth of approximately 20 GHz for both the I- and Q-path, combined with an I/Q-imbalance below 0.7 dB over the entire bandwidth as shown in figure 2.27 on the left. A measurement of the 300 GHz LO leaking through the balanced mixer cells results in values below −17 dBm for LO input powers up to 6 dBm. Thus, the leaked LO power is at least 9 dB below the desired transmit signal. The results of this measurement are shown in figure 2.27 on the right.

Since the mixer's IF bandwidth is significantly reduced compared to the single stage measurements shown above, the MMIC is also measured with an LO signal of 90 GHz, resulting in a carrier frequency of 270 GHz.

With this, the achieved IF bandwidth exceeds 50 GHz, but with a slightly reduced output power and an increased I/Q-imbalance of approximately 1.5 dB. This indicates that the mixer itself provides the intended bandwidth, but is limited by the frequency response of the used amplifier. The increase in imbalance is introduced due to the LO frequency shift. Since the tandem coupler is designed for a frequency of 300 GHz, the coupling behavior might be reduced causing different LO powers for the I- and Q-mixer cells as well as inside the balanced mixer stages. This effect needs to be verified by measurements on the stand-alone tandem coupler as soon as it is available. A redesign of the amplifier will improve the bandwidth performance and the existing MMIC can be optimized by adjusting the gate voltages for the I- and Q-cell as explained above.

2.3.3 Comparison to state of the art

A comparison of the shown 300 GHz circuits to the state of the art is not easy to provide. There are only a few transmit and receive MMICs published in the 300 GHz frequency range and most of them are not optimized for communication purposes. To provide a complete comparison, the realized designs are not only compared to the exiting MMICs, but since they will be used in a communication system, also already existing communication transmitters and receivers in this frequency range, i.e optical and opto-electrical systems, will be taken into account.
The overview of the state of the art, visualized in table 2.5 by the main characteristics technology (Tech.), configuration of the circuit (Type), center frequency f_c, LO input frequency f_{LO}, conversion gain CG, 3-dB IF bandwidth and output power P_{out}, lists separately electrical and opto/opto-electrical devices. As can be seen, the performance of the developed chipset is exceeding the current state of the art of 300 GHz communication systems in bandwidth, conversion gain and output power. When considering the chipset shown in [4], the achieved performance is comparable but with an increased conversion gain as well as bandwidth in the transmitter and the chipset operates at a higher carrier frequency.

Table 2.5: Comparison of the 300 GHz MMICs with the state of the art.

Reference	CG (dB)	B_{IF} (GHz)	f_c (GHz)	f_{LO} (GHz)	P_{out} (dBm)	Type	Tech.
[OHP12] [1,3]	-14	8	320	17.7	n/a	dconv	HBT
[HHC12] [2,3]	-25	22	300	n/a	n/a	dconv	SD
[KTM+09] [1,3]	-19	0.05	300	150	n/a	dconv	mHEMT
[TML+11] [1]	15	0.1	300	100	n/a	Rx	mHEMT
[4] [2]	3.8	15	240	120	n/a	Rx	mHEMT
[4] [2]	-0.6	35	240	120	-3.6	Tx	mHEMT
[CALL11]	-6.3	15	307	153.6	-9.8	Tx	diode
[SMKN11]	-	1	300	n/a	-20	Tx + Rx	PD + RTD
[SAW+10]	-	19	300	n/a	-3	Tx + Rx	UTC + SD
[NHM+13]	-	10	300	n/a	-15	Tx + Rx	UTC+SD
this work	9	12	300	100	n/a	Rx	mHEMT
this work	5	20 / 50	300 / 270	100 / 90	-3	Tx	mHEMT

[1] MMIC, [2] mmW waveguide module, [3] dconv = downconverter

2.4 Discussion

In this chapter, the development of MMIC-based analog frontends for use in high data rate wireless communication links is described for the E-band as well as for the frequency bands around 240 and 300 GHz.
For the design of broadband up- and downconverters in the high millimeter-wave regime, it is argued that the resistive mixer approach is, despite all its drawbacks, the most suitable circuit topology. Using this, a broadband receiver for the E-band, integrating a single-ended mixer stage with a two-stage low noise amplifier is developed and characterized. The achieved results for the MMICs are comparable to the state of the art and surpass already existing circuits published in literature in terms of IF bandwidth. Concerning the receiver module, the bandwidth performance is reduced, but still comparable to already published circuits in this frequency range

on chip-level. The design of an E-band transmitter shows a good linearity behavior combined with a bandwidth covering the desired frequency band. When comparing this device to the state of the art, it is revealed that only few transmitters without an integrated RF amplification stage are published. Compared to these, the output power and conversion gain of the device realized here is significantly lower. However, in a fair comparison with upconverters without amplification stage, the achieved conversion gain and output power is similar. In terms of bandwidth, the achieved results surpasses the state of the art. The measurement results of the realized LO sources show spurs existent in the stabilized VCO's output signal which are even increased in power after the frequency multiplier stages. Those spurs are not present in the multiplier's output signal when it is driven by a commercial signal source. Thorough system analyses which will be performed in the following chapter have to show whether the transmission quality is influenced by these spurs.
When considering the 240 GHz frontend components, comprising the up- and downconverters, the characterization indicates the feasibility of a high data rate wireless link using this components. Following [DGM99], the maximum achievable data rate in a communication system can be estimated by the relation: maximum data rate $\leq 2 \times$ bandwidth. With the achieved IF bandwidth of approximately 20 GHz, a data rate of approximately 40 Gbit/s should be possible.
The analysis of the 300 GHz chipset shows the feasibility of integrated circuits with ultra-broadband IF ports combined with reasonable conversion behavior. Furthermore, the feasibility of a higher monolithic integration, in this case the integration of a frequency multiplier, a buffer stage, a mixer stage and either a four stage low noise amplifier or a two stage power amplifier, even at these elevated mmw frequencies, is shown. The measurement results confirm that the circuit behavior can be predicted precisely by a thorough simulation. When comparing the achieved results of the realized transmitter and receiver with the state of the art, not only amongst MMICs but also with opto- and opto-electrical devices for communication purposes published in the literature, it can be seen that the achieved combination of IF bandwidth, conversion behavior and out-

put power surpasses all existing devices. Following the considerations combining reliable simulations and thorough power budgeting, the latest generation of transmitter and receiver which is currently under production, will most probably show even better results and thereby build the basis for a future high-speed communication system providing data rates of 100 Gbit/s and more.

3 System Setup and Characterization

While in the previous chapter, the mmw frontend modules were characterized by their static behavior, i.e. by the use of mono-frequent test signals, in this chapter the frontends' performance using time-varying signals in form of PRBS test signals will be investigated. The transmitter and receiver will be connected via waveguide attenuators to make the measurement independent from influences caused by radio channel characteristics. To gain comprehensive results for the communication system, the used test signals range from simple ASK formats to more elaborate modulation schemes with higher spectral efficiencies, such as QAM and phase shift keying (PSK) signals.

This chapter is divided into four parts. In the first part, an introduction to the theoretical evaluation of wireless link performance and measures as well as a relation to the frontend characteristics measured in chapter 2 is given. With these influences of the frontend non-idealities, i.e. I/Q-imbalances and LO phase distortions, on the transmitted data determined, the performance of each frontend system can be estimated. In the two following parts, back-to-back measurements for the E-band and the 240 GHz system are set up and the systems' data transmission capabilities for different modulation formats and data rates are evaluated. Finally, the expected performance for the 300 GHz system based on the theoretical influence of frontend non-idealities is given.

3.1 Characterization and design measures for wireless links

As described in chapter 1.2.6, the baseband test signals for the system characterization measurements are generated either using an AWG in combination with a real-time oscilloscope and an integrated VSA software, or by using a BERT system in combination with a sampling oscilloscope. The signal quality will be determined in terms of bit error rate measurements with the BERT system or in terms of error vector magnitudes extracted from constellation diagrams when using a combination of AWG as data source and real-time oscilloscope as data sink. In the latter setup, the EVM measurement is performed by offline processing in the VSA software. In the following section, the different measures of transmission quality, i.e BER, SNR and EVM, their relation amongst each other, as well as their dependency on system non-idealities will be discussed.

3.1.1 BER, SNR and EVM as measures of transmission quality

The determination of bit errors introduced during the transmission of data by a communication system is the most important measure for the system's performance. Commonly expressed as the number of erroneous bits divided by the total number of transmitted bits, the bit error rate can either be measured using a BERT as explained in chapter 1.2.6.1 as a serial comparison of the received bit stream against a known bit sequence, or estimated by applying known statistics to the measurement of the additive white Gaussian noise disturbed signal's ″zero″ and ″one″ rails in an eye diagram [MW10]. As a BERT system determines the total number of erroneous bits in a transmitted signal, a measurement with such a system delivers an exact value for the introduced errors. While this method can be easily applied for two level transmission formats like on-off keying (OOK) or BPSK, the measurement effort increases enormously for higher order modulation formats. Also, this method is only applicable when the

received signal is demodulated using a hardware demodulator. Another drawback of the direct measurement method is explained in [FSN+12]: To achieve statistical meaningful results, a certain number of erroneous bits have to be detected, which can lead to long measurement times, especially for systems with BER performances better than 1×10^{-9}. On the contrary, the estimation method by evaluating an eye diagram measurement is much faster, but only applicable if the only or predominant disturbance in the communication system is additive white Gaussian noise. By evaluating the quality factor

$$Q = \frac{V_{\text{one}} - V_{\text{zero}}}{\sigma_{\text{one}} + \sigma_{\text{zero}}} \tag{3.1}$$

of the eye diagram, represented by the difference of the voltage levels of the "one" and "zero" rails $V_{\text{zero/one}}$ divided by the sum of the standard deviation of both values $\sigma_{\text{zero/one}}$, and by applying known signal statistics, as described in detail in [FSN+12], the minimum bit error can be estimated as

$$BER_{\text{min}} = \frac{1}{2}\,\text{erfc}(\frac{Q}{\sqrt{2}})\,. \tag{3.2}$$

Thereby, the Q-factor can be interpreted as the signal-to-noise ratio of a time domain voltage signal. One has to distinguish between the measurement with a BERT system, giving an actual measurement of occurred errors which allows to extrapolate for errors occurring in the future, and the estimation of bit errors based on signal-to-noise measurements. Therefore in the following, the estimated bit errors will be referred to as bit error probability P_{b}.

Since for complex modulated data signals, the measurement of eye diagrams is only possible after the demodulation process, it is much more

convenient and easier to directly determine the signal's SNR[1] in the frequency domain by measuring the signal amplitude in relation to the existent noise in the signal spectrum. The essential measure necessary to estimate the bit error rate is the bandwidth-independent ratio between signal energy per bit E_b and the power spectral density of the corresponding noise N_0, also known as *SNR per bit*. For an OOK signal, this value equals the measured SNR, since the bit rate of the signal is directly related to its covered bandwidth. When considering more bandwidth-efficient complex modulated signals, the measured power in the spectrum is not directly related to the energy of the individual bits since several bits can be represented by specific complex signal levels. Therefore, the measured SNR has to be corrected by the relationship between bandwidth B and bit rate R_b to achieve the correct E_b/N_0 value:

$$\frac{E_b}{N_0} = SNR \cdot \frac{B}{R_b} \,. \tag{3.3}$$

When considering the SNR per bit of an OOK or BPSK modulated signal extracted in the frequency domain, and substituting BER_{min} by the bit error probability P_b, equation (3.2) can be rewritten to estimate the resulting bit errors

$$P_b = \frac{1}{2} \operatorname{erfc}\left(\sqrt{\frac{E_b}{N_0}}\right) . \tag{3.4}$$

[1]The terms SNR and carrier-to-noise ratio (CNR) are often used interchangeably in publications concerning communication systems. Both measures express the amount of decibels by which the signal level is exceeding the noise present in the signal's bandwidth, and it is often confusing which term to use. However, in most cases, the CNR is used to express this relationship in the RF domain, i.e. before the demodulator, while the SNR is used to relate the signal power of the demodulated signal in the baseband to the corresponding noise. Since the measurements in this work are performed on a baseband signal captured by a fast real-time scope and converted to the frequency domain by using fast Fourier transform (FFT), the term SNR is used, although the data signal's extremely high bandwidths may be considered as RF signals and the demodulation is only performed in software.

Following [Gu05], the bit error probability for the most common modulation formats can be calculated on the basis of an SNR measurement in the frequency domain in combination with slight modifications of equation (3.3) and (3.4) for each modulation format. However, the shown relation between measured SNR and bit error probability only holds for signals with disturbances following Gaussian distributions, i.e. where additive white Gaussian noise is the predominant system imperfection.

To evaluate communication systems with perturbations different from AWGN, such as I/Q-imbalances, phase noise distortions and carrier leakage, a different method has to be applied. Here, the constellation diagram representation in combination with an error vector magnitude measurement is the most suitable solution, which even can be applied earlier in the demodulation process than a BER measurement, since it is based on the comparison between measured and expected symbols instead of single bits, and which is independent from the modulation format [SRI06]. Furthermore, this method gives an insight into the origin of transmission errors, since specific non-idealities show a specific impact on the constellation diagram and influences the EVM in a specific way [Tec05, Tec10, GT03]. The EVM is a performance measure for communication systems used in many specifications for transmitter and receiver standardization, such as [IEE99]. It is defined as the mean-square-error between the samples of the actual and the ideal symbol vectors in the constellation diagram, normalized by the average power of the ideal symbol [Gu05]. Mathematically the EVM can be expressed as:

$$EVM_{\mathrm{rms}} = \sqrt{\frac{\frac{1}{N}\sum_{n=1}^{N}|S_{\mathrm{r}} - S_{\mathrm{i}}|^2}{\frac{1}{N}\sum_{n=1}^{N}|S_{\mathrm{i}}|^2}} = \sqrt{\frac{\frac{1}{N}\sum_{n=1}^{N}|S_{\mathrm{r}} - S_{\mathrm{i}}|^2}{P_{\mathrm{avg}}}}\,, \tag{3.5}$$

where N represents the total number of symbols, S_{r} the nth normalized received symbol, S_{i} the ideal normalized constellation point of the nth symbol and P_{avg} is the average symbol power.
When considering communication systems predominantly AWGN dis-

turbed, the EVM can be related to the considerations of BER and SNR above by using

$$EVM_{\mathrm{rms}} \approx \frac{1}{\sqrt{SNR}} \tag{3.6}$$

or

$$EVM_{\mathrm{rms}}|_{\mathrm{dB}} \approx -SNR|_{\mathrm{dB}} \tag{3.7}$$

as shown in [SRI06]. However, as exhibited by [MA09], this relation holds only for data-aided receivers, where known data sequences, such as pilot tones or synchronization sequences are used to ensure a reliable synchronization between transmitter and receiver. For non data-aided receivers, i.e receivers without any kind of synchronization sequence or pilot tones as used for the transmission experiments conducted in this work, and low SNR values, the authors show a calculation for the resulting EVM dependent on the modulation scheme. Nevertheless, the authors also show that for SNR values higher than approximately 15 dB and amplitude modulation schemes up to 64-QAM, the resulting EVM for data-aided and non data-aided receivers are comparable. Another drawback of equation (3.6) is that imperfections caused by the RF frontend are not taken into account. Since the wireless links considered in this work may suffer from different non-idealities such as I/Q-amplitude and -phase imbalances, LO leakage and phase noise, a predominance of AWGN is no longer ensured, i.e. a Gaussian distribution of the signal disturbance is not necessarily given. Although the shown estimations of the bit error probability as well as the resulting EVM on the basis of the measured SNR are not inevitably wrong, the received signal has to be evaluated carefully before concluding a bit error probability from the measured EVM value. One possibility is to compare the measured EVM to a measurement of the signal's SNR. When both measurements deliver comparable results, i.e. the wireless link is working in a SNR-limited regime, it can be assumed that the signal

perturbation is dominated by AWGN.
The research on solutions for estimating the error vector magnitude on the basis of known imperfections and SNR values is the topic of many publications. However, most of them only consider one perturbation to be present at a time or assume them to be independent from each other [Geo04, MA09, CD10, NOS13, DK12, Gu05]. Furthermore, none of these publications take the ultra-broadband systems into account which will be considered in this thesis. In such systems, the transmitter's and receiver's conversion gains are no longer constant over the frequency band used for the modulation. Additionally, the I/Q-imbalances vary over this frequency band and the part of the spectrum corrupted by LO phase noise is negligibly small compared to the overall signal bandwidth. Besides, the data signals will be AC-coupled to the frontends due to the used baseband amplifiers and the RF signals might be distorted due to poorly matched frontend ports. The most complete consideration of imperfection influences on the EVM is given in [CD10]. Well aware of the fact that this work is also based on the assumption of data-aided transmitters, the influence of the different frontend imperfections will nevertheless be evaluated on the basis of this publication since all imperfections substantial for the wireless links in this work as well as their interdependencies are dealt with in [CD10]. In the following, the influences of different non-idealities on the transmission performance of a wireless link are introduced on the basis of this publication.

3.1.2 EVM estimation considering RF frontend imperfections

The underlying system model for estimating the EVM penalty introduced by non-idealities in the modulator and demodulator stages, i.e. the Tx and Rx in the cases considered here, comprises a quadrature modulator followed by an RF amplifier on the transmitter side, and an LNA and a quadrature demodulator on the receiver side. The transmission channel is modeled as an AWGN channel and the demodulator's outputs are lowpass filtered. Thereby, this model fully describes the system concept

selected for the intended wireless links in this work as shown in figure 1.12. The transmitter imperfections are modeled with different DC-offsets $d_{\mathrm{i/q,Tx}}$ for the I- and Q-channels as well as the factors k_{Tx} and ϕ_{Tx} for the I/Q-amplitude and -phase imbalances. Considering the I- and Q- input signals of the quadrature modulator expressed as $s(t) = [s_{\mathrm{i}}(t),\ s_{\mathrm{q}}(t)]^T$ and the modulator's imperfections represented by both the DC-offset vector $d_{\mathrm{Tx}} = [d_{\mathrm{i,Tx}},\ d_{\mathrm{q,Tx}}]^T$ and the imbalance matrix $T(t) = 2\,[k_{\mathrm{Tx}}\cos(\omega t),\ \sin(\omega t + \phi_{\mathrm{Tx}})]$, where ω represents the carrier angular frequency and the factor 2 is inserted to keep the gain of the entire link at a value of one, the modulator's time-varying output signal can be expressed as

$$u(t) = T(t)\,[s(t) + d_{\mathrm{Tx}}]\ . \tag{3.8}$$

The receiver model also comprises a DC-offset vector $d_{\mathrm{Rx}} = [d_{\mathrm{i,Rx}},\ d_{\mathrm{q,Rx}}]^T$, a factor α_{d}, representing a constant phase offset between the transmitter and the receiver LO due to non-ideal synchronization, as well as the I/Q-amplitude and -phase imperfection of the demodulator described by k_{Rx} and ϕ_{Rx} , expressed through the imbalance matrix $R(t) = [k_{\mathrm{Rx}}\cos(\omega t + \alpha_{\mathrm{d}}),\ \sin(\omega t + \phi_{\mathrm{Tx}} + \alpha_{\mathrm{d}})]^T$. With the term $n(t)$ denoting an AWGN channel, the demodulator output after a lowpass filtering can be expressed as

$$y(t) = \mathrm{LPF}\,\langle R(t)\,T(t)\,s(t) + R(t)\,T(t)\,d_{\mathrm{Tx}} + d_{\mathrm{Rx}} + R(t)\,n(t)\rangle\ , \tag{3.9}$$

where $\mathrm{LPF}\,\langle\rangle$ represents the lowpass filter function. In (3.9), the term $R(t)\,T(t)\,s(t)$ describes the influence due to the I/Q-imperfections, $R(t)\,T(t)\,d_{\mathrm{Tx}} + d_{\mathrm{Rx}}$ describe the influence introduced by the transmitter and receiver DC-offsets and the term $R(t)\,n(t)$ represents the influence of the AWGN channel. With the assumption that the signal bandwidth is smaller than the bandwidth of the lowpass filter, and that the RF carrier frequency is sufficiently high to be suppressed by this filter, equation (3.9) can be

rewritten to

$$r(t) = H\,s(t) + \psi + n_{\mathrm{r}}(t)\ . \tag{3.10}$$

Here, terms related to I/Q-imperfection are represented by the time-independent error matrix

$$H = \mathrm{LPF}\,\langle R(t)\,T(t)\rangle \tag{3.11}$$

$$= \begin{bmatrix} k_{\mathrm{Tx}}\,k_{\mathrm{Rx}}\cos(\alpha_{\mathrm{d}}) & k_{\mathrm{Rx}}\sin(\phi_{\mathrm{Tx}}-\alpha_{\mathrm{d}}) \\ k_{\mathrm{Tx}}\sin(\phi_{\mathrm{Rx}}+\alpha_{\mathrm{d}}) & \cos(\phi_{\mathrm{Rx}}-\phi_{\mathrm{Tx}}+\alpha_{\mathrm{d}}) \end{bmatrix}, \tag{3.12}$$

the signal-independent, constant offset is expressed by the term $\psi = H\,d_{\mathrm{Tx}} + d_{\mathrm{Rx}}$ and the received channel noise is given as $n_{\mathrm{r}}(t) = \mathrm{LPF}\,\langle R(t)\,n(t)\rangle$. By assuming an ideal synchronization of the sampling time, the output signal can be expressed via the received symbols n

$$r(n) = H\,s(n) + \psi + n_{\mathrm{r}}(n)\ . \tag{3.13}$$

By calculating the error vector $e(n) = r(n) - s(n)$ for each symbol, the EVM normalized to the received power can be calculated via the expectation of ensemble averages following [CD10] to

$$EVM_{\mathrm{norm}} = \sqrt{\underbrace{\frac{1}{2}\,\mathrm{Tr}(H^T H) - \mathrm{Tr}(H) + 1}_{\text{I/Q-imperfections}} + \underbrace{\frac{k_{\mathrm{Rx}}^2 + 1}{4\,E_{\mathrm{S}}/N_0}}_{\text{AWGN}} + \underbrace{\frac{\psi^T\,\psi}{P_{\mathrm{r}}}}_{\text{offsets}}}\ . \tag{3.14}$$

Here, first term describes the contribution of the I/Q-imperfections to the EVM, the second term represents the contribution of the AWGN channel's noise and the last term expresses the contribution of the constant I/Q-offsets in the Tx and Rx dependent on the received signal power P_{r}. The

term $\psi^T \psi$ is calculated by

$$\psi^T \psi = d_{\mathrm{Tx}}^T H^T H d_{\mathrm{Tx}} + d_{\mathrm{Tx}}^T H^T d_{\mathrm{Rx}} + d_{\mathrm{Rx}}^T H d_{\mathrm{Tx}} + d_{\mathrm{Rx}}^T d_{\mathrm{Rx}} \,. \tag{3.15}$$

3.1.3 EVM estimation considering RF frontend imperfections in combination with phase noise

Further following [CD10], also the contribution of phase noise of the Tx's and Rx's LO signals on the EVM can be estimated. This phase noise introduces two additional effects to the signal perturbation: On the one hand, the phase imbalances in the modulator and demodulator change from static impacts to random ones. On the other hand, a random phase difference between the two LO signals arises. In a first approach, the phase noise will be approximated as a zero-mean Gaussian noise $\mathcal{N}$ with a variance defined as the LO's root-mean-square (rms) phase noise power density Φ_{rms}. This value can either be calculated from phase noise measurement data or, as shown in [RDPC06], with a spectrum analyzer, measuring the single-sideband phase noise power $\mathrm{PN}_{\mathrm{SSB}}(\Delta\omega)$ in a 1 Hz bandwidth at the distinct offset frequency $\Delta\omega$ from the carrier, and by applying

$$\Phi_{\mathrm{rms}}(\Delta\omega) = \sqrt{2 \cdot 10^{\mathrm{PN}_{\mathrm{SSB}}(\Delta\omega)/10}}\ [\mathrm{rad}/\sqrt{\mathrm{Hz}}] \,. \tag{3.16}$$

To calculate the combined EVM penalty introduced by Tx and Rx imperfections and phase noise, the phase offset factor α has to be extended to $\alpha = \alpha_{\mathrm{d}} + \alpha_{\mathrm{r}}$, where α_{d} is the constant phase difference between Tx and Rx LO introduced above and α_{r} represents a Gaussian distributed phase noise with $\alpha_{\mathrm{r}} \sim \mathcal{N}(0, \Phi_{\mathrm{rms}}^2)$. Substituting this relation into the error matrix

equation (3.12) results in

$$H = \begin{bmatrix} k_{\mathrm{Tx}}\, k_{\mathrm{Rx}} \cos(\alpha_{\mathrm{d}} + \alpha_{\mathrm{r}}) & k_{\mathrm{Rx}} \sin(\phi_{\mathrm{Tx}} - \alpha_{\mathrm{d}} - \alpha_{\mathrm{r}}) \\ k_{\mathrm{Tx}} \sin(\phi_{\mathrm{Rx}} + \alpha_{\mathrm{d}} + \alpha_{\mathrm{r}}) & \cos(\phi_{\mathrm{Rx}} - \phi_{\mathrm{Tx}} + \alpha_{\mathrm{d}} + \alpha_{\mathrm{r}}) \end{bmatrix}, \tag{3.17}$$

which can be simplified for $\Phi_{\mathrm{rms}} \ll 1$ according to [CD10] to

$$\begin{aligned} H &= H_{\mathrm{d}} + \alpha_{\mathrm{r}}\, H_{\mathrm{r}} \\ &= \begin{bmatrix} k_{\mathrm{Tx}}\, k_{\mathrm{Rx}} \cos(\alpha_{\mathrm{d}}) & k_{\mathrm{Rx}} \sin(\phi_{\mathrm{Tx}} - \alpha_{\mathrm{d}}) \\ k_{\mathrm{Tx}} \sin(\phi_{\mathrm{Rx}} + \alpha_{\mathrm{d}}) & \cos(\phi_{\mathrm{Rx}} - \phi_{\mathrm{Tx}} + \alpha_{\mathrm{d}}) \end{bmatrix} \\ &\quad + \alpha_{\mathrm{r}} \begin{bmatrix} -k_{\mathrm{Tx}}\, k_{\mathrm{Rx}} sin(\alpha_{\mathrm{d}}) & -k_{\mathrm{Rx}} \cos(\phi_{\mathrm{Tx}} - \alpha_{\mathrm{d}}) \\ k_{\mathrm{Tx}} \cos(\phi_{\mathrm{Rx}} + \alpha_{\mathrm{d}}) & -\sin(\phi_{\mathrm{Rx}} - \phi_{\mathrm{Tx}} + \alpha_{\mathrm{d}}) \end{bmatrix}. \end{aligned} \tag{3.18}$$

Furthermore, equation (3.13) has to be extended by a term $\alpha_{\mathrm{r}}\, H_{\mathrm{r}}\, (s(n) + d_{\mathrm{Tx}})$ representing the influence of the LO phase noise on the received signal:

$$r(n) = H_{\mathrm{d}}\, s(n) + \alpha_{\mathrm{r}}\, H_{\mathrm{r}}\, (s(n) + d_{\mathrm{Tx}}) + \psi + n_{\mathrm{r}}(n)\,, \tag{3.19}$$

where term ψ still represents the constant offset factor, now calculated from $\psi = H_{\mathrm{d}}\, d_{\mathrm{Tx}} + d_{\mathrm{Rx}}$. This offset increases dependent on the phase noise value since the phase relation of the Tx's and Rx's LO signal now varys randomly causing effects similar to the LO self-mixing process explained in chapter 1.2.4.
Following the same assumptions as above, the normalized EVM taking LO phase noise influences into account can now be calculated via the expectation of ensemble averages of the different error vectors $e(n)$ and

equation (3.14) according to [CD10] expands to

$$EVM_{\mathrm{norm}} = \sqrt{\underbrace{\frac{1}{2}\,\mathrm{Tr}(H_{\mathrm{d}}^{T}\,H_{\mathrm{d}}) - \mathrm{Tr}(H_{\mathrm{d}}) + 1}_{\text{static I/Q imperfections}} + \underbrace{\frac{k_{\mathrm{Rx}}^{2}+1}{4\,E_{\mathrm{S}}/N_{0}}}_{\text{AWGN}} + \underbrace{\frac{\Phi_{\mathrm{rms}}^{2}}{2}\,\mathrm{Tr}(H_{\mathrm{r}}^{T}\,H_{\mathrm{r}})}_{\text{PN influence}} + \underbrace{\frac{\Phi_{\mathrm{rms}}^{2}\,d_{\mathrm{Tx}}^{T}\,H_{\mathrm{r}}^{T}\,H_{\mathrm{r}}\,d_{\mathrm{Tx}} + \psi^{T}\,\psi}{P_{\mathrm{r}}}}_{\text{offsets}}}\,. \tag{3.20}$$

In this equation, the first and the second term again represent the static influences of the modulator and demodulator I/Q-imperfections and the AWGN channel's influences as in equation (3.14), respectively. The two mechanisms causing an increased EVM due to LO phase noise, distortion of the received data stream and increased DC-offset are accounted for in the third and fourth term, respectively.

With equation (3.20) a powerful relation between the different non-idealities present in a wireless RF frontend is given, which, although originally only valid for data-aided reception, can be used to estimate the resulting EVM for given imperfections in systems operating in a high SNR regime.

3.1.4 Specific considerations concerning the wireless link and measurement equipment used in this work

In good approximation, the high gain line of sight (LOS) wireless links discussed in this thesis can be considered to provide AWGN-channels without any kind of multi-path fading. The noise at the receiver is independent of the signal power and the SNR can be calculated as shown in

[SWP+12] using

$$SNR = \frac{P_r}{FkTB}\,, \tag{3.21}$$

where P_r describes the received signal power and F represents the noise factor of the receiver, B represents the signal bandwidth, T the temperature and k is the Boltzman constant. Thus, to estimate the SNR for a given receiver system, only the received power of the transmission has to be known and the corresponding noise power can be calculated for RF bandwidth covered by the transmitted signal.
As discussed before, filtering is not used for the data transmission considered here, i.e. the used data signals are rectangular signals in the time domain implying a theoretically infinite signal in the frequency domain. However, in reality the signal's bandwidth is limited by the analog bandwidth of the used measurement equipment as well as the bandwidth limitations of the different wireless links. Therefore, for the experiments and investigations in this thesis, the bandwidth covered by the data transmission will be determined by the first-zero crossing of the signal's spectrum, resulting in a bandwidth of twice the symbol rate. To determine for example the SNR of a data signal with a symbol rate of 5 GBd, it will be treated as covering an RF bandwidth of 10 GHz.

For the evaluation of the received complex modulated data signals in the following measurements, the real-time oscilloscope in combination with the VSA software, introduced in chapter 1.2.6, is used to demodulate the signal and calculate the error vector magnitude. Furthermore, the VSA software normalizes the measured EVM to the peak symbol power $|S_p|^2$ instead of the average symbol power $|S_i|^2$ as used for the assumptions above. To achieve comparable EVM values between measurement and estimation as well as between different modulation formats, a normalization to the average symbol power is needed. The EVM values calculated

by the software can be converted to the values normalized to the average symbol power by using

$$EVM_{\mathrm{rms},P_{\mathrm{avg}}} = EVM_{\mathrm{rms},P_{\mathrm{peak}}} \cdot \sqrt{PAR}\,, \tag{3.22}$$

with the ratio between peak and average power PAR

$$PAR = \frac{|S_{\mathrm{p}}|^2}{\frac{1}{N}\sum_{n=1}^{N}|S_{\mathrm{i}}|^2}\,. \tag{3.23}$$

For modulation formats using only a single amplitude level, i.e. PSK modulated signals, PAR is equal to one. For amplitude modulation, PAR has to be determined dependent on the respective constellation. The PAR values for the most common modulation formats are shown in [SNW+12]. For the 16/32/64-QAM modulations used in this work, the corresponding PAR values are 1.8, 1.7 and 2.33, respectively.

The notation of the measured EVM values varies amongst different fields of research. While in the optical domain the EVM is mostly given in terms of percent, in the field of mobile communication it is commonly given as a power value measured in dB. Both values are related via

$$EVM_{\mathrm{rms}}|_{\mathrm{dB}} = 20 \cdot \log\left(\frac{EVM_{\mathrm{rms}}|_{\%}}{100}\right). \tag{3.24}$$

Since the notation in terms of dB provides the advantage of directly relating the EVM results to the SNR given in dB as can be derived from (3.6), in the following chapters, the $EVM_{\mathrm{rms}}|_{\%}$ expressed as a percentage relative to the maximum constellation magnitude as measured by the VSA software, will be transformed to $EVM_{\mathrm{rms}}|_{\mathrm{dB}}$.

For all measurements evaluating the wireless link's performance for com-

plex modulated data signals, the synchronization in terms of carrier recovery to generate a synchronous link, as demanded for such a transmission in chapter 1.2, is done by the VSA software as explained in chapter 1.2.6.2. Since this synchronization is continuously updated for each demodulation process of a certain number of symbols, the constant phase offset α_d between the Tx and Rx LO as introduced above will be approximately 0. The drift between both LOs is already incorporated in the phase noise term α_r. Knowing this, the error matrices in (3.11) and (3.18) simplify to

$$H \approx \begin{bmatrix} k_\mathrm{Tx}\, k_\mathrm{Rx} & k_\mathrm{Rx} \sin(\phi_\mathrm{Tx}) \\ k_\mathrm{Tx} \sin(\phi_\mathrm{Rx}) & \cos(\phi_\mathrm{Rx} - \phi_\mathrm{Tx}) \end{bmatrix} \tag{3.25}$$

and

$$\begin{aligned} H \approx & \begin{bmatrix} k_\mathrm{Tx}\, k_\mathrm{Rx} & k_\mathrm{Rx} \sin(\phi_\mathrm{Tx}) \\ k_\mathrm{Tx} \sin(\phi_\mathrm{Rx}) & \cos(\phi_\mathrm{Rx} - \phi_\mathrm{Tx}) \end{bmatrix} \\ & + \alpha_\mathrm{r} \begin{bmatrix} 0 & -k_\mathrm{Rx} \cos(\phi_\mathrm{Tx}) \\ k_\mathrm{Tx} \cos(\phi_\mathrm{Rx}) & -\sin(\phi_\mathrm{Rx} - \phi_\mathrm{Tx}) \end{bmatrix}. \end{aligned} \tag{3.26}$$

For the estimation of the phase noise influence on the wireless link's performance, the Φ_{rms} for the used LO sources has to be determined. As thoroughly investigated in [KKP+14] and [MKM+14], for communication systems with high symbol rates, the phase noise noise floor at high offset frequencies from the carrier shows a much more significant impact on the system's performance than the effects introduced by the near carrier phase noise. This is obvious when assuming, that the amount of spectrum which is disturbed by the near carrier phase noise, commonly ranging up to a few MHz, is negligibly small compared to the overall modulation bandwidth in the range of several GHz. On the contrary, the phase perturbation due to the noise floor introduced by the phase noise accumulates over the system's bandwidth since it extents over the entire modulation bandwidth.

Reliable and precise phase noise measurements are difficult to perform at the elevated frequency ranges used for the carrier signals in this thesis and require special measurement equipment. Since such equipment was not available, the disturbances caused by the LO signal's phase noise is estimated following the above considerations by integrating the noise floor of the used LO source over the bandwidth B covered by the data signal and by adding the phase noise increase due to the frequency multiplication as expressed by equation 2.2 in chapter 2.1.3. The phase noise behavior near the carrier, i.e. at offset frequencies below 100 MHz is neglected and only the noise floor in this region is taken into account.
The integration over the constant noise floor can be simplified by multiplying the noise floor N_{floor} with the bandwidth B of integration, which is equivalent to adding a factor of $10\log(B)$ to the noise value given in dBc/Hz. This approach is used in equation (3.27), to determine the phase noise power density Φ_{rms}. In this equation, the phase noise increase due to the frequency multiplication by a factor of n is already taken into account by the term $20\log(n)$.

$$\Phi_{rms} = \sqrt{2 \cdot 10^{\frac{N_{\text{floor}}+10\log(B)+20\log(n)}{10}}} \tag{3.27}$$

Due to the extremely high modulation bandwidths and necessary multiplication factors to achieve the carrier frequencies in the mmw range, the influence of the carrier phase noise is expected to be significant. Thus, it would be desirable to generate the carrier signal in a different way. One solution would be to use a signal generated by optical heterodyning, i.e. combining two optical signals onto a UTC-PD such that the differential mixing product is in the desired frequency range. As shown in [29, S. 13] and [HKT+12], the optical approach used there demands a complex optical setup and the phase noise of the resulting signal carrier is comparable to the results achieved by electrical generation, i.e. by using a signal source operating in the lower GHz regime followed by appropriate frequency multiplication. On the other hand, the optical approach discussed in [PWB+13], which is much more complex than the systems discussed be-

fore, provides an advantage compared to electrically generated carrier signals. A generation of a 110 GHz signal results in a phase noise of approximately −105 dBc/Hz at an offset of 100 kHz from the carrier, unfortunately no information about the noise floor is given. In comparison, the VCOs with the attached multipliers developed for the E-band link considered in this work provide a phase noise of approximately −90 dBc/Hz at the same offset. In summary, to achieve a better phase noise through optical generation, an incomparably more complex setup than for the electrical generation is needed. More information and further research on the topic of optical generated carrier frequencies will be necessary to determine whether this approach can be a viable and practical solution for future mmw wireless systems but is out of the scope of this thesis.

3.2 E-band frontend characterization

To gain comprehensive insights into the E-band frontend module's performance and behavior, the system is set up in a back-to-back measurement and evaluated in terms of non-ideality influences and feasibility of different modulation formats. Also, the maximum achievable data rates are determined.

3.2.1 Link setup

To evaluate the performance of the overall E-band system, the frontend components from chapter 2.1, packaged in waveguide modules, are set up with transmitter and receiver modules connected back-to-back and with the LO sources and frequency multipliers which will later be used in the wireless link. A schematic of the measurement setup is shown in figure 3.1. Between the transmitter and receiver module, a WR-10[2] waveguide attenuator (Att) ensures linear Rx behavior and prevents damage in the mixer's LNA stage. The LO signals for both the transmitter and

[2]The WR-10 waveguide standard confer the frequency range from 75 to 110 GHz. This standard is also called W-band.

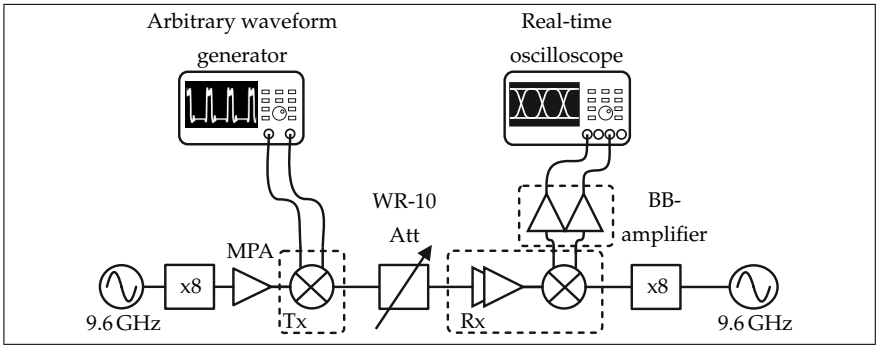

Figure 3.1: Measurement setup for the back-to-back measurement of the E-band frontend, with a WR-10 waveguide attenuator between the Tx and Rx module to prevent saturation or damage of the receiver's LNA.

receiver, are generated using the frequency multiplier-by-eight modules shown in chapter 2.1.3. These multipliers are driven by two independent frequency synthesizers operating at 9.6 GHz. At the transmitter side, an additional medium power amplifier (MPA) is used to generate the necessary LO power of 15 dBm for the balanced upconverter. For the receiver module, an optimum signal quality is achieved by using an LO power of 8 dBm. The AWG and oscilloscope introduced in chapter 1.2.6 are used as data source and sink, respectively. At the Rx's I- and Q-outputs, a phase-matched broadband baseband amplifier provides a gain of approximately 22 dB in combination with a noise figure of approximately 5 dB. Furthermore, in the entire setup phase-matched cables are used to minimize the influence of the measurement setup on the system's phase performance.

3.2.2 Expected link performance

Using the theoretical relations between the frontend non-idealities and the resulting EVM found in section 3.1.1, the performance of the E-band link can be estimated. To verify the applicability of this relation for the E-band link, a comparison of the resulting EVM for measured QPSK mod-

ulated signals, transmitted in a setup as shown above, is done. To see the genuine distortions due to the frontend components, equalization cannot be used in this measurement. When considering the E-band frontend's conversion characteristic shown in chapter 2.1, it can be seen, that the receiver's conversion gain shows a dip at an IF frequency of 6 GHz. Such a behavior can easily be compensated by the use of equalization, but for the measurements here, this behavior introduces signal distortions which cannot be described with equation (3.20) since a frequency dependency of the imperfections is not regarded. Hence, for the following verification, symbol rates of 2 and 5 GBd, are used. Both signals do not extend beyond the mentioned frequency dip. Additionally both signals are within the AWG's analog bandwidth of 5 GHz. The values of I/Q-imbalance at the transmitter k_{Tx} and receiver k_{Rx} are extracted from the Tx and Rx measurements shown in chapter 2.1 by averaging the measured imbalance over the used signal bandwidth. The phase imperfection $\phi_{\mathrm{Tx,Rx}}$ is extracted from the coupler measurement shown in figure 2.4 and assumed to be identical for the transmitter and receiver, since in both MMICs the identical coupler is used. The rms phase error Φ_{rms} is calculated by integrating the noise floor of approximately −148 dBc of the used commercial signal source,[3] increased by the factor due to the frequency multiplication as represented by equation (2.2), over the signal bandwidth using equation (3.27). The received power $P_{\mathrm{r,BB}}$ is measured from the signal spectrum in the VSA software and the SNR is calculated according to the used signal bandwidth and by taking the Rx module's and baseband amplifier's noise figures of 2.85 and 5 dB into account. Due to the high gain of the receiver chain, the noise influence of the oscilloscope is negligible and the receiver's total noise figure can be calculated by using equation (2.1) to be approximately 3.5 dB. Using equation (3.21) with a temperature of 300 K results in SNR

[3]For the measurements, an Agilent PSG series generator as well as a Wiltron signal generator are used to generate the 9.6 GHz signal for the frequency multipliers. While according to the data sheets both generators provide similar phase noise performance, only for the Agilent instrument an noise floor is given [Tec12a]. For all further measurements, the same phase noise and noise floor behavior is assumed for both the Agilent and the Wiltron generator.

Table 3.1: Parameter used to estimate the E-band system's EVM performance.

Symbol rate (GBd)	k_{Tx} (dB)	k_{Rx} (dB)	$\phi_{\mathrm{Tx,Rx}}$ (°)	Φ_{rms} (rad)	P_{r} (dBm)
2	1	0.1	3	0.0201	-1.5
5	1	0.4	3	0.0318	-2.3

values of 42.1 and 37.3 dB for the 2 and 5 GBd signals, respectively. All parameters used for the EVM estimation are summarized in table 3.1.
The estimated EVM values for the 2 and 5 GBd signals are −18.9 and −17.0 dB, respectively. The measurements with the VSA software reveal EVM values of −16.4 and −15.5 dB. The large divergence between the estimated and measured linear EVM values results in a relative error of 33 % and 19.8 % for the 2 and 5 GBd signal, respectively. The deviation can be explained by the contribution of the AWG's imperfections to the overall signal distortion. To determine the signal degradation due to the wireless frontend alone, as described by the EVM estimation in equation (3.20), the influence of the non-ideal AWG output signal needs to be separated. A measurement of the AWG's output, directly connected to the real-time oscilloscope, reveals an EVM of −20.4 dB for the 2 GBd and −21.2 dB for the 5 GBd signal. As shown in [Gu05], to sum up different contributions to a total EVM, the following equation can be used:

$$EVM_{\mathrm{tot,lin}} = \sqrt{\sum_{\mathrm{k}} EVM_{\mathrm{k,lin}}^2} \,. \tag{3.28}$$

Applying this relation to the measured EVM values of −16.4 and −15.5 dB, the EVM degradations due to the wireless frontend alone are determined to −18.6 and −16.9 dB for the 2 and 5 GBd signal, respectively.
Now, a calculation of the relative error between the linear estimated EVM values and the corrected measurement values shows a deviation of 3.6 % for the 2 GBd signal and of only 2.1 % for the 5 GBd signal. When consid-

ering all uncertainties in the measured link parameter due to difficult and limited measurement capability at the used frequency range, this relative error is acceptable. The reason for the higher relative error at a lower symbol rate can be explained by the influence of the near-carrier phase noise, which is neglected for the estimation, but relative to the signal bandwidth shows a more severe impact for lower symbol rate.

With the validation of equation 3.20 to correctly estimate the E-band link's performance, the influence of the different non-idealities can be evaluated and the starting point for system improvements can be defined. With respect to the thesis's goals of achieving as high as possible data rates, this evaluation will be done at 5 GBd.
In figure 3.2, the I/Q-amplitude imbalances at the Tx and Rx, $k_{\mathrm{Tx,Rx}}$, are varied between 0 and 2 dB, while the corresponding other value is kept constant at the value given in table 3.1. The achieved value of the corresponding parameter from the MMIC measurement is marked with a dashed line. The resulting EVM for a 5 GBd signal is calculated for different sets of phase imperfections $\phi_{\mathrm{Tx,Rx}}$, varied between 0 and 5°, where the used values are equal for the Tx and Rx. This procedure is chosen, since the used 90° coupler is identical in both the transmitter and receiver circuit. As can be seen in the left plot of figure 3.2, while an improvement of the Tx's phase imperfection would only lead to a marginal reduction of the error vector magnitude, a decrease in amplitude imbalance would allow for significantly better results. A similar imbalance as for the Rx MMIC of 0.4 dB would decrease the EVM to a value of approximately −20.4 dB. For amplitude imbalances below 0.4 dB, also the influence of the phase imperfection is getting more distinct. The right plot reveals that the link's performance is mainly dominated by the Tx non-idealities, even an improvement of the phase imperfection to unrealistic 0° results in an EVM reduction of only 0.5 dB. For a reduction of the Rx's I/Q-amplitude imbalance, the minimum achievable EVM is approximately −20 dB. The impact of the LO phase noise on a 5 GBd signal in dependency of the I/Q-amplitude imbalance, varied between 0 and 2 dB in 0.2 dB steps, is evaluated in the estimations shown in figure 3.3. In this consideration,

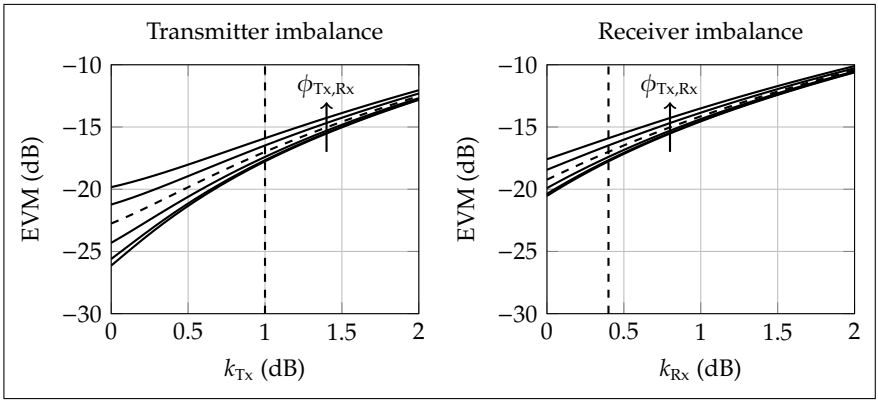

Figure 3.2: Estimated EVM dependency of a 5 GBd signal on Tx (left) and Rx (right) I/Q-amplitude imbalances $k_{\mathrm{Tx,Rx}}$ for different phase imperfections $\phi_{\mathrm{Tx,Rx}}$, varied between 0° and 5° in 1° steps. All other parameters are set to the values given in table 3.1. The present frontend performance is shown in dashed lines.

the LO source's rms phase error is varied between an ideal LO source with an phase error of 0 rad (only theoretically possible) and an LO source with a noise floor at −132 dBc, corresponding to an rms phase error of 0.2 rad. The influences of the phase imperfections are neglected and the corresponding parameter's $\phi_{\mathrm{Tx,Rx}}$ set to 0°, while again all other parameters are kept at the values given in table 3.1 and the curves for the MMIC parameter are shown as dashed lines. As the variations of the Tx's and Rx's I/Q-amplitude imbalance reveal, the EVM is mainly dominated by the transmitter's I/Q-imbalance and even the use of an ideal LO source would result in an EVM of only −18.1 dB. Only when using LO sources with a phase error Φ_{rms} higher than 0.1 rad, corresponding to a noise floor of −138 dBc and higher, the influence of the rms phase error starts to dominate the transmission quality.

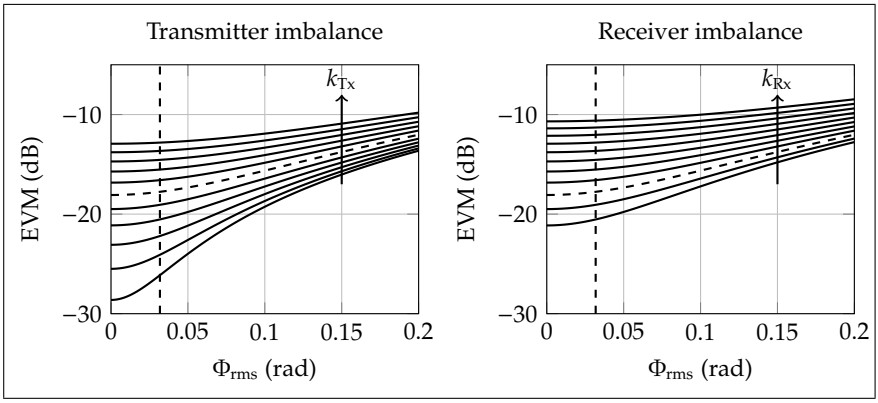

Figure 3.3: Estimated EVM dependency of a 5 GBd signal on the LO's rms phase error in terms of Φ_{rms} for Tx (left) and Rx (right) I/Q-amplitude imbalances $k_{Tx,Rx}$ varied between 0 and 2 dB in 0.2 dB steps. The present frontend performance is shown in dashed lines.

3.2.3 Receiver sensitivity measurement

To be able to set up a reliable link budget calculation as well as to ensure the optimum receiver performance when using the frontend modules in a wireless link, the sensitivity of the receiver module has to be characterized. Ideally, an upconverter different from the one used in the later system, should be used to generate the transmit signal for this characterization. Since there is no commercial device available capable of providing the high IF bandwidths needed to fully characterize the E-band receiver, in the following measurement, the E-band transmitter described in chapter 2.1.2 is used, resulting in a measurement setup as shown in figure 3.1. The drawback of this approach is that the resulting quality measure shows the combined effects of transmitter and receiver influences, so that a statement concerning the behavior of the stand-alone receiver in a different setup is not possible. The characterization is performed with symbol rates of 6 and 12 GBd. The required bandwidth for a data signal with a symbol rate of 6 GBd, is close to the AWG's analog bandwidth limit, of 5 GHz as given in

chapter 1.2.6.2. Hence, for the symbol rate of 12 GBd, the maximum rate which can be generated with the AWG, the available analog bandwidth is not sufficient to achieve an undistorted output signal. Nevertheless, by keeping this drawback in mind, the measurements with the 12 GBd signal, although suffering from the AWG's analog bandwidth limitation, will give an insight into the wireless system's behaviour.
For the measurement, the WR-10 attenuator is used to accurately adjust the input power into the receiver's RF port. For the measurement, the transmitter's LO power is set to 15 dBm to achieve maximum linearity, while the IF power is set to approximately 4 dBm. This results in the optimum conversion behavior for the transmitter, corresponding to a maximum output power of −3.5 dBm for the 6 GBd QPSK signal. For the 16-QAM signal, the average input power into the Rx has to be corrected due to the different peak-to-average ratio compared to a QPSK modulation. Additionally, due to the AWG's bandwidth limitation, its output power for 12 GBd modulated signals is approximately 1.5 dB lower than for a signal modulated at 6 GBd. The resulting EVM values are related to the average signal power as described by equation (3.22). To control the receiver's input power, the WR-10 attenuator is varied from 20 to 60 dB in 2 dB steps, where the minimum attenuation value of 20 dB is set by the maximum allowed input power into the receiver's LNA, and the maximum attenuation is limited by the available attenuators in the considered frequency band. For all measurements, the VSA's built-in equalizer over a length of 55 symbols is used to optimize the received signal, the EVM values are extracted from the constellation diagrams and averaged over 409 600 symbols[4].

The results of the sensitivity measurement for QPSK and 16-QAM modulated signals with symbol rates of 6 and 12 GBd are shown in figure 3.4 as hollow and solid symbols, respectively. For Rx input powers below −57 and −50 dBm, the 6 and 12 GBd 16-QAM signals cannot be demodulated

[4]The number of averaged symbols result from the demodulation of 4096 symbols combined with an average over 100 measurements.

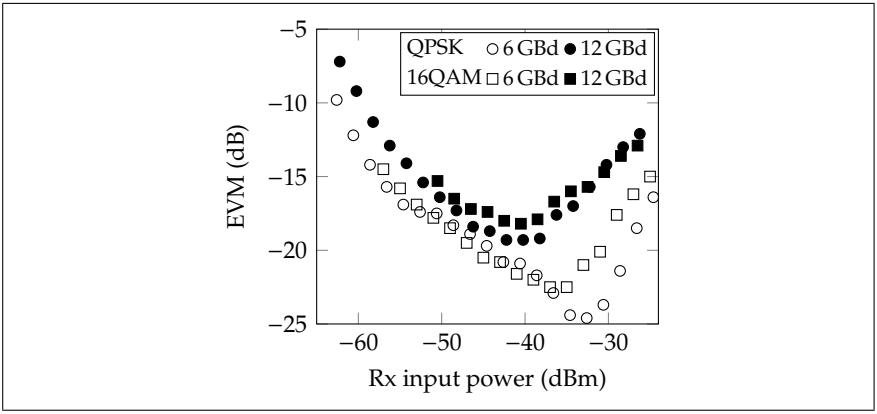

Figure 3.4: Receiver sensitivity measurement for the E-band frontend modules. The measurement is done for QPSK and 16-QAM modulated signals with symbol rates of 6 and 12 GBd, respectively. The resulting EVM is plotted versus the receiver input power, set by the waveguide attenuator.

anymore, while for the QPSK signals the gradient of the EVM curve is approximately one. For an increasing input power, an individual error floor at an EVM depending on the symbol rate, is reached. For further increasing power levels the EVM increases again.
When evaluating the part of the sensitivity curve representing low Rx input powers in figure 3.4, the slope of the curves for both QPSK modulated signals is approximately one. This indicates that the transmission is SNR-limited in this operating region, and the SNR's behavior is proportional to the resulting EVM as indicated by equation (3.6). The difference between the 6 GBd and 12 GBd signals' resulting EVM is approximately 3 dB as would have been expected due to the 3 dB increase in noise due to the doubling of the bandwidth. In this region, the resulting EVM value for the QPSK and 16-QAM modulated signal are more or less equal, the results are independent from any kind of non-ideality. In the region of the error floor, an increasing receive power does not result in an accordingly

decreasing EVM, indicating that in this region the transmission quality is not limited by SNR but restrained by non-idealities, i.e. I/Q-imperfections and LO phase noise as explained above. The difference in error floor is more than the 3 dB that was observed in the SNR-limited regime. Also, the error floor for the 12 GBd signals already occurs for lower input powers. This is due to the LO phase noise influence resulting in a higher phase error which in this case is accumulated over a higher bandwidth. Also, the more severe influences of I/Q-imbalances and conversion gain shapes over the higher bandwidth, which cannot be fully corrected by the equalization process, causes an increase of the error floor. The latter influence also leads to the better results in the region of the error floor between the QPSK and 16-QAM signals. For the latter, the signal is much more affected by the non-idealities causing worse results of the equalization process.
For further increased input powers, i.e. in the region, where the EVM rises again, there are two remarkable observations. The increase of EVM appears to be independent of the modulation scheme, indicating that this increase is not caused by compression effects in the Rx's LNA. Those would affect the 16-QAM much more severely than the QPSK signals. The second effect is, that the gradients of the curves for symbol rates of 6 and 12 GBd in this region are not identical. The curves for the 6 GBd signals, with their error floor at lower EVMs show a steeper gradient, indicating an intercept of both curves for an input power of approximately −17 dBm. There are two possible explanations for the observed behavior. Due to the increased RF input power, both the low noise amplifier and the mixer stage are operated close to their 1-dB compression point. This can cause third order modulation products which would influence the error vector magnitude. Additionally, since the receiver's mixer stage is not balanced, the leaked LO signal through the downconverter goes through a mixing process with the leaked LO signal out of the uponverter. This mixing generates low frequency and DC components which affect the EVM. While the low frequency components can corrupt the signal evaluation, the DC-components are not considered due to the baseband amplifier's AC-coupling. With an increasing input power, there is more power in the spectral component of the leaked transmitter LO signal, which due to

the mixing of the two LOs causes more power in those low frequency components. Since the relative portion of the spectrum influenced by those low frequency components to the overall signal bandwidth increases with decreasing symbol rates, the EVM for the 6 GBd signal might increase much faster than for higher symbol rates. To determine the exact reason for the observed effect, further measurements using a balanced receiver as well as a receiver with a higher third-order intermodulation point are necessary. Thereby, it will be possible to suppress one of the named effects and to investigate the influence of the respective other.
From the above considerations, an optimum receiver input power of −40 dBm can be determined for 12 GBd modulated signals, while for 6 GBd signals the error floor is reached for an input power of approximately −35 dBm.

3.2.4 Influence of spurs in the LO signal

To evaluate the influences of non-idealities existent in the LO signal, apart from the phase noise influences already considered above, two sets of PLL-stabilized VCOs, as introduced in chapter 2.1.3, for the Tx's and Rx's LO generation are available in addition to the commercial signal generators as used in the previous sections. For this measurement, the setup shown in figure 3.1 is used, with the waveguide attenuator set to the optimum Rx input power of −35 dBm, as obtained from the receiver sensitivity measurements. To separate the LO's influences from other non-idealities, a symbol rate of 1 GBd in combination with a simple BPSK modulation is used for the measurements. Thus, only few disturbances due to I/Q-imperfections or amplitude variances over the modulation bandwidth will impact the transmission. For every constellation diagram, 4096 symbols are demodulated and the results are averaged over 100 measurements. Also, no equalizer was used during this measurement.
As shown in chapter 2.1.3, while the signal generator's output only provides the desired carrier frequency of 9.6 GHz, in the output signal of both sets of VCOs, a distinct spur at a frequency of ±50 MHz around the desired carrier signal exists. After the frequency multiplier, VCO 1 set provides

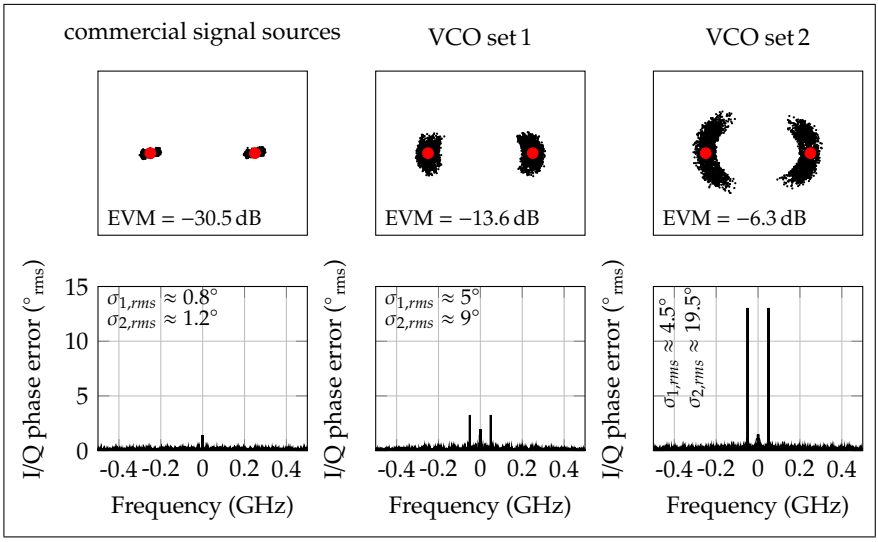

Figure 3.5: Influence evaluation of spurs in the LO signal on the transmission performance. In the left column, the results for an LO signal generated by commercial signal sources is shown. In the middle and right column the results for an LO generation using custom made VCOs with different phase noise and spur behavior are shown.

a suppression of these spurs of approximately 24 dBc. The calculation of the phase noise at 77 GHz with the use of equation (2.2) results in approximately −85 dBc/Hz at an offset frequency of 100 kHz. On the contrary, after the frequency multiplication VCO 2 shows a better phase noise performance of approximately −88 dBc/Hz at 100 kHz offset frequency, but simultaneously the spurs at ±50 MHz only show a suppression of 8 dBc. In the following measurements, shown in figure 3.5, the results obtained with the commercial signal sources are used in the left column of the plot. The constellation diagram shows a slight amplitude variation, indicated by the elongated constellation points and the resulting EVM is measured to be −30.5 dB. For the first set of VCOs, the one with the better spur sup-

pression shown in the middle column of figure 3.5, the measured EVM is −13.6 dB. The amplitude variation is approximately equal to what is shown in the measurements using the commercial signal sources. On the contrary, the constellation points are vertically smeared, indicating a phase distortion. When considering the measurement results using the second set of VCOs, the one with the better phase noise but worse spur suppression shown in the right column, it can be seen that the signal is even more distorted. Here, the measured EVM is only −6.3 dB and the constellation diagram reveals the arch-shaped constellation points typical for heavy phase distortion as explained in [NA00].
To gain more insight into the disturbances, the VSA software is used to evaluate the I/Q-phase error over time, i.e. the phase difference between the ideal and the measured constellation vector at each sample time. When performing a fast Fourier transform (FFT) on this time signal, the resulting spectrum provides the rms phase error contribution of each frequency component. As shown in the bottom row of figure 3.5 for each measurement, this phase error spectrum is calculated between −0.5 and 0.5 GHz, where this frequency range as well as the resolution bandwidth of 244 kHz is determined by the VSA's demodulation settings. The results for the two sets of VCOs, in the middle and on the right in figure 3.5, show an error peak at ±50 MHz, which corresponds to the spurs existent in the VCOs output signal. To separate the influence of the LO phase noise and the phase error introduced by the 50 MHz spur, two values, $\sigma_{1,rms}$ and $\sigma_{2,rms}$, are calculated by integrating over the phase error spectrum. While $\sigma_{1,rms}$ shows the total phase error in a frequency range from 244 kHz to approximately 49 MHz, i.e. the phase error contribution caused by the phase noise close to the carrier, $\sigma_{2,rms}$ gives the phase error over the entire bandwidth of interest, i.e. the combination of all phase errors and the spurious signal in the considered 500 MHz range. Both values are given within the corresponding graphs.
This evaluation reveals that, while for the measurement using the signal generators the phase error is predominantly caused by frequency components close to the carrier, the phase error in the measurements using the different sets of VCOs is mainly caused by the 50 MHz spurs existent

in the signal. Furthermore, the phase error contribution of the first set's higher phase noise signal is negligibly small and results in a phase error increase of only 0.5°. The phase error in the entire frequency range consideration is approximately 9°. On the contrary, the higher spurs caused by the second set of VCOs result in a much more severe signal distortion with a phase error of approximately 19.5° for the considered bandwidth. In conclusion, it can be stated that the consideration of near carrier phase noise alone is not sufficient to determine the performance of a wireless link as considered here. Unwanted spurs in the LO signal may cause severe signal distortion with a much higher impact on the signal quality.

3.2.5 Link performance for different modulation formats

With the influence of different non-idealities on the transmission quality determined, now the performance of the wireless link for data signals modulated with different complex modulation schemes will be examined. To determine the performance of the frontend modules without the imperfections of the distorted LO-sources revealed above, the commercial signal sources are used in all further measurements. The AWG is used to generate data streams with both phase and amplitude modulated signals at symbol rates up to 12 GBd and the receiver input power is set to an input power of −37 dBm. For all measurements, the VSA's built in equalizer over a length of 55 symbols is used to optimize the received signal[5].
In figure 3.6, the constellation diagrams with the resulting EVM values for QPSK, 8-QAM and 16-QAM modulated signals, each with a symbol rate of 12 GBd are shown. Higher order modulation formats, i.e. 32- or 64-QAM cannot be transmitted at this symbol rate, since the VSA software's carrier recovery algorithm is not able to lock onto the received signal. For all measurements, the constellation points are uniformly distributed but with

[5]If not otherwise stated, for this and all following measurements in this thesis, an equalizer length of 55 symbols is used. Furthermore, all EVM values are extracted from the constellation diagrams by averaging over 100 measurements with 4096 symbols each. Also, for each measurement, the analysis bandwidth of the VSA software is set to a value of 110 % of the complex baseband bandwidth to simulate a realistic hardware baseband filter [Tec10].

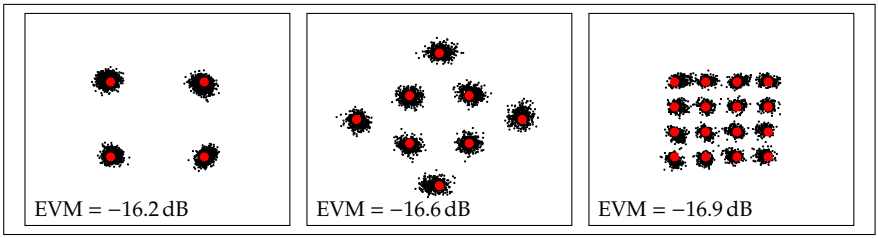

Figure 3.6: Constellation diagrams for 12 GBd modulated signals with, from left to right, QPSK, 8-QAM and 16-QAM schemes. For each constellation diagram the corresponding EVM normalized to the average symbol power is extracted. The ideal constellation points are shown as red dots.

slight deviations from the ideal ones, causing a rhombus shape, which is an indicator for a phase imperfection, i.e. a non-ideal 90° phase difference between the I- and Q-branch [Tec10]. The quadrature error calculated by the VSA software is around 4.5°, which is higher than the phase imperfection of 3° assumed for the theoretical performance calculation above. This is due to the higher bandwidth used in this measurement, for which the phase deviation of the used 90°-hybrid is higher. An I/Q-amplitude imbalance cannot be observed in the constellation diagrams, the imbalance measured by the VSA software is below 0.5 dB, indicating, that the equalization algorithm is able to partly correct the I/Q-amplitude imbalance introduced by the frontend modules. Neither of the measured signals show distinct signatures of phase noise or non-linearity. All signals show an EVM around −16.5 dB. For the QPSK signal, the constellation points are well separated, implying that the wireless link is capable of transmitting even higher symbol rates. For the 8-QAM and 16-QAM signals, some measurement points are located between two different constellation points, which would cause an increase in BER.
When reducing the symbol rate to a value of 6 GBd, resulting in an RF bandwidth which is permitted for E-band wireless links as shown in chapter 1.2.1, also 32- and 64-QAM modulated signals can be transmitted in

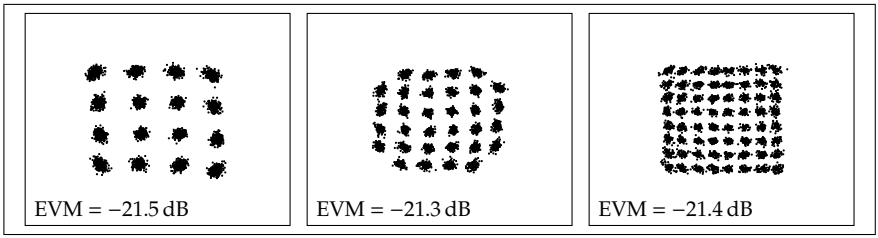

Figure 3.7: Constellation diagrams for 16-QAM (left), 32-QAM and 64-QAM signals at a symbol rate of 6 GBd and the corresponding EVM normalized to the average symbol power.

addition to the already shown modulation formats. The results are shown in figure 3.6. The same increase in signal quality as previously explained for the receiver sensitivity measurement can be observed here. Also for the higher order modulations, i.e. 32-QAM and 64-QAM, the constellations diagrams do not show any signature of severe phase noise, but in all three measurements, a slight compression effect indicated by a flattening of the outer most constellation points can be observed. The measured I/Q-imbalance and quadrature error by the VSA software are below 1 dB and around 4°, respectively. One reason, why the compression effect is not visible in the 12 GBd measurements could be the increased noise due to higher bandwidth in this measurements. A further investigation of this effect, using a setup with a variable gain amplifier in the transmitter and in the receiver's IF path, would be necessary to ensure identical SNR and power conditions, thereby allowing for comparable measurements.
Since for the reasons explained in chapter 1.2.6.1, no BERT system can be used to determine the BER performance for the transmission system, in the following a different approach will be applied: With the bit pattern of the transmitted PRBS sequences known and after the successful demodulation of the received signal with the VSA software, a comparison of the received bits with the transmitted sequence can be performed. While this approach reveals an insight into the BER performance, is it limited to a great extent. Due to the finite memory depth of the real-time

oscilloscope, only a certain, symbol-rate-dependent signal length can be recorded. Furthermore, these recordings require an excessive amount of hard disk storage. Thus, when comparing the complete recorded bit stream without an error occurring, the BER performance can only be estimated. Assuming in a worst case that the received bit following the last one contained in the recording will be wrong, then the resulting BER would be

$$BER = \frac{1}{\text{number of compared bits} + 1} \,. \tag{3.29}$$

For the measurements in this thesis, BERs in the order of 1×10^{-7}, depending on the actual symbol rate, can be achieved.
Applying this to the measurements shown above, the 12 GBd 8-QAM and 16-QAM signals result in BERs of 2.9×10^{-5} and 1.0×10^{-3}, respectively. For the QPSK signal, in 1 687 552 transmitted bits no error occurred. Thus, the BER for this signal is better than 5.9×10^{-7}. Considering the signals with a symbol rate of 6 GBd, the BER for the 16-QAM signal is better than 6.1×10^{-7} and the 32- and 64-QAM signals result in BERs of 9.6×10^{-6} and 4.7×10^{-3}, respectively.

As a result of the above performance evaluations, it can be concluded that the E-band frontend is capable of transmitting symbol rates up to 12 GBd in a 16-QAM modulation scheme. This results in data rates up to 48 Gbit/s. Furthermore, the frontend is sufficiently linear to transmit modulated signals up to 64-QAM without only slight distortions visible in the constellation diagrams.

3.3 240 GHz system setup

The performance and behavior of the 240 GHz system shall be evaluated in similar manner as the E-band system. Therefore, the system is

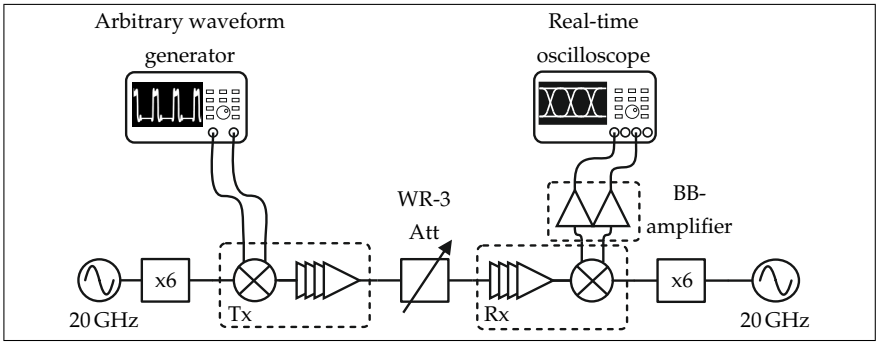

Figure 3.8: Back-to-back measurement setup for the 240 GHz frontend characterization with the Tx and Rx connected via a WR-3 waveguide attenuator to control the Rx's input power. Two phase-matched baseband amplifiers in the Rx's IF path and phase-matched cables in the entire measurement setup minimize the phase distortion due to the measurement setup.

set up with the Tx and Rx connected via an attenuator and the frontend's performance is evaluated in terms of imperfection influences and the capability to transmit complex modulated data signals. Further, the maximum achievable data rate is determined. The following results have been partially published in [17] and [21].

3.3.1 Link setup

To evaluate the 240 GHz frontend components shown in chapter 2.2 in terms of transmission capability, an incoherent back-to-back setup is used, i.e. two independent LO sources are used for transmitter and receiver. The Tx's and Rx's subharmonic LO signals at 120 GHz are generated by two commercial signal sources, the same sources as used for the characterization of the E-band frontend but this time operating at an output frequency of 20 GHz. In combination with the frequency multiplier-by-six modules, the necessary 120 GHz signal can be provided for the frontend modules. Between the RF-ports of the transmitter and the receiver, a WR-3 (220 to

Table 3.2: Parameter used to estimate the 240 GHz system's EVM performance.

Symbol rate (GBd)	k_{Tx} (dB)	k_{Rx} (dB)	$\phi_{Tx,Rx}$ (°)	Φ_{rms} (rad)	P_r (dBm)
5	0.01	0.7	0.4	0.0478	-10.6
10	0.02	1.02	3	0.0676	-11

325 GHz) waveguide attenuator is used to control the Rx's input power and its linear behavior. The transmitter input power is −10 dBm as determined by the module measurement, while the LO power for both modules is 7 dBm at 120 GHz. The Rx baseband I- and Q-signals are post-amplified using two phase-matched 24 dB broadband amplifiers with a noise figure of approximately 5 dB. To ensure accurate phase relations for the baseband data, phase-matched coaxial cables are used in the entire setup. The baseband I/Q data signals for different complex modulation schemes are generated using an AWG[6], while at the receiver, the real-time oscilloscope described in chapter 1.2.6.2 is used to capture the received baseband signals. A schematic of this back-to-back measurement setup is shown in figure 3.8.

3.3.2 Expected link performance

Using the above setup, the received power P_r can be determined from the signal spectrum obtained via the VSA software. The resulting SNR can be calculated, as discussed for the E-band link, to 27.1 and 23.7 dB for a 5 and 10 GBd signal, respectively by taking an overall noise figure of 12.3 dB into account. In combination with the average I/Q-imperfection parameters extracted by averaging over the used signal bandwidths from the frontend module measurement data in chapter 2.2, this information can be used to estimate the system's transmission quality by applying equation (3.20). The Tx and Rx phase imperfections are extracted from a

[6]The used AWG is a Tektronix 7122B with an analog bandwidth of 5.6 GHz, 10 bit resolution and an available sampling rate of 10 GS/s.

measurement of the 90°-hybrid used in both circuits, which is shown in [LDAF15]. All parameter for the EVM estimation are given in table 3.2.
For this setup, the same signal generators as for the E-band link measurements are used. The generators' noise floors are approximately identical for output signals of 10 GHz and 20 GHz[7]. Therefore, the rms phase error Φ_{rms} can be calculated by integrating the noise floor of −148 dBc/Hz of the used signal sources. Further, the noise increase due to the frequency multiplier-by-six and the internal frequency doubling in the subharmonic mixer stage is taken into account. The approach is identical to the one described for the E-band link, with an estimation for symbol rates of 5 and 10 GBd. The estimation results are compared to a measurement of QPSK modulated signals without the use of equalization.
Using the above assumptions, the EVM values for the 5 and 10 GBd signals are estimated to −20.8 and −16.7 dB, respectively. Since for these measurements, as stated above, a different AWG is used, for which a measurement of the instrument's EVM performance is not available, the errors introduced by the instrument itself are approximated by the values for the Agilent AWG used for the measurements of the E-band link. Due to the comparable bandwidth performance and the fact that the used QPSK modulation only consists of two amplitude levels, whereby constraints due to the reduced resolution compared to the Agilent instrument are not expectable, this approximation is suitable. In the measurements, EVM values of −18.4 and −15 dB are achieved for the entire link, while the AWG's output signals show an EVM of −21.2 dB for the 5 GBd and −19.1 dB for the 10 GBd signal. Using equation (3.28), the isolated EVM degradation due to the wireless frontend alone can be calculated to −21.6 and −17.1 dB for the 5 and 10 GBd signals, respectively.
When considering the relative error between the calculation and the measurement of the linear EVM value, an error of −8.4 % for the 5 GBd signal and an error of −4.6 % for the 10 GBd signal is revealed. The negative er-

[7] Following [Tec13], the instrument's noise floor only depends on the instruments output stage. Thus, if the same output stage is used, the noise floor can be identical although the frequency is doubled. Furthermore, in the instrument data sheet [Tec12a], the given noise floor for both 10 and 20 GHz output signals is identical.

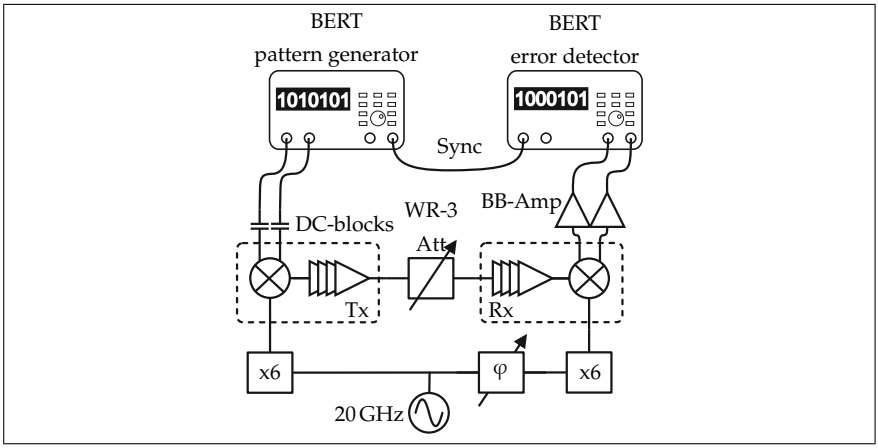

Figure 3.9: Receiver sensitivity measurement at 240 GHz using a coherent back-to-back setup. A BERT provides signals at data rates between 25 and 40 Gbit/s, with its OOK modulated output signal transformed to a BPSK signal by the use of DC-blocks. The errors introduced by the frontend modules are counted by the BERT's error detector. The 240 GHz receiver's input power is controlled by a WR-3 waveguide attenuator.

ror for both symbol rates indicates that the measured EVM value is better than the estimated one. This can only be explained by an underestimation of the used AWG's performance. If the AWG performs much better than expected by the measurement of the Agilent instrument, the correction of the measured EVM value by equation (3.28) leads to too optimistic values for the frontend performance. However, the small relative error for both symbol rate indicate that the estimation of the wireless link's performance give reasonable results.

3.3.3 Receiver sensitivity analysis

To determine the sensitivity of the 240 GHz receiver as well as the receiver's optimum input power, a sensitivity measurement is performed in

a coherent back-to-back transmission setup using a BERT system providing OOK modulated data streams at data rates between 25 and 40 Gbit/s. At the transmitter's input ports, DC-blocks are used to transform the OOK data stream into BPSK data by removing its DC-component. As explained in chapter 1.2.6.1, the coherent setup, where the transmitter and receiver share the same LO signal, is necessary since the BERT does not provide any kind of carrier recovery. Coherence is ensured by the use of a phase shifter in the Rx's LO path. The receiver's input power is controlled by a variable WR-3 waveguide attenuator, while a set of baseband amplifiers ensure proper input power for the BERT's error detector. A schematic of the used measurement setup is shown in figure 3.9.
The measurement results in figure 3.10 show the receiver sensitivity in terms of BER as a function of the transmitted data rate and the receiver's input power. The data rate is varied between 25 and 40 Gbit/s, while the Rx input power is adjusted in steps of 2.5 dB. For an input power of −31 dBm, a BER of 1.7×10^{-4} is achieved at a data rate of 40 Gbit/s. For 25 Gbit/s, a BER of 1.1×10^{-11} is achieved for an input power of −28.5 dBm. Although the measurement using a BERT system does not reveal as much insight into the system's non-idealities as it is the case for a measurement using the error vector magnitude as measure of quality, the BER provides an absolute measure for the system performance. For a low receiver input power, the transmission quality is SNR limited: With increasing signal power, the BER decreases. For input powers greater than −32 dBm, the BER levels at an error floor. With further increasing input powers, the BER stays constant, since the used BPSK signal is robust against compression effects in the receiver's LNA. The effect of decreasing signal quality for higher input powers, as observed for the EVM measurement of the E-band frontends in figure 3.4 cannot be seen in this measurement. Due to the high SNR, the "zero" and "one" rails of the received signal are well separated and the BERT's detection level can be placed with sufficient margin in between them. The distortion effects leading to the signal degradation observed in figure 3.4 first occur at the transitions between "zeros" and "ones" and contribute only little to the measured BER.
For the 40 Gbit/s measurement, a slight onset of distortion can be observed.

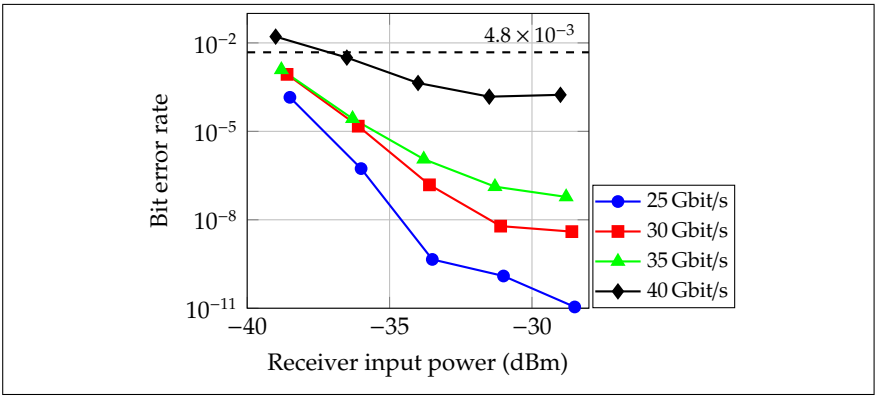

Figure 3.10: Receiver sensitivity measurement for the 240 GHz frontend modules for data rates between 25 and 40 Gbit/s. In the plot, also the 4.8×10^{-3} forward error correction (FEC) limit as published in [COM10] is shown.

The BER for an input power of −28 dBm is slightly higher than the one for −31.5 dBm. To observe the same effect for the lower data rates, higher receiver input powers would be necessary, which would lead to severe damage of the receiver's LNA stage. With an increasing data rate, the BER increases due to the transmission system's limited bandwidth and the more severe distortion due to the higher cumulated phase errors.
As discussed in chapter 2.2, the resulting 3-dB bandwidth for the 240 GHz system of approximately 20 GHz will allow for a maximum data rate of approximately 40 Gbit/s, which is confirmed in this measurement. The receiver sensitivity measurement also indicates that an optimum input power for the 240 GHz receiver module, averaged over all data rates, is approximately −31 dBm.

3.3.4 Characterization for phase and amplitude modulated signals

With the optimum receiver input power determined by the sensitivity measurement, now the transmission of different complex modulated signals will show the further performance of the frontends. As described above, the available AWG is capable of providing symbols rates up to 10 GBd, which is small compared to the bandwidths and data rates used for the sensitivity measurements. Therefore it will not be suitable for investigating the frontend's performance limits in terms of bandwidth. Nevertheless, in this measurement, the influence of the frontends' non-idealities can be observed, which is not possible for the BERT measurement. The measurement is set up as described in section 3.3.1.
The constellation diagrams with corresponding EVM for symbols rates of 5 and 10 GBd for QPSK modulated data signals are shown in the top and bottom row of figure 3.11. In the left and right column, the results for the received signals without and with use of the VSA's feed-forward equalizer can be seen.
As expected from an extrapolation of the sensitivity measurement, the constellation points are well separated, indicating a low BER. Nevertheless, for these measurements, the influence of the analog frontend is more visible. For both symbol rates, the constellation points without equalization are slightly arch-shaped, indicating a disturbance through phase noise [NA00]. An evaluation of the phase error in the frequency domain reveals, that the influence of phase noise is nearly equally distributed over the entire frequency range. The equalizer reduces the magnitude error by approximately 1.6 dB. The rms phase error influence, calculated with the VSA software in the same way as described for the E-band link above, is 5.2° and 10.0° for the 5 and 10 GBd signal without equalization, respectively. With the equalization, the influence of phase noise can be reduced to values of 3.3° and 5.1° and now is barely visible in the constellation plots[8].

[8] Although the equalizer can only account for linear distortions, as explained in chapter 1.2.6.2, the influence of the phase noise can be reduced. As shown in [CD10] for a

When comparing the measured EVM values to the sensitivity measurements, it is obvious that, since the transmission is not SNR limited as explained in chapter 3.1.1, an estimation from the measured EVM to the BER is not possible. When converting the measured EVM value of −14 dB for the 10 GBd measurement to a BER using the relations in [SRI06], this results in a BER of approximately 6.5×10^{-6}. On the contrary, an extrapolation of the sensitivity measurement to a data rate of 5 Gbit/s, which is essentially the data rate in both the I- and Q-channel when transmitting a 10 GBd QPSK signal, gives reason to expect a BER in the order of 1×10^{-15}, even though the decision space for correct signal detection around the constellation point is only half compared to the BPSK modulation used for the sensitivity measurement. Also here, a determination of the actual BER, as explained for the E-band system above, is performed. For the 5 and 10 GBd QPSK signals no error occurred in the recorded bit stream. This results in BERs of better than 1.3×10^{-6} and 6.3×10^{-7}.
The transmission of an 8-PSK modulated signal, as shown in figure 3.12, reveals the performance limits of this system. An 8-PSK modulated signal is much more susceptible to phase distortions than a QPSK modulated signal, represented by the higher density of constellation points at the same amplitude level in the constellation diagram. While this signal can still be demodulated at a symbol rate of 5 GBd without the use of the equalizer and shows well separated constellation points, at 10 GBd the VSA software is not able to demodulate the signal without equalization anymore. With the use of equalization the demodulation is still possible and results in a constellation diagram with only few sample points located in the area of the decision borders, indicating a low BER. For the 5 GBd signal, no bit error occurred. Thus, the resulting BER will be better than 8.8×10^{-7}. Considering the 10 GBd signal, the evaluation results in a BER of 3.1×10^{-4}.

16-QAM signal, the phase noise influence increases for constellation points with a higher symbol power. Thus, when using the equalizer on the received signal, the symbol power for all symbols is equalized resulting in a reduced impact of the phase distorted constellation points.

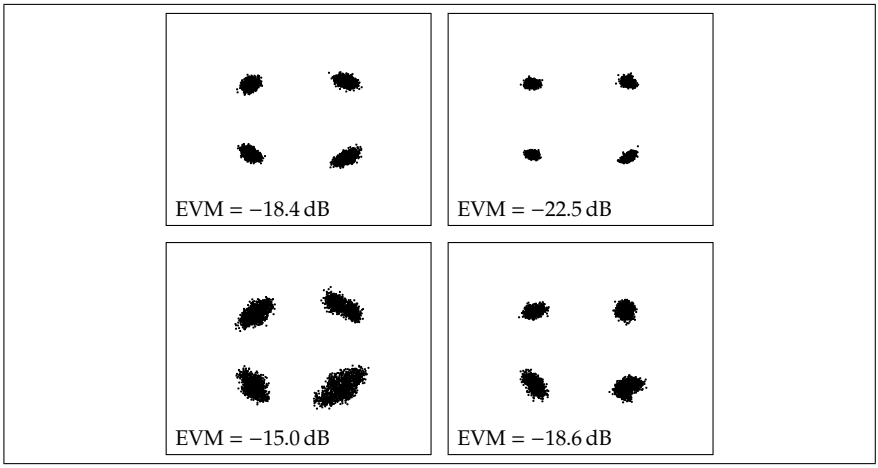

Figure 3.11: Constellation diagrams with corresponding EVM for QPSK back-to-back transmission using the 240 GHz frontend. The measurements in the top row show a symbol rate of 5 GBd, the ones in the bottom row 10 GBd. On the left column, measurements without, on the right measurements with the use of the VSA's feed-forward equalizer are shown.

In addition to phase modulated signals, the feasibility of amplitude modulated signals is investigated. The result of a 16-QAM transmission at a symbol rate of 5 GBd is shown in figure 3.13. As can be seen, the VSA software is not able to demodulate the signal and the three amplitude levels of the signal are compressed to one level. A few measurement points appear at what seems to be a different amplitude level.
This effect occurs due to the RF post-amplifier which is used in the 240 GHz transmitter, as explained in chapter 2.2.2, combined with the transmitter's LO leakage: The amplifier's output related 1-dB compression point is measured to be around −4 dBm, while the leaked LO signal generates a quasi noise floor at −11 dBm. This causes a limited dynamic range, which is not sufficient to transmit the necessary amplitude levels of the 16-QAM signal.

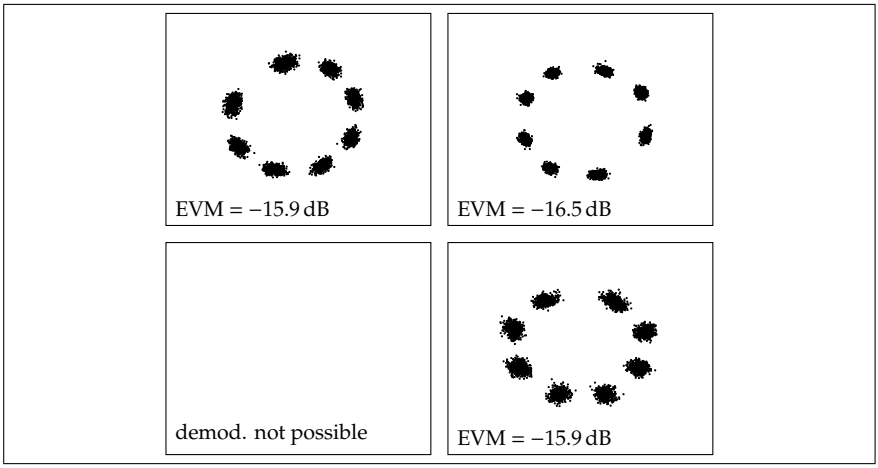

Figure 3.12: 8-PSK back-to-back transmission using the 240 GHz frontend for a symbol rate of 5 GBd (top row) and 10 GBd (bottom row). On the left, measurements without, on the right measurements with the use of equalization are shown. For the 10 GBd signal, a demodulation without equalization is not possible due to severe signal distortion.

For the presented measurement, the signal's dynamic range of 9.6 dB at the transmitter input is compressed to only 2.3 dB at the transmitter's output port. Due to this heavy signal distortion, the algorithms in the VSA software are no longer able to detect the correct modulation and demodulate the data stream.

As a result of the above investigations, it can be concluded that the 240 GHz frontend is capable of transmitting symbol rates up to 10 GBd in an 8-PSK modulation scheme. This results in data rates up to 30 Gbit/s. However, due to a limited dynamic range, the system is only capable of transmitting modulation schemes with a single amplitude level, in our case phase modulated signals.

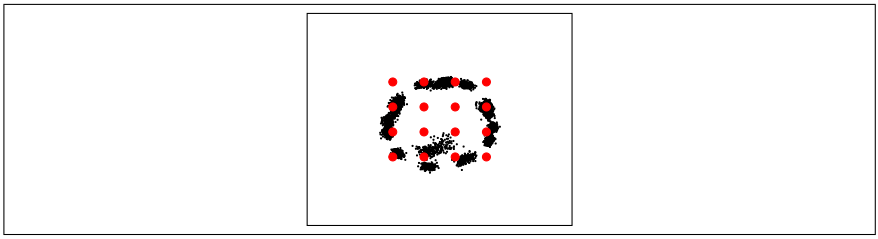

Figure 3.13: Due to the limited dynamic range of the 240 GHz transmitter module, the three different amplitude levels of the 16-QAM signal are compressed to one, a demodulation using the VSA software is not possible.

3.4 Performance estimation for the 300 GHz wireless system

Although up to now the 300 GHz frontend components only exist on chip level on a multi-project wafer at the Fraunhofer IAF, a reliable performance estimation for the 300 GHz is feasible with the validity of equation (3.20) from section 3.1.1 shown above for the E-band and 240 GHz link with deviation errors compared to the measurement of less than 8.4 %[9].

Table 3.3: Parameters used to estimate EVM performance of the 300 GHz system.

Signal source	Symbol rate (GBd)	k_{Tx} (dB)	k_{Rx} (dB)	$\phi_{Tx,Rx}$ (°)	Φ_{rms} (rad)
SG	10	0.57	0.35	0.95	0.2027
SG	25	0.68	0.33	0.95	0.3205
DDS	10	0.57	0.35	0.95	0.1342
DDS	25	0.68	0.33	0.95	0.2121

[9]Even a deviation in a range below 4 % can be expected, when neglecting the values obtained for the 240 GHz measurements, in which the exact performance of the used AWG is unknown.

The estimation for symbol rates of 10 and 25 GBd is done on the basis of the transmitter and receiver MMIC's on-wafer measurement results for I/Q-imbalance and the simulation of the tandem coupler's phase deviation shown in chapter 2.3.1. The 300 GHz transmit and receive MMICs use an internal frequency multiplier-by-three in their LO paths. Thus, the LO signal can be applied at 100 GHz as explained in chapter 2.3.2. In the planned system, this 100 GHz signal will be provided via a frequency multiplier-by-twelve with an input signal at 8.333 GHz. Consequently, for the phase noise estimation, the data for the two commercial signal generators, already used for the E-band and 240 GHz system, but this time operating at the frequency of 8.333 GHz, can be considered. The resulting noise floor at 300 GHz, after the multiplication by a factor of 36, can be calculated using equation (2.2) to be approximately −116.9 dBc/Hz.
Additional to the commercial ones, two signal sources based on a direct digital synthesis (DDS) system[10] are available[11]. These DDS-based sources can also be used together with the mentioned frequency multiplier-by-twelve to provide the 100 GHz LO signal for the 300 GHz transmitter and receiver. When driven by this DDS-based source, the resulting noise floor of the frequency multiplier's output is around −130 dBc/Hz at 100 GHz. This value is measured using a spectrum analyzer[12]. After the multiplication by three with the MMIC's internal frequency tripler, the resulting noise floor for the 300 GHz LO signal can be calculated by using equation (2.2). This results in approximately −120.5 dBc/Hz.
The used parameters for the estimation, comprising I/Q-amplitude and

[10] Direct digital synthesis is an approach to generate arbitrary waveforms by the use of a digital-to-analog converter, converting digital samples at the rate of a reference clock into samples of a sinusoidal signal waveform [TRG71, Gre11]. By using this approach, highly stable low-noise frequency sources can be realized, but with the drawback that due to the necessary high filtering effort for low-noise operation, only limited operating ranges can be achieved [LZL10].

[11] The DDS system together with the frequency multiplier was developed in the framework of the TERAPAN project by the Fraunhofer IAF, Freiburg.

[12] The used spectrum analyzer is an Agilent PXA signal analyzer with an attached smart harmonic mixer for a frequency range from 75 to 110 GHz and a phase noise measurement option.

phase imbalances, $k_{\mathrm{Tx,Rx}}$ and $\phi_{\mathrm{Tx,Rx}}$, for the Tx and Rx MMIC and the phase errors Φ_{rms} for the different symbol rates and LO sources, are given in table 3.3. For the LO sources, the DDS-based signal generation as well as the signal generation with the use of commercial signal generators (SG) are considered separately. The values for each imperfection are determined as described above.
It should be noted that the used parameters for the Tx and Rx imperfection are given based on MMIC on-wafer measurements. To realize a complete wireless transmission system, the MMICs have to be packaged or integrated into some kind of module, which will most probably decrease to performance results, i.e. cause additional I/Q-imperfections due to parasitic effects in the bond wires as well as phase mismatches and non-ideal frequency responses in the baseband signal routing. While the I/Q-amplitude imbalance can be partly corrected by the separated control voltages for the I- and Q-path of the mixer stage shown in chapter 2.3, there is no access to adjust the resulting phase mismatches. These influences will lead to a decreased system performance compared to the one calculated here. Hence, the performance results which will be shown in the following, depict the best possible system performance assuming an ideal module integration.
When evaluating the resulting EVM as a function of the SNR at the receiver as shown in figure 3.14 on the left, it can be seen, that for SNRs higher than 25 dB an error floor of approximately −15.2 dB for the 10 GBd signal and approximately −12.1 dB for the 25 GBd signal is reached when using the DDS-system as LO source. With the use of the commercial signal generators, as used for the E-band and 240 GHz systems, the signal distortion increases, resulting in worse EVM values due to the higher noise floor of these sources.
To further investigate the contribution of the different non-idealities to the estimated EVM value for a symbol rate of 25 GBd, the influence of the MMIC imperfections and the phase noise are considered separately in the right plot of figure 3.14. While the red curve represents the estimated value when using the imperfections as given in table 3.3, for the black curve, the Tx and Rx imperfections, i.e. I/Q-amplitude and phase imperfections,

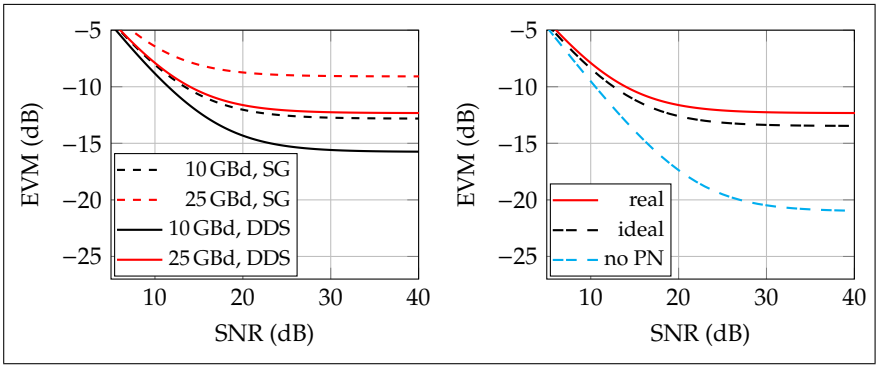

Figure 3.14: Estimated EVM dependency on the achieved SNR at the Rx depending on the used signal source, commercial signal generator oder the DDS-system, for 10 and 25 GBd modulated signals and the MMIC imperfections given in table 3.3(left). Comparison of the influence of MMIC imperfections and phase error on the estimated EVM in dependency on the achieved SNR (right).

are set to zero, representing an ideal transmitter and receiver, and only the contribution of the LO's phase error is present. As can be seen, the improvement can be neglected for low SNR values between 10 and 20 dB and the error floor is only reduced by 1.3 dB compared to the estimation with realistic Tx and Rx imperfections. On the contrary, when considering the system performance for an ideal LO signal without any phase noise at all, the EVM error floor drops to values around −21 dB and its onset occurs for SNRs above 30 dB. For SNR values up to 15 dB, the curves nearly follows the ideal EVM to SNR relation for AWGN-dominated systems shown in (3.6).

Now knowing that with a reduction of the MMIC's non-idealities only marginally improvements of the resulting EVM are feasible, the imperfection with the highest impact needs to be identified to enable an efficient improvement process . Simultaneously, the EVM increase due to additional I/Q-imbalances introduced by a module integration of the MMICs, is of great interest.

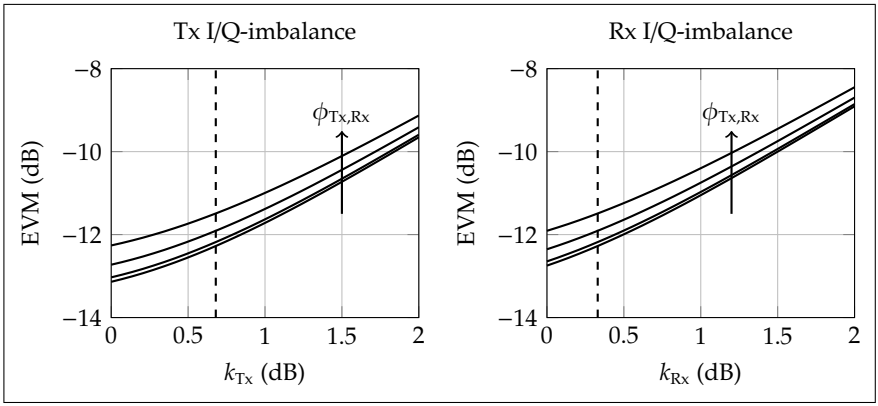

Figure 3.15: Estimated EVM dependency on Tx (left) and Rx (right) I/Q-amplitude imbalances $k_{Tx,Rx}$ for different phase imperfections $\phi_{Tx,Rx}$, varied between 0° and 6° in 2° steps. All other parameters are set to the values given in table 3.3 and the actual amplitude imbalances are indicated by dashed lines.

Therefore, the dependence of the resulting EVM on the influence of the Tx and Rx amplitude and phase imbalances are plotted in figure 3.15. As can be seen, even a decrease of the I/Q-phase imbalance to a value of 0° improves the resulting EVM only marginally. Also an increase of the I/Q-phase imbalance $\phi_{Tx,Rx}$ up to a value of 6° only results in an EVM increase of 0.8 dB for both the transmitter and receiver. When considering the influence of the I/Q-amplitude imbalance, it can be seen that a decrease in imbalance in the Rx improves the EVM by less than 1 dB. When decreasing the I/Q-amplitude imbalance on the Tx, an EVM improvement of approximately 1.1 dB can be achieved. Thus, if a redesign to improve the 300 GHz system's performance needs to be done in the future, the first approach should be to optimize the Tx's amplitude imbalance. When further considering the potential influences of a module integration, an imbalance increase of 0.5 dB causes a 1-dB penalty in the resulting EVM if introduced at the Tx, and a 1.2 dB penalty if introduced at the Rx. For

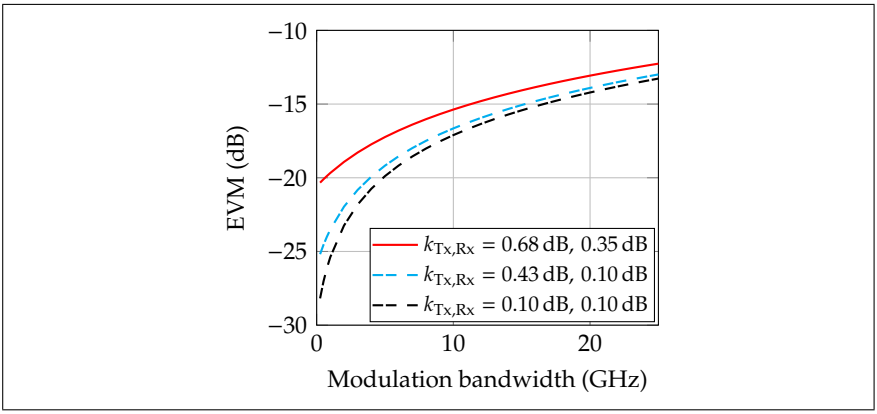

Figure 3.16: Estimated influence of the modulation bandwidth on the 300 GHz link's EVM performance for different values of I/Q-amplitude imbalances in the Tx and Rx MMIC and a phase imperfection of 0.95°. The SNR is kept constant at 33 dB, the I/Q-imbalances are assumed to be constant for all modulation bandwidths.

amplitude imbalances higher than approximately 0.8 dB at the transmitter and approximately 0.5 dB at the receiver, the slope of the EVM versus the imbalance curve is two, i.e. for each further 0.5 dB of introduced imbalance, the EVM increases by an additional 1 dB.

The influence of the modulation bandwidth on the transmission quality directly correlates with the integrated phase noise, as discussed in section 3.1.4 and expressed by equation (3.27). A further investigation shows, whether it will be more advantageous to transmit a combination of several data streams with a relatively small bandwidth in a multi-channel approach, instead of one extremely broadband modulated data stream, which covers the same bandwidth as the combination of all of the multi-channels together. In this case, the resulting SNR per channel in the multi-channel approach is identical to the SNR of one single but broad-

band modulation[13], but the impact of the integrated phase noise in each channel will be smaller compared to one broadband transmission. This allows for a better signal quality in each of the multi-channels and therefore, although the transmission rate is unchanged, a better transmission quality can be expected.
An evaluation of this multi-channel approach for the 300 GHz link using the DDS-based LO generation introduced above, is shown in figure 3.16 for the actual MMIC I/Q-imbalance performance, indicated as solid lines. For assumed improvements of the frontend's imperfections, which can be achieved by adjusting the I- and Q-mixer's gate voltage as explained in chapter 2.3, the resulting EVM performances are shown as dashed lines. The cyan colored curve represents an amplitude improvement of 0.25 dB in both the Tx and Rx. The black curve represents an I/Q-imbalance of 0.1 dB on each side, which is considered to be a feasible average value that can be achieved over several 5 GHz bands by adjusting the mixer's DC voltages. The SNR and for simplification the I/Q-imbalances are kept constant for each modulation bandwidth. The approach of also keeping the I/Q-imbalances constant at the values evaluated for a modulation bandwidth of 25 GHz in table 3.3 for the smaller bandwidths is not realistic for a future system, but serves as a good approximation for a first approach here. In reality, compared to the values used here, the I/Q-imbalances will most probably decrease when considering the individual channel but vary between the different channels. Thus, the results presented here represent the minimum achievable performance.
When evaluating figure 3.16, it can be seen, that an improvement of approximately 5 dB in EVM can be achieved when reducing the modulation bandwidth from 25 to 5 GHz for the actual MMIC performance. As the bandwidth of the intended frontend MMICs is sufficiently large, as discussed in chapter 2.3, it will be possible to transmit a signal which consists of five parallel data streams, each with a modulation bandwidth of 5 GHz,

[13]This assumption is true when considering that the Tx's output power which is distributed over the entire bandwidth in the case of the broadband modulation, is split up into several bands for the multi-channel transmission and simultaneously the noise power in each band is reduced due to the smaller bandwidths in the latter case.

and even separate them by a distinct stop band to prevent cross talk and thereby achieve at least the same overall transmission rate as for a 25 GHz signal but with a better EVM performance.
A further benefit of the multi-channel approach can be identified, when considering the influence of different I/Q-amplitude imbalances in figure 3.16. While for a modulation bandwidth of 25 GBd, a reduced imbalance only marginally improves the resulting EVM due to the domination of the phase error as discussed above, the same imbalance improvement can further reduce the resulting EVM by up to 3 dB when the modulation bandwidth is reduced to 5 GBd.
The slope of all EVM curves change at modulation bandwidths between 4 and 5 GHz, implying that for higher bandwidths, the influences of the frontend imperfections are dominated by the phase noise. Thus, to improve the system's transmission performance, modulation bandwidths in the range of 5 GHz should be chosen for the proposed multi-channel approach.
The drawback of this approach is, that the generation and evaluation of such multi-channel signals is much more complicated than for one very broadband modulation: Either high-speed DACs and ADCs have to be used to process the signals in the digital domain, which will come along with a increased effort in the digital domain. Or component intensive analog multiplexing, mixing and filtering have to be used to combine the different baseband data to a single broadband signal at the transmitter and shift the different received channels back to baseband for processing at the receiver. A further analysis and evaluation of such baseband setups and their performance is out of the scope of this thesis but is considered feasible.

3.5 Discussion

This chapter was concerned with the evaluation of transmission quality in the back-to-back connected setups of the mmw frontend components. The error vector magnitude as a figure of merit to assess transmission

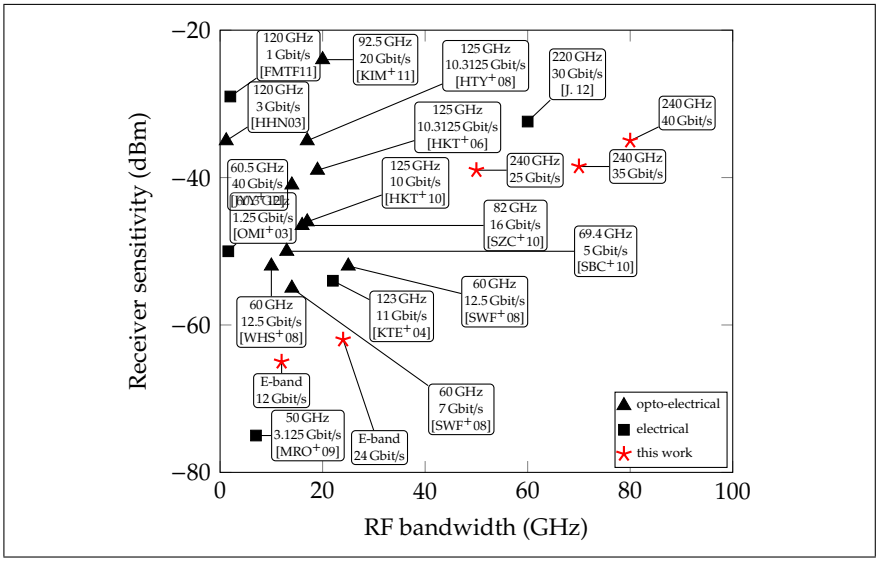

Figure 3.17: Comparison of the achieved receiver sensitivity performance of the E-band and 240 GHz system to the current state of the art. The star-shaped points represent the values achieved in this work, the already published values are separated by pure electrical systems (squares) and opto-electrical (triangles) systems.

quality as a function of various frontend imperfections was derived. The presented model for a theoretical analysis of the resulting EVM under the influence of such imperfections, i.e. I/Q-amplitude and phase imbalances as well as LO phase noise, shows that the simple relation between achieved SNR at the receiver and resulting EVM for AWGN-limited systems, given in equation (3.6), is in our case not true any more. Further, due to the invalidity of equation (3.6), a simple estimation of the resulting bit error rate is not possible but has to be performed depending on the used modulation format in combination with the distinct imperfections [MMMFOM11].
The presented EVM model is used to estimate to frontend performances

of the E-band and the 240 GHz system and the findings were compared to measurements performed using an arbitrary waveform generator and a real-time oscilloscope with a vector signal analysis software to generate and analyze complex modulated data signals. This comparison between estimated and measured EVM results in a deviation with a relative error of less than 8.4 % for the 240 GHz system, where the exact performance of the signal generation AWG is not know. For the E-band system, the AWG's performance is well known and its influence can be separated from the effects introduced by the wireless link. Here, the relative error between estimation and measurement is as low as 3.6 %. Considering the extreme bandwidths and the variety of effects and parameters which influence the system performance, these very small deviations are remarkable. Furthermore, it is the first time that such an investigation was performed on wireless systems operating at such elevated frequencies and particularly with such extreme IF bandwidths, and that the results of this performance estimation can be directly compared to measurements of the examined wireless links.

Besides the investigation of the wireless system's performance, the receiver sensitivity, indicating the minimum input power for the receiver to achieve a certain BER was determined. This sensitivity, setting a limit to the achievable dynamic range of the receiver, is an important measure for system developers when designing a wireless link. In figure 3.17, recently published receiver sensitivity performances for a BER of 1×10^{-3} versus the RF bandwidth of the transmission are compared. The achieved data rates and the used carrier frequencies are provided in the annotations. Where not explicitly given, the resulting 1×10^{-3} performance is extrapolated from given sensitivity plots. While for the 240 GHz system the receiver sensitivity was measured in terms of BER, the obtained EVM values for the E-band link needs to be transformed to BER values. Since in the measurement the systems was observed to be clearly SNR-limited for low receiver input powers, the 1×10^{-3} BER limit can be approximated by using equation (3.6) and the SNR to BER dependency from [Gu05].
When comparing the achieved results to the state of the art, both the E-

band and the 240 GHz link show outstanding performances as can be seen from the star-shaped points in figure 3.17. The E-band system provides an approximately 10 dB better sensitivity compared to systems operating in the same frequency range. For only one system operating with a RF bandwidth comparable to the 240 GHz system, a receiver sensitivity measurement is published. But even compared to the achieved results for systems operating at a fourth of the bandwidth and with much lower carrier frequencies, the achieved sensitivity is remarkably high. Both the E-band and 240 GHz system set new standards for the state of the art, not only in their operating frequency and bandwidth range but also for more narrowband systems operating with lower carrier signals.

To determine the maximum achievable capacity of the wireless systems, the transmission performance of both the E-band and the 240 GHz system is evaluated for transmitting extremely broadband PSK and QAM modulated signals.
The E-band link shows a measured EVM after equalization of approximately −17 dB for symbol rates of 12 GBd and approximately −21 dB for symbol rates of 6 GBd. When using QPSK, 8-PSK and 16-QAM modulation schemes, this results in bit rates of 24, 36 and 48 Gbit/s for the symbol rate of 12 GBd. With a symbol rate of 6 GBd, 16-, 32- and 64-QAM modulated signals are transmitted, which results in data rates of 24, 30 and 36 Gbit/s.
With the 240 GHz system, EVMs of −22.5 and −18.6 dB are achieved for QPSK modulations with symbol rates of 5 and 10 GBd, while for 8-PSK modulated signals EVMs of −16.5 and −15.9 dB are achieved for these symbol rates. The resulting data rates are 10 and 20 Gbit/s for the QPSK modulated signals and 15 and 30 Gbit/s for the 8-PSK modulation. The attempted transmission of a 16-QAM modulated signal reveals a severe linearity problem in the 240 GHz system's transmitter, limiting the usable transmission scheme to PSK signals.
For both systems, a comparison to the state of the art is not possible, since at the time of writing no electrical system using a direct conversion scheme with complex modulated data signals exists. Even when considering sys-

tems with lower data rates or systems using opto-electrical transmitters, no publication providing comparable performance data can be found.

A first evaluation of both systems' BER performance is done by comparing the received bit stream after the demodulation with the VSA software against the transmitted one. While for measurements with high error rates, this approach is sufficient to determine the actual BER, it is only useable to a limited extent for systems with a low error rate. Due to the finite recording length of the captured signals, for systems which show no error in the captured bit stream, only a worst case calculation can be given.
With this approach applied to the measurements of the E-band system, the link's performance is determined. While the BER results for the 16-QAM modulated signal indicate a performance better than 6.1×10^{-7}, the higher order modulations result in values of 9.6×10^{-6} and 4.7×10^{-3}, respectively. Considering the maximum symbol rate of 12 GBd, the QPSK signal shows a BER performance better than 5.9×10^{-7}. The more elaborate 8- and 16-QAM signals with result in BERs of 2.9×10^{-5} and 1.0×10^{-3}, respectively.
Also, for the 240 GHz system, a determination of the BER is performed using the same approach. For the 5 and 10 GBd QPSK signals, resulting in data rates of 10 and 20 Gbit/s, no error occurred in the recorded bit streams. This results in BERs of better than 1.3×10^{-6} and 6.3×10^{-7}, respectively. For the more elaborate 8-PSK modulation, with its higher sensitivity to phase noise influences, also no bit error occurred when using a symbol rate of 5 GBd. Thus, for this signal, the resulting BER is better than 8.8×10^{-7}. Considering the same modulation scheme with a symbol rate of 10 GBd, the evaluation results in a BER of 3.1×10^{-4}.
As a limit for feasible data transmission, the work published in [COM10] shows that an uncorrected BER of 4.8×10^{-3} can be corrected to a BER of 2.0×10^{-8} by using appropriate forward error correction (FEC) with a 7 % overhead[14]. This approach is suitable for data rates up to 100 Gbit/s.

[14] 'In practice, FEC is implemented by adding to the transmitted signal data that en-

Thus, for the two systems in the E-band and at 240 GHz, the achieved BERs for all measurements are sufficiently low to be corrected with this FEC. Thus, the maximum achieved data rates of 48 Gbit/s in the E-band and of 30 Gbit/s at 240 GHz can be corrected to be error free, i.e. to BERs below 1×10^{-15}. Due to the 7 % overhead, the net data rate for this data signals, i.e. the useable data rate after the redundant bits necessary for the error correction are removed, will be 44.64 Gbit/s for the E-band system and 27.9 Gbit/s for the 240 GHz system.

An estimation of the EVM performance for the 300 GHz MMICs reveals, that this system's performance will be mostly dominated by phase error. Due to the high necessary multiplication factor in combination with the intended broadband IF signals, the phase noise influence can hardly be reduced. Its dominating influence allow only for marginal quality improvements by reduced the frontend's I/Q-imbalances.
To overcome this limitation, an approach of combining several modulation bands with modulation bandwidths in the order of 5 GHz to a multi-channel transmission is suggested, which reduces the influence of the phase error in each channel in combination with an SNR comparable to a transmission with a single broadband modulation. While with the considerations above, the approximated BER limit of 1×10^{-3} for the 25 GBd signal will already be reached for a QPSK modulated signal, for the more narrow band multi-channel approach, a 16-QAM transmission is with correctable error rates. The resulting bit rate for the 25 GBd modulation is 50 Gbit/s, the multi-channel system achieves a total data rate of 100 Gbit/s by simultaneously transmitting five data streams at a symbol rate of 5 GBd with a comparable performance.

ables the receiver to detect and evaluate the data errors' [COM10]. These additional bits introduced by the parity code are called overhead. Related to the measurements with an uncorrected limit of 1×10^{-3}, 7 % of the achieved data rate has to be used for the parity bits of this particular FEC.

4 Wireless Data Transmission

After characterizing the frontend modules' behavior for both the E-band and the 240 GHz system, on module and system level in terms of RF performance and data transmission capability in the preceding chapters, these modules will now be used to set up actual point-to-point wireless links. Thereby, the system's behavior in application-oriented environments and under the influence of realistic distortions due to the propagation of the electromagnetic waves will be investigated.

The chapter is subdivided into three parts. In the first part, an introduction to link budget theory relevant for the design of wireless links is given, including the influences of atmospheric effects, i.e. the specific attenuation of the propagating signal due to gaseous absorption, fog and rain in the transmission path. The parameters determining the maximum transmission distance and the maximum transmittable data rate are discussed. In the two following parts, the transmission experiments with the E-band and the 240 GHz system are described. For each experiment, the achieved transmission performance results are compared to the theory. Furthermore, for each link, the maximum achievable distance and data rate are calculated on the basis of these theoretical relations.

4.1 Link budget considerations

Since the expectable performance of a fixed wireless link not only depends on the frontend module characteristics but also on the propagation effects of the electromagnetic wave, in the following, the influences of path loss and atmospheric attenuation on the link performance will be discussed. The relevant effects are identical for the entire millimeter wave frequency

range, but gain an increasing influence at higher frequencies. Therefore, the attenuating effects will first be discussed in general, before focusing on the transmission bands used by the wireless links in this thesis.

4.1.1 Free space path loss and Friis' equation

As depicted by Friis in [Fri46] and shown in equation (4.1), the received power P_r at the receiver's antenna output of a wireless link depends on the transmitted power P_t fed into the transmit antenna, the gains of the transmit and receive antennas $G_{Tx/Rx}$, the wavelength λ and the distance d between the two antennas.

$$P_r = P_t G_{Tx} G_{Rx} \cdot \left(\frac{\lambda}{4\pi d}\right)^2 \tag{4.1}$$

Alternatively, P_r can be given as a function of the transmitted frequency f_c:

$$P_r = P_t G_{Tx} G_{Rx} \cdot \left(\frac{c_0}{4\pi d f_c}\right)^2 . \tag{4.2}$$

Here, c_0 represents the speed of light.
However, this equation only is valid for plane wave fronts at the receiver, i.e. if the receiver is located in the farfield of the transmit antenna. The term $(\lambda/4\pi d)^2$ is referred to as free-space path loss (FSPL), describing the redistribution of the available power over a sphere with its radius being equal to the transmission distance[1], as already mentioned in chapter 1.1.1. Friis

[1] The term *loss* can be misleading, since this term seems to indicate an increasing attenuation with increasing frequency. In fact, the effect of decreasing receive power with increasing distance is independent from the frequency. The available power is only redistributed over a sphere with the area $(4\pi d)^2$. The frequency dependence is introduced by the antenna gain, which is related to the effective antenna area via $G = \frac{4\pi}{\lambda^2} \cdot A$, where A is the effective antenna area. Since it is common to assume the antenna gain to be independent from frequency, this

showed a quadratical dependency of the received power and the transmission frequency and distance. For practical link budget calculations, it is advantageous to rewrite equations (4.1) and (4.2) to a logarithmic scale, resulting in:

$$P_{\mathrm{r,dBm}} = P_{\mathrm{t,dBm}} + G_{\mathrm{Tx,dBi}} + G_{\mathrm{Rx,dBi}} + 20\log\left(\frac{\lambda}{4\pi d}\right) \tag{4.3}$$

or

$$P_{\mathrm{r,dBm}} = P_{\mathrm{t,dBm}} + G_{\mathrm{Tx,dBi}} + G_{\mathrm{Rx,dBi}} + 20\log\left(\frac{c_0}{4\pi d f_{\mathrm{c}}}\right) . \tag{4.4}$$

In combination with the bandwidth, this relation is essential to calculate the maximum achievable distance of a wireless link and estimate its performance as a function of P_{r}.

4.1.2 Fresnel zone

For an unobstructed signal transmission, in addition to the direct path between transmitter and receiver of a wireless link, i.e. the LOS, the so-called Fresnel zones[2] have to be evaluated for disturbances of the propagating electromagnetic wave. The nth Fresnel zone is defined as an ellipsoid surrounding the direct path between Tx and Rx with its foci located at the transmitting and receiving points, for which the sum of the distances between the transmitter and receiver and a point on this ellipsoid is n half-wavelengths longer than the direct path. Consequently, the dimensions of the different Fresnel zones depend on the path length as well as on the propagating wavelength. The additional path length inside a

dependency is shifted to the path loss term.

[2] Fresnel accounted for the diffraction of light by postulating that the cross section of an optical wavefront is divided into zones of concentric circles separated by half-wavelengths. These zones alternate between constructive and destructive interference, resulting in a sequence of dark and light bands when diffracted light is viewed on a screen.[Smi93, pp.553]

specific ellipsoid causes a phase shift for the propagation wave, leading to an interference at the receiver between all signals reflected at points inside this specific Fresnel zone and the LOS path signal [Mol11].

For point-to-point links, as considered in this work, the first Fresnel zone, which can be thought of as containing the main propagating energy of the electromagnetic wave, is the most relevant, since objects located inside this zone result in significant signal perturbation at the receiver. A special case for such a disturbance is the positioning of the transmitter and receiver station above the ground. Assuming the Tx and Rx of a point-to-point link are not placed high enough, so that the first Fresnel zone touches the ground, the resulting interference can cause a reduction of signal strength at the receiver below the value calculated by Friis' equation (4.3). Following this consideration, when setting up a wireless link, an obstacle free line of sight is not sufficient to achieve the calculated receive power, but the clearance of the first Fresnel zone has to be ensured. The maximum radius $r_{1,\max}$ of the first Fresnel zone can be calculated using equation (4.5) [Ber00]:

$$r_{1,max} = \frac{\sqrt{\lambda \cdot d}}{2} \,. \tag{4.5}$$

One essential advantage of the high mmw carrier frequencies used for the wireless link in this thesis is revealed by this consideration of the first Fresnel zone. Compared to commercially available links in the lower GHz range, the dimension of the first Fresnel zone at these elevated frequencies is much smaller and thereby an unimpaired zone is more likely to be achieved.

4.1.3 Atmospheric influences

In addition to the free space path loss, electromagnetic wave propagation suffers from several attenuation effects caused by atmospheric influences

as briefly explained in chapter 1.1.1. In a clear atmosphere, these result from absorption effects introduced by atmospheric gases, mainly oxygen and water molecules. Adverse weather like rain and fog, but also clouds, lead to additional attenuation[3] effects.
In the following section, the atmospheric attenuation mechanisms for millimeter-wave frequencies are discussed.

4.1.3.1 Attenuation in clear atmosphere

The specific attenuation of the atmosphere, caused by molecule oscillation of gases and water molecules can be calculated following the models in [Rec09a] for different values of barometric pressure, temperature and humidity. Figure 1.1 in chapter 1.1.1 shows the specific attenuation in a clear atmosphere for frequencies up to 400 GHz at sea level, i.e. at an barometric pressure of 1013 hPa. The temperature and water vapor density are chosen to be 293.15 K and 7.5 g/m^3, which corresponds to a temperature of 20 °C and a relative humidity of 43.4 %[4].
The graph shows the oxygen resonances at 60 and 118 GHz as well as resonances due to water molecules at 22, 183, 325 and 380 GHz. The so-called atmospheric windows between those resonances can be used for communication links, providing moderate additional attenuation of 0.5 to 0.4 dB/km in the E-band and 3 to 4.4 dB/km in the frequency band from 200 to 280 GHz.

[3] Although the underlying effects disturbing the propagation of the electromagnetic waves are scattering, diffraction and refraction mechanisms, and therefore, are not classical forms of attenuation, these effects cause a reduction of received power and appear as a loss factor in the link budget calculation. Therefore, all effects reducing the received power will be summarized in the term attenuation in the following for simplicity reasons.

[4] Water vapor density can be transformed into relative humidity by using the following relation:

$$\text{Relative humidity} = \frac{\text{actual vapor density}}{\text{saturation vapor density}} \times 100\% \ .$$

For a temperature of 20 °C, the saturation vapor density is 17.3 g/m^3.

4.1.3.2 Attenuation due to fog and clouds

In fogs and clouds, the water vapor condenses, producing water droplets with a diameter smaller than 0.01 cm. The electromagnetic wave is scattered at these droplets, causing an attenuation for the transmitted signal. In [Rec09b], this attenuation is modeled as Rayleigh scattering, valid for frequencies up to 200 GHz. Following this approximation, the specific attenuation γ_c due to clouds or fog can be calculated as

$$\gamma_c = k_l M \, \mathrm{dB/km} \,, \tag{4.6}$$

where k_l is the specific attenuation coefficient in (dB/km)/(g/m^3) and M is the liquid water density inside the cloud or fog given in g/m^3. The liquid water density in fog is typically around 0.05 g/m^3 for medium fog, corresponding to a visible range in the order of 300 m, and around 0.5 g/m^3 for thick fog, corresponding to a visibility in the order of 50 m [Rec09b, SWP+12]. The specific attenuation coefficient k_l and the complex dielectric permittivity of water are given in Appendix A. As can be seen from equation (4.6), the attenuation is directly proportional to the liquid water content existent in the fog or cloud.
The expected attenuation due to fog with different water vapor densities, resulting from the above equation, are shown for frequencies up to 400 GHz in the left plot of figure 4.1. The ambient temperature is set to 5 °C. The results show that even for a visible range of 50 m, the attenuation due to fog stays below 10 dB/km at a frequency of 400 GHz. For the frequency ranges of the wireless links considered in this thesis, the expected attenuations are between 0.1 and 0.2 dB/km in the E-band as well as between 0.5 and 0.8 dB/km in frequency range of the 240 GHz for medium fog. For thick fog the calculated attenuation values are between 1.5 and 1.8 dB/km and between6 and 8 dB/km, respectively.
The calculation of the resulting attenuation due to clouds in principle follows the same mathematical models as used for fog, but the ITU recommends an ambient temperature of 0 °C to approximate the prevailing temperature inside clouds [Rec09b]. Also, the water vapor density in

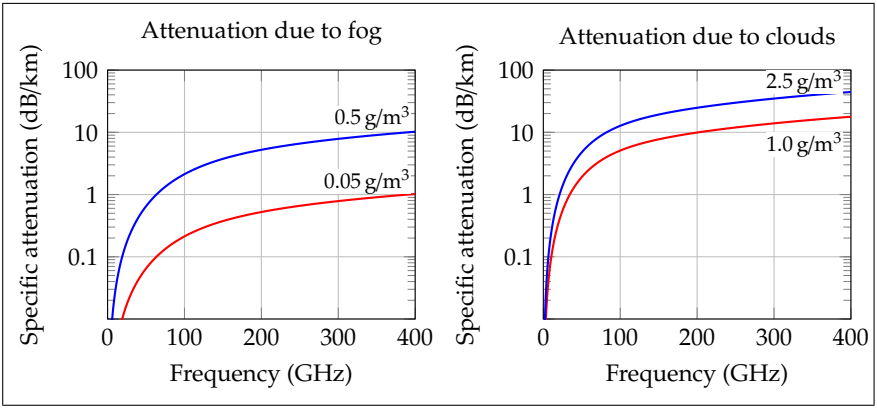

Figure 4.1: Specific attenuation due to fog (left) and clouds (right) for different water vapor densities. For fog, an ambient temperature of 5 °C, for clouds a temperature of 0 °C is chosen.

clouds is higher than in fog. Referring to [aK50], it varies between 0.2 g/m^3 and 2.5 g/m^3 depending on the type of cloud[5]. The specific attenuation for frequencies up to 400 GHz, shown on the right of figure 4.1, reveals the more severe impact on an electromagnetic wave due to the higher liquid water content in clouds.

4.1.3.3 Attenuation due to rain

When considering the influence of rain on the propagation of electromagnetic waves, severe impacts especially in the millimeter-wave range can be found. The resulting attenuation can be calculated following the ITU recommendation [Rec05] by

$$\gamma_r = k_r R^\beta \text{ dB/km} , \tag{4.7}$$

[5] As shown in [aK50], a water vapor density of 0.2 g/m^3 prevails in Altostratus clouds, while densities up to 2.5 g/m^3 are reached in Cumulus congestus clouds.

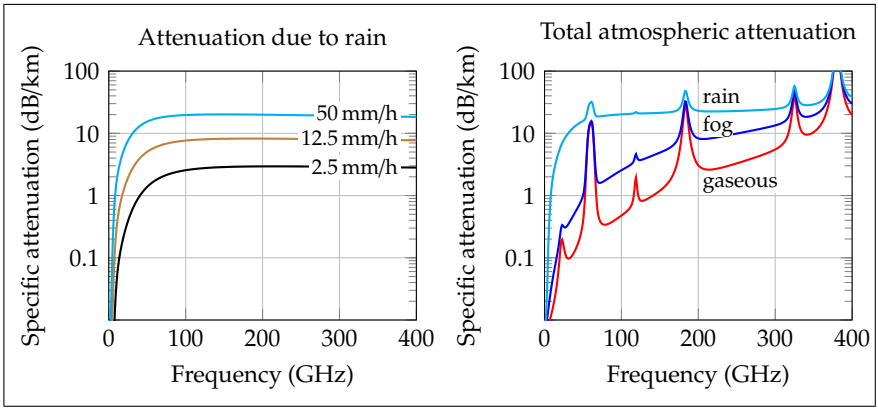

Figure 4.2: Specific attenuation due to rain for different rain rates (left) and total atmospheric attenuation by superposition of gaseous, fog and rain effects (right).

where the specific coefficients k_r and β are determined as functions of the carrier frequency in the range from 1 to 1000 GHz (calculated as given in Appendix A). The factor R represents the rain rate. The size of the rain drop is inherently included in the rain rate factor, by assuming a specific drop size to be necessary to form the corresponding rain rate.
The resulting attenuations for horizontally polarized waves and rain rates of 2.5, 12.5 and 50 mm/h are shown in figure 4.2, where a rain rate of 2.5 mm/h represents a light rain in a temperate climate zone, while rain rates of 50 mm/h and higher only occur at tropical convective events. It is notable that for frequencies above 100 GHz, the additional attenuation due to rain seems to be almost constant for all frequencies up to 400 GHz at a given rain rate. For the frequencies of the wireless links considered in this work, the expected attenuations for rain rates of 2.5 and 50 mm/h are 2.2 and 18.7 dB/km at 77 GHz and 2.9 and 19.6 dB/km at 240 GHz, respectively.

4.1.3.4 Total atmospheric attenuation

The total atmospheric attenuation, achieved by superposition of the different effects discussed above, is shown in figure 4.2 on the right hand side. The red curve represents the attenuation in a clear atmosphere where only attenuation due to gaseous and molecule resonance effects occurs. In the blue curve, the attenuation due to a fog with a visibility of 50 m superposes this gaseous attenuation and in the cyan curve, the attenuation in clear weather is superposed by a rain of 50 mm/h. While in the case of fog, the slope of the attenuation curve is still dominated by gaseous attenuation, at heavy rain, these attenuation effects only dominate at frequencies where molecule resonances occur. For all other frequencies, the attenuation is dominated by the effects introduced by the rain.

When reviewing publications evaluating the accuracy and validity of the introduced prediction models for rain and fog, a huge variety of results can be found. While in some experiments, the measured attenuation due to rain matches the prediction by the ITU model in [Rec05], in others high deviations are observed. In [HYT+09], the measured attenuation introduced by rain, averaged over specific time constants correlates very well with the ITU prediction. Nevertheless, the degradation of the examined wireless transmission quality for a 120 GHz link is significantly higher than theoretically expected from the measured attenuation value, indicating that the signal is not only degraded by the attenuation but also by additional effects introduced due to the rain. In [KJYC13, KJC12], experiments at 73 GHz are performed, showing that the ITU models severely underestimate the measured attenuation. They also show that this attenuation varies considerably for different measurements at the same rain rate. The same results are found in [AO85], stating that the ITU models are not suitable for high rain rate events like tropical rain. The divergence between modeled and measured attenuation is also discussed in [MO13], showing the differences in rain modeling and the benefits and drawbacks of the different approaches. The divergence is mainly introduced by a variation of rain drop size and the amount of rain drops. The same con-

clusions can be drawn for the prediction of attenuation due to fog. Even in the publication building the basis of the ITU model published by Liebe et al. [LMH89], a high scattering in measured data points can be seen.
It can be concluded that the ITU provides a general-purpose model which is suitable to easily estimate the additional attenuation introduced by fog and rain averaged over long time spans and common weather events, but for specific and severe weather events, this estimation is not necessarily correct. The same conclusion is drawn by Garcia-Rubia et al. in [GRRGdPB13]: "Empirical models need less input data, making their application easier for a wider number of locations. This is the case of the ITU-R model, which provides very reasonable errors in this case with the use of only one value as climatic input data." Therefore, to correctly predict the expected attenuation when planning a specific wireless link, one has to take into account information about the local weather conditions as well as more specific prediction models involving a larger set of parameters for the calculation than used for the ITU models.
In the following, the attenuation of the propagating electromagnetic wave due to weather events is still calculated by using the ITU recommendations, since these are worldwide acknowledged calculation methods.

4.2 Wireless transmission using the E-band frontend

To prove the feasibility of high-speed data transmission over several kilometers in the E-band, the frontend setup from figure 3.1 in chapter 3.2 is extended by different amplifiers in the Tx and Rx. A Cassegrain antenna system with a simulated gain of 45.7 dBi per antenna is used to radiate the signal. The frontend components as well as the antenna system are integrated into a waterproof and temperature stabilized housing[6], mounted

[6]The antenna system as well as the housings are designed and developed by Radiometer Physics GmbH, Meckenheim, in the framework of the GISALI project. All RF amplifiers are designed and realized by the Fraunhofer IAF in the framework of the same project.

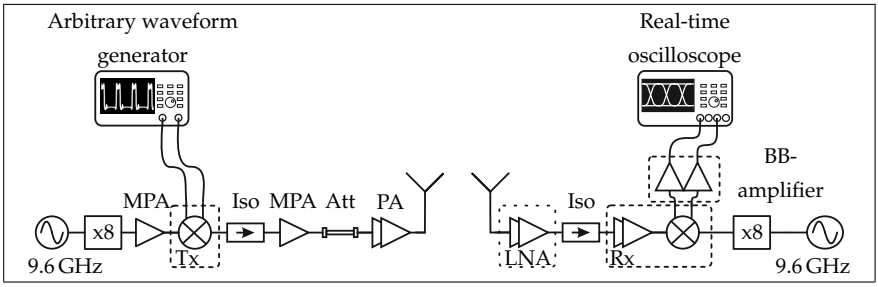

Figure 4.3: Measurement setup for the E-band long range transmission experiments. To provide sufficient transmit power, a medium power as well as a power amplifier is used, to boost the Tx's output signal. If needed, an additional LNA can be used in front of the E-band receiver. Cassegrain antennas at the Tx and Rx provide an antenna gain of 45.7 dBi each.

onto adjustable tripods. A schematic of the extended measurement setup is shown in figures 4.3.

On the transmitter side, the setup is modified as follows: To achieve an as high as possible transmit power, an amplifier chain to boost the Tx's output signal is used. An MPA, providing a gain of 10 dB in combination with a saturated output power of 15 dBm [Tes14], builds the first stage of this amplifier chain. Due to insufficient impedance matching between the amplifiers' and mixer's in- and output ports, a waveguide isolator (Iso) is used between the Tx and the MPA to prevent signal distortion. To further increase the transmit power, an additional power amplifier (PA) with a saturated output power of 22 dBm [23] is used. Also the insufficient impedance matching at the interface between MPA and PA results in a distorted signal. A 3-dB attenuator (Att) is used between the MPA and PA to improve the transmission performance. These modifications result in an output power delivered to the Tx antenna of approximately 16 dBm. Simultaneously a linear operation of the PA is ensured.

At the receiver side, additionally to the LNA integrated with the down-converter inside the Rx module, an LNA waveguide module, providing

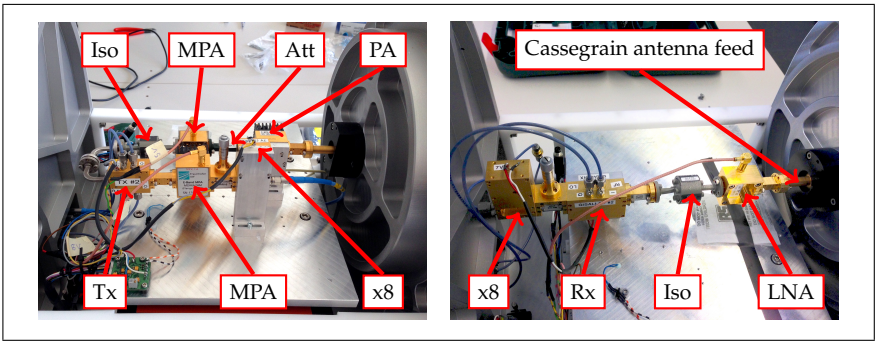

Figure 4.4: Photographs of the Tx (left) and Rx (right) housings as used for the E-band long range transmission experiments. In both, the frequency multiplying and mixing stages as well as the additional amplifiers can be seen.

a small signal gain of approximately 22 dB combined with a noise figure below 2.5 dB over the desired bandwidth [Tes14], is available. This LNA module can be used in front of the Rx module if needed. Also at the interface between LNA and Rx module signal distortions, resulting in a ripple in the received signal, occur. An additional isolator between both modules reduces this effect.

Due to the frequency response of the additional amplifiers in the Tx and Rx as well as the waveguide components and baseband cables necessary to mount the system into the housing, the initial system performance as shown in chapter 3.2 is not maintained. The system bandwidth is reduced, leading to a maximum achievable symbol rate of 7 GBd as determined in a measurement of the entire system in a back-to-back setup.

In the photograph in figure 4.4, all frontend components as introduced in the schematic in figure 4.3, are shown, mounted into the Tx and Rx housings. The Cassegrain antennas are integrated into this housings. In the photographs only their backsides with the antenna feed can be seen. The following results have been partially published in [34].

Table 4.1: Link budget parameter for the E-band system.

B (GHz)	$P_{t,\,avg}$ (dBm)	G_{Tx} (dBi)	L_{atm} (dB)	$L_{rain,1/2}$ (dB)	$L_{fog,1/2}$ (dB)	G_{Rx} (dBi)	NF_{Rx} (dB)
7	16	45.7	0.41	2.2 / 18.7	0.17 / 1.7	45.7	2.5

4.2.1 Link budget considerations

To determine the maximum transmission distance for the planned E-band link with a symbol rate of 7 GBd, the link budget parameters given in table 4.1 are used. The Tx's transmit power $P_{t,\,avg}$ and the Rx's conversion gain $CG_{Rx,\,avg}$ are averaged over the used signal bandwidth. The atmospheric attenuation L_{atm} is calculated at a relative humidity of 53 %, a temperature of 20 °C and an atmospheric pressure of 1013 hPa. For the calculation of the rain attenuation, two different scenarios are considered. $L_{rain,1}$ describes the additional attenuation for a very common medium rain shower with a rain rate of 2.5 mm/h[7], $L_{rain,2}$ represents a heavy thunderstorm with a rain rate of 50 mm/h[8], a very rare and localized event. For the attenuation due to fog, also two different scenarios are considered. While $L_{fog,1}$ describes a fog with a 300 m visibility, $L_{fog,2}$ represents a thick fog with a visibility of only 50 m. The temperature for both is set to 5 °C, a temperature where in combination with a high humidity such dense fogs occur [ALM+08]. All attenuations are calculated for the carrier frequency of 77 GHz.
Using these parameters together with equation (4.3), the acceptable path loss for a fixed SNR for the demodulation can be calculated. A target SNR of minimum 15 dB is chosen, a value for which the resulting BER of

[7] http://www.deutscher-wetterdienst.de/lexikon/?ID=N&DAT=Niederschlagsintensita et, last accessed 10-26-2014.

[8] http://www.dwd.de/sid_FNYhS1VTT9N4tn4pXP5pf4L0lYj9gR4WD1SfL4XQMhtc ZTDTBd2S!873310975!197315392!1392481779510/bvbw/appmanager/bvbw/dwdwwwDesk top?_nfpb=true&_pageLabel=dwdwww_result_page&portletMasterPortlet_i1gsbDocume ntPath=Navigation%2FKatastrophenschutz%2FWarnmanagment%2FDauerregen__node.ht ml%3F__nnn%3Dtrue, last accessed 10-26-2014.

BPSK, QPSK and 16-QAM modulated signals will be well below 1×10^{-3} when operating with an AWGN-limited link, as already discussed in the previous chapter. With an RF bandwidth of 14 GHz for a 7 GBd signal and a total receiver noise figure of approximately 2.5 dB, a noise power of −70 dBm is calculated. To achieve the intended SNR of 15 dB, a minimum received signal power of −55 dBm has to be achieved.
Resulting from this, the maximum tolerable path loss is 162 dB, which together with a clear atmospheric attenuation of 0.41 dB/km results in a maximum transmission distance of approximately 17.5 km. Taking the two different rain events of 2.5 and 50 mm/h into account, the maximum achievable distances reduce to 6.2 and 1.5 km, respectively. For foggy weather, the achievable distances are 14.8 km for the 300 m visibility and 7.1 km for the 50 m visibility.
Considering the wireless backhaul applications discussed in chapter 1, the presented link budget calculations show that the transmission distances of 1 to 5 km necessary in urban and suburban areas can be covered by the proposed E-band link even under heavy weather conditions. During fair weather, transmission distances of more than 17 km can be achieved. Following [AH13], such distances are required for wireless backhauling in rural areas. Furthermore as discussed above, one has to take the local rain probabilities and rates into account to determine the atmospheric influences on a specific link. Depending on the rain drop distribution, the resulting attenuation values can vary. For the link calculations above, an equal distribution and constant rain rate over the entire transmission distance is assumed. In reality, the rain rate varies significantly inside a rain cell and the extent of the rain cell reduces with increasing rain rate. Especially heavy rain events with rain rates above 20 mm/h are very localized, the rain cell size ranges in the order of 3 kilometer and only last for a few minutes [Cra80]. Thus, the presented transmission distances represent worst case scenarios.

4.2.2 Long range data transmission

The link budget considerations above suggest that a transmission experiment over several kilometers will be feasible even with an additional loss due to medium rain showers. To verify this, a system measurement in a scenario allowing for such high transmission distances, preferably in an elevated position, is necessary. Such a location is found in the Aalen communication tower[9] in Aalen, Germany. On this tower, the E-band transmitter system is placed at a height of 75 m for two different transmission experiments. For the first experiment, access to the rooftop of a factory building near the city of Aalen is gained. Here, the receiver system is set up in a height of 7 m. The line of sight distance between Tx and Rx is determined to be 4.1 km. For the second experiment, a significantly increased transmission distance is targeted. Therefore, a second communication tower in the surrounding of Aalen is located. On this tower, the receiver is placed on a platform with a height of 25 m above ground. The line of sight distance between the two towers is determined to be 15.7 km, close to the maximum distance determined by the link budget analysis. All distances are verified via an online tool[10]. These two revealed distances fit very well to the transmission scenarios addressed by wireless backhauling as discussed in chapter 1 and thereby allow the investigation of the E-band system in a realistic environment.

4.2.2.1 Data transmission over 4.1 km

In figure 4.5 a map and photographs of the 4.1 km experiment's locations can be seen. The top right photo shows a view from the transmitter on top of the communication tower towards the receiver. To shelter the

[9] The Aalen communication tower, or Sender Aalen in german, is a radio and television communication tower, operated by the Südwestrundfunk (Southwest Broadcasting, SWR), a regional public broadcasting corporation serving the southwest of Germany. The tower with a total height of 139 m is located at 722 m above NN, near the Braunenberg, a hill near Aalen. Further information can be found via http://de.wikipedia.org/wiki/Sender_Aalen, last accessed 10-26-2014

[10] To determine the distances between the Tx and Rx location, an online tool accessible at http://geo.ebp.ch/gelaendeprofil/, last accessed 10-26-2014, is used.

necessary measurement equipment, i.e. DC-supplies, the AWG and the frequency synthesizer, a waterproof and temperature stabilized housing was designed. In this, the measurement equipment can be operated on top of the communication tower independently from weather conditions. Besides, the housings allow for a remote connection to all instruments, enabling to conduct the measurements from within a control room at the foot of the communication tower. In the bottom left photo of figure 4.5, a view from the receiver on top of the factory building towards the transmitter is shown. The communication tower, located on top of the ridge in the background, can be seen blurry through the clouds. The silo in the foreground does not influence the transmission. The maximum radius of the first Fresnel zone for a transmission distance of 4.1 km can be calculated using equation (4.5) to approximately 2 m. The silo located is approximately 50 m in front of the receiver, where the radius of the first Fresnel zone below its maximum radius, and more than 10 m apart from the transmission path.
To align the wireless link, in a first step an alignment using a spotting scope is performed. Due to the high distance in combination with the limited optical magnification of the spotting scope, with this approach the transmitter can only coarsely be aligned to the receiver, i.e. it can be assured, that the transmitter points towards the building on which the receiver is located and vice versa. For a refined alignment, a single sine tone is transmitted and observed in a spectral measurement. The link is than adjusted for a maximum receive power.
During the measurements, the temperature at the transmitter side varied between 16 and 25 °C and the relative humidity between 62 and 32 %. Translated into an atmospheric attenuation value, these parameters result in an additional attenuation between 1.6 and 1.4 dB over the transmission distance, which is visibly in the order of the measurement accuracy. The link budget parameters for this experiment are summarized in table 4.2. An estimation of the link budget using equation 4.3 results in an expected power of −36.6 dBm at the receiver's antenna port which, as shown in chapter 3.2.3, is close to the optimum input power for the receiver. Thus, the additional LNA, shown in the schematic in figure 4.3, will not used

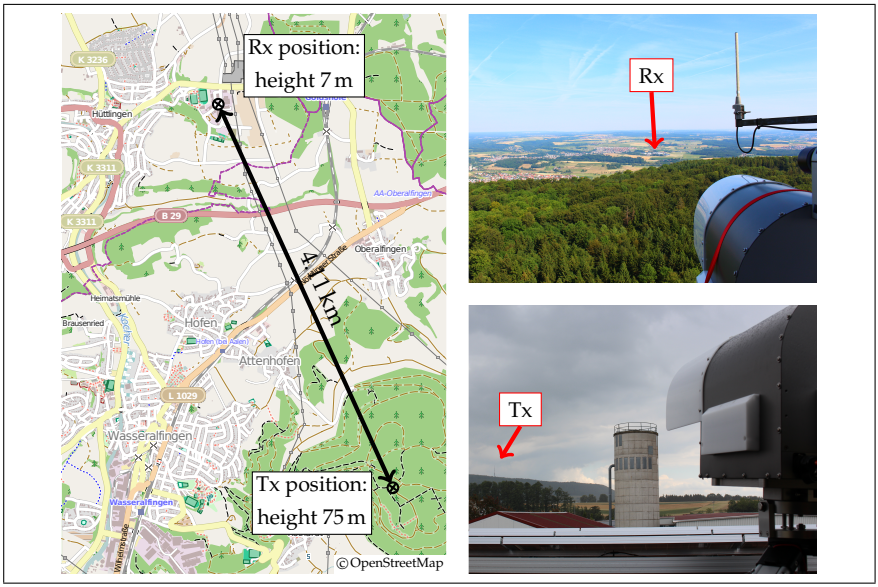

Figure 4.5: Map and photograph of the 4.1 km transmission experiment using the E-band system, setup between the communication tower at a height of 75 m, and a factory rooftop with a height of 7 m.

during this experiment and the Rx module is directly connected to the receive antenna. This results in an overall receiver noise figure NF_{Rx} of 3.5 dB, as discussed in chapter 3.2.2 for the back-to-back measurements. By taking into account the Rx's conversion gain as well as the baseband amplifier's gain, a power of approximately −6.1 dBm is expected be received at the oscilloscope.

The measured signal power is −8.3 dBm for a QPSK modulated 7 GBd signal, indicating an additional loss of 2.2 dB compared to the calculated link budget. This additional loss can be explained by cable losses in the measurement setup which is uncalibrated, as well as a slight misalignment of the wireless link. Together with an RF bandwidth of 14 GHz, needed

Table 4.2: Link budget parameters for the E-band transmission experiment over a distance of 4.1 km.

$P_{t,\,avg}$ (dBm)	G_{Tx} (dBi)	L_{FSPL} (dB)	L_{atm} (dB)	G_{Rx} (dBi)	NF_{Rx} (dB)
16	45.7	142.4	1.4 - 1.6	45.7	3.5

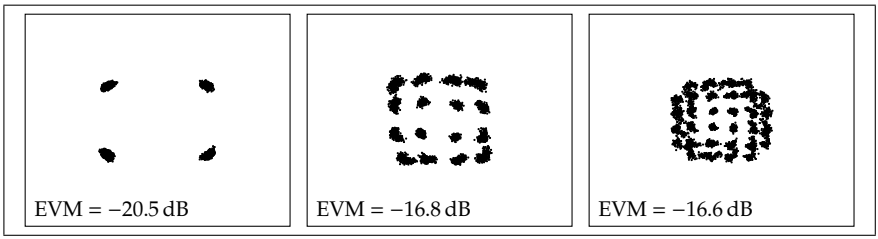

Figure 4.6: Constellation diagrams and resulting error vector magnitudes for the wireless transmission of QPSK, 16-QAM and 32-QAM modulated data signals at a symbol rate of 3 GBd over a distance of 4.1 km.

for the maximum symbol rate of 7 GBd, an SNR of approximately 30.2 dB can be calculated for this experiment by using equation 3.21.
To evaluate the wireless link's capability, both the performance of different modulation schemes as well as the maximum achievable data rate are considered. Thus, in the first experiment, signals with a symbol rate of 3 GBd, allowing the use of QAM modulation up to 32-QAM in this specific setup, is evaluated to investigate how the different modulation schemes are influenced by the transmission. To determine the maximum achievable data rate, in the second experiment the maximum symbol rate of 7 GBd is used. Also here, different modulation schemes are compared to each other. But at this symbol rate, the system is only capable of transmitting QAM modulated signals up to 16-QAM.
The measurement results in form of constellation diagrams and EVM together with the use of feed-forward equalization for the symbol rate of 3 GBd are shown in figures 4.6 The evaluation shows an EVM of −20.5 dB

and very distinct constellation points for the QPSK modulated signal. For the 16-QAM and 32-QAM signals, the signal quality decreases, resulting in a raised EVM of −16.8 and −16.6 dB, respectively. This, on the one hand, is caused by the deteriorated frequency response of the wireless frontend due to the additional amplification stages explained above, showing a more severe influence of the more demanding 16- and 32-QAM modulation scheme. On the other hand, also the performance in terms of signal quality and output power of the used AWG decreases when generating higher order modulations, as already mentioned in chapter 3.2. This will result in an already worse input signal delivered to the system's transmitter compared to QPSK modulated signals. Furthermore, in the constellation of the 16-QAM signal, a slight influence of phase deviation can be identified due to the arched-shaped outer constellation points. Nevertheless, the constellation points of this signal are mostly well separated. On the contrary, for the 32-QAM modulated signal, although the constellation points are still small, many of the outer and middle points can not be clearly separated any more, indicating severe signal distortions. To determine the maximum data rate which can be transmitted across this distance, the symbol rate is set to the above discussed 7 GBd. The measurement results in figure 4.7 reveal that a transmission of QPSK modulated signals, resulting in a data rate of 14 Gbit/s, is possible with high signal quality, i.e. an EVM of −17.5 dB. To further increase the data rate, higher order modulation formats are used, resulting in a EVMs of −15.7 and −14.5 dB for the 8-QAM and 16-QAM modulated signals, resulting in data rates of 21 and 28 Gbit/s, respectively. While for 8-QAM, the constellation points are still mostly separated, the signal disturbances for the 16-QAM signal are more severe.
When comparing the two transmission experiments against each other, an SNR decrease of approximately 3.7 dB is expected. This is caused by the increases bandwidth necessary to transmit the higher symbol rate, resulting in an increased noise power. The EVM increase of 3 dB for the QPSK and 2.3 dB for the 16-QAM modulation reveal that the system is still operating in the region of optimum receive power, i.e. the link performance is mainly affected by the frontend non-idealities and the influences

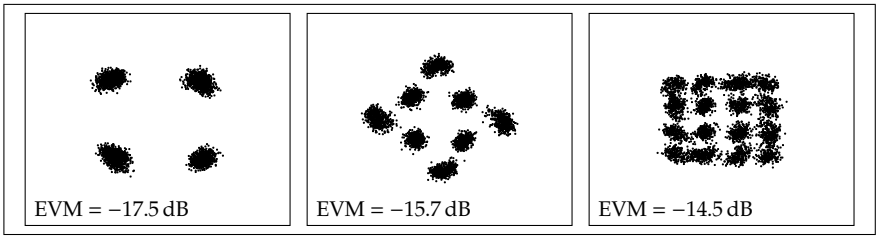

Figure 4.7: Measurement results for the wireless transmission of QPSK, 8-QAM and 16-QAM modulated data signals at a symbol rate of 7 GBd over a distance of 4.1 km.

of the baseband equipment.

As for the back-to-back measurements in chapter 3, also an evaluation of the resulting BER is possible for the signals measured here. When considering the signals with a symbol rate of 3 GBd, for the QPSK modulation, no error occurred in the evaluated bit stream. Thus, the resulting BER is better than 1.1×10^{-7}. For the 16- and 32-QAM modulated signals, which already revealed distortions in the constellation diagrams, the resulting BERs are 3.2×10^{-3} and 2.7×10^{-2}, respectively.
The evaluation of the signals with a symbol rate of 7 GBd reveals that for the QPSK modulation also at this symbol rate, no bit error occurred in the captured data stream. Thus, the resulting BER is better than 4.8×10^{-8}. For the 8-QAM and 16-QAM modulation schemes, the BER increases to 6.3×10^{-4} and 1.8×10^{-2}, respectively.

4.2.2.2 Data transmission over 15.7 km

With the transmission over a distance of 4.1 km successfully demonstrated, now the receiver location is moved to the second communication tower at a distance of 15.7 km. The increased transmission distance by a factor of approximately 3.8, will result in a decreased SNR of approximately 18.6 dB. As for the 4.1 km experiment, also here the system will be evaluated in terms of influence on different modulation formats and

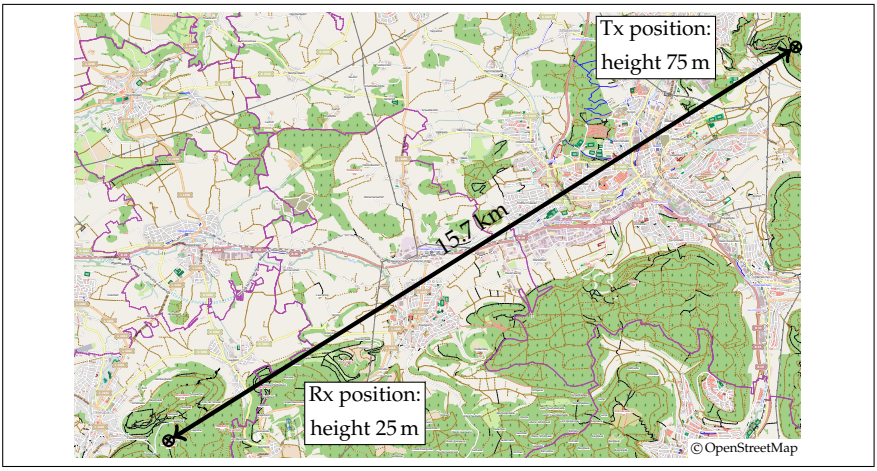

Figure 4.8: Map of the 15.7 km E-band transmission experiment between the two communication towers.

maximum achievable data rate. Due to the reduced SNR, the system performance is expected to decrease significantly.
A map of the experiment environment is shown in figure 4.8. A calculation of the first Fresnel zone reveals a radius of 3.9 m. With the same online tool as used for the 4.1 km experiment, it can be justified that the Tx and Rx location, both located at 730 m above mean sea level, are at least 54 m higher than the hills along the transmission path, without the height of the used tower platforms taken into account. The transmitter and receiver of the wireless system are aligned in the same way as done for the 4.1 km experiment. The coarse alignment is more difficult due to the much higher distance. Nevertheless, after adjusting the system in a way that Tx and Rx face each other, the refined alignment is possible by optimizing to a maximum receive power.
To get an impression of the experiment's setup and surrounding, according photographs are shown in figure 4.9. In the left photograph, the Tx mounted on its tripod is shown on the Aalen communication tower. The

Figure 4.9: Photographs of the 15.7 km transmission experiment with the setup of the transmitter system shown on the left. The photographs on the right show the view from the receiver towards the transmitter site under clear and adverse weather conditions. The Tx's communication tower can be faintly seen in the hills in the background.

five green coax cables provide the LO signal as well as the four I/Q-signals for the balanced upconversion, i.e. the balancing is done with the AWG directly. On the right corner of this photo, the above mentioned water-proof housing containing the measurement equipment can be seen. The photo on the top right shows a scene as seen from the receiver towards the transmitter at clear weather conditions, with the Tx's communication tower faintly in the hills in the background. The right bottom photo shows the same view during adverse weather conditions as will be discussed in the following sections. During the first experiment at this distance, the weather was cloudy with a temperature of 17 °C and a relative humidity of 83 % at the transmitter site and a 16 °C in combination with 65 % relative

Table 4.3: Link budget parameters for the E-band transmission experiment over a distance of 15.7 km.

$P_{t,\,avg}$ (dBm)	G_{Tx} (dBi)	L_{FSPL} (dB)	L_{atm} (dB)	G_{Rx} (dBi)	NF_{Rx} (dB)
16	45.7	154	7.5	45.7	2.5

humidity at the receiver site[11]. These values translate into an additional atmospheric attenuation of 0.56 dB/km at the Tx and 0.4 dB/km at the Rx. Since no further information about the atmospheric conditions along the transmission path can be obtained, the total atmospheric attenuation for the distance of 15.7 km is calculated as an average of these two values to a total of 7.5 dB.

Considering the expected link budget, the free-space path loss, calculated using equation (4.3), is 154 dB. To compensate for the increased path loss, the additional LNA is used in this experiment. Due to this LNA's gain of 22 dB in combination with a noise figure below 2.5 dB, the overall receiver noise figure NF_{Rx} decreases to approximately 2.5 dB. Together with the other link budget parameters as given in table 4.3, the expected power at the Rx input is approximately −54 dBm. In combination with the amplification of the additional LNA, the conversion gain of the receiver frontend of approximately 8.5 dB, and the baseband amplifier's gain of 22 dB, the measured baseband power at the oscilloscope is estimated to −1.6 dBm. Although, due to the additional LNA, the Rx will be operated in the region of optimum input power, the link performance significantly decreases compared to the 4.1 km transmission due to lower SNR.

A measurement of the maximum achievable symbol rate for QPSK modulated signals, reveal a limit of 6 GBd. The measured receive power for this signal is −3.8 dBm. Using equation (3.21) results in an SNR of approxi-

[11] The data from weather stations in proximity to the Tx and Rx are available online at http://www.meteo-europ.com/de/de/baden-wurttemberg/aalen-almanach.html, last accessed 10-26-2014, and http://www.meteo-europ.com/de/de/baden-wurttemberg/heubach-almanach.html, last accessed 10-26-2014, for the 11th July, 2014, the date of the measurement.

mately 14.5 dB. The deviation between calculated and measured received power of −2.2 dB is identical to the deviation observed for the 4.1 km experiment. Since the baseband components of both setups are identical, the approximation which is made above for the distribution of atmospheric loss factors along the transmission is valid. Also, the alignment quality of the wireless link is comparably accurate as for the measurements over the distance of 4.1 km.
Considering the determined receive power of −54 dBm and relating it to the receiver sensitivity measurement shown in chapter 3.2.3, it is noteworthy that the system will be operating in the SNR-limited regime, i.e. the dominating signal distortion is caused by AWGN.

As mentioned above, the system will be evaluated in terms of its influence on different modulation formats as well as the maximum achievable data rate. An evaluation of the transmission quality using the constellation diagram representation and the corresponding error vector magnitude shows a significant decrease compared to the 4.1 km experiment, as expected from the SNR considerations discussed above. For the transmission considered here, QAM modulations up to 16-QAM are feasible up to a symbol rate of 2 GBd. Thus, the results for QPSK, 8-QAM and 16-QAM modulated signals at this symbol rate are shown in figure 4.10. The corresponding EVM values are −16.8, −14.7 and −14.4 dB. All signals clearly show disturbances due to AWGN, expressed as symmetrical distribution of the measurement points around the ideal location. Additionally, the 16-QAM signal shows a deformation on one side of the constellation diagram, possibly caused by interstage matching effects between the different frontend modules. While for the QPSK and 8-QAM signal the constellation points are still separated, additional to the deformation, the 16-QAM signal is already heavily distorted. This indicates that for the transmission with this modulation format, many symbol errors will occur.
An evaluation of the BER performance for the QPSK modulated signal shows no error in the recorded data stream, revealing a BER of better than 1.7×10^{-7} for this 4 Gbit/s signal. For the 8-QAM modulated signal, resulting in a data rate of 6 Gbit/s, the BER determined to 7.9×10^{-5}. Finally,

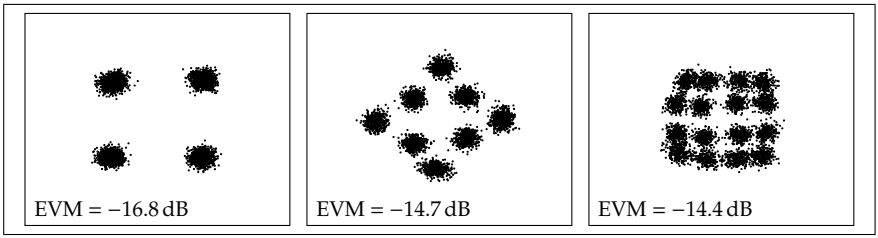

Figure 4.10: Constellation diagrams and corresponding EVMs for the transmission of QPSK, 8-QAM and 16-QAM modulated data signal at a symbol rate of 2 GBd over a distance of 15.7 km.

for the 16-QAM modulation with a data rate of 8 Gbit/s, the resulting BER increases significantly to 1.3×10^{-2}, as already suggested by the heavy distortions visible in the constellations diagram.

To determine the maximum achievable data rate, the transmitted symbol rate needs to be maximized. Limited by the VSA software's capability to detect heavily distorted signals, for QPSK and 8-QAM modulations, signals up to a symbol rate of 6 and 5 GBd can be measured, respectively. The resulting constellation diagrams are shown in figure 4.11. Both the QPSK and 8-QAM signals show an even more severe influence due to AWGN than the corresponding 2 GBd signals. The increase in noise due to the extended bandwidth should directly translate to the measured EVM. For the QPSK modulation, the bandwidth increase should result in an increase in EVM of approximately 4.8 dB. For the 8-QAM signal the degradation should be approximately 3.9 dB. As can be seen from the measurements, for both signals, the increase in EVM is slightly higher than the theoretical value. This indicates that additionally to the SNR decrease, the signal is also affected by the frontend's performance. Nevertheless, the performance decrease by at least the value added due to additional noise proves, that the system operates in the SNR-limited regime as assumed above.
As for the former measurements, also here the BER performance of the

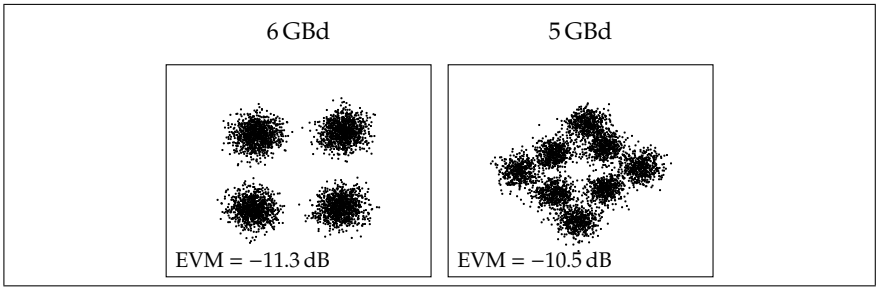

Figure 4.11: Measurement results for the highest achievable symbol rates for the wireless transmission over a distance of 15.7 km using QPSK and 8-QAM modulation.

system is evaluated. The QPSK signal, resulting in a data rate of 12 Gbit/s, shows a BER of 1.2×10^{-4}. For the 8-QAM signal, a BER of 4.8×10^{-3} is determined. Although the error rate for the latter signal is high, the FEC approach discussed in chapter 3.2 will be able to correct the received signal to a BER better than 1×10^{-6}.

In an additional measurement, the wireless link's behavior is tested under the influence of slight rain and heavy fog and clouds. Due to the high transmission distance, an exact determination of the weather conditions is difficult. According to the local weather reports for the experiment date[12], the rain density was 0.5 mm/h. In online archives, a rain rate of 1 mm/h is reported for the receiver site, while 0 mm/h is reported for the transmitter site. Thus, an average rain rate of 0.5 mm/h will be assumed. This rain rate results in an additional attenuation of 0.69 dB/km, which sums up to a total attenuation of 10.8 dB for the entire transmission distance. During the measurements for different rain events, which lasted between 40 and 60 minutes, the rain density visibly varied and the rain cell moved from

[12]The experiments described here are conducted on 10th July, 2014. The weather information can be found online at http://www.meteo-info.be/de/europa/deutschland/wetter-aalen-stadtwerke/details/S107481/, last accessed 10-26-2014, and are partially available in the online archive accessible via the links provided for the 4.1 km experiment.

the receiver side towards the transmitter. The measured temperature at the transmitter during the experiments was around 13 °C.
To determine the influence of the rain, the received baseband signal power $P_{r,BB}$ is measured for a 1 GBd QPSK signal each time the weather changed. During the experiment, the next rain cell reached the receiver before the last measurement was done, causing two different rain events moving along the transmission path. Compared to the −1.8 dBm achieved for clear weather conditions, the power is now reduced to the values given in table 4.4.
As can be seen, the received power varies with the changing weather conditions between values of −7.2 and −3.7 dBm, which results in additional attenuations due to rain of 5.4 and 1.9 dB. The resulting EVM value for each measurement is provided in row three. As can be seen, a change in received power does not always correspond to a change in EVM. This can be explained by the feed-forward equalization resulting in slightly different results for each measurement, and by the uncertainty due to variances in the EVM measurement itself. Assuming a constant rain rate and taking into account the attenuation constant for a 0.5 mm/h rain of 0.69 dB/km as calculated above, the measured attenuations can be translated into the rain cell length (RCL) along the transmission path, which is provided in the forth row of table 4.4.
In a second experiment, the rain influence on the transmission of QPSK signals with different symbol rates is investigated. The additional attenuation due to rain result in a maximum achievable symbol rate of 5 GBd. To determine the influence of the rain event in relation to the used bandwidth, symbol rates of 3, 4 and 5 GBd will be evaluated and compared to measurements performed without rain.
As shown in figure 4.12, for the symbol rates of 3 and 4 GBd, the EVM measured during rain increases in the order of 4 dB compared to the measurements without rain. This corresponds to the measured receive powers, which are similar for both symbol rates. When considering the 5 GBd signal, the EVM increases by 4.7 dB, but also the received power decreased by approximately 0.7 dB compared to the measurements without rain. This indicates, that the rain distribution in the transmission path

Table 4.4: Measured receive power for a 1 GBd QPSK signal under the influence of rain.

t (min)	T_0	T_0 + 8	T_0 + 11	T_0 + 15	T_0 + 19	T_0 + 22	T_0 + 34	T_0 + 39	T_0 + 49
$P_{r,BB}$ (dBm)	−6.7	−7.2	−5.3	−5.0	−3.7	−3.9	−4.5	−4.3	−6.1
EVM (dB)	−15.6	−15.0	−16.8	−16.8	−17.5	−17.4	−17.0	−17.2	−15.7
RCL (km)	7.1	7.8	5.0	4.6	2.8	3.0	3.9	3.6	6.2

have changed when the measurement for the 5 GBd signal is performed. Nevertheless, although heavily distorted, even the 5 GBd signal, resulting in a data rate of 10 Gbit/s, can be demodulated and shows an EVM of −8.6 dB. The comparison of transmitted and received bits results in a BER of 4.6×10^{-3}, which can by corrected with an appropriate FEC to a value better than 1×10^{-12} [COM10].

As a result from the long range transmission experiments in the E-band, it is shown that data rates up to 14 Gbit/s, resulting from a QPSK modulated signal at a symbol rate of 7 GBd, can be transmitted over a distance of 4.1 km under clear weather conditions with a BER better than 4.8×10^{-8}. The highest data rate at this distance, with an error performance still correctable with an appropriate FEC, is 21 Gbit/s with a BER of 6.3×10^{-4}. As suggested by the link budget calculation in section 4.2.1, the transmission distance can be increased to 15.7 km, the distance between the two communication towers. In this experiment, data rates up to 15 Gbit/s can be achieved even in foggy weather, by using a 5 GBd 8-QAM modulated signal. A BER evaluation for this transmission results in 4.8×10^{-3}, which is sufficiently low to be corrected by an appropriate FEC
Furthermore, the measurements of different modulation formats and symbol rates during rain events prove that adaptive modulation, i.e. a change of modulation format and symbol rate, is a feasible approach to overcome adverse weather conditions. A data transmission using a 10 Gbit/s QPSK modulated signal during a rain event reveals a BER of 4.6×10^{-3}. Also

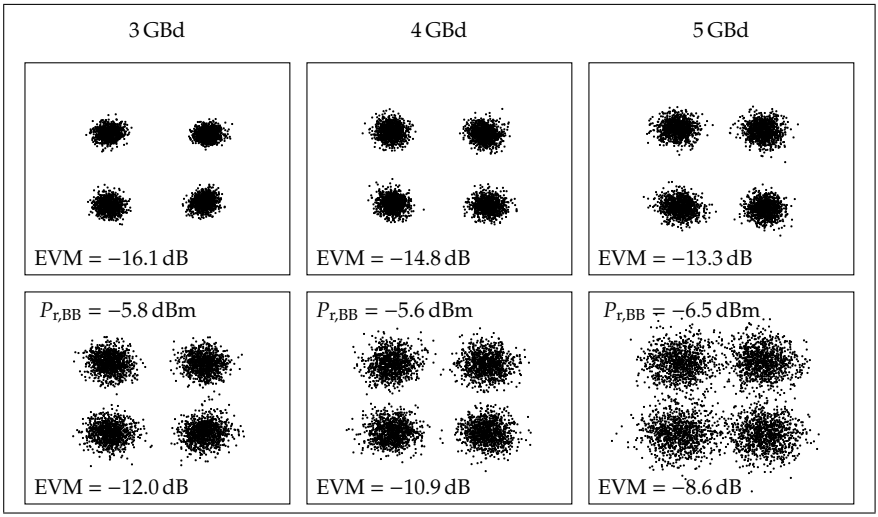

Figure 4.12: Influence of rain on the signal quality of a QPSK modulated signal in the 15.7 km transmission experiment. In the top row, the results without rain, in the bottom row, the results with rain are shown.

this signal can be corrected using an appropriate FEC.
This was the first time such a high transmission distance was bridged with a multi-gigabit system operating at such high carrier frequencies.

4.3 Wireless transmission using the 240 GHz frontend

To test the feasibility of wireless communication links at 240 GHz, the frontend components described in chapter 2.2 and characterized in chapter 3.3, are used to perform transmission experiments over different distances. Indoor measurements, transforming the back-to-back measurements from chapter 3.3 into wireless transmissions, provide an insight into influences introduced by the free space interface, wave propagation and link mis-

alignment in a still controllable environment. Outdoor measurements performed over a high transmission distances, provide real world conditions and reveal the influences of atmospheric effects on the transmission quality. The following results have partially been published in [21] and [35].

4.3.1 Indoor measurements

For the indoor experiments, the back-to-back setup shown in figure 3.8 is modified to realize a wireless data transmission link. Instead of the waveguide attenuator, now WR-3 horn antennas with attached lenses are used at the RF-ports of the transmitter and receiver modules. The distance between Tx and Rx is 40 m, the length of the corridor where the measurements are performed. To ensure proper link alignment, the frontend modules together with the antenna-lense combinations are mounted onto three-way adjustable tripods. The link is aligned by transmitting a narrowband signal and adjusting the link from a maximum received power with the help of a spectral measurement. To ensure linear behavior and prevent saturation of the Rx's LNA stage, an approximately 5 dB waveguide attenuator is used between the receiving antenna and the Rx module to limit the RF input power. Apart from that, the setup is identical to the one described in chapter 3.3.1. To get an impression of the setup, figure 4.13 shows a photograph of the receiver module with the attached waveguide attenuator and the antenna-lense combination mounted onto an adjustable tripod with the baseband amplifiers and the real-time oscilloscope in the background.
The calculation of a link budget for this transmission experiment is difficult, since the exact gain of the horn antennas in combination with the lenses is not known. The transmit power $P_{\mathrm{t,\,avg}}$ and Rx conversion gain $CG_{\mathrm{Rx,\,avg}}$ are extracted from module measurements and averaged over the used signal bandwidth. The atmospheric losses L_{atm} are calculated at a relative humidity of 46 % at room temperature to be around 0.1 dB for the transmission distance. This is visibly below the measurement accuracy and will therefore be neglected. The path loss L_{FSPL} over a distance of

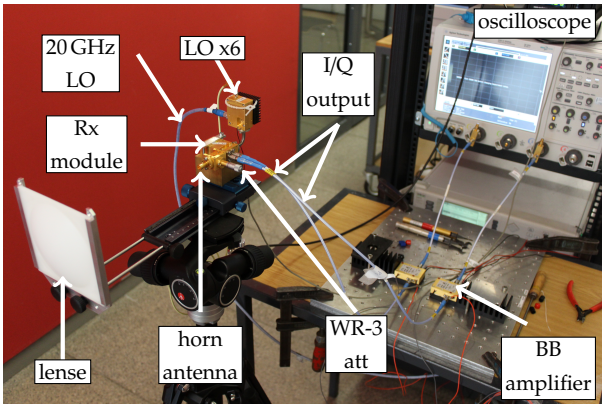

Figure 4.13: Photograph of the 240 GHz Rx during the 40 m indoor transmission experiment with the setup components labeled.

40 m is 112 dB. With a received power of −11 dBm of the baseband signal, the gain of the baseband amplifier, the Rx's conversion gain and by taking into account the additional 5 dB attenuation from the measurement setup, a gain for the antenna-lense combinations of approximately 42.3 dBi each can be estimated. With the Rx module's and baseband amplifier's noise figures of 11 and 5 dB, the noise figure of the complete receiver NF_{Rx} can be calculated to approximately 12.3 dB, whereas the influence of the oscilloscope is negligibly small. For the experiment, QPSK and 8-PSK modulated data signals with symbol rates of 5 and 10 GBd are transmitted, whereat the maximum symbol rate is limited by the AWG's maximum sample rate of 10 GS/s. Combining all link budget parameters, as summarized in table 4.5, SNR values of 24.9 and 21.9 dB can be calculated for the 5 and 10 GBd signals.
The constellation diagrams for the QPSK and 8-PSK transmission are plotted in figures 4.14 and 4.15 with the EVM values extracted from the constellation diagrams. The QPSK transmission shows an EVM of −20.5 and −19.1 dB for the 5 and 10 GBd transmission, respectively. For the 8-PSK transmission, the resulting EVMs are −16.8 and −16.3 dB. The results

Table 4.5: Link budget parameters for the 240 GHz 40 m wireless transmission experiment.

$P_{t,\,avg}$ (dBm)	G_{Tx} (dBi)	L_{FSPL} (dB)	L_{atm} (dB)	G_{Rx} (dBi)	CG_{Rx} (dB)	G_{BB} (dB)	NF_{Rx} (dB)
-4.5	42	112	0.1	42	1.8	24	12.3

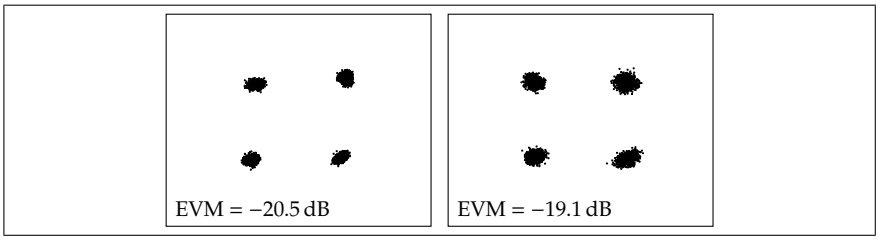

Figure 4.14: Constellation diagram and resulting error vector magnitude for the wireless data transmission of 5 (left) and 10 GBd (right) QPSK modulated signals over a distance of 40 m.

for the 10 GBd 8-PSK signal show that some of the constellation points smear into each other indicating a heavy signal distortion due to phase noise. Compared to the back-to-back measurement in 3.3.4, the signal quality of the wireless transmission varies around ±1 dB, which indicates that the link still does not operate in the SNR-limited range and that the optimum receiver input power depends on the modulation bandwidth. While the input power is reduced by approximately 4 dB compared to the back-to-back measurement, in an SNR-limited setup, one would also expect a decrease in signal quality by 4 dB. Furthermore, this decrease should be independent of the modulation format. Instead, compared to the back-to-back measurements, the signal quality increases for the 10 GBd QPSK and 8-PSK signal, while it decreases for the 5 GBd QPSK signal. This indicates, that the optimum receive power varies for different modulation schemes and modulation bandwidths. A similar behavior was observed in the receiver sensitivity measurement in chapter 3.2.3 for

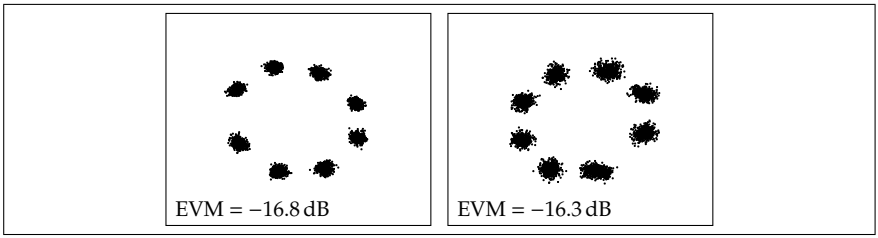

Figure 4.15: Constellation diagram and resulting error vector magnitude for the wireless data transmission of 5 (left) and 10 GBd (right) 8-PSK modulated signal over a distance of 40 m.

the 77 GHz link where the error floor was dependent on the modulation bandwidth and modulation format.
Nevertheless, the constellation points for all signals are well separated. To further evaluate the system's performance, the same BER evaluation approach as for the E-band system is used. For both the 5 and 10 GBd QPSK modulated signals, resulting in data rates of 10 and 20 Gbit/s, no error occurred in the captured bit stream. Thus, the resulting BERs are better than 1.3×10^{-6} and 6.4×10^{-7}, respectively. The 8-PSK modulated signal with a symbol rate of 5 GBd, i.e. with a data rate of 15 Gbit/s, shows a BER of 1.8×10^{-5}. The maximum data rate in this transmission experiment is achieved with the 8-PSK modulated signal with a symbol rate of 10 GBd. This is corresponding to a data rate of 30 Gbit/s. An evaluation of this signal's BER results in a value of 3.5×10^{-4}.
Taking further the additional attenuation of 5 dB introduced by the WR-3 attenuator in front of the receiver into account, the maximum achievable transmission distance can be obtained by using equation (4.3) and converting the additional attenuation into an acceptable path loss. Thus, the shown indoor link setup is capable of transmitting the data rate of 30 Gbit/s over distances of approximately 70 m with the same performance.

4.3.2 Long range demonstration

To prove the feasibility of a multi-gigabit wireless link at 240 GHz apart from laboratory setups and for high distances similar as for the E-band system, a data transmission over several 100 m for demonstration purposes shall be realized. Therefore, the frontend components are integrated into a temperature-stabilized and waterproof housing with an integrated Cassegrain antenna system[13] providing a simulated antenna gain of 55.1 dBi. To achieve a high transmission distance without any obstacles within the first Fresnel zone, the experiment is set up on the rooftop of two of the highest buildings on the Vaihingen campus of Stuttgart of University, Germany. The transmitter is located on top of a university tower with a height of approximately 45 m, the receiver site is located on the rooftop of the IMS[14] building with a height of approximately 15 m. The resulting distance between the two sides is approximately 0.85 km. By following equation (4.5), the resulting radius of the first Fresnel zone for the targeted distance is calculated to be 0.515 m, which can be identified as obstacle free in the photograph shown in figure 4.16. On the left side of figure 4.16, a map identifying the experiment's setting on the Vaihingen campus is shown to give an impression of the distance and the surrounding buildings. On the top photograph on the right side of figure 4.16, the transmitter housing including the integrated Cassegrain antenna pointing towards the marked yellow building with the Rx station is shown. The attached spotting scope is used for coarse link alignment. The link is then adjusted for maximum received power using a spectral measurement as discussed for the E-band link. On the bottom photograph in figure 4.16, the view from the Rx station towards the transmitter is shown.
The baseband I/Q data signals in this experiment are provided using the an 8 bit DAC[15], featuring a sampling rate of 64 GS/s in combination with an analog 3-dB bandwidth of 15 GHz introduced in chapter 1.2.6.3.

[13] The antenna system as well as the housing are designed and developed by Radiometer Physics GmbH, Meckenheim in the framework of the Millilink project.

[14] Institut für Mikroelektronik Stuttgart (IMS CHIPS)

[15] The used digital-to-analog converter is provided by Fujitsu Semiconductors for this measurements. Further information about the DAC can be found in [Ded11] and [Fuj12].

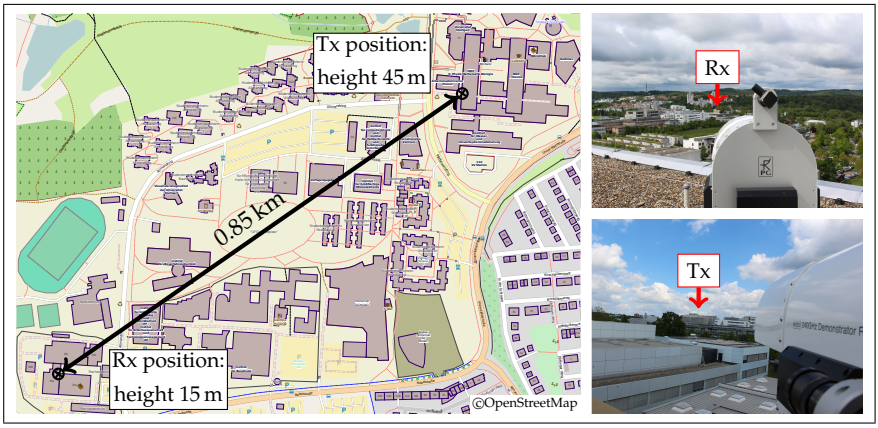

Figure 4.16: Map and photographs of the 0.85 km transmission experiment using the 240 GHz system. The top photograph shows the view from the Tx towards the Rx location (on top of the yellow building). At the bottom photograph, the view from the Rx towards the Tx is shown.

Two or three-time oversampling is used to generate symbol rates of 32 and 21.333 GBd, respectively. At the receiver side, the 33 GHz real-time oscilloscope, described in chapter 1.2.6.2, is used to capture the received I- and Q- baseband streams. In front of the oscilloscope, phase-matched baseband amplifiers with a gain of 22 dB provide sufficient input power for the oscilloscope. A schematic of the measurement setup is shown in figure 4.17.

To estimate the maximum achievable transmission distance, a link budget analysis is performed. The influence of the additional attenuation L_{atm} due to atmospheric gases at a temperature of 12 °C and a relative humidity of approximately 57 % during the measurements[16] is estimated using [Rec09a] to be approximately 1.7 dB for the planned transmission

[16]This weather data for the 13$^{\text{th}}$ May, 2014, the day of the measurements, are provided by a meteorological station operated by the University of Stuttgart.

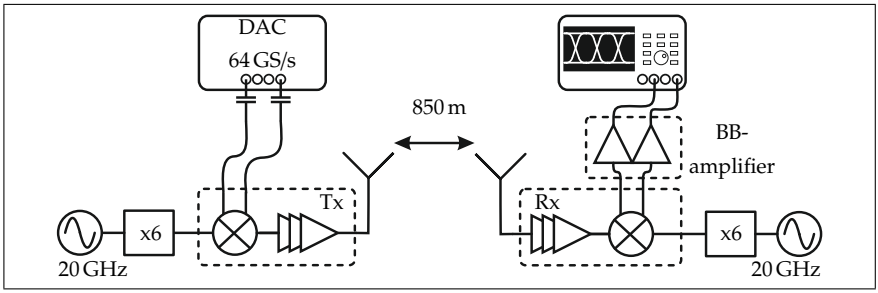

Figure 4.17: Measurement setup for the 850 m transmission experiment using two 55.1 dBi Cassegrain antennas.

Table 4.6: Link budget parameters for the 240 GHz transmission experiment over 0.85 km.

$P_{t,\,avg}$ (dBm)	G_{Tx} (dBi)	L_{FSPL} (dB)	L_{atm} (dB)	G_{Rx} (dBi)	CG_{Rx} (dB)	G_{BB} (dB)	NF_{Rx} (dB)
-4.5	55.1	138.6	1.7	55.1	-1	22	12.3

distance. The free-space path loss L_{FSPL} over this distance is 138.6 dB. Using equation (4.3) together with the values provided in table 4.6, an expected receiver input power of approximately −35 dBm is calculated, which is close to the Rx's optimal input power as shown in chapter 3.3.3. For the link budget, the values for the transmit power $P_{t,\,avg}$ and the receiver's conversion gain $CG_{Rx,avg}$ are extracted from the characterization measurements shown in chapter 2.2 and averaged over the used signal bandwidth. A calculation of the expected SNR values for the transmitted signal bandwidths of 42.666 and 64 GHz, results in approximately 20.8 dB for the 21.333 GBd and approximately 19 dB for the 32 GBd signal.

The overall received signal power is measured to be −13.5 dBm for the 32 GBd transmission. This is about 0.5 dB more than expected by the link budget calculation, which is most probably caused by uncertainties in the

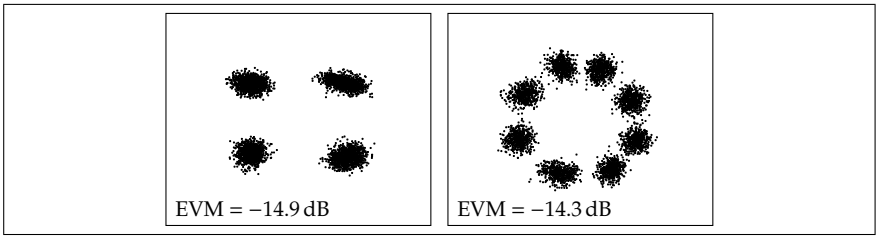

Figure 4.18: Measured constellation diagram with corresponding EVM of QPSK and 8-PSK modulated signals at a symbol rate of 21.333 GBd, transmitted over 850 m.

measurement of the transmit power at 240 GHz as well as by a deviation of the actual gain of the used Cassegrain antenna system from its simulated value. Simultaneously, the measured receive power proves that no severe losses are introduced due to a misalignment of the link.
For the demodulation, the VSA's feed-forward equalizer is used. The resulting constellation diagrams with the corresponding EVM values for the 21.333 GBd signals are shown in Fig.4.18. For the QPSK signal, in the left diagram, the constellation points are clearly separated and the measured EVM is −14.9 dB. For the 8-PSK signal, some symbols cannot unambiguously be assigned to a specific constellation point and the resulting EVM is slightly worse than for the QPSK signal. This increase in EVM is caused by an already worse output signal out of the DAC compared to the QPSK signal. Due to increased requirements on the signal quality for 8-PSK modulation compared to QPSK, the resulting BER will also increase.
When increasing the symbol rate to the maximum of 32 GBd, the resulting EVM decreases corresponding to the measured SNR by a factor of 3 dB. The corresponding constellation diagrams are shown in figure 4.19. For the QPSK signal, the constellation points, although more disturbed than for the 21.333 GBd, are still distinguishable. The constellation diagram of the 8-PSK signal on the right of figure 4.19 shows, that although a demodulation is momentarily possible, the symbols cannot be assigned to a certain constellation point. Mostly, the VSA software is not able to

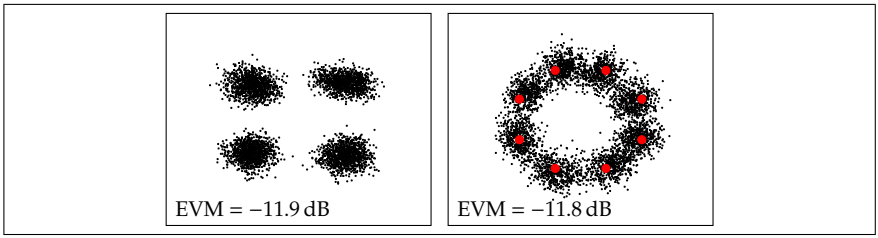

Figure 4.19: Measured constellation diagram with corresponding EVM of a QPSK and a 8- PSK modulated 32 GBd signal, transmitted over 850 m.

demodulate the signal at all.
An evaluation of the system's BER performance for this experiment reveals a BER better than 9.5×10^{-8} for the QPSK modulated 21.333 GBd signal, resulting in data rates of 42.666 Gbit/s. For the 8-PSK signal, corresponding with a data rate of 63.999 Gbit/s, the BER is determined to be 3.0×10^{-3}. Considering the QPSK modulated signal with the maximum symbol rate of 32 GBd, i.e. a data rate of 64 Gbit/s, the resulting BER is 9.5×10^{-5}. All of these signal can be corrected to be error free by an appropriate FEC.

4.4 Discussion

In this chapter, the advancement of the back-to-back measured mmw frontend components to realistic wireless links as well as link budget parameters are described. The effects which disturb the propagating signals range from obstacles in the transmission path (considered by the so-called Fresnel zones), to atmospheric effects in terms of gases, water droplets, i.e. fog and rain, are described. Altogether they result in a decrease of the received signal strength. Although distinct frequency bands in the high mmw regime show advantages due to a lower atmospheric attenuation in so-called atmospheric attenuation windows, and a smaller first Fresnel radius, making it easier to ensure a undisturbed propagation of the signal, the atmospheric attenuation in the mmw regime is significantly

higher than in the microwave region.
For extreme rain events, i.e. for rain rates higher than 50 mm/h, it is suggested that all frequencies above 50 GHz experience an identical attenuation. However, it is also discussed that the calculation basis provided by the ITU is not unconditionally correct. The actual attenuation due to specific rain conditions may differ from the calculated values, depending on the type of rain and its drop size. The same holds for fog and clouds. Therefore, when planning a wireless link, for the prediction of expectable attenuation and link availabilities, the specific local rain distribution and type have to be taken into account.

To relate the transmission results achieved in the long range transmission experiments with the E-band and the 240 GHz system to the actual state of the art, the comparison discussed in the introductory chapter shall be picked up again. As shown in figure 4.20, both realized wireless links exceed the state of the art in terms of transmission distance and achieved data rate, where the results for the 240 GHz indoor transmission would even allow for higher distances with the additional attenuation in front of the receiver removed. The results for the outdoor transmission results were enabled by the high gain Cassegrain antenna systems. The comparison shows the advantages of complex modulation compared to the up to now widely used ASK modulation, as well as the benefits from the use of MMIC-based transmit and receive components for the realization of high transmission distances.
Additionally to the results shown and discussed in this thesis, also a data rate of 100 Gbit/s over a distance of 20 m, shown as a red triangular data point in figure 4.20, are achieved in an indoor measurement setup. These results were achieved in a collaboration with a partner institute by combining the 240 GHz receiver discussed in this thesis, with a photonic UTC-PD-based transmitter and using complex modulation schemes. The measurement setup and results are thoroughly discussed in [Kön14] and [S. 13].

The data transmission experiments over distances of 4.1 and 15.7 km using

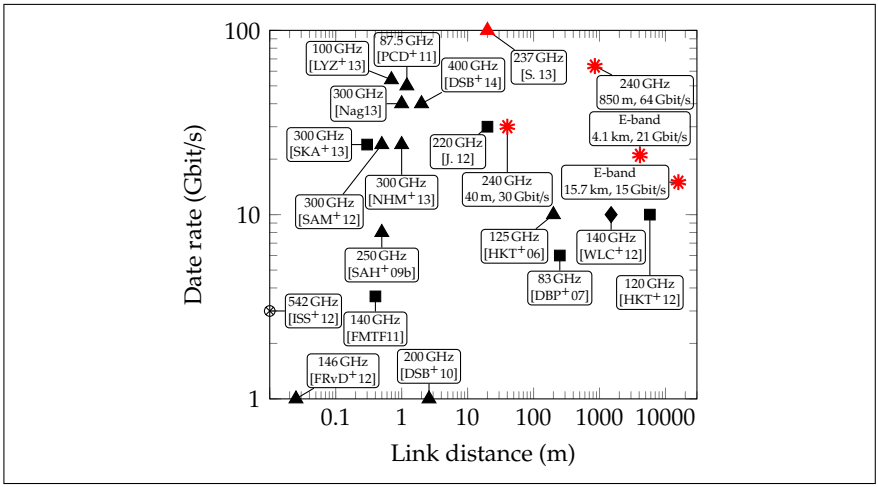

Figure 4.20: Comparison of the achieved results in the data transmission experiments with the E-band and 240 GHz link to the state of the art. The results of this thesis are shown as red stars.

the E-band system show the feasibility of high data rate wireless links in this frequency range. Furthermore, the achieved distances meet the required distances for such wireless link in backhaul application scenarios as already discussed in chapter 1. A comparison of the received signal power to corresponding link budget calculations shows that the links can be set up without introducing severe misalignments. This was the first time that a transmission bridging a distance of more than 6 km using this frequency band was realized. Furthermore, as can be seen from the state of the art comparison, in both E-band transmission experiments new benchmarks for the combination of transmission distance and achieved data rate are set.

For the experiments over a distance of 4.1 km, a symbol rate of 7 GBd can be transmitted with QPSK and 8-QAM modulated signals, which result in data rates of 14 and 21 Gbit/s, respectively. Although already disturbed by AWGN, the system does not operate in the SNR-limited region but, as

revealed by the calculation and the measurement of the received power, just below the receiver's optimum input power. An evaluation of these signals' transmission performance reveals a BER better than 4.8×10^{-8} for the data rate of 14 Gbit/s, and a BER of 6.3×10^{-4} for the 21 Gbit/s. With the FEC published in [COM10], the latter signal can be corrected to a BER of better than 1×10^{-15}. The necessary 7 % overhead for the FEC reduces the useable data rate to 19.53 Gbit/s.
When considering the results of the 15.7 km transmission, data rates of 12 and 15 Gbit/s are achieved using QPSK and 8-QAM modulated signals. In this experiment, the system operates in the SNR-limited regime. The evaluation of the system's BER shows that the 12 Gbit/s signal can be transmitted with a BER of 1.2×10^{-4}. The 15 Gbit/s signal shows a BER of 4.8×10^{-3}. Both signals can be corrected using the above mentioned FEC algorithms. The necessary overheads reduce the net data rates to 11.16 and 13.95 Gbit/s, respectively.
When evaluating the wireless system's performance when the link is influenced by rain with a rain rate of approximately 0.5 mm/h, QPSK signals up to a symbol rate of 5 GBd, resulting in data rates up to 10 Gbit/s, can be transmitted with bit error rates better than 4.6×10^{-3}. The step-wise variation of the symbol rate during the rain event and the results for the different kinds of modulation formats suggest that an adaptive variation of modulation scheme and bandwidth can be a viable solution to maintain the link during adverse weather, though with reduced data rates.
Considering the occurring degradations of signal quality for the E-band link, the performance and thus the achievable data rate is significantly reduced. Compared to the maximum symbol rate of 12 GBd achieved in the back-to-back measurements, the complete system is now only capable of transmitting symbol rates up to 7 GBd and shows severe performance losses for higher order modulations, i.e. 16-, 32- and 64-QAM. Further investigations on the influence of impedance mismatches as well as their distortion contributions will be necessary to redesign the existing MMIC components and achieve better transmission qualities. In addition, it might be possible to overcome the influence of these mismatches by using a signal pre-distortion for the Tx's baseband signals. Therefore, an

accurate measurement method in the desired frequency range has to be developed or a relation between module characterization and the module's performance for complex data signals has to be found. Furthermore, another signal source to generate the baseband signals would be necessary, since the dynamic range and maximum output signal of the one used in the experiments here does not provide enough output power for the transmitter when using digital pre-distortion.
Furthermore, to make statements about the link reliability, stability and reproducibility, long-term measurements with a continuous signal and a power tracking mechanism would be necessary, which was neither possible nor available during the short measurement campaigns organized for this work's experiments.

The results achieved with the 240 GHz wireless link for both indoor and outdoor experiments prove that complex modulation is also feasible at such elevated frequencies. While the results of the indoor experiments are clearly limited by the available bandwidth of the baseband equipment, in a 0.85 km outdoor transmission with a data rate of 64 Gbit/s a new state of the art, not only in achieved transmission distance at the frequency range around 240 GHz but also for achieved data rate in the entire mmw range is set. This data rate can either be achieved by using a robust QPSK modulation scheme together with a symbol rate of 32 GBd, or by using a more bandwidth efficient 8-PSK modulation, which allow for a transmission of the same amount of data with a saving in bandwidth of 33.3 % but with a higher BER. While the 8-PSK signal reveals the system's performance limit due to heavy phase noise distortion, the limit for QPSK modulated signals is again not set by the frontend but by the baseband equipment being limited to a symbol rate of 32 GBd. The constellation diagram of this signal still reveals a performance margin, as can be seen by the clearly separated constellation points with only few distorted measurements points. As shown in figure 4.20, the 64 Gbit/s transmission with a resulting BER of 9.5×10^{-5} and the 100 Gbit/s transmission, both realized with 240 GHz components, provide the highest data rates for in- and outdoor scenarios in the entire mmw range.

5 Conclusions and Future Prospects

The ever growing demand on high speed wireless data transmission and the limitations of both technical and regulatory nature at microwave frequencies raise the question for new approaches. Solutions for multi-gigabit capacity connections in in- and outdoor applications are provided by systems operating in the high mmw region. Specific frequency bands shown in figure 1.1 provide advantages due to the moderate atmospheric attenuation in these bands but also due to large available and allocated bandwidths for broadband wireless communication. In combination with the use of millimeter wave integrated circuits powerful, efficient and compact systems for radio back- and fronthaul, operating in the range from few hundred meters up to several kilometers, but also for short range applications like wireless data kiosk in the range of one meter, and personal area networks for a range up to ten meters, can be realized and are the topic of several research programs.
While first wireless links in the E-band are already commercially available and first research results considering circuits but also data transmission in the mmw region are published, none of them has so far exploited the entire capability concealed in this approach. In particular, up to now there had not been a system, combining MMIC-based I/Q-transmitters and receivers to directly modulate a carrier signal and thereby transmit complex data signals, realizing a wireless link with multi-gigabit capability. Nor was there theoretical transmission quality analysis with comparisons to a system measurement carried out for a wireless system operating in this frequency range. The main advantage of the approach pursued in this thesis based on electrical transmitters and receivers, is achieved by the utilization of complex modulation, leading to significantly higher data rates. Compared to existing opto-electrical systems, the deployment of

MMICs leads to a more compact and efficient system setup with an additional advantage in achieved output power.

From the findings in this thesis, a set of conclusions can be drawn for the future use of millimeter wave wireless communication links for diverse in- and outdoor applications. Following the entire development process starting from chip level in chapter 2, via system characterization in laboratory setups in chapter 3, to in- and outdoor wireless data transmission experiments with a complete system setup in chapter 4, not only the general feasibility of such systems is shown but also a new state of the art for both achieved data rate and transmitted distance is set. For each development step, a detailed analysis of the realized components and devices has been performed, their limitations have been revealed and the potentials of improvements have been shown.

For the realization of monolithic integrated, broadband mixer circuits, applicable for high data rate mmw wireless communication links and utilizing complex modulated data signals for increased bandwidth efficiency, the resistive mixer approach is found to be a viable solution. A comparison to the state of the art reveals that the IF-bandwidth achieved with this approach can be significantly increased, while all other parameters are comparable. This advantage of higher achievable IF-bandwidths lead to increased modulation bandwidths, directly corresponding to higher usable data rates.
The circuit's drawback of a high required LO power is easily compensated by an additional amplifier module in the LO path. During MMIC design cycles for transmit and receive structures as well as their characterization both on-wafer and after waveguide module packaging, the critical design aspects for the later systems are identified to be the bandwidth performance of the different stages, i.e. couplers, mixer cells and amplifiers, as well as the impedance matching between the different stages.

The back-to-back system measurements prove that data transmission with extremely broadband complex modulated data signals is feasible with ac-

ceptable error rates. They clearly reveal the advantage of complex modulated data formats in terms of achieved data rate compared to simple and less bandwidth efficient modulation techniques, e.g. ASK. By adapting known performance metrics for transmission quality such as EVM to the broadband devices used in this work, it can be shown that the measurements can precisely be predicted by the EVM estimation. Using the same approach, the performance limitations of the systems can be identified.
While the presented E-band system is limited by the transmitter's I/Q-amplitude imbalance, the expected performance of the 300 GHz system reveals a distinct domination of LO phase noise disturbances. This indicates that for applications in this high frequency range a transmission scheme utilizing a multi-channel approach instead of one extremely broadband channel should be used.
Thus, when designing communication system's in the 300 GHz region, particular development effort is needed to improve the LO sources, but also an appropriate multi-channel approach has to be developed in the design phase already, to minimize the influence LO phase noise and frontend imperfections. Due to the verification of the EVM estimation's validity in this thesis, in the future, the optimization of the system performance can already be considered during the MMIC design process and system development.
When combining the developed Tx and Rx modules with the amplification stages necessary for long range transmission, a decrease in signal quality is observed. This reveals that for such broadband communication systems an optimization for mono-frequent signals during the design process is not sufficient. To achieve the best possible results, also the amplifier stages have to be optimized for broadband modulated data signals and, furthermore, need to be adapted to other frontend components.
A comparison of the achieved receiver sensitivity for the E-band and 240 GHz system reveals that both perform beyond the state of the art even in relation to systems operating at much lower carrier frequencies and with less RF bandwidth. These results are achieved due to the superior noise performance of the chosen transistor technology, proving the initial choice of technology to be right.

Finally, the feasibility of actual wireless data transmission is shown in different in- and outdoor experiments over distances up to 15.7 km, where both the E-band system, achieving 15 Gbit/s over a distance of 15.7 km, and the 240 GHz system, achieving 64 Gbit/s over a distance of 0.85 km, set new benchmarks in both transmitted data rate and achieved transmission distance compared to the state of the art. Corresponding to typical transmission distances for backhauling in urban as well as rural areas, a solution for future high-speed wireless connections in mobile backbone networks for satisfying the mobile customer's growing demand has been found in this thesis.

The different influences on the propagating wave which have to be considered in a link budget calculation were discussed. A thorough literature research reveals that the attenuation models for rain and fog attenuation provided by the ITU are not unconditionally true, and that for an accurate prediction the local circumstances have to be taken into account. Furthermore, in addition to the rain rate and liquid water content, to achieve relevant results, the exact size of the droplets as well as their quantity has to be known.

When comparing the measured receive power of all transmission measurements with the results from the corresponding link budget analyses, it is found that the behavior of the link can precisely be predicted. Despite the extremely high antenna gain, the wireless links can be set up without introducing distinct misalignment losses.

Measurements during a rain event prove the feasibility of transmitting complex modulated data signals during adverse weather conditions with expected decreases of transmission quality. It should be noted that the exact rain rate during the experiment was not known but estimated from the data of local weather stations. The results of a modulation bandwidth variation prompt that adaptive bandwidth and modulation schemes will lead to a much more flexible system with a significantly increased availability.

Future research

Concerning chip-level improvements, the results from this thesis can be used to optimize the MMIC during the design process already for their use in the transmission system. Special effort has to be devoted to the combination of the different frontend components, their balanced performance and the interstage impedance matching. Additionally, in a further development step, all building blocks of the frontend can be integrated into one single MMIC to reduce the system size.
The pursued solution with a direct detection scheme in combination with extremely high bandwidths leads to difficulties which have to be encountered in order to realize a fully useable system of commercial interest.
First of all, the use of a direct conversion I/Q transmission scheme mandates the existence of synchronous reception. In this thesis, this is realized by the use of offline processing with a software-based carrier recovery. For future use, this has to be realized in a real-time approach or by the use of an analog carrier recovery. First research results have already proved the feasibility of such solutions [HYW+11], but only for limited data rates.
Furthermore, with the feasibility of such systems shown, and theoretical approaches to determine their transmission quality provided, these results can be used to increase the systems' performance by applying optimized data formats and modulation schemes, as for example discussed for the multi-channel approach and the 300 GHz link. With the existing transmission systems and also the recently developed 300 GHz system, comprehensive results concerning the influence of atmospheric effects in general and broadband data transmission systems in particular, can be obtained by long-term transmission experiments allowing for evaluations based on convincing statistical data.

A Calculation of the atmospheric attenuation

To calculate the attenuation of propagation electromagnetic waves due to atmospheric influences, amongst others, the ITU provides recommendations concerned with the influence of fog, clouds, and rain. In the following, the calculation methods for these different attenuation effects are shown.

A.1 Attenuation due to fog and clouds

As discussed in chapter 4.1.3 and following [Rec09b], the specific attenuation γ_c due to fog and clouds can be calculated by using

$$\gamma_c = k_l M \,(\mathrm{dB/km})\,, \tag{A.1}$$

where k_l is the specific attenuation coefficient in (dB/km)/(g/m^3) and M is the liquid water density inside the cloud or fog given in g/m^3.
This approach is valid for frequencies below 200 GHz in fog or clouds consisting entirely of small droplets with a diameter of less than 0.1 mm. Only then, the assumed Rayleigh approximation is valid and the resulting attenuation can be expressed as a function of the liquid water density.

The specific attenuation coefficient k_l in equation (A.1) can be calculated for frequencies up to 1000 GHz using

$$k_l = \frac{0.819 f}{\epsilon''(f)(1+\eta^2)} \,(\mathrm{dB/km})/(\mathrm{g/m^3})\,. \tag{A.2}$$

Here, f represents the frequency of the propagating wave given in GHz and η is a function of the complex dielectric permittivity $\epsilon(f) = \epsilon'(f)+\epsilon''(f)$ of water:

$$\eta = \frac{2 + \epsilon'(f)}{\epsilon''(f)} \,. \tag{A.3}$$

The complex dielectric permittivity of water is given by:

$$\epsilon'(f) = \frac{\epsilon_0 - \epsilon_1}{\left[1 + (f/f_\mathrm{p})^2\right]} + \frac{\epsilon_1 - \epsilon_2}{[1 + (f/f_\mathrm{s})^2]} + \epsilon_2 \tag{A.4}$$

and

$$\epsilon''(f) = \frac{f(\epsilon_0 - \epsilon_1)}{f_\mathrm{p}\left[1 + (f/f_\mathrm{p})^2\right]} + \frac{f(\epsilon_1 - \epsilon_2)}{f_\mathrm{s}\left[1 + (f/f_\mathrm{s})^2\right]} \,, \tag{A.5}$$

where

$$\epsilon_0 = 77.6 + 103.3(\theta - 1) \,, \tag{A.6}$$
$$\epsilon_1 = 5.48 \,, \tag{A.7}$$
$$\epsilon_2 = 3.51 \,, \tag{A.8}$$
$$\theta = 300/T \,, \tag{A.9}$$

with T the temperature given in K.
The principal and secondary relaxation frequencies f_p and f_s can be calculated using:

$$f_\mathrm{p} = 20.09 - 142(\theta - 1) + 249(\theta - 1)^2 \text{ (GHz)} \,, \tag{A.10}$$

$$f_s = 590 - 1500(\theta - 1)\ \text{(GHz)}\,. \tag{A.11}$$

A.2 Attenuation due to rain

As used in chapter 4.1.3 and following [Rec05], the specific attenuation γ_r due to rain with a certain rain rate R can be calculated for horizontal or vertical polarization using

$$\gamma_r = k_r R^{\beta}\ \text{(dB/km)}\,. \tag{A.12}$$

In this equation, R is given in mm/h. This relation is valid for frequencies between 1 and 1000 GHz. The coefficients k_r and β can be calculated with

$$\log_{10}(k_r) = \sum_{j=1}^{4} a_j \exp\left[-\left(\frac{\log_{10}(f) - b_j}{c_j}\right)^2\right] + m_k \log_{10}(f) + c_k\,, \tag{A.13}$$

$$\beta = \sum_{j=1}^{5} a_j \exp\left[-\left(\frac{log_{10}(f) - b_j}{c_j}\right)^2\right] + m_\beta \log_{10}(f) + c_\beta\,, \tag{A.14}$$

where

$$f : \text{frequency in GHz}\,, \tag{A.15}$$

$$k_r : \text{either } k_{r,h} \text{ or } k_{r,v}\,, \text{ for horizontal or vertical polarization}\,, \tag{A.16}$$

$$\beta : \text{either } \beta_h \text{ or } \beta_v\,, \text{ for horizontal or vertical polarization}\,. \tag{A.17}$$

The coefficients for horizontal polarization are given in the following tables. The respective coefficients for vertical polarization can be found in [Rec05].

Table A.1: Coefficients for calculating k for horizontal polarization.

j	a_j	b_j	c_j	m_k	c_k
1	-5.33980	-0.10008	1.13098	-0.18961	0.71147
2	-0.35351	1.26970	0.45400		
3	-0.23789	0.86036	0.15354		
4	-0.94158	0.64552	0.16817		

Table A.2: Coefficients for calculating β for horizontal polarization.

j	a_j	b_j	c_j	m_β	c_β
1	-0.14318	1.82442	-0.55187	0.67849	-1.95537
2	0.29591	0.77564	0.19822		
3	0.32177	0.63773	0.13164		
4	-5.37610	-0.96230	1.47828		
5	16.1721	-3.29980	3.43990		

B State of the art for millimeter wave low noise amplifiers

To support the graphical comparison of published low noise amplifiers in the mmw regime in terms of noise figure as given in figure 1.10, chapter 1.2.5, the important device characteristics, i.e. center frequency f_c, 3-dB bandwidth, gain G and the corresponding noise figure NF, for these LNAs are listed in table B.1. As can be seen, the mHEMT technology surpasses other technologies not only in terms of noise figure but also in achieved bandwidth in the frequency band targeted in this thesis.

Table B.1: State of the art for millimeter wave LNAs.

Reference	Technology	f_c / GHz	$B_{3\text{-dB}}$ / GHz	G / dB	NF / dB
[TMW+13]	50 nm GaAs mHEMT	83	53	16.4	2.1
[TMW+13]	50 nm GaAs mHEMT	92	36	14.5	2.8
[WKW+10]	50 nm GaAs mHEMT	140	30	20	4.0
[LKT+11]	20 nm GaAs mHEMT	145	60	20	4.0
[KVK+06]	100 nm GaAs mHEMT	155	30	19.1	6.7
[THL+14] [1]	35 nm GaAs mHEMT	232	70	35.2	5.0
[THL+14] [1]	50 nm GaAs mHEMT	243	68	30.6	5.6
[LTD+13] [1]	35 nm GaAs mHEMT	300	70	24	6.1
[LKS+13]	35 nm InP HEMT	140	48	20	3.0
[FRV+13]	35 nm InP HEMT	239	30	16.3	9.0
[VLF+12]	35 nm InP HEMT	246	16	19	7.5
[DLM+10]	30 nm InP HEMT	280	46	20	8.4
[Dea10] [1]	30 nm InP HEMT	308	40	15	9.5
[SLL+11] [1]	30 nm InP HEMT	325	50	38	8.3
[HUL+12]	0.125 µm InP DHBT	370	50	22	17.1
[LS13]	0.13 µm SiGe HBT	55	30	22.5	7.2
[CBYK+11]	0.12 µm SiGe HBT	73	7	18	5.5
[CBCL10]	0.18 µm SiGe HBT	77	14.5	14.5	6.9
[GJH10]	0.18 µm SiGe HBT	86	27	19	9.0
[LS13] [2]	0.13 µm SiGe HBT	105	70	25	7.0
[WDS+10]	0.13 µm SiGe HBT	122	19	14.8	10.0
[ZXW+12]	0.13 µm SiGe HBT	146	28	21	8.5
[SBM+12]	0.13 µm SiGe HBT	245	8	18	11.0
[MKS+11]	65 nm CMOS	73	15	9.4	6.7
[TGV10]	65 nm CMOS	88	15	27	6.8
[ICU+11]	45 nm CMOS	95	-	11	6.0
[WCN+14]	32 nm CMOS	210	15	18	11.0

[1] mmW waveguide module [2] NF between 78 and 110 GHz

Bibliography

[Abi95] A.A. Abidi. Direct-conversion radio transceivers for digital communications. *Solid-State Circuits, IEEE Journal of*, 30(12):1399–1410, Dec 1995.

[AGW+11] Morteza Abbasi, S.E. Gunnarsson, N. Wadefalk, R. Kozhuharov, J. Svedin, S. Cherednichenko, I. Angelov, I. Kallfass, P. Leuther, and H. Zirath. Single-Chip 220-GHz Active Heterodyne Receiver and Transmitter MMICs With On-Chip Integrated Antenna. *Microwave Theory and Techniques, IEEE Transactions on*, 59(2):466–478, 2011.

[AH13] B. Ayvazian and C. Hetting. Second-generation e-band solutions: Opportunities for carrier-class lte backhaul. White paper, Heavy Reading, February 2013.

[aK50] H. J. aufm Kampe. Visibility and liquid water content in clouds in the free atmosphere. *Journal of Meteorology*, 7(1):54–57, 2014/11/15 1950.

[ALL+05] Dan An, Bok-Hyung Lee, Byeong-Ok Lim, Mun-Kyo Lee, Sung-Chan Kim, Jung-Hun Oh, S.-D. Kim, Hyung-Moo Park, Dong-Hoon Shin, and Jin-Koo Rhee. High switching performance 0.1-μm metamorphic HEMTs for low conversion loss 94-GHz resistive mixers. *Electron Device Letters, IEEE*, 26(10):707–709, Oct 2005.

[ALM+08] M.S. Awan, E. Leitgeb, Marzuki, M.S. Khan, F. Nadeem, and C. Capsoni. Evaluation of fog attenuation results for optical wireless links in free space. In *Satellite and Space Communications, 2008. IWSSC 2008. IEEE International Workshop on*, pages 112–116, Oct 2008.

[AO85] G. Olalere Ajayi and Roderic L. Olsen. Modeling of a tropical raindrop size distribution for microwave and millimeter wave applications. *Radio Science*, 20(2):193–202, 1985.

[Arm21] E.H. Armstrong. A new system of short wave amplification. *Radio Engineers, Proceedings of the Institute of*, 9(1):3–11, Feb 1921.

[Ber00] Henry L. Bertoni. *Radio propagation for modern wireless systems: [state-of-the-art propagation prediction techniques and models; accurate new models to account for buildings; terrain and foliage, detailed comparisons with actual measurements taken in the field; multipath models, wave propagation, diffraction and more]*. Prentice Hall PTR, Upper Saddle River, NJ, 2000.

[BNe11] BNetzA. *Schnittstellenbeschreibung für Punkt-zu-Punkt Richtfunkanlagen im 71-76 GHz und 81-86 GHz-Bereich; SSB FE–OE 023*. Bundesnetzagentur für Elektrizität, Gas, Telekommunikation, Post und Eisenbahnen, 06 2011.

[CAC+09] E. Ciaramella, Y. Arimoto, G. Contestabile, M. Presi, A. D'Errico, V. Guarino, and M. Matsumoto. 1.28 terabit/s (32x40 Gbit/s) wdm transmission system for free space optical communications. *Selected Areas in Communications, IEEE Journal on*, 27(9):1639–1645, December 2009.

[CALL11] M. Y W Chia, C.K. Ang, B. Luo, and S.W. Leong. Wideband 307 GHz transceiver system for high speed digital wireless at 12.5 Gbps. In *Microwave Symposium Digest (MTT), 2011 IEEE MTT-S International*, pages 1–4, 2011.

[Cam98] Edmar Camargo. *Design of FET frequency multipliers and harmonic oscillators*. Artech House microwave library. Artech House, Boston, 1998.

[CBCL10] A.Y.-K. Chen, Y. Baeyens, Young-Kai Chen, and Jenshan Lin. A Low-Power Linear SiGe BiCMOS Low-Noise Amplifier for Millimeter-Wave Active Imaging. *Microwave and Wireless Components Letters, IEEE*, 20(2):103–105, Feb 2010.

[CBYK+11] R. Carmon, R. Ben-Yishay, O. Katz, B. Sheinman, and D. Elad. A 71-76GHz low noise amplifier with integrated image reject filter and single balanced down converter mixer. In *Microwaves, Communications, Antennas and Electronics Systems (COMCAS), 2011 IEEE International Conference on*, pages 1–4, Nov 2011.

[CD10] Zhenqi Chen and Fa Foster Dai. Effects of LO Phase and Amplitude Imbalances and Phase Noise on M -QAM Transceiver Per-

formance. *Industrial Electronics, IEEE Transactions on*, 57(5):1505–1517, 2010.

[Che04] S. Cherry. Edholm's law of bandwidth. *Spectrum, IEEE*, 41(7):58–60, July 2004.

[Cis11] Cisco. Cisco visual networking index: Global mobile data traffic forecast update, 2010-2015. online: http://newsroom.cisco.com/dlls/ekits/Cisco_VNI_Global_Mobile_Data_Traffic_Forecast_2010_2015.pdf, 02 2011. last accessed 03-02-2014.

[Cis14] Cisco. Cisco visual networking index: Global mobile data traffic forecast update, 2013-2018. online: http://www.cisco.com/c/en/us/solutions/collateral/service-provider/visual-networking-index-vni/white_paper_c11-520862.html, 02 2014. last accessed 03-02-2014.

[CK94] Chang C.Y. and Francis Kai. *GaAs High-Speed Devices: Physics, Technology, and Circuit Applications*. Wiley, 1. ed. edition, 1994.

[CLC03] Tien-Yu Chang, Chun-Lin Liao, and Chun-Hsiung Chen. Coplanar-waveguide tandem couplers with backside conductor. *Microwave and Wireless Components Letters, IEEE*, 13(6):214–216, 2003.

[Cle10] A. Clegg. Sharing between radio astronomy and active services at THz frequencies. *IEEE802 Pleanry Session, Dallas, IEEE 802.15 Document 10-0829-00-0thz*, 2010.

[COM10] F. Chang, K. Onohara, and T. Mizuochi. Forward error correction for 100 G transport networks. *Communications Magazine, IEEE*, 48(3):S48–S55, March 2010.

[Cos57] J.P. Costas. Synchronous communications. *Communications Systems, IRE Transactions on*, 5(1):99–105, March 1957.

[Cra80] R.K. Crane. Prediction of Attenuation by Rain. *Communications, IEEE Transactions on*, 28(9):1717–1733, Sep 1980.

[DBP+07] V. Dyadyuk, J.D. Bunton, J. Pathikulangara, R. Kendall, O. Sevimli, L. Stokes, and D.A. Abbott. A multigigabit millimeter-wave communication system with improved spectral efficiency. *Microwave Theory and Techniques, IEEE Transactions on*, 55(12):2813–2821, 2007.

[DDN12] A. Dearn, L. Devlin, and J. Nelson. A sub-harmonic E-band IRM/SSB realized on a low cost PHEMT process. In *Microwave Integrated Circuits Conference (EuMIC), 2012 7th European*, pages 282–284, Oct 2012.

[Dea10] W.R. Deal. Solid-state amplifiers for terahertz electronics. In *Microwave Symposium Digest (MTT), 2010 IEEE MTT-S International*, pages 1–1, May 2010.

[Ded10] Ian Dedic. 56 GS/s ADC: Enabling 100GbE. In *Optical Fiber Communication Conference*, page OThT6. Optical Society of America, 2010.

[Ded11] Ian Dedic. 55 - 65Gs/s ADC's and DAC's in CMOS technology. In *PH-ESE Electronics Seminars, CERN, Zurich*, 04 2011. https://indico.cern.ch/event/121657/, last accessed 04-07-2014.

[DGM99] University of California David G. Messerschmidt. How Digital Communication Works. online: http://www.eecs.berkeley.edu/~messer/netappc/Supplements/20-digicom.pdf, 1999. last accessed 11-13-2014.

[DK12] C. Dudak and N.D. Kahyaoglu. A descriptive study on AM-AM and AM-PM conversion phenomena through EVM-SNR relations. In *Power Amplifiers for Wireless and Radio Applications (PAWR), 2012 IEEE Topical Conference on*, pages 69–72, Jan 2012.

[DLM+10] W.R. Deal, K. Leong, X.B. Mei, S. Sarkozy, V. Radisic, J. Lee, P. H Liu, W. Yoshida, J. Zhou, and M. Lange. Scaling of InP HEMT Cascode Integrated Circuits to THz Frequencies. In *Compound Semiconductor Integrated Circuit Symposium (CSICS), 2010 IEEE*, pages 1–4, Oct 2010.

[DSB+10] G. Ducournau, P. Szriftgiser, D. Bacquet, A. Beck, T. Akalin, E. Peytavit, M. Zaknoune, and J.F. Lampin. Optically power supplied Gbit/s wireless hotspot using 1.55 μm THz photomixer and heterodyne detection at 200 GHz. *Electronics Letters*, 46(19):1349–1351, Sept 2010.

[DSB+14] G. Ducournau, P. Szriftgiser, A. Beck, D. Bacquet, F. Pavanello, E. Peytavit, M. Zaknoune, T. Akalin, and J.-F. Lampin. Ultrawide-Bandwidth Single-Channel 0.4-THz Wireless Link Combining

Broadband Quasi-Optic Photomixer and Coherent Detection. *Terahertz Science and Technology, IEEE Transactions on*, PP(99):1–10, 2014.

[E-b12] E-band communications, LCC. Industry's Most Advanced E-Band Radio for Next Generation 4G & LTE Wireless Networks. online: http://www.e-band.com/index.php?id=822, 04 2012. last accessed 04-04-2014.

[Ema13] Shahriar Emami. *UWB Communication Systems: Conventional and 60 GHz : Principles, Design and Standards*. SpringerLink : Bücher. Springer, New York, NY, 2013.

[EMG+13] M. Elkhouly, Yanfie Mao, S. Glisic, C. Meliani, F. Ellinger, and J.C. Scheytt. A 240 GHz direct conversion IQ receiver in 0.13 μm SiGe BiCMOS technology. In *Radio Frequency Integrated Circuits Symposium (RFIC), 2013 IEEE*, pages 305–308, 2013.

[Eri13] Ericsson. Ericsson mobility report. online: http://www.ericsson.com/ericsson-mobility-report, 11 2013. last accessed 02-03-2014.

[Eri14] Ericsson. Ericsson mobility report, intermin update. online: http://www.ericsson.com/ericsson-mobility-report, 02 2014. last accessed 02-03-2014.

[Esm06] R. Esmailzadeh. *Broadband Wireless Communications Business: An Introduction to the Costs and Benefits of New Technologies*, chapter 1.4. Wiley, 2006.

[ETS06] ETSI. *Fixed Radio Systems; Point-to-Point equipment; Radio equipment and antennas for use in Point-to-Point Millimetre wave applications in the Fixed Services (mmwFS) frequency bands 71 GHz to 76 GHz and 81 GHz to 86 GHz; ETSI TS 102 524 V1.1.1*. European Telecommunications Standards Institute, 07 2006.

[ETS09] ETSI. *Fixed Radio Systems; Characteristics and requirements for point-to-point equipment and antennas; Part 3: Equipment operating in frequency bands where both frequency coordinated or uncoordinated deployment might be applied; Harmonized EN covering the essential requirements of article 3.2 of the R and TTE Directive; ETSI EN 302 217-3 V1.3.1*. European Telecommunications Standards Institute, 07 2009.

[FGK11] G. Fettweis, F. Guderian, and S. Krone. Entering the path towards terabit/s wireless links. In *Design, Automation Test in Europe Conference Exhibition (DATE), 2011*, pages 1–6, 2011.

[FM10] John Federici and Lothar Moeller. Review of terahertz and subterahertz wireless communications. *Journal of Applied Physics*, 107(11):–, 2010.

[FMTF11] R. Fujimoto, M. Motoyoshi, K. Takano, and M. Fujishima. A 120 GHz / 140 GHz dual-channel ASK receiver using standard 65 nm CMOS technology. In *Microwave Conference (EuMC), 2011 41st European*, pages 1189–1192, Oct 2011.

[Fri44] H.T. Friis. Noise Figures of Radio Receivers. *Proceedings of the IRE*, 32(7):419–422, July 1944.

[Fri46] H.T. Friis. A Note on a Simple Transmission Formula. *Proceedings of the IRE*, 34(5):254–256, 1946.

[FRV+13] A. Fung, T. Reck, M. Varonen, Choonsup Lee, M. Soria, G. Chattopadhyay, P. Kangaslahti, L. Samoska, S. Sarkozy, and R. Lai. Low noise amplifier modules from 220-270 GHz. In *Microwave Integrated Circuits Conference (EuMIC), 2013 European*, pages 224–227, Oct 2013.

[FRvD+12] M. J. Fice, E. Rouvalis, F. van Dijk, A. Accard, F. Lelarge, C. C. Renaud, G. Carpintero, and A. J. Seeds. 146-GHz millimeter-wave radio-over-fiber photonic wireless transmission system. *Opt. Express*, 20(2):1769–1774, Jan 2012.

[FSN+12] W. Freude, R. Schmogrow, B. Nebendahl, M. Winter, A. Josten, D. Hillerkuss, S. Koenig, J. Meyer, M. Dreschmann, M. Huebner, C. Koos, J. Becker, and J. Leuthold. Quality metrics for optical signals: Eye diagram, Q-factor, OSNR, EVM and BER. In *Transparent Optical Networks (ICTON), 2012 14th International Conference on*, pages 1–4, 2012.

[Fuj12] Fujitsu Semiconductor Europe. Fujitsu demonstrates ultra high-speed short-reach data transmission based on multi-level signalling and advanced adc/dac technology. online: http://www.fujitsu.com/emea/news/pr/fseu-en_20120906-1036-fujitsu-high-speed-data-transmission.html, 09 2012. last accessed 04-07-2014.

[Geo04] A. Georgiadis. Gain, phase imbalance, and phase noise effects on error vector magnitude. *Vehicular Technology, IEEE Transactions on*, 53(2):443–449, 2004.

[GFG+09] M. Gavell, M. Ferndahl, S.E. Gunnarsson, M. Abbasi, and H. Zirath. An Image Reject Mixer for High-Speed E-Band (71-76, 81-86 GHz) Wireless Communication. In *Compound Semiconductor Integrated Circuit Symposium, 2009. CISC 2009. Annual IEEE*, pages 1 –4, oct. 2009.

[GJH10] L. Gilreath, V. Jam, and P. Heydan. A W-band LNA in 0.18-μm SiGe BiCMOS. In *Circuits and Systems (ISCAS), Proceedings of 2010 IEEE International Symposium on*, pages 753–756, May 2010.

[Gre11] Andrei Grebennikov. *RF and microwave transmitter design*. Wiley series in microwave and optical engineering. Wiley, Hoboken, N.J, online-ausg. edition, c2011.

[GRRGdPB13] J.M. Garcia-Rubia, J.M. Riera, P. Garcia-del Pino, and A Benarroch. Attenuation Measurements and Propagation Modeling in the W-Band. *Antennas and Propagation, IEEE Transactions on*, 61(4):1860–1867, April 2013.

[GSL+13] J.M. Guerra, A. Siligaris, J.-F. Lampin, F. Danneville, and P. Vincent. A 283 GHz low power heterodyne receiver with on-chip local oscillator in 65 nm CMOS process. In *Radio Frequency Integrated Circuits Symposium (RFIC), 2013 IEEE*, pages 301–304, 2013.

[GT03] Sunrise Telecom Broadband Gerard Terreault. QAM Signal Impairments and Their Effects on MER and BER. online: http://docsis.beckitrue.com/documents/sunrise/QAM_Impairment_Effects_on_MER_BER_104.pdf, 1 2003. last accessed 07-31-2014.

[Gu05] Qizheng Gu. *RF system design of transceivers for wireless communications*. Springer, New York, NY, 2005.

[GWS+08] S.E. Gunnarsson, N. Wadefalk, J. Svedin, S. Cherednichenko, I. Angelov, H. Zirath, I. Kallfass, and P. Leuther. A 220 GHz Single-Chip Receiver MMIC With Integrated Antenna. *Microwave and Wireless Components Letters, IEEE*, 18(4):284–286, 2008.

[GZFG10] M. Gavell, H. Zirath, M. Ferndahl, and S.E. Gunnarsson. A linear 70-95 GHz differential IQ modulator for E-band wireless communication. In *Microwave Symposium Digest (MTT), 2010 IEEE MTT-S International*, pages 788 –791, may 2010.

[HC13] B. Henderson and E. Camargo. *Microwave Mixer Technology and Applications:*. Microwave & RF. Artech House, Incorporated, 2013.

[HE11] J. Hansryd and J. Edstam. Microwave capacity evolution. Review paper, Ericsson Research, January 2011.

[HHC12] J. Hesler, Kai Hui, and T. Crowe. Ultrafast millimeter-wave and THz envelope detectors for wireless communications. In *Microwave Photonics (MWP), 2012 International Topical Meeting on*, pages 93–94, 2012.

[HHN03] Akihiko Hirata, M. Harada, and T. Nagatsuma. 120-GHz wireless link using photonic techniques for generation, modulation, and emission of millimeter-wave signals. *Lightwave Technology, Journal of*, 21(10):2145–2153, Oct 2003.

[HHR05] Juo-Jung Hung, T.M. Hancock, and G.M. Rebeiz. A 77 GHz SiGe sub-harmonic balanced mixer. *Solid-State Circuits, IEEE Journal of*, 40(11):2167–2173, Nov 2005.

[HKT+06] Akihiko Hirata, T. Kosugi, H. Takahashi, R. Yamaguchi, F. Nakajima, T. Furuta, H. Ito, H. Sugahara, Y. Sato, and T. Nagatsuma. 120-GHz-band millimeter-wave photonic wireless link for 10-Gb/s data transmission. *Microwave Theory and Techniques, IEEE Transactions on*, 54(5):1937–1944, May 2006.

[HKT+10] A. Hirata, T. Kosugi, H. Takahashi, J. Takeuchi, K. Murata, N. Kukutsu, Y. Kado, S. Okabe, T. Ikeda, F. Suginosita, K. Shogen, H. Nishikawa, A. Irino, T. Nakayama, and N. Sudo. 5.8-km 10-Gbps data transmission over a 120-GHz-band wireless link. In *Wireless Information Technology and Systems (ICWITS), 2010 IEEE International Conference on*, pages 1 –4, 282010-sept.3 2010.

[HKT+12] Akihiko Hirata, T. Kosugi, H. Takahashi, J. Takeuchi, H. Togo, M. Yaita, N. Kukutsu, K. Aihara, K. Murata, Y. Sato, T. Nagatsuma, and Y. Kado. 120-GHz-Band Wireless Link Technologies for Outdoor 10-Gbit/s Data Transmission. *Microwave Theory and Techniques, IEEE Transactions on*, 60(3):881–895, March 2012.

[HTY+08] Akihiko Hirata, H. Takahashi, R. Yamaguchi, T. Kosugi, K. Murata, T. Nagatsuma, N. Kukutsu, and Y. Kado. Transmission Characteristics of 120-GHz-Band Wireless Link Using Radio-on-Fiber Technologies. *Lightwave Technology, Journal of*, 26(15):2338–2344, Aug 2008.

[HUL+12] J. Hacker, M. Urteaga, R. Lin, A. Skalare, I. Mehdi, J-S Rieh, and M. Kim. 400 GHz HBT Differential Amplifier Using Unbalanced Feed Networks. *Microwave and Wireless Components Letters, IEEE*, 22(10):536–538, Oct 2012.

[HW11] Kao-Cheng Huang and Zhaocheng Wang. *Millimeter wave communication systems*. IEEE Press series on digital and mobile communication. Wiley, Hoboken, N.J, online-ausg. edition, c2011.

[HYT+09] A. Hirata, R. Yamaguchi, H. Takahashi, T. Kosugi, K. Murata, N. Kukutsu, and Y. Kado. Effect of Rain Attenuation for a 10-Gb/s 120-GHz-Band Millimeter-Wave Wireless Link. *Microwave Theory and Techniques, IEEE Transactions on*, 57(12):3099 –3105, dec. 2009.

[HYW+11] Shih-Jou Huang, Yu-Ching Yeh, Huaide Wang, Pang-Ning Chen, and Jri Lee. W -Band BPSK and QPSK Transceivers With Costas-Loop Carrier Recovery in 65-nm CMOS Technology. *Solid-State Circuits, IEEE Journal of*, 46(12):3033–3046, Dec 2011.

[ICU+11] O. Inac, B. Cetinoneri, M. Uzunkol, Y.A. Atesal, and G.M. Rebeiz. Millimeter-Wave and THz Circuits in 45-nm SOI CMOS. In *Compound Semiconductor Integrated Circuit Symposium (CSICS), 2011 IEEE*, pages 1–4, Oct 2011.

[IEE99] IEEE. Ieee standard 802.11a: Standard for wireless lan medium access control (mac) and physical layer (phy) specifications: High speed physical layer in the 5ghz band, 1999.

[IEE13] IEEE. IEEE FORMS STUDY GROUP TO EXPLORE 100 Gbps TRANSMISSION OVER EXTREMELY HIGH FREQUENCY WIRELESS POINT-TO-POINT LINKS. online: http://standards.ieee.org/news/2013/ieee_802.15.3_sg.html, October 2013. last accessed 03-03-2014.

[IKM+04] H. Ito, Satoshi Kodama, Y. Muramoto, T. Furuta, T. Nagatsuma, and T. Ishibashi. High-speed and high-output InP-InGaAs

unitraveling-carrier photodiodes. *Selected Topics in Quantum Electronics, IEEE Journal of*, 10(4):709–727, July 2004.

[ISS+12] K. Ishigaki, M. Shiraishi, S. Suzuki, M. Asada, N. Nishiyama, and S. Arai. Direct intensity modulation and wireless data transmission characteristics of terahertz-oscillating resonant tunnelling diodes. *Electronics Letters*, 48(10):582–583, May 2012.

[ITU12] ITU. *Radio Regulations Edition of 2012, Articles*. International Telecommunications Union, 2012.

[J. 12] J. Antes, S. Koenig, A. Leuther, H. Massler, J. Leuthold, O. Ambacher, I. Kallfass. 220 GHz wireless data transmission experiments up to 30 Gbit/s. *in Proc. IEEE MTT-S Int. Microwave Symposium, Montreal*, June 2012.

[JK10] T.K. Johansen and V. Krozer. An InP HBT sub-harmonic mixer for E-band wireless communication. In *Microwave Integrated Circuits Conference (EuMIC), 2010 European*, pages 198–201, Sept 2010.

[JPS+10] C. Jastrow, S. Priebe, B. Spitschan, J. Hartmann, M. Jacob, T. Kurner, T. Schrader, and T. Kleine-Ostmann. Wireless digital data transmission at 300 GHz. *Electronics Letters*, 46(9):661 –663, 29 2010.

[JYY+12] Wen-Jr Jiang, Hejie Yang, Yi-Ming Yang, Chun-Ting Lin, and A. Ng'oma. 40 Gb/s RoF signal transmission with 10 m wireless distance at 60 GHz. In *Optical Fiber Communication Conference and Exposition (OFC/NFOEC), 2012 and the National Fiber Optic Engineers Conference*, pages 1–3, March 2012.

[KBYC+12] O. Katz, R. Ben-Yishay, R. Carmon, B. Sheinman, F. Szenher, D. Papae, and D. Elad. A fully integrated SiGe E-BAND transceiver chipset for broadband point-to-point communication. In *Radio and Wireless Symposium (RWS), 2012 IEEE*, pages 431–434, Jan 2012.

[Kel77] AJ. Kelly. Fundamental limits on conversion loss of double sideband resistive mixers. *Microwave Theory and Techniques, IEEE Transactions on*, 25(11):867–869, Nov 1977.

[KHK+08] N. Kukutsu, A. Hirata, T. Kosugi, H. Takahashi, R. Yamaguchi, T. Nagatsuma, and Y. Kado. 10-Gbit/s wireless link using 120-

GHz-band MMIC technologies. In *Infrared, Millimeter and Terahertz Waves, 2008. IRMMW-THz 2008. 33rd International Conference on*, pages 1 –2, sept. 2008.

[KIM+11] A. Kanno, K. Inagaki, I. Morohashi, T. Sakamoto, T. Kuri, I. Hosako, T. Kawanishi, Y. Yoshida, and K. Kitayama. 40 Gb/s W-band (75-110 GHz) 16-QAM radio-over-fiber signal generation and its wireless transmission. In *Optical Communication (ECOC), 2011 37th European Conference and Exhibition on*, pages 1–3, 2011.

[KJC12] Jong Ho Kim, Myoung-Won Jung, and Young Jun Chong. Rain attenuation at 73GHz terrestrial link. In *ICT Convergence (ICTC), 2012 International Conference on*, pages 456–457, Oct 2012.

[KJYC13] Jong Ho Kim, Myoung-Won Jung, Young Keun Yoon, and Young Jun Chong. The measurements of rain attenuation for terrestrial link at millimeter Wave. In *ICT Convergence (ICTC), 2013 International Conference on*, pages 848–849, Oct 2013.

[KKK+10] Min-Soo Kang, Bong-Su Kim, Kwang-Seon Kim, Woo-Jin Byun, Myung-Sun Song, and Seung-Hyeub Oh. Wireless ptp system in e-band for gigabit ethernet. In *Advanced Communication Technology (ICACT), 2010 The 12th International Conference on*, volume 1, pages 733–736, Feb 2010.

[KKKB14] Minsoo Kang, Bongsu Kim, Kwangseon Kim, and Woojin Byun. 70/80ghz transceiver module for gbps wireless p2p link. In *Wireless and Microwave Technology Conference (WAMICON), 2014 IEEE 15th Annual*, pages 1–3, June 2014.

[KKP+14] M.R. Khanzadi, D. Kuylenstierna, A. Panahi, T. Eriksson, and H. Zirath. Calculation of the Performance of Communication Systems From Measured Oscillator Phase Noise. *Circuits and Systems I: Regular Papers, IEEE Transactions on*, 61(5):1553–1565, May 2014.

[KM13] Ning Kong and L.B. Milstein. SNR Increase Per-Bit-Increase for MPSK and MQAM Signals and SNR Penalty of Using MPSK over MQAM for a Rayleigh Fading Channel. In *Military Communications Conference, MILCOM 2013 - 2013 IEEE*, pages 775–780, Nov 2013.

[Kön14] Swen König. *Semiconductor Optical Amplifiers and mm-Wave Wireless Links for Converged Access Networks*. PhD thesis, Karlsruher Institut für Technologie (KIT), Karlsruhe, 2014. Zugl.: Karlsruhe, KIT, Diss., 2013.

[KTE+04] T. Kosugi, M. Tokumitsu, T. Enoki, M. Muraguchi, A. Hirata, and T. Nagatsuma. 120-GHz Tx/Rx chipset for 10-Gbit/s wireless applications using 0.1 μm-gate InP HEMTs. In *Compound Semiconductor Integrated Circuit Symposium, 2004. IEEE*, pages 171 – 174, oct. 2004.

[KTM+09] I. Kallfass, A. Tessmann, H. Massler, D. Lopez-Diaz, A. Leuther, M. Schlechtweg, and O. Ambacher. A 300 GHz active frequency-doubler and integrated resistive mixer MMIC. In *Microwave Integrated Circuits Conference, 2009. EuMIC 2009. European*, pages 200–203, 2009.

[Kür12] Thomas Kürner. Towards Future THz Communications Systems. *Journal Terahertz & Technology*, 5(1):11–17, March 2012.

[Kür13] Thomas Kürner. THz Communications – An Option for Wireless 100 Gbps. Telecommunications Forum, FTW Forschungszentrum Telekommunikation Vienna, http://www.ftw.at/events/telecommunications-forum/thz-communications-an-option-for-wireless-100-gbps, last accessed 03-03-2014, March 2013.

[Kur14] Michael Kuri. personal correspondence. Fraunhofer IAF, 2014.

[KVK+06] M. Kantanen, M. Varonen, M. Karkkainen, T. Karttaavi, R. Weber, A. Leuther, M. Seelmann-Eggebert, T. Narhi, and K.A.I. Halonen. Coplanar 155 GHz MHEMT MMIC low noise amplifiers. In *Microwave Conference, 2006. APMC 2006. Asia-Pacific*, pages 173 –176, dec. 2006.

[LAL+07] Sang Jin Lee, Dan An, Mun Kyo Lee, Tae Jong Baek, Byoung-Chul Jun, Sung-Woon Moon, and Chang Hyun Park. 94 GHz single balanced cascode mixer using CPW tandem couplers. In *Microwave Integrated Circuit Conference, 2007. EuMIC 2007. European*, pages 187–190, 2007.

[Lan69] J. Lange. Interdigitated Strip-Line Quadrature Hybrid. In *Microwave Symposium, 1969 G-MTT International*, pages 10–13, May 1969.

[LDAF15] Daniel Lopez-Diaz, Oliver Ambacher, and Fraunhofer IAF Freiburg. *Broadband Transceiver Circuits for Millimeter-Wave Wireless Communication*. Fraunhofer Verlag, Stuttgart, 2015.

[LDKT+12] D. Lopez-Diaz, I. Kallfass, A. Tessmann, A. Leuther, S. Wagner, M. Schlechtweg, and O. Ambacher. A subharmonic chipset for gigabit communication around 240 GHz. In *Microwave Symposium Digest (MTT), 2012 IEEE MTT-S International*, pages 1–3, 2012.

[Lee03] C. D. Lee. DC offset elimination analysis in zero-IF receiver. In *Communications, 2003. APCC 2003. The 9th Asia-Pacific Conference on*, volume 2, pages 675–679 Vol.2, Sept 2003.

[LETM14] E. Larsson, O. Edfors, F. Tufvesson, and T. Marzetta. Massive MIMO for next generation wireless systems. *Communications Magazine, IEEE*, 52(2):186–195, February 2014.

[LHC+09] L. B. Lok, C.-J. Hwang, H.M.H. Chong, I.G. Thayne, and K. Elgaid. A W-band MMIC vector modulator utilizing tandem couplers and 50nm MHEMTs. In *Microwave Conference, 2009. EuMC 2009. European*, pages 1251–1254, 2009.

[LK95] E.W. Lin and W.H. Ku. Device considerations and modeling for the design of an InP-based MODFET millimeter-wave resistive mixer with superior conversion efficiency. *Microwave Theory and Techniques, IEEE Transactions on*, 43(8):1951–1959, Aug 1995.

[LKS+13] P.V. Larkoski, P. Kangaslahti, L. Samoska, R. Lai, S. Sarkozy, and S.E. Church. Low noise amplifiers for 140 GHz wide-band cryogenic receivers. In *Microwave Symposium Digest (IMS), 2013 IEEE MTT-S International*, pages 1–4, June 2013.

[LKT+11] A. Leuther, S. Koch, A. Tessmann, I. Kallfass, T. Merkle, H. Massler, R. Loesch, M. Schlechtweg, S. Saito, and O. Ambacher. 20 nm metamorphic HEMT with 660 GHz fT. In *Compound Semiconductor Week (CSW/IPRM), 2011 and 23rd International Conference on Indium Phosphide and Related Materials*, pages 1–4, May 2011.

[LLL+08] Mun-Kyo Lee, Byeong-Ok Lim, Sang-Jin Lee, Dong-Sik Ko, Sung-Woon Moon, Dan An, Yong-Hoh Kim, Sam-Dong Kim, Hyun-Chang Park, and Jin-Koo Rhee. A Novel 94-GHz MHEMT-Based Diode Mixer Using a 3-dB Tandem Coupler. *Microwave and Wireless Components Letters, IEEE*, 18(9):626–628, 2008.

[LMH89] H.J. Liebe, T. Manabe, and George A Hufford. Millimeter-wave attenuation and delay rates due to fog/cloud conditions. *Antennas and Propagation, IEEE Transactions on*, 37(12):1617–1612, Dec 1989.

[LP09] D. Lockie and D. Peck. High-data-rate millimeter-wave radios. *Microwave Magazine, IEEE*, 10(5):75–83, August 2009.

[LRPR04] P. Laferriere, D. Rahn, C. Plett, and J. Rogers. A 5 GHz direct-conversion receiver with DC offset correction. In *Circuits and Systems, 2004. ISCAS '04. Proceedings of the 2004 International Symposium on*, volume 4, pages IV–269–72 Vol.4, May 2004.

[LS13] Gang Liu and H. Schumacher. Broadband Millimeter-Wave LNAs (47-77 GHz and 70-140 GHz) Using a T-Type Matching Topology. *Solid-State Circuits, IEEE Journal of*, 48(9):2022–2029, Sept 2013.

[LTD+07] A. Leuther, A. Tessmann, M. Dammann, C. Schworer, M. Schlechtweg, M. Mikulla, R. Lösch, and G. Weimann. 50 nm MHEMT Technology for G- and H-Band MMICs. In *Indium Phosphide Related Materials, 2007. IPRM '07. IEEE 19th International Conference on*, pages 24 –27, may 2007.

[LTD+13] A. Leuther, A. Tessmann, M. Dammann, H. Massler, M. Schlechtweg, and O. Ambacher. 35 nm mHEMT Technology for THz and ultra low noise applications. In *Indium Phosphide and Related Materials (IPRM), 2013 International Conference on*, pages 1–2, May 2013.

[LTM+11] U. Lewark, A. Tessmann, H. Massler, A. Leuther, and I. Kallfass. Active frequency multiplier-by-nine MMIC for millimeter-wave signal generation. In *Microwave Conference (GeMIC), 2011 German*, pages 1–4, March 2011.

[LTM+12] Ulrich J. Lewark, A. Tessmann, H. Massler, P. Leuther, and I. Kallfass. E-band active frequency-multiplier-by-eight MMIC with >20 dB conversion gain and excellent spurious suppression. In

Microwave Symposium Digest (MTT), 2012 IEEE MTT-S International, pages 1–3, 2012.

[LTW+12] U.J. Lewark, A. Tessmann, S. Wagner, A. Leuther, T. Zwick, and I. Kallfass. 255 to 330 GHz active frequency tripler MMIC. In *Integrated Nonlinear Microwave and Millimetre-Wave Circuits (INMMIC), 2012 Workshop on*, pages 1–3, 2012.

[Lyo08] Richard Lyon. Quadrature signals: Complex, but not complicated. IEEE, Long Island section, online: http://www.ieee.li/pdf/essay/quadrature_signals.pdf, October 2008. last accessed 04-07-2014.

[LYT+13] Wei-Heng Lin, Hong-Yuan Yang, Jeng-Han Tsai, Tian-Wei Huang, and Huei Wang. 1024-QAM High Image Rejection E -Band Sub-Harmonic IQ Modulator and Transmitter in 65-nm CMOS Process. *Microwave Theory and Techniques, IEEE Transactions on*, 61(11):3974–3985, Nov 2013.

[LYZ+13] Xinying Li, Jianjun Yu, Junwen Zhang, Ze Dong, Fan Li, and Nan Chi. A 400G optical wireless integration delivery system. *Opt. Express*, 21(16):18812–18819, Aug 2013.

[LZL10] Jiang Lan, Zhonghua Zhang, and Zhengkun Li. A high accurate signal generator based on direct digital frequency synthesis. In *Precision Electromagnetic Measurements (CPEM), 2010 Conference on*, pages 484–485, June 2010.

[M. 13] M. Grigat. Propagation Aspects of Terahertz Outdoor Fixed Wireless Link. *IEEE802 Pleanry Session, Orlando, IEEE 802.15 Document 13-0175-00-0thz*, March 2013.

[MA09] H.A. Mahmoud and H. Arslan. Error vector magnitude to SNR conversion for nondata-aided receivers. *Wireless Communications, IEEE Transactions on*, 8(5):2694–2704, 2009.

[Maa87] S.A. Maas. A GaAs MESFET Mixer with Very Low Intermodulation. *Microwave Theory and Techniques, IEEE Transactions on*, 35(4):425–429, Apr 1987.

[Maa93] Stephen A. Maas. *Microwave mixers*. Artech House microwave library. Artech House, Boston [u.a.], 2. ed. edition, 1993.

[Mak12] S. Makovejs. Wired or wireless? online: http://www.corning.com/opticalfiber/fiberbasics/companion/wireless/default.aspx, 2012. last accessed 04-14-2014.

[MHO+06] Sung-Woon Moon, Min Han, Jung-Hun Oh, Jin-Koo Rhee, and Sam-Dong Kim. V-band CPW 3-dB Tandem coupler using air-bridge structure. *Microwave and Wireless Components Letters, IEEE*, 16(4):149–151, 2006.

[Mim02] T. Mimura. The early history of the high electron mobility transistor (HEMT). *Microwave Theory and Techniques, IEEE Transactions on*, 50(3):780–782, Mar 2002.

[MKM+14] H. Mehrpouyan, M.R. Khanzadi, M. Matthaiou, A.M. Sayeed, R. Schober, and Yingbo Hua. Improving bandwidth efficiency in E-band communication systems. *Communications Magazine, IEEE*, 52(3):121–128, March 2014.

[MKS+11] A. Mineyama, Y. Kawano, M. Sato, T. Suzuki, N. Hara, and K. Joshin. A millimeter-wave CMOS low noise amplifier using transformer neutralization techniques. In *Microwave Conference Proceedings (APMC), 2011 Asia-Pacific*, pages 223–226, Dec 2011.

[MM00] S. Mirabbasi and Ken Martin. Hierarchical QAM: a spectrally efficient dc-free modulation scheme. *Communications Magazine, IEEE*, 38(11):140–146, Nov 2000.

[MMMFOM11] A. Moscoso-Martir, I. Molina-Fernandez, and A. Ortega-Monux. Signal constellation distortion and ber degradation due to hardware impairments in six-port receivers with analog i/q generation. In *Progress In Electromagnetics Research*, volume 121, pages 225–247, 2011.

[MO13] S. J. Malinga and P. A. Owolawi. Obtaining raindrop size model using method of moment and its applications for south africa radio systems. *Progress In Electromagnetics Research B*, 46:119–138, 2013.

[Mol11] Andreas F. Molisch. *Wireless communications*. Wiley, Chichester, 2. ed. edition, 2011.

[Moo98] G.E. Moore. Cramming more components onto integrated circuits. *Proceedings of the IEEE*, 86(1):82–85, Jan 1998.

[MP05] M. Marcus and B. Pattan. Millimeter wave propagation; spectrum management implications. *Microwave Magazine, IEEE*, 6(2):54–62, June 2005.

[MRO+09] A. Man, M.R.C. Rose, M.N. Osman, S. Yaakob, M.R. Yahya, and A.F.A. Mat. Short-range point-to-point gigabit wireless transmission at 50 GHz. In *Communications (MICC), 2009 IEEE 9th Malaysia International Conference on*, pages 709–712, Dec 2009.

[MSB+13] Yanfei Mao, K. Schmalz, J. Borngräber, J.C. Scheytt, and C. Meliani. 245 GHz subharmonic receivers in SiGe. In *Radio Frequency Integrated Circuits Symposium (RFIC), 2013 IEEE*, pages 101–104, 2013.

[MSBS12] Yanfei Mao, K. Schmalz, J. Borngraber, and J.C. Scheytt. 245 GHz subharmonic receiver in SiGe. In *Microwave Integrated Circuits Conference (EuMIC), 2012 7th European*, pages 183–186, 2012.

[MTA08] E. Moldovan, S.-O. Tatu, and S. Affes. A 60 GHz Multi-port Receiver with Analog Carrier Recovery for Ultra Wideband Wireless Personal Area Networks. In *Microwave Conference, 2008. EuMC 2008. 38th European*, pages 1779–1782, Oct 2008.

[MW10] J. Moreira and H. Werkmann. *An Engineer's Guide to Automated Testing of High-Speed Interfaces*. Artech House microwave library. Artech House, 2010.

[N. 13] N. Sekine, A. Kanno, T. Kuri, I. Morohashi, A. Kasamatsu, I. Hosako, T. Kawanishi. 30-Gbps-class terahertz transmission using optical sub-harmonic IQ mixer for backhaul/fronthaul directly connected to optical networks. *IEEE802 Pleanry Session, Dallas, IEEE 802.15 Document 13-0653-00-0thz*, Nov 2013.

[NA00] T. Nakagawa and K. Araki. Effect of phase noise on RF communication signals. In *Vehicular Technology Conference, 2000. IEEE-VTS Fall VTC 2000. 52nd*, volume 2, pages 588–591 vol.2, 2000.

[Nag13] T. Nagatsuma. Generating millimeter and terahertz waves by photonics for communications and sensing. In *Microwave Symposium Digest (IMS), 2013 IEEE MTT-S International*, pages 1–3, June 2013.

[NAM13] J.A. Nessel, R.J. Acosta, and F.A. Miranda. Preliminary experiments for the assessment of V/W-band links for space-earth communications. In *Antennas and Propagation Society International Symposium (APSURSI), 2013 IEEE*, pages 1616–1617, July 2013.

[NEC14] NEC corporation. Compact e-band radio enables ultra high speed transmissions for small cell backhaul, wireless fiber broadband extensions and cpri for cloud ran. online: http://www.nec.com/en/press/201402/global_20140213_03.html, 02 2014. last accessed 04-04-2014.

[NHM+13] Tadao Nagatsuma, Shogo Horiguchi, Yusuke Minamikata, Yasuyuki Yoshimizu, Shintaro Hisatake, Shigeru Kuwano, Naoto Yoshimoto, Jun Terada, and Hiroyuki Takahashi. Terahertz wireless communications based on photonics technologies. *Opt. Express*, 21(23736-23747), 2013.

[NIS+13] R. Nalinggam, W. Ismail, M.J. Singh, M.T. Islam, and P.S. Menon. Development of rain attenuation model for southeast asia equatorial climate. *Communications, IET*, 7(10):1008–1014, July 2013.

[NLA+13] I. Nasr, B. Laemmle, K. Aufinger, G. Fischer, R. Weigel, and D. Kissinger. A 70-90-GHz High-Linearity Multi-Band Quadrature Receiver in 0.35-μm SiGe Technology. *Microwave Theory and Techniques, IEEE Transactions on*, 61(12):4600–4612, Dec 2013.

[NOS13] A. Nassery, S. Ozev, and M. Slamani. Analytical modeling for EVM in OFDM transmitters including the effects of IIP3, I/Q imbalance, noise, AM/AM and AM/PM distortion. In *Test Symposium (ETS), 2013 18th IEEE European*, pages 1–6, 2013.

[OHP11] E. Ojefors, B. Heinemann, and U.R. Pfeiffer. A 220GHz subharmonic receiver front end in a SiGe HBT technology. In *Radio Frequency Integrated Circuits Symposium (RFIC), 2011 IEEE*, pages 1–4, 2011.

[OHP12] E. Ojefors, B. Heinemann, and U.R. Pfeiffer. Subharmonic 220- and 320-GHz SiGe HBT Receiver Front-Ends. *Microwave Theory and Techniques, IEEE Transactions on*, 60(5):1397–1404, 2012.

[OMI+03] K. Ohata, K. Maruhashi, M. Ito, S. Kishimoto, K. Ikuina, T. Hashiguchi, K. Ikeda, and N. Takahashi. 1.25 Gbps wireless Gi-

gabit ethernet link at 60 GHz-band. In *Radio Frequency Integrated Circuits (RFIC) Symposium, 2003 IEEE*, pages 509–512, June 2003.

[ONFI05] T. Ohno, F. Nakajima, T. Furuta, and H. Ito. A 240-GHz active mode-locked laser diode for ultra-broadband fiber-radio transmission systems. In *Optical Fiber Communication Conference, 2005. Technical Digest. OFC/NFOEC*, volume 6, pages 3 pp. Vol. 5–, 2005.

[PCD+11] Xiaodan Pang, Antonio Caballero, Anton Dogadaev, Valeria Arlunno, Robert Borkowski, Jesper S. Pedersen, Lei Deng, Fotini Karinou, Fabien Roubeau, Darko Zibar, Xianbin Yu, and Idelfonso Tafur Monroy. 100 Gbit/s hybrid optical fiber-wireless link in the W-band (75-110 GHz). *Opt. Express*, 19(25):24944–24949, Dec 2011.

[Poz05] David M. Pozar. *Microwave engineering*. Wiley, Hoboken, NJ, 3. ed. edition, 2005. Previous ed.: 1998.

[PTF+10] F. Palma, F. Teppe, A.E. Fatimy, R. Green, J. Xu, Y. Vachontin, A. Tredicucci, G. Goltsman, and W. Knap. Thz communication system based on a thz quantum cascade laser and a hot electron bolometer. In *Infrared Millimeter and Terahertz Waves (IRMMW-THz), 2010 35th International Conference on*, pages 1–2, Sept 2010.

[PWB+13] Stefan Preußler, Norman Wenzel, Ralf-Peter Braun, Nina Owschimikow, Carlo Vogel, Anselm Deninger, Avi Zadok, Ulrike Woggon, and Thomas Schneider. Generation of ultra-narrow, stable and tunable millimeter- and terahertz- waves with very low phase noise. *Opt. Express*, 21(20):23950–23962, Oct 2013.

[Raz97] B. Razavi. Design considerations for direct-conversion receivers. *Circuits and Systems II: Analog and Digital Signal Processing, IEEE Transactions on*, 44(6):428–435, Jun 1997.

[RDPC06] John W. M. Rogers, Foster F. Dai, Calvin Plett, and Mark S. Cavin. Design and Characterization of a 5.2 GHz/2.4 GHz fractional-N Frequency Synthesizer for Low-phase Noise Performance. *EURASIP J. Wirel. Commun. Netw.*, 2006(2):26–26, April 2006.

[Rec05] I.T.U. Recommendation. Specific attenuation model for rain for use in prediction methods. In *ITU-P P.838-3*, 2005.

[Rec07] I.T.U. Recommendation. Characteristics of precipitation for propagation modelling. In *ITU-P P.837-5*, 2007.

[Rec09a] ITU Recommendation. Attenuation by atmospheric gases. In *ITU-R P.676-8*, 10 2009.

[Rec09b] I.T.U. Recommendation. Attenuation due to clouds and fog. In *ITU-R P.840-4*, 10 2009.

[S. 13] S. Koenig, D. Lopez-Diaz, J. Antes, F. Boes, R. Henneberger, A. Leuther, A. Tessmann, R. Schmogrow, D. Hillerkuss, R. Palmer, T. Zwick, C. Koos, W. Freude, O. Ambacher, J. Leuthold, I. Kallfass. Wireless sub-THz communication system with high data rate. *Nature Photonics*, Oct. 2013.

[SAH+09a] H.-J. Song, K. Ajito, A. Hirata, A. Wakatsuki, T. Furuta, N. Kukutsu, and T. Nagatsuma. Multi-gigabit wireless data transmission at over 200-GHz. In *Infrared, Millimeter, and Terahertz Waves, 2009. IRMMW-THz 2009. 34th International Conference on*, pages 1 –2, sept. 2009.

[SAH+09b] H.-J. Song, K. Ajito, A. Hirata, A. Wakatsuki, Y. Muramoto, T. Furuta, N. Kukutsu, T. Nagatsuma, and Y. Kado. 8 Gbit/s wireless data transmission at 250 GHz. *Electronics Letters*, 45(22):1121–1122, October 2009.

[Sal71] A.A.M. Saleh. *Theory of Resistive Mixers*. Number Bd. 2 in M.I.T. Press. Research Monographs. M.I.T. Press, 1971.

[SAM+12] H.-J. Song, K. Ajito, Y. Muramoto, A. Wakatsuki, T. Nagatsuma, and N. Kukutsu. 24 Gbit/s data transmission in 300 GHz band for future terahertz communications. *Electronics Letters*, 48(15):953–954, 2012.

[SAW+10] Ho-Jin Song, K. Ajito, A. Wakatsuki, Y. Muramoto, N. Kukutsu, Y. Kado, and T. Nagatsuma. Terahertz wireless communication link at 300 GHz. In *Microwave Photonics (MWP), 2010 IEEE Topical Meeting on*, pages 42 –45, oct. 2010.

[SBC+10] A. Stohr, S. Babiel, P.J. Cannard, B. Charbonnier, F. Van-Dijk, S. Fedderwitz, D. Moodie, L. Pavlovic, L. Ponnampalam, Cyril C. Renaud, D. Rogers, V. Rymanov, A. Seeds, A.G. Steffan, A. Umbach, and M. Weiss. Millimeter-Wave Photonic Components for Broadband Wireless Systems. *Microwave Theory and Techniques, IEEE Transactions on*, 58(11):3071–3082, Nov 2010.

[SBM+12] K. Schmalz, J. Borngraber, Yanfei Mao, H. Rucker, and R. Weber. A 245 GHz LNA in SiGe Technology. *Microwave and Wireless Components Letters, IEEE*, 22(10):533–535, Oct 2012.

[Sen85] John M. Senior. *Optical fiber communications : principles and practice*. Prentice-Hall international series in optoelectronics. Prentice-Hall International, New York, NY [u.a.], 1985.

[Sha84] C.E. Shannon. Communication in the presence of noise. *Proceedings of the IEEE*, 72(9):1192–1201, 1984.

[SKA+13] Ho-Jin Song, Jae-Young Kim, K. Ajito, M. Yaita, and N. Kukutsu. Fully Integrated ASK Receiver MMIC for Terahertz Communications at 300 GHz. *Terahertz Science and Technology, IEEE Transactions on*, 3(4):445–452, July 2013.

[SLL+11] S. Sarkozy, K. Leong, R. Lai, R. Leakey, W. Yoshida, X. Mei, J. Lee, P.-H. Liu, B. Gorospe, and W. R. Deal. Broadband sub-millimeter wave amplifer module with 38dB gain and 8.3dB noise figure. In *Proc. SPIE 8023*, volume 8023 of *Terahertz Physics, Devices, and Systems V: Advance Applications in Industry and Defense, 80230G*, pages 80230G–80230G–6, May 2011.

[SMBF12] Ke Su, Lothar Moeller, Robert B. Barat, and John F. Federici. Experimental comparison of performance degradation from terahertz and infrared wireless links in fog. *J. Opt. Soc. Am. A*, 29(2):179–184, Feb 2012.

[Smi93] David R. Smith. *Digital transmission systems*. van Nostrand Reinhold, New York, 2. ed. edition, 1993.

[SMKN11] T. Shiode, T. Mukai, M. Kawamura, and T. Nagatsuma. Gigabit wireless communication at 300 GHz using resonant tunneling diode detector. In *Microwave Conference Proceedings (APMC), 2011 Asia-Pacific*, pages 1122–1125, 2011.

[SNW+12] R. Schmogrow, B. Nebendahl, M. Winter, A. Josten, D. Hillerkuss, S. Koenig, J. Meyer, M. Dreschmann, M. Huebner, C. Koos, J. Becker, W. Freude, and J. Leuthold. Error Vector Magnitude as a Performance Measure for Advanced Modulation Formats. *Photonics Technology Letters, IEEE*, 24(1):61–63, 2012.

[SRI06] R.A. Shafik, S. Rahman, and R. Islam. On the Extended Relationships Among EVM, BER and SNR as Performance Metrics. In

Electrical and Computer Engineering, 2006. ICECE '06. International Conference on, pages 408–411, 2006.

[STK+11] M. Schlechtweg, A. Tessmann, I. Kallfass, A. Leuther, V. Hurm, H. Massler, M. Riessle, R. Losch, and O. Ambacher. Millimeter-wave circuits and modules up to 500 GHz based on metamorphic HEMT technology for remote sensing and wireless communication applications. In *New Circuits and Systems Conference (NEWCAS), 2011 IEEE 9th International*, pages 269–272, June 2011.

[SVP+13] S. Sarkozy, M. Vukovic, J.G. Padilla, J. Chang, G. Tseng, P. Tran, P. Yocom, W. Yamasaki, K.M.K.H. Leong, and W. Lee. Demonstration of a G-Band Transceiver for Future Space Crosslinks. *Terahertz Science and Technology, IEEE Transactions on*, 3(5):675–681, Sept 2013.

[SWF+08] Andreas Stoehr, Mario Weiss, Sascha Fedderwitz, Dieter Jaeger, Mathieu Huchard, and Benoit Charbonnier. 60 GHz Wireless Photonic Link System for 12.5Gb/s Data Transmission. In *Photonic Networks, 2008 ITG Symposium on*, pages 1–4, April 2008.

[SWL10] F. Schwierz, H. Wong, and J.J. Liou. *Nanometer CMOS*. Pan Stanford, 2010.

[SWP+12] T. Schneider, A. Wiatrek, S. Preubler, Ralf-Peter Braun, and M. Grigat. Maximum transmittable data rates for Millimeter-wave fixed wireless links. In *ELEKTRO, 2012*, pages 94–98, May 2012.

[SZC+10] R. Sambaraju, D. Zibar, A. Caballero, I.T. Monroy, R. Alemany, and J. Herrera. 100-GHz Wireless-Over-Fiber Links With Up to 16-Gb/s QPSK Modulation Using Optical Heterodyne Generation and Digital Coherent Detection. *Photonics Technology Letters, IEEE*, 22(22):1650–1652, Nov 2010.

[Tec] Agilent Technologies. How do the 89400 and 89600 families of vector signal analyzers (VSA) perform carrier-locking on a digitally-modulated signal and what is the lock loop or carrier-tracking bandwidth? online: http://www.home.agilent.com/agilent/editorial.jspx?ckey=451012&id=451012&nid=-11143.0.00&lc=eng&cc=US. last accessed 07-31-2014.

[Tec05] Agilent Technologies. 8 Hints for Making and Interpreting EVM Measurements. online: http://cp.literature.agilent.com/litweb/pdf/5989-3144EN.pdf, 5 2005. last accessed 07-31-2014.

[Tec10] Agilent Technologies. Digital Signal Analysis. online: http://www.home.agilent.com/upload/cmc_upload/All/PPT4_AGILENT_La-modulation-numerique.pdf, 5 2010. last accessed 07-31-2014.

[Tec11] Agilent Technologies. Option AYA Flexible Modulation Analyses, 89600 Vector Signal Analysis Software, Focus on Adaptive Equalization - Self-guided Demonstration. online: http://literature.cdn.keysight.com/litweb/pdf/5989-7410EN.pdf, 02 2011. last accessed 10-30-2014.

[Tec12a] Agilent Technologies. Agilent E8257D PSG Microwave Analog Signal Generator Data Sheet. online: cp.literature.agilent.com/litweb/pdf/5989-0698EN.pdf, 08 2012. last accessed 07-31-2014.

[Tec12b] Agilent Technologies. Vector Signal Analysis Basics Application Note. online: http://cp.literature.agilent.com/litweb/pdf/5990-7451EN.pdf, 11 2012. last accessed 07-31-2014.

[Tec13] Agilent Technologies. Understanding Phase Noise Needs and Choices in Signal Generation. online: cp.literature.agilent.com/litweb/pdf/5991-1744EN.pdf, 01 2013. last accessed 07-31-2014.

[Tek14] Inc. Tektronix. AWG70000A Series Datasheet. online: http://www.tek.com/datasheet/awg70000a/awg70000a-series-datasheet, 01 2014. last accessed 04-08-2014.

[Tes05] A Tessmann. 220-GHz metamorphic HEMT amplifier MMICs for high-resolution imaging applications. *Solid-State Circuits, IEEE Journal of*, 40(10):2070–2076, Oct 2005.

[Tes14] Axel Tessmann. personal correspondence. Fraunhofer IAF, 2014.

[TGV10] A. Tomkins, P. Garcia, and S.P. Voinigescu. A Passive W-Band Imaging Receiver in 65-nm Bulk CMOS. *Solid-State Circuits, IEEE Journal of*, 45(10):1981–1991, Oct 2010.

[THL+14] Axel Tessmann, Volker Hurm, Arnulf Leuther, Hermann Massler, Rainer Weber, Michael Kuri, Markus Riessle, Hans-Peter Stulz, Martin Zink, Michael Schlechtweg, Oliver Ambacher, and Tapani

Närhi. 243 GHz low-noise amplifier MMICs and modules based on metamorphic HEMT technology. *International Journal of Microwave and Wireless Technologies*, FirstView:1–9, 2 2014.

[TKB+13a] K. Tsukashima, M. Kubota, O. Baba, T. Kawasaki, A. Yonamine, T. Tokumitsu, and Y. Hasegawa. E-band receiver and transmitter modules with simply reflow-soldered 3-d wlcsp mmic's. In *Microwave Conference (EuMC), 2013 European*, pages 1559–1562, Oct 2013.

[TKB+13b] K. Tsukashima, M. Kubota, O. Baba, T. Kawasaki, A. Yonamine, T. Tokumitsu, and Y. Hasegawa. E-band receiver and transmitter modules with simply reflow-soldered 3-D WLCSP MMIC's. In *Microwave Integrated Circuits Conference (EuMIC), 2013 European*, pages 588–591, Oct 2013.

[TKY+11] K. Tsukashima, M. Kubota, A Yonamine, T. Tokumitsu, and Y. Hasegawa. E-band radio link communication chipset in cost effective Wafer Level Chip Size Package (WLCSP) technology. In *Microwave Integrated Circuits Conference (EuMIC), 2011 European*, pages 29–32, Oct 2011.

[TLM+08] A Tessmann, A Leuther, H. Massler, M. Kuri, and R. Loesch. A Metamorphic 220-320 GHz HEMT Amplifier MMIC. In *Compound Semiconductor Integrated Circuits Symposium, 2008. CSIC '08. IEEE*, pages 1–4, Oct 2008.

[TLM+10] A. Tessmann, A. Leuther, H. Massler, V. Hurm, M. Kuri, M. Zink, M. Riessle, and R. Losch. High-gain submillimeter-wave mHEMT amplifier MMICs. In *Microwave Symposium Digest (MTT), 2010 IEEE MTT-S International*, pages 53–56, 2010.

[TML+11] A. Tessmann, H. Massler, U. Lewark, S. Wagner, I. Kallfass, and A. Leuther. Fully Integrated 300 GHz Receiver S-MMICs in 50 nm Metamorphic HEMT Technology. In *Compound Semiconductor Integrated Circuit Symposium (CSICS), 2011 IEEE*, pages 1–4, 2011.

[TMW+13] F. Thome, H. Massler, S. Wagner, A. Leuther, I. Kallfass, M. Schlechtweg, and O. Ambacher. Comparison of two W-band low-noise amplifier MMICs with ultra low power consumption based on 50nm InGaAs mHEMT technology. In *Microwave Sym-*

posium Digest (IMS), 2013 IEEE MTT-S International, pages 1–4, June 2013.

[TRG71] Joseph Tierney, C.M. Rader, and B. Gold. A digital frequency synthesizer. *Audio and Electroacoustics, IEEE Transactions on*, 19(1):48–57, Mar 1971.

[TV05] David Tse and Pramod Viswanath. *Fundamentals of Wireless Communication*. Cambridge University Press, New York, NY, USA, 2005.

[VFG07] S. Vitali, E. Franchi, and A. Gnudi. RF I/Q Downconverter With Gain/Phase Calibration. *Circuits and Systems II: Express Briefs, IEEE Transactions on*, 54(4):367–371, April 2007.

[VLF+12] M. Varonen, P. Larkoski, A. Fung, L. Samoska, P. Kangaslahti, T. Gaier, R. Lai, and S. Sarkozy. 160-270-GHz InP HEMT MMIC Low-Noise Amplifiers. In *Compound Semiconductor Integrated Circuit Symposium (CSICS), 2012 IEEE*, pages 1–4, Oct 2012.

[WCN+14] Zheng Wang, Pei-Yuan Chiang, P. Nazari, Chun-Cheng Wang, Zhiming Chen, and P. Heydari. A CMOS 210-GHz Fundamental Transceiver With OOK Modulation. *Solid-State Circuits, IEEE Journal of*, 49(3):564–580, March 2014.

[WDS+10] W. Winkler, W. Debski, K. Schmalz, J. Borngraber, and C. Scheytt. LNA and mixer for 122 GHz receiver in SiGe technology. In *Microwave Conference (EuMC), 2010 European*, pages 529–532, Sept 2010.

[Wea56] D.K. Weaver. A third method of generation and detection of single-sideband signals. *Proceedings of the IRE*, 44(12):1703–1705, Dec 1956.

[Web07] William Webb. *Wireless communications: the future*, chapter 6.3.5. Wiley, Chichester, 2007.

[Wel09] J. Wells. Faster than fiber: The future of multi-G/s wireless. *Microwave Magazine, IEEE*, 10(3):104–112, May 2009.

[WHS+08] M. Weiss, M. Huchard, A. Stohr, B. Charbonnier, S. Fedderwitz, and D.S. Jager. 60-GHz Photonic Millimeter-Wave Link for Short- to Medium-Range Wireless Transmission Up to 12.5 Gb/s. *Lightwave Technology, Journal of*, 26(15):2424–2429, Aug 2008.

[Wil60] E.J. Wilkinson. An N-Way Hybrid Power Divider. *Microwave Theory and Techniques, IRE Transactions on*, 8(1):116–118, January 1960.

[Wil84] James C. Wiltse. History of millimeter and submillimeter waves. *Microwave Theory and Techniques, IEEE Transactions on*, 32(9):1118–1127, Sep 1984.

[WKW+10] E. Weissbrodt, I. Kallfass, R. Weber, A. Tessmann, H. Massler, and A. Leuther. Low-noise amplifiers in D-band using 100 nm and 50 nm mHEMT technology. In *German Microwave Conference, 2010*, pages 55 –58, March 2010.

[WL72] R. Waugh and D. Lacombe. Unfolding the Lange Coupler (Short Papers). *Microwave Theory and Techniques, IEEE Transactions on*, 20(11):777–779, Nov 1972.

[WLC+12] Cheng Wang, Changxing Lin, Qi Chen, Xianjin Deng, and Jian Zhang. 0.14THz high speed data communication over 1.5 kilometers. In *Infrared, Millimeter, and Terahertz Waves (IRMMW-THz), 2012 37th International Conference on*, pages 1–2, Sept 2012.

[WLS+12] E. Weissbrodt, A. Leuther, M. Schlechtweg, I. Kallfass, and O. Ambacher. Highly integrated switching calibration front-end MMIC with active loads for w-band radiometers. In *Microwave Integrated Circuits Conference (EuMIC), 2012 7th European*, pages 203–206, Oct 2012.

[Yhl07] K. Yhland. Simplified Analysis of Resistive Mixers. *Microwave and Wireless Components Letters, IEEE*, 17(8):604–606, Aug 2007.

[YXVG11] Su-Khiong Yong, Pengfei Xia, and Alberto Valdes-Garcia. *60GHz Technology for Gbps WLAN and WPAN: From Theory to Practice*. Wiley Publishing, 2011.

[Zir06] Herbert Zirath. MMIC Design Seminar. IEEE MMIC seminar Bergen, June 2006.

[ZXW+12] Bo Zhang, Yong-Zhong Xiong, Lei Wang, Sangming Hu, and Le-Wei Li. Gain-enhanced 132-160 GHz low-noise amplifier using 0.13 μm SiGe BiCMOS. *Electronics Letters*, 48(5):257–259, March 2012.

List of own publications

[1] F. Boes, T. Messinger, **J. Antes**, D. Meier, A Tessmann, A. Inam, and I. Kallfass. Ultra-Broadband MMIC-Based Wireless Link at 240 GHz Enabled by 64 GS/s DAC. In *39th Conference on Infrared, Millimeter and THz Waves, 2014*, Sep. 2014.

[2] F. Boes, **J. Antes**, T. Mahler, U. Lewark, D. Meier, T. Messinger, R. Henneberger, A Tessmann, T. Zwick, and I Kallfass. Experimental validation of adverse weather effects on a 240 GHz multi-gigabit wireless link. In *Microwave Symposium (IMS), 2014 IEEE MTT-S International*, pages 1–3, June 2014.

[3] F. Boes, **J. Antes**, D. Meier, T Messinger, D Mueller, A. Tessmann, and I. Kallfass. Performance comparison of raised cosine shaped and rectangular pulsed signals in e-band wireless communication systems. In *accepted for presentation at Radio and Wireless Symposium (RWS), 2015 IEEE*, Jan 2015.

[4] D. Lopez-Diaz, A. Tessmann, S. Wagner, M. Schlechtweg, O. Ambacher, F. Kurz, S. Koenig, **J. Antes**, F. Boes, R. Henneberger, I. Kallfass. A 240 GHz Quadrature Receiver and Transmitter for Data Transmission up to 40 Gbit/s. *in Proc. European Microwave Week, Nuremberg*, pages 1–4, 2013.

[5] D. Lopez-Diaz, S. Koenig, **J. Antes**, F. Boes, F. Kurz, R. Henneberger, A. Tessmann, S. Wagner, M. Schlechtweg, I. Kallfass. 240 GHz Receiver and Transmitter Modules for Wireless Data Transmission up to 40 Gbit/s. *in Proc. IEEE Int. Microwave Symp., Seattle*, pages 1–4, 2013.

[6] W. Freude, S. Koenig, D. Lopez-Diaz, **J. Antes**, F. Boes, R. Henneberger, A. Leuther, A. Tessmann, R. Schmogrow, D. Hillerkuss, R. Palmer, T. Zwick, C. Koos, O. Ambacher, J. Leuthold, and I. Kallfass. Wireless communications on THz carriers takes shape. In *Transparent Optical Networks (ICTON), 2014 16th International Conference on*, pages 1–4, July 2014.

[7] I. Kallfass, A. Tessmann, **J. Antes**, D. Lopez-Diaz, M. Kuri, H. Massler, A. Leuther. Wireless DVB-C Transmission at 220 GHz Using Active Single-Chip Receive and Transmit MMICs. *in Proc. IEEE Int. Microwave Symposium, Baltimore*, 2011.

[8] I. Kallfass, D. Lopez-Diaz, S. Diebold, **J. Antes**, A. Tessmann, A. Leuther. Active MMIC Technology for 240 GHz Wireless Data Links. *IEEE P802.15 Working Group for Wireless Personal Area Networks, Dallas, available at https://mentor.ieee.org/802.15/documents*, Nov. 2010.

[9] I. Kallfass, **J. Antes**, D. Lopez-Diaz, A.Tessmann, A. Leuther. Broadband Active Integrated Circuits for Terahertz Communication. *invited, in Proc. 18th European Wireless Conference, Poznan*, pages 1–5, Apr. 2012.

[10] I. Kallfass, **J. Antes**, T. Schneider, F. Kurz, D. Lopez-Diaz, S. Diebold, H. Massler, A. Leuther, A. Tessmann. All Active MMIC Based Wireless Communication at 220 GHz. *IEEE Trans. on Terahertz Science and Technology*, 1(2):477–487, Nov. 2011.

[11] I. Kallfass, **J. Antes**, U. Lewark, D. Lopez-Diaz. MHEMT-Based MMIC Frontends for THz Radar and Communication. *in Proc. Workshop Signal Generation, Amplification, Detection and System Implementation at THz Frequencies, Int. Microwave Symp. IMS and RFIC, Seattle*, 2013.

[12] I. Kallfass, U. Lewark, **J. Antes**, D. Lopez-Diaz, A. Tessmann, A. Leuther. MMIC Chip Sets for Wireless Communication up to 480 GHz. *IEEE802 Plenary Session, San Diego*, July 2012.

[13] **J. Antes**, D. Lopez-Diaz, A. Tessmann, A. Leuther, H. Massler, T. Zwick, O. Ambacher, I. Kallfass. MMIC based wireless data transmission of a 12.5 Gbit/s signal using a 220 GHz carrier. *in Proc. European Micrwoave Integrated Circuit Conf., Manchester*, pages 238–241, 2011.

[14] **J. Antes**, D. Lopez-Diaz, A. Tessmann, A. Leuther, H. Massler, T. Zwick, O.Ambacher, I. Kallfass. Wireless multi-Gigabit data transmission using active MMIC components at 220 GHz. *Int. Journal of Microwave and Wireless Technologies*, 4:291–298, Jun. 2012.

[15] **J. Antes**, D. Lopez-Diaz, M. Schlechtweg, S. Diebold, H. Gulan, F. Poprawa, F. Kurz, R. Henneberger, E. Roppelt, S. König, J. Leuthold, T. Schneider, T. Zwick, O. Ambacher, I. Kallfass. Systemkonzept und Realisierung einer Millimeterwellen-Richtfunkstrecke mit Datenraten über 12,5 Gbit/s. *VDE-ITG-Fachtagung Mobilkommunikation 16*, Mobilkommunikation. Technologien und Anwendungen : Vorträge der 16. ITG-Fachtagung(ITG-Fachbericht 230, ISBN: 978-3-8007-3352-1):27–33, May 2011.

[16] **J. Antes**, D. Lopez-Diaz, U. J. Lewark, S. Wagner, A. Tessmann, A. Leuther, I. Kallfass. A high linearity I/Q Mixer for High Data Rate E-Band Wireless

Communication Links. *in Proc. European Microwave Conf., Amsterdam*, pages 1–4, 2012.

[17] **J. Antes**, F. Boes, A. Tessmann, R. Henneberger, I. Kallfass. High Data Rate Wireless Communication using a 240 GHz carrier. *IEEE802 Interim Meeting, Los Angeles*, January 2014.

[18] **J. Antes**, F. Boes, D. Meier, U. Lewark, A. Tessmann, A. Leuther, R. Henneberger, I. Kallfass. Multi-Gigabit Data Transmission using MMIC-based E-Band Frontends. *in Proc. Radio Wireless Week (RWW)*, pages 1–3, Jan. 2014.

[19] **J. Antes**, J. Reichart, D. Lopez-Diaz, A. Tessmann, F. Poprawa, F. Kurz, T. Schneider, H. Massler, I. Kallfass. System concept and implementation of a mmW wireless link providing data rates up to 25 Gbit/s. *in Proc. 3rd Int. IEEE Conf. on Microwaves, Communications, Antennas and Electronic Systems, COMCAS, Tel Aviv*, Nov. 2011.

[20] **J. Antes**, S. Koenig, A. Leuther, H. Massler, J. Leuthold, O. Ambacher, I. Kallfass. 220 GHz wireless data transmission experiments up to 30 Gbit/s. *in Proc. IEEE MTT-S Int. Microwave Symposium, Montreal*, June 2012.

[21] **J. Antes**, S. Koenig, D. Lopez-Diaz, F. Boes, A. Tessmann, O. Ambacher, T. Zwick, I. Kallfass. Data transmission of an 8-PSK modulated 30 Gbit/s signal using an MMIC-based 240 GHz wireless link. *in Proc. IEEE Int. Microwave Symp., Seattle*, pages 1–4, 2013.

[22] **J. Antes**, T. Mahler, T. Zwick, A. Tessmann, O. Ambacher, I. Kallfass. Study on data transmission of complex modulated signals using an MMIC-based 220GHz wireless link. *in Proc. International Symposium on Signals, Systems and Electronics, Potsdam*, pages 1–4, Oct. 2012.

[23] **J. Antes**, U. J. Lewark, A. Tessmann, S. Wagner, T. Zwick, I. Kallfass. MMIC-based chipset for multi-Gigabit Satellite Links in E-Band. *in Proc. IEEE Int. Conf. on Wireless Information Technology and Systems, Hawaii*, pages 1–4, Dec. 2012.

[24] S. Koenig, D. Lopez-Diaz, **J. Antes**, F. Boes, R. Henneberger, A. Leuther, A. Tessmann, R. Schmogrow, D. Hillerkuss, R. Palmer, T. Zwick, C. Koos, W. Freude, O. Ambacher, J. Leuthold, and I. Kallfass. Wireless sub-THz communication system with high data rate enabled by RF photonics and active MMIC technology. In *IEEE Photonics Conference (IPC'14)*, pages 1–3, Oct 2014, (invited).

[25] M. Schlechtweg, I. Kallfass, A. Tessmann, F. Thome, A. Leuther, H. Massler, M. Riessle, M. Zink, D. Lopez-Diaz, **J. Antes**, U.J. Lewark. Metamorphic HEMT Based Terahertz Monolithic Integrated Circuits. *in Proc. Workshop WS4: Recent Advances in MMW, Submmwave and THz MMICs for Novel System Design, International Wireless Symposium (IWS), Beijing*, April 2013.

[26] D. Meier, **J. Antes**, F. Boes, T. Messinger, D. Müller, R. Henneberger, A. Tessmann, and I. Kallfass. Reliability of an E-Band Wireless Link for Transmission Distances up to 15.7 km. In *submitted for publication to German Microwave Conference, 2015*, 2015.

[27] T. Messinger, D. Müller, **J. Antes**, S. Wagner, A. Tessmann, and I. Kallfass. Divide-by-8 Phase Detector MMIC for PLL-based Carrier Recovery in E-Band Communication. In *submitted for publication to German Microwave Conference, 2015*, 2015.

[28] S. Koenig, D. Lopez-Diaz, **J. Antes**, F. Boes, R. Henneberger, A. Leuther, A. Tessmann, R. Schmogrow, D. Hillerkuss, R. Palmer, T. Zwick, C. Koos, W. Freude, O. Ambacher, J. Leuthold, I. Kallfass. Wireless sub-THz communication system with high data rate. *Nat Photon*, 7(12):977–981, 12 2013.

[29] S. Koenig, F. Boes, D. Lopez-Diaz, **J. Antes**, R. Henneberger, R. Schmogrow, D. Hillerkuss, R. Palmer, T. Zwick, C. Koos, W. Freude, O. Ambacher, I. Kallfass, J. Leuthold. 100 Gbit/s Wireless Link with mm-Wave Photonics. *in Proc. OFC, Anaheim*, 2013.

[30] S. Koenig, **J. Antes**, D. Loez-Dias, I. Kallfass, T. Zwick, W. Freude and J. Leuthold. Multi-Gigabit Wireless Signals over Fiber. In *Workshop for Modelling of optical Components & Systems*. ITG-Fachgruppe 5.3.1, Nov. 2011.

[31] S. Koenig, **J. Antes**, D. Lopez-Diaz, I. Kallfass, T. Zwick, C. Koos, W. Freude, J. Leuthold. High-Speed Wireless Bridge at 220 GHz Connecting Two Fiber-Optic Links Each Spanning up to 20 km. *in Proc. Optical Fiber Communication Conference (OFC)*, Mar. 2012.

[32] S. Koenig, **J. Antes**, D. Lopez-Diaz, R. Schmogrow, T. Zwick, C. Koos, W. Freude, J. Leuthold, I. Kallfass. 20 Gbit/s Wireless Bridge at 220 GHz Connecting Two Fiber-Optic Links. *Journal of Optical Communications and Networking (IEEE/OSA)*, 6(1):54–61, 2014.

[33] **J. Antes**, F. Boes, D. Meier, T. Messinger, U. Lewark, A Tessmann, S. Wagner, and I Kallfass. Ultra-wideband single-balanced transmitter-MMIC for 300

GHz communication systems. In *Microwave Symposium (IMS), 2014 IEEE MTT-S International*, pages 1–3, June 2014.

[34] **J. Antes**, F. Boes, D. Meier, T. Messinger, U. J. Lewark, A Tessmann, S. Wagner, and I Kallfass. 15 km, 15Gbit/s E-band Data Transmission. *IEEE Trans. on Microwave Theory and Techniques*, submitted for publication.

[35] **J. Antes**, F. Boes, T. Messinger, U. J. Lewark, T. Mahler, A Tessmann, R. Henneberger, T. Zwick, and I Kallfass. Multi-Gigabit Millimeter Wave Wireless Communication in Realistic Transmission Environments. *IEEE Trans. on Terahertz Science and Technology*, accepted for publication.

[36] **J. Antes** and I Kallfass. Performance Estimation for Broadband Multi-Gigabit Millimeter and Sub-Millimeter Wave Wireless Communication Links. *IEEE Trans. on Microwave Theory and Techniques*, PP(99):1–13, 2015.

[37] U. J. Lewark, **J. Antes**, M. Kuri, R. Henneberger, A. Tessmann, S. Wagner, A. Leuther, T. Zwick, I. Kallfass. MMIC-Based Module-Level Frequency Generation for E-Band Communication Systems. *in Proc. Radio Wireless Week*, pages 1–4, Jan. 2014.

[38] U. Lewark, **J. Antes**, H. Massler, A. Leuther, I. Kallfass. Active Frequency Multiplier MMICs for W-Band Signal Sources in Millimeter-Wave Communication Systems. *in Proc. 12. GMM/ITG-Fachtagung ANALOG, Erlangen*, Nov. 2011.

[39] U. Lewark, **J. Antes**, H. Massler, A. Leuther, I. Kallfass. E-Band Active Frequency-Multiplier-By-8 MMIC with >20 dB Conversion Gain and Excellent Spurious Suppression. *in Proc. IEEE MTT-S Int. Microwave Symposium, Montreal*, pages 1–4, June 2012.

[40] U.J. Lewark, **J. Antes**, J. Walheim, J. Timmermann, T. Zwick, I. Kallfass. Link budget analysis for future E-band gigabit satellite communication links (71-76 and 81-84 Ghz). *CEAS Space Journal*, pages 1–6, 2013.